

THE UNIVERSITY OF HULL

Design and investigation of novel photoactive liquid crystalline
organic-inorganic hybrids.

being a Thesis submitted for the Degree of Doctor of Philosophy

in the University of Hull

by

Ana João Tavares Ferreira

May, 2013

ACKNOWLEDGEMENTS

I would like to thank to my supervisor, Professor Georg Mehl, for his support throughout this period. I would also like to express my appreciation for his time and patience for answering to my endless number of questions.

I would like to thank to Dr. Mike Hird, my second supervisor, for helpful advice.

I would like to thank all the group colleagues with whom I had the pleasure to work with and always helped me out when I needed: Dr. Alex Kohlmeier, Dr. Becky Batheclor, Dr. Eric Yu, Dr. Fabio Lodato, Dr. Chris Schubert, Ionut Ichim, Bai Jai Tang, Faleh Alqahtany, Ziauddin Ahmed, James Hussey, Eman Alluhaybi and Amos Olusegun. I would especially like to thank to Dr. Chris Welch and Dr. Maria-Gabriela Tamba, for always being available to discuss my work and for allowing me to learn with them about synthesis, OPM, DSC, X-ray and much more.

Thanks to Dr. Rob Lewis for his help with the NMR, Mr. Bob Knight for lending me NMR tubes for photosensitive materials which made my life much easier.

I would like to thank Prof. Stumpe and Jaroslaw Tomczyk for having me in the the Fraunhofer Institute in Potsdam, Germany, as part of the MC-ITN-“Dendreamers” project, where some of the work presented here was done.

Finally I would like to thank my family and friends whom despite being far away, were always there, advising, listening, laughing...thank you, so very much! I would like to thank my brother, for the precious and inspiring phone conversations that we had. And to Chris, muito obrigada.

To conclude I would like to dedicate this work to my grandparents: Ferreira, Madalena, Te, Alberto and Armanda; from whom I have learned so much and make me feel very humble.

ABSTRACT

This work describes and discusses the design, synthesis and characterization of novel photoactive liquid crystalline silsesquioxanes. The investigations carried out include the initial design, chemical synthesis and characterization, photochemical properties, liquid crystalline behaviour and optical properties.

The new materials were carefully designed in order to target the specific requirements of incorporating azobenzene moieties as photoactive groups and exhibiting liquid crystalline properties, specifically nematic mesophases and glassy states at room temperature. In order to achieve these properties four series of monodisperse inorganic/organic hybrids were synthesised. The liquid crystalline properties were tuned using a multiple-mesogen approach similar to the one used in polymeric systems. Tools used were variation of mesogen groups and the use of a combination of laterally and terminally connected mesogens. Chemical characterization of the materials was carried out and mesogen composition determined.

Photochromic behaviour was investigated followed by a study of the liquid crystalline properties using several techniques including OPM, DSC and XRD studies. The phase structure was determined by means of detailed temperature dependent XRD studies using both mechanically and magnetically aligned samples. New assembly modes such as lamellar nematic phases were proposed.

The optical properties were investigated by means of photoorientation and SRG studies in thin film samples which were carried out by me in collaboration with Jaroslaw Tomczyk and Professor Joachim Stumpe in the Fraunhofer Institute in Potsdam, Germany, during my visit as part of the MC-ITN-“Dendreamers” project.

ABBREVIATIONS

DNA	Deoxyribonucleic acid
LCD	Liquid crystal display
LC	Liquid crystals
LCP	Liquid crystal polymers
N_B	Biaxial nematic
SmC	Smectic C
N	Nematic
LamN	Lamellar nematic
SmA	Smectic A
SmI	Smectic I
Col_h	Columnar hexagonal
Col_r	Columnar rectangular
Col_o	Columnar oblique
Col_s	Columnar square
OPM	Optical polarizing microscopy
DSC	Differential scanning calorimetry
XRD	X-ray diffraction
N_C	Calamitic nematic
N_D	Discotic nematic
POSS	Polyhedral octa(dimethylsiloxy)octasilsesquioxane
NMR	Nuclear magnetic resonance
EA	Elemental analysis
g	Glass
T_g	Glass transition
Cr	Crystal
N*	Chiral nematic
Iso	Isotropic
SmX	Smectic X
BC	Bent core
5CB	4-Cyano-4'-pentylbiphenyl
UV	Ultra violet
CPL	Circularly polarized light
EPL	Eliptically polarized light

Vis	Visible
IR	Infrared
LCE	Liquid crystal elastomer
NLO	Non linear optics
SRG	Surface relief grating
HDS	Holographic data storage
CD	Compact disc
LbL	Langmuir Blodgett layer
BS	Beam splitter

CONTENTS

CHAPTER 1: INTRODUCTION TO LIQUID CRYSTALS	1
1.1 Brief history of liquid crystals	1
1.2 Definition of liquid crystals	1
1.3 Classification of liquid crystals	2
1.4 Characterization of liquid crystals	9
1.4.1 Optical polarizer microscopy (OPM)	9
1.4.2 Differential scanning calorimetry (DSC)	12
1.4.3 X-ray diffraction (XRD)	16
1.4.3.1 X-ray diffraction general concepts	16
1.4.3.2 X-ray diffraction of liquid crystals	17
CHAPTER 2: DENDRIMERS	26
2.1 Dendrimers general concepts	26
2.2 Dendrimers structure	27
2.3 Synthesis of dendrimers	28
2.4 Liquid crystalline dendrimers	29
2.4.1 Silicon containing dendrimers	30
2.5 Polyhedral octa(dimethylsiloxy)octasilsesquioxane (POSS)	32
2.5.1 Nomenclature and structure of POSS	33
2.5.2 Synthesis of POSS	34
2.5.3 Functionalization of POSS by hydrosilylation	38
2.6 LC silsesquioxanes	39
CHAPTER 3: PHOTOCROMIC AZOBENZENE CONTAINING MATERIALS	56
3.1 Photochromism: general concepts	56
3.2 Azobenzenes	56
3.3 Changes induced by photoisomerization of azobenzenes, from molecular level to macroscale	58
3.3.1 Molecular motion	61
3.3.2 Motion at domain level	62
3.3.3 Macroscopic motions	65

3.4	Dendrimers containing azobenzene groups	69
3.5	POSS in azobenzene moieties	71
CHAPTER 4: PHOTOORIENTATION		76
4.1	Photoorientation: general concepts	76
4.2	Optically induced anisotropy in azobenzene containing materials	77
4.3	Holographic data storage (HDS): history and general concepts	80
4.4	Surface relief gratings	82
4.4.1	Surface relief gratings inscription in azobenzene containing materials	84
4.4.1.1	Guest-host systems	84
4.4.1.2	Azobenzene functionalized systems	85
CHAPTER 5: MOTIVATION AND AIMS		94
CHAPTER 6: EXPERIMENTAL		95
6.1	Synthesis of 1-nitro-4-(octyloxy)benzene (93)	96
6.2	Synthesis of 4-(octyloxy)aniline (94)	96
6.3	Synthesis of 4-((octyloxy)phenyl)diazenyl)phenol (95)	97
6.4	Synthesis of 4-((4-octyloxy)phenyl)diazenyl)phenol 4-(octyloxy)-2-(pent-4-enyloxy)benzoate (96)	98
6.5	Synthesis of Cyanobiphenyl derivatives (97-99)	99
6.6	Synthesis of allyl-4-hydroxybenzoate (100)	100
6.7	Synthesis of methyl 4-(allyloxy)benzoate (101)	101
6.8	Synthesis of methyl 4-(allyloxy)benzoic acid (102)	101
6.9	Synthesis of methyl 4'-cyano-[1,1'-biphenyl]-4-yl-4(allyloxy)benzoate (103)	102
6.10	Synthesis of POSS derivatives	102
CHAPTER 7: DISCUSSION		106
DISCUSSION PART I		106
7.1	Synthesis and characterization of low molar mass mesogens	106
7.2	Synthesis and characterization of POSS derivatives	114
7.3	Liquid crystalline properties of low molar mass mesogens	118

7.4	Liquid crystalline properties of POSS derivatives	123
7.5	Photochromic studies of the materials synthesized	145
	DISCUSSION PART II	151
7.6	Phase structure assignment based on XRD studies	151
7.6.1	Low molecular weight mesogen	151
7.6.2	High molecular weight materials	153
	DISCUSSION PART II	230
7.7	Discussion of photoorientation and SRG inscription	230
	CHAPTER 8: CONCLUSIONS AND OUTLOOK	239
8.1	Conclusions	239
8.2	Outlook	240
	CHAPTER 9: REFERENCES	241

FIGURES INDEX

Figure 1: Molecules (1), ⁵ (2), ⁶ (3) ⁷ and (4) ⁸ are examples of calamitic molecules.....	2
Figure 2: Molecules (5) ⁹ and (6) ¹⁰ are examples of discotic liquid crystals.	2
Figure 3: Example of a pyramidic liquid crystalline molecule. ¹¹	3
Figure 4: Example of bent core liquid crystalline molecules. ¹¹	3
Figure 5: Organization of liquid crystals. ²¹	4
Figure 6: Schematic representation of a uniaxial nematic phase of a) calamitic and b) discotic mesogens.....	5
Figure 7: Representation of the biaxial nematic phase (N_B), formed by board-like molecules.....	5
Figure 8: Representation of tetrapode systems that show a biaxial nematic phase (N_B). ^{38, 39}	6
Figure 9: Representation of systems showing lamellar nematic phases. ⁴⁹⁻⁵⁴	7
Figure 10: Representation of polymeric system showing lamellar nematic phases. ⁵⁵⁻⁵⁸ ..	7
Figure 11: Schematic representation of a) smectic A and b) smectic C phase.	8
Figure 12: Schematic representation of a discotic columnar phase.	9
Figure 13: Plane polarized light.	10
Figure 14: Optical polarizing microscope. ⁶¹	10
Figure 15: Interaction of unpolarized light with a birefringent medium.	10
Figure 16: Birefringent specimen between cross polarizers and its interaction with light. ⁶¹	11
Figure 17: Representation of a) homeotropic alignment and b) planar alignment for calamitic liquid crystal molecules	12
Figure 18: Example of a DSC curve for a liquid crystal with four mesophases.....	15
Figure 19: Diffraction from parallel planes.	16
Figure 20: Definition of the scattering vector Q	17
Figure 21: Origin of powder patterns.....	17
Figure 22: a) Molecular organization of an aligned nematic sample. b) Representation of the diffraction pattern of an aligned nematic sample	18
Figure 23: Representation of the radial plot of intensities of a nematic sample.....	19
Figure 24: Molecular organization, on the left and representation of the diffraction pattern of a nematic with cybotactic clusters of an aligned sample, on the right.	19
Figure 25: Diffraction pattern obtained for the N_B phase observed in lyotropic systems of potassium laurate and 1-decanol in D_2O , investigated by Gallerne <i>et al.</i> ²⁷⁻²⁹	20
Figure 26: Representation of goethite particles shape studied by van den Pol <i>et al.</i> ⁷² ...	20

Figure 27: Top- SAXS pattern with magnetic field parallel to x-ray beam and different intensities: a) 3 mT, b) 40 mT and c) magnetic field perpendicular to x-ray beam. Bottom: intensity profiles of a), b) and c) respectively. The horizontal integrations are represented by the solid line and the vertical direction is plotted in dashed line. ⁷²	21
Figure 28: Molecular organization of the biaxial nematic phase in a magnetic field perpendicular to the paper, in the systems studied by van den Pol <i>et al.</i> ⁷²	21
Figure 29: Molecular organization of the biaxial nematic phase in a magnetic field perpendicular to the paper. In systems studied by van den Pol <i>et al.</i> ⁷²	22
Figure 30: a) diffraction pattern of the LamN phase, b) radial distribution of intensities c) azimuthal distribution of the wide angle scattering. ⁴⁹	22
Figure 31: Molecular organization of bolaamphiphilic systems in the lamellar nematic phase. ^{49, 73}	23
Figure 32: Molecular organization, on the left and representation of the diffraction pattern of a SmA phase.	24
Figure 33: Representation of the radial plot of intensities of a smectic sample.	24
Figure 34: a) Molecular organization of an aligned SmC sample. b) Representation of the diffraction pattern of an aligned SmC sample.....	25
Figure 35: Molecular organization of aligned SmC samples on the right and representation of the corresponding diffraction patterns.	25
Figure 36: Analogy between architecture and a branching tree, where the name dendrimers took inspiration.....	26
Figure 37: Classification of Dendrimers. ⁸⁰	27
Figure 38: Dendrimers constitution.	28
Figure 39: Representation of divergent synthesis of dendrimers. ⁸²	28
Figure 40: Representation of convergent synthesis of dendrimers. ⁸²	29
Figure 41: a) Main chain LC dendrimers; b) Side chain LC dendrimers. ⁸⁴	29
Figure 42: System studied by Shibaev. ⁸⁸	30
Figure 43: Molecular assembly of the molecules represented in Figure 42 in the SmA phase. ^{88, 89}	31
Figure 44: System studied by Mehl <i>et al.</i> ⁹⁰	31
Figure 45: System studied by Kieffer and co-workers. ⁴⁹	32
Figure 46: Chemical structures of different types of silsesquioxanes. ⁹⁶	33
Figure 47: Cubic silsesquioxanes. a) T ₈ R ₈ (T = carbon-SiO _{1.5}). b) Q ₈ (Q = SiO ₄). c) Typical sizes/volumes. ⁹⁶	34
Figure 48: Synthesis of POSS cubes (Q ₈ type) Hesegawa and co-workers. ^{113, 114}	35

Figure 49: Examples of functionalization of POSS cores through hydrosilylation. ⁹⁶	36
Figure 50: Synthesis of POSS derivatives by nitration, iodination, bromination. ⁹⁶	37
Figure 51: Synthesis of a POSS derivative starting with a partial condensed silsesquioxane. ¹¹⁵	37
Figure 52: Hydrosilylation of silsesquioxanes.	38
Figure 53: α - and β - addition in hydrosilylation reactions. ¹²³	39
Figure 54: In this figure, the general components of a silsesquioxane core dendrimer. ¹²³	40
Figure 55: System studied by Mehl <i>et al.</i> ¹³⁵	40
Figure 56: Representation of interdigitation of molecules represented in Figure 55.....	41
Figure 57: System studied by Saez and co-workers. ¹³⁶	42
Figure 58: Representation of possible organization of molecules in Sm phases. ¹³⁶	43
Figure 59: System studied by Sellinger <i>et al.</i> ¹³⁷	43
Figure 60: System studied by Zang <i>et al.</i> ¹³⁸	44
Figure 61: System studied by Elsäßer and co-workers. ¹⁴⁰	46
Figure 62: System studied by Karahaliou <i>et al.</i> ⁴⁷	47
Figure 63: System studied by Saez <i>et al.</i> ¹⁴¹	48
Figure 64: System studied by Chujo <i>et al.</i> ¹⁴²	49
Figure 65: System studied by Chujo <i>et al.</i> ¹⁴³	50
Figure 66: System studied by Pan <i>et al.</i> ¹⁴⁴	52
Figure 67: System studied by Soltysiak <i>et al.</i> ¹⁴⁵	53
Figure 68: System studied by Wang <i>et al.</i> ¹⁴⁶	54
Figure 69: Representation of absorption spectra of a photochromic system.	56
Figure 70: Molecular structure of azobenzenes	57
Figure 71: Azobenzene <i>trans</i> isomer can be converted into its <i>cis</i> form by irradiation with UV light. Back isomerisation to the <i>trans</i> form is accomplished thermally or by irradiation with a distinct wavelength light.....	57
Figure 72: Simplified state model for azobenzene chromophres where ϵ denotes the extinction coefficients, ϕ denotes the photoisomerisation quantum yields and k represents the rate of thermal relaxation. ¹⁵⁰	57
Figure 73: Representation of isomerisation mechanisms. ¹⁴⁷	58
Figure 74: Scheme of hierarchical organization from molecule to materials of azobenzene containing materials and some representative research targets for each hierarchy. ¹⁵⁵	59

Figure 75: Schematic representation of statistical photoorientation. An isotropic distribution of chromophers aligns when irradiated with polarised light. Isotropic state is recovered by irradiation or circularly polarized light. ¹⁵⁰	61
Figure 76: Representation of the effect of trans-cis isomerization in N-Iso transition in guest-host liquid crystals. The liquid crystal used is 4-cyano-4'-pentylbiphenyl (5CB). ¹⁶⁰	63
Figure 77: System studied by Finkelmann <i>et al.</i> ¹⁸¹	66
Figure 78: System used by Li <i>et al.</i> ¹⁸⁸	66
Figure 79: LCE studied by Jiang <i>et al.</i> ¹⁹⁰	68
Figure 80: First photochromic dendrimer reported. ¹⁹⁹	70
Figure 81: Structural formula of the dendrimer used by Shibaev. ¹⁹⁴	71
Figure 82: System studied by Xie <i>et al.</i> ²⁰²	72
Figure 83: System studied by Su <i>et al.</i> ²⁰⁵	72
Figure 84: System studied by Bialecka-Florjanczyk <i>et al.</i> ²⁰⁴	74
Figure 85: System studied by Todorov <i>et al.</i> ²¹⁴	77
Figure 86: Example of the polar graphics introduced by Anderle <i>et al.</i> ²²¹	78
Figure 87: Azotolane polymers studied by Okano <i>et al.</i> ²³⁷	79
Figure 88: Representation of a surface relief grating in azobenzene containing materials.	83
Figure 89: Systems studied by Victor <i>et al.</i> ²⁶³	85
Figure 90: Different processes that occur during SRG inscription. a) SRGS gratings, b) density grating, c) photoorientation of the molecules irradiated and c) <i>trans-cis</i> isomerization. ²⁷⁵	87
Figure 91: Multiple SRGs recorded by rotation of the azobenzene containing film. ²⁷⁸ ..	88
Figure 92: System studied by Eich <i>et al.</i> First liquid crystalline polymer where birefringence and dichroism were induced. ²³⁵	89
Figure 93: System studied by Yu <i>et al.</i> ²⁸³	91
Figure 94: Systems studied by Tomczyk <i>et al.</i> ²⁸⁴	92
Figure 95: Silsesquioxane core used in the synthesis of compounds 104 – 116.	103
Figure 96: Synthesis of mesogen 96.	106
Figure 97: ¹ H NMR spectra of compound 94; before (Spectrum A) and after (Spectrum B) being purified by chromatography.	108
Figure 98: ¹ H NMR spectra of compound 96. Spectrum A, first spectrum carried; Spectrum B was carried after 1 hour in light and Spectrum C was performed after the sample be in the dark.....	111

Figure 99: Scheme of synthesis of compounds 97 –99.....	111
Figure 100: Reaction scheme for the synthesis of compound 102. ²⁹⁰	112
Figure 101: Compound 100.	112
Figure 102: ¹ H NMR spectra of compound 102 (Spectrum A) and compound 100 (Spectrum B).	113
Figure 103: Scheme of the strategy used to synthesise compound 103.....	113
Figure 104: Siloxane core I and mesogens used to the syntheses of compounds 104 to 116.....	114
Figure 105: ¹ H NMR spectra of compound 112 in Spectrum A and mesogens 96 and 99 in Spectrum B and C.	116
Figure 106: Texture obtained by OPM for compound 96.....	119
Figure 107: DSC curves a) 97, b) 98, c) 99 and d) 103.	120
Figure 108: Textures of compound 97 obtained by OPM.....	120
Figure 109: Schlieren texture obtained by OPM for 98.....	121
Figure 110: OPM textures of compound 99.....	121
Figure 111: DSC curves for compound 103.	122
Figure 112: Texture obtained by OPM for compound 103. a) Marbled texture at 130 °C. b) Marbled texture at 160 °C.....	122
Figure 113: DSC curves of 104: a) sample weight 5.37 mg, and heating/cooling rates of 10 °C/ min for curves 1 and 2 and 5 °/min in curve 3 b) sample weight 3.6 mg, and heating/cooling rates of 10 °C/ min for all the curves.	124
Figure 114: DSC curves for 104. The same sample was subject to different cooling rates. a) 2 °/min, b) 10 °C/min and c) 20 °C/min.....	125
Figure 115: DSC curves for 104. Experiments made using a open pan system and different heating/cooling rates were used. a) 2 °/min, b) 10 °C/min and c) 20 °C/min.	126
Figure 116: Micrographs of the nematic phase of 104. a) marbled texture; b) marbled texture with Sclieren features; c) and d) marbled texture after shearing.	127
Figure 117: Micrographs of the nematic phase of 106.	128
Figure 118: DSC cuves of compound 106.	128
Figure 119: Micrographs of the nematic phase of 105.	130
Figure 120: Micrographs of the smectic phase of 108.....	131
Figure 121: Micrographs of the nematic phase of compound 109.....	131
Figure 122: Micrographs of the nematic phase of 110.	132
Figure 123: DSC curves of 111. Heating/cooling rate is 10 °C/min.....	133

Figure 124: Micrographs for 111.	133
Figure 125: OPM textures for compound 112.	134
Figure 126: DSC curves for compound 112.	135
Figure 127: Micrographs obtained for 113 during OPM studies.	135
Figure 128: DSC curves for 113.	136
Figure 129: Texture observed with polarized optical microscope of compound 114...	136
Figure 130: DSC curves for compound 114.	137
Figure 131: Micrographs obtained for 115 during OPM studies.	138
Figure 132: Micrographs of N-Iso transition 115.	139
Figure 133: DSC curves of 115.....	139
Figure 134: Micrographs obtained for 116.	140
Figure 135: DSC curves obtained for 116.....	140
Figure 136: Compound 96.	142
Figure 137: Thermal gravimetric spectra of compound 115. Analysis carried under N ₂	144
Figure 138: OPM images for irradiation of 96 with light.	145
Figure 139: OPM images for irradiation of 104 with light.	146
Figure 140: OPM images for irradiation of 106 with light.	147
Figure 141: UV/Vis spectra of a solution of 96 in DCM, conc. 1.56×10^{-4} mol dm ⁻³ .	148
Figure 142: UV-Vis spectra of 104 in solution Under UV irradiation (313 nm).....	149
Figure 143: UV-Vis spectra of 115 in solution under UV irradiation (313 nm).....	149
Figure 144: ¹ H NMR spectra for compounds 96 and 104 in the <i>trans</i> form and in the photostationary state.....	150
Figure 145: X-ray diffraction data from compound 96. a) 2D diffraction pattern, b) radially integrated scans, c) and d) azimuthally integrated scans of peaks A and B, respectively.	152
Figure 146: Scheme of series I.....	153
Figure 147: Diffraction pattern of an unaligned sample of compound 104.	154
Figure 148: a) Radially integrated scans, b), c) and d) Azimutthaly integrated scans for peak A, peak B and peak C respectively.....	155
Figure 149: a) Representation of the process of preparation of fibre samples. b) Example of the fibres used in the XRD experiments.	156
Figure 150: X-Ray diffraction data from compound 104. a) 2D diffraction pattern. b) radially integrated scans, black curve data collected parallel to \vec{H} and blue line data	

integrated perpendicular to \vec{H} . c), d) and e) azimuthally integrated scans of peaks A, B and C, respectively.	156
Figure 151: Top: System studied by Karahaliou <i>et al.</i> ⁴⁸ Bottom: a) 2D diffraction pattern of mesogen b) 2D diffraction pattern of silsesquioxane derivative.	157
Figure 152: Left: Systems studied by Tschierske <i>et al.</i> b) Diffraction pattern of compound 10 ⁴⁹ c) Model proposed for the LamN phase of compound 10. ⁴⁹	159
Figure 153: Representation of an antiparallel organization in 104.	160
Figure 154: Proposed molecular arrangement of the azobenzene mesogens in turn of the silsesquioxane core.	161
Figure 155: Representation of a cylindrical model.	161
Figure 156: Molecular arrangement considering the minimum thickness possible for 104.	162
Figure 157: Molecular arrangement of 104 considering four mesogenes on top and bottom of the silsesquioxane core.	162
Figure 158: Molecular arrangement of 104 considering three mesogenes on top and bottom of the silsesquioxane core.	162
Figure 159: Model proposed for the lamellar nematic phase of compound 104.	163
Figure 160: 2D diffraction patterns for 104 collected on cooling. The data was collected every 5 °C for 1800 s.	164
Figure 161: Diffraction pattern represented in Figure 160, T = 30 °C.	164
Figure 162: X-ray diffraction data from compound 104-exp.1. a) radially integrated scans, b), c), d) and e) azimuthally integrated scans of peaks A, B, C, and D, respectively.	165
Figure 163: a) Temperature dependence of the diffraction angle for 104 at 30 °C. b) Temperature dependence of the distribution of intensities at 30 °C.	166
Figure 164: a) scheme of the experimental set up. b) 2D diffraction pattern of compound 104-exp2. c) Radially integrated scans. d) Azimuthally integration for peaks A to D.	167
Figure 165: 2D diffraction patterns for 104 exp. 3 collected on cooling. The data was collected every 1K for 1800 s.	169
Figure 166: x-ray diffraction data from compound 104-exp.3. a) radially integrated scans, b), c) and d) azimuthally integrated scans of peaks A, B and C, respectively. ...	169
Figure 167: Diffractogram of compound 106.	171
Figure 168: Radially integrated pattern of compound 106. a) Integration parallel to the magnetic field \mathbf{H} and b) Integration perpendicular to the magnetic field \mathbf{H}	172

Figure 169: a) Amplification of the small angle region of the 2D diffraction pattern of compound 106. b) Radially integrated pattern for the region represented in a) Blue plot integration above the equator, black plot integration below the equator.	173
Figure 170: a) Diffractogram of compound 106 and representation of the are integrated of 2θ over χ . b) Azimuthally integrated XRD pattern.....	173
Figure 171: Temperature dependence of the distribution of intensities for the area represented in Figure 170 a).....	174
Figure 172: Azimuthally integrated XRD patterns of 106. a) b) and c) represent the χ plots for peaks A, B and C respectively.....	174
Figure 173: Schematic representation of the lamellar nematic phase.	175
Figure 174: Representation of the molecular unit cell of 106.....	177
Figure 175: Representation of molecular packing of 108 considering the model proposed.....	178
Figure 176: Lamellar nematic molecular arrangement for 106.	178
Figure 177: a) 2D diffraction pattern of compound 105. b) Radially integrated pattern of 105.....	179
Figure 178: Diffractogram of compound 108 at 25 °C.....	180
Figure 179: Diffractograms of compound 108 at 85°C and 125 °C.....	180
Figure 180: Radially integrated plots parallel to the magnetic field H at a) 85 °C and b) 125°C.	181
Figure 181: Radially integrated plots perpendicular to the magnetic field H at a) 85 °C and b) 125°C.	181
Figure 182: Variation of the layer spacing of compound 108 with temperature.	182
Figure 183: a) to d) azimuthally integrated plots for peaks D and C at 85 °C and 125 °C.	183
Figure 184: a) Diffraction pattern and representation of azimuthally integrated region. b) Azimuthally integrated plot for compound 108 at 85 °C. c) Azimuthally integrated plot for compound 108 at 125 °C.....	183
Figure 185: Model representing the self-assembly of 108.....	184
Figure 186: Scheme of series II.	186
Figure 187: Diffractograms of compound 109 at different temperatures.	187
Figure 188: Radially integrated plots for 109: a) 30 °C; b) 45 °C; c) 60 °C; d) 70 °C.	188
Figure 189: Azimuthally integrated plots of peak A for compound 109 at several temperatures.	189

Figure 190: Azimuthally integrated plots of peak B for compound 109. a) 30 °C and b) 70 °C.	190
Figure 191: Azimuthally integrated plots of peak C for compound 109. a) 30 °C and b) 70 °C.	190
Figure 192: Representation of possible packing of molecules in the Lam N phase in 109.	192
Figure 193: Diffraction patterns for compound 110, where the green sequence corresponds to Program I and the Blue to Program II.	193
Figure 194: Radially integrated patterns of compound 110 for a) 25 °C, b) 45 °C, c) 60 °C and d) 80 °C.	194
Figure 195: Radially integrated scans with temperature b) variation of distance with temperature.	195
Figure 196: Azimuthally integrated plots of peak A for compound 110 for several temperatures, the plots show that the splitting of the peak for temperatures above 25 °C these intensities have merged.	195
Figure 197: Azimuthally integrated plots of peak B for compound 110 at several temperatures, top figure shows at 25 °C a splitting of the peak. Above this temperature the intensities have merged.	196
Figure 198: Amplification of the small angle region of the diffractograms of compound 110 at 25 °C top image and 80 °C bottom image.	197
Figure 199: Azimuthally integrated plots of peak C for compound 110 at several temperatures.	197
Figure 200: Representation of the molecular unit cell of compound 110.	199
Figure 201: Representation of molecular packing of 110 considering the model proposed.	199
Figure 202: Diffractograms of compound 111 at different temperatures.	200
Figure 203: Radially integrated patterns of 111 for a) 155 °C, b) 120 °C and c) 180 °C.	201
Figure 204: Azimuthally integrated plots of peak A for compound 111 at several temperatures.	202
Figure 205: Azimuthally integrated plots of peak B for compound 111 at several temperatures.	203
Figure 206: Azimuthally integrated plots of peak C for compound 111 at several temperatures.	203
Figure 207: Scheme of series III.	204

Figure 208: Diffractograms of compound 112 at different temperatures.	205
Figure 209: Radially integrated patterns of 112 for a) 25 °C, b) 37 °C, c) 49 °C and d) 97 °C.	206
Figure 210: Dependence of θ scans with temperature.	207
Figure 211: Azimuthally integrated plots of peak A for compound 112 at several temperatures.	207
Figure 212: Azimuthally integrated plots of peak B for compound 112 at several temperatures.	208
Figure 213: Amplification of the small angle region of the diffractogram of compound 112 at 25 °C.....	208
Figure 214: Azimuthally integrated plots of peak C for compound 112 at several temperatures.	209
Figure 215: Proposed molecular packing for compound 112.	210
Figure 216: Proposed molecular arrangement on the lamellar nematic of compound 112.	210
Figure 217: Diffractograms of compound 114 at different temperatures.	211
Figure 218: Amplification of the wide angle region of 114 at 25 °C and 105 °C.	212
Figure 219: Radially integrated patterns of 114 for a) 25 °C, b) 105 °C, c) 125 °C and d) 165 °C.	212
Figure 220: Radially integrated patterns of 114 for a) 25 °C, b) 105 °C, c) 125 °C and d) 165 °C, integration of the equator region.....	213
Figure 221: Azimuthally integrated plots of peak 1 for compound 114 at several temperatures.	214
Figure 222: Amplification of the small angle region of the 2D diffraction pattern of 114 at 25 °C.....	215
Figure 223: Azimuthally integrated plots of peak C and D for compound 114 at several temperatures.	215
Figure 224: Azimuthally integrated plots of peak D for compound 114 at several temperatures.	216
Figure 225: Azimuthally integrated plots of peak A and B for compound 114 at several temperatures.	216
Figure 226: Molecular packing proposed for compound 114.....	217
Figure 227: Scheme of series IV.....	218
Figure 228: Diffractograms of compound 115. Top: Program I and bottom: Program II.	219

Figure 229: θ -scans for compound 115, obtained from data collected from program I.	220
Figure 230: Azimuthally integrated plots for peaks A to C in the mesophase (45 °C) and in the isotropic state 170 °C) for program I.	221
Figure 231: θ -scans for compound 115, obtained from data collected during Program II.	222
Figure 232: Radially integrated scans for compound 115 at 30 °C. Data collected during Program II	224
Figure 233: Representation of the molecular unit cell of 115.....	225
Figure 234: Representation of the molecular packing considering the above model. ..	225
Figure 235: Diffractograms of compound 116 at the mesophase (25 °C) and in the isotropic state (190 °C).	226
Figure 236: Radially integrated patterns of 116 for a) 25 °C and b) 190 °C.	226
Figure 237: Dependence of θ -scans with temperature. a) For the entire temperature range collected and b) Variation of d (Å) with temperature.	227
Figure 238: a) and b) Steps for the preparation of the thin films. c) Shows two substrates, one is loaded and a yellow coloration can be observed. The other is clean and transparent d) Example of a non homogeneous sample.....	231
Figure 239: UV/Vis spectra of the non irradiated sample.....	232
Figure 240: UV/Vis spectra of irradiated samples.....	233
Figure 241: Polar plots of the absorbance at 365 nm in the initial film (black line) and after linear polarized irradiation (488nm).	234
Figure 242: Representation of the measurements of the thickness of the samples using a profilometer.....	234
Figure 243: Experimental set up used to record SRGS. ²⁸⁶	235
Figure 244: Recording of SRGS, where 1 st , 2 nd and 3 rd order diffractions can be observed.	236
Figure 245: Sample observed by OPM after SRG inscription.....	245
Figure 246: Profile of the surface of the sample after SRGS inscription.	237

TABLES INDEX

Table 1: Phase transitions for compounds studied by Zhang <i>et al.</i> ¹³⁹	45
Table 2: Phase transitions for compounds studied by Elsässer <i>et al.</i> ¹⁴¹	46
Table 3: Phase transitions for the systems studied by Chujo <i>et al.</i> ¹⁴⁴	51
Table 4: Phase transitions for the systems studied by Pan <i>et al.</i> ¹⁴⁶	52
Table 5: Phase transitions for the systems studied by Soltysiak <i>et al.</i> ¹⁴⁷	54
Table 6: Phase transitions for the systems studied by Wang <i>et al.</i> ¹⁴⁸	55
Table 7: Composition of the POSS derivatives studied by Su <i>et al.</i> ²⁰⁵	73
Table 8: Transition temperatures and ration of 84 to 85 in the systems studied by Bialecka-Florjanczyk <i>et al.</i> ²⁰⁶	74
Table 9: Summary of characterization of compounds 104 to 116.	117
Table 10: Liquid crystalline properties of compounds 96 to 99 and 103.....	119
Table 11: Summary of the liquid crystalline properties of silsesquioxene derivatives 104-116.	141
Table 12: Calculated distances for compound 96.	152
Table 13: Calculated distances for compound 104.	156
Table 14: Calculated distances for the 2 θ -plot shown in Figure 162.....	165
Table 15: Calculated distances for the 2 θ -scan presented in Figure 164.	167
Table 16: Calculated distances for the plots represented in Figure 166	170
Table 17: Calculated distances for the plots represented in Figure 168.	172
Table 18: Calculated distances for compound 105.	179
Table 19: d values calculated for the 2 θ scans represented in Figure 180.	181
Table 20: d values calculated for the 2 θ scans represented on Figure 181.	182
Table 21: d values calculated for the 2 θ scans represented on Figure 188.	188
Table 22: d values calculated for the 2 θ scans represented on Figure 194.	194
Table 23: Calculated distances for the 2 θ values obtained at 115 °C.	201
Table 24: Calculated distances for the 2 θ values obtained at 25 °C.	213
Table 25: Calculated distances determined by X-ray diffraction for compound 115. ...	220
Table 26: Calculated values for the peaks in the parallel integration data collected at 30 °C.	223
Table 27: Calculated distances for plot b in Figure 236.	226

CHAPTER 1: INTRODUCTION TO LIQUID CRYSTALS

1.1 - Brief History of Liquid Crystals

The discovery of liquid crystals is attributed to an Austrian botanist named Friedrich Reinitzer. In 1888, whilst trying to determine the exact molecular formula and weight of cholesterol he isolated cholesterol benzoate and noticed that this compound exhibited what seemed to be two melting points. At 145.5°C this (crystalline solid) melted into a cloudy fluid and after that, at 178.5°C a completely clear transparent liquid was obtained. Reinitzer wrote to the German physicist Otto Lehmann who believed that the material was a crystal with “weak mechanical strength”, and in 1890 he published the first scientific paper about liquid crystals.¹

Liquid crystals were mostly an object of scientific curiosity until the liquid crystal displays era started with the discovery of the twisted nematic effect in 1971.²

Liquid crystals are usually based on anisotropic building blocks, which can be molecules, polymers, micelles, aggregates, etc. They combine the fluidity of liquids and anisotropy of crystals, which confer them with particular characteristics that make them suitable for a range of applications. Liquid crystal materials are extremely diverse, and can be found in nature like DNA and a growing number of liquid crystals are now found in everyday life: from Kevlar to LCDs.³

1.2 – Definition of liquid crystals

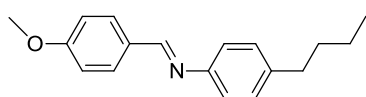
In a mesomorphic state the degree of molecular ordering in matter is intermediate between that found in a perfect solid and an isotropic liquid. The LC state is a mesomorphic state having a long-range orientational order and either 0D, 1D or 2D positional order. This state of matter occurs between the crystalline solid and the isotropic liquid state on varying, for instance, the temperature at a constant pressure. Liquid crystals combine properties of a liquid (e.g., flow) and of a crystalline solid (e.g., anisotropy of some physical properties) and are usually based on anisotropic building blocks.^{3,4}

1.3 - Classification of Liquid crystals

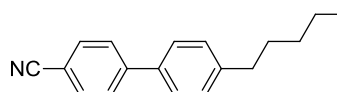
In thermotropic liquid crystals (LC), mesophases arise from varying temperature at a constant pressure. Lyotropic LC, on the other hand, are obtained by dissolving an amphiphilic mesogen in a suitable solvent under appropriate conditions of concentration, pressure and temperature.⁴

According to molecular shape, low-molar-mass LC can be classified as, for example:

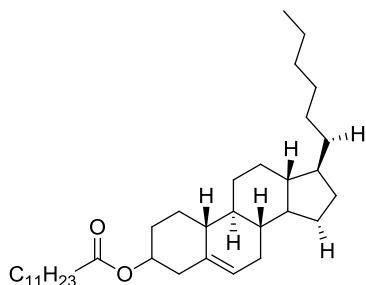
– calamitic, if the mesogens are composed of rod- or lath-like molecules (see Figure 1);



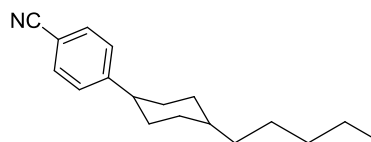
(1) Tg -72.0 Cr 22.4 N 48.0 Iso



(2) Cr 24 N 35.3 Iso



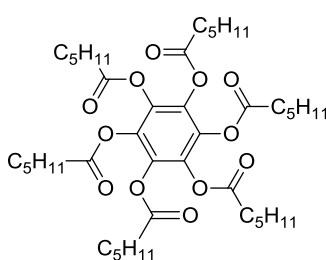
(3) Cr 92.4 (SmA 80.2 N* 88.9) Iso



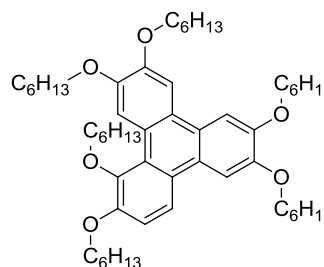
(4) Cr 31.0 N 55.0 Iso

Figure 1: Molecules (1),⁵ (2),⁶ (3)⁷ and (4)⁸ are examples of calamitic molecules.

– discotic, if the mesogens are composed of relatively flat, disc- or sheet- shaped molecules (see Figure 2);



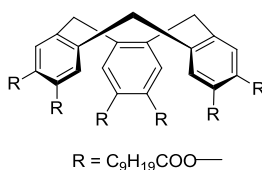
(5) Cr 68.3 D_{rd} 86.0 Iso



(6) Cr 68.0 D_{ho} 97.0 Iso

Figure 2: Molecules (5)⁹ and (6)¹⁰ are examples of discotic liquid crystals.

– pyramidics, if the mesogens are composed of molecules containing a semi-rigid conical core (see Figure 3).



(7) Cr 23.9 Columnar 152.6 Iso

Figure 3: Example of a pyramidic liquid crystalline molecule.¹¹

-bent core, when two mesogens are linked in a non collinear way via a semi-rigid group, an example is depicted in Figure 4. These molecules were initially reported by Vorländer in 1929.^{12, 13} Later in the 1990s, the interest in these molecules arose from the possibility of forming polar mesophases from these achiral molecules.¹⁴ Lately this class of molecules has been actively investigated due to the theoretical prediction of the formation of biaxial nematic phases that will be shortly discussed in the next section.¹⁵⁻

19

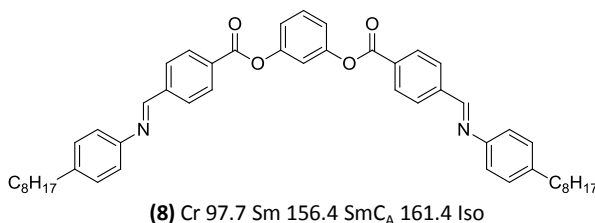


Figure 4: Example of bent core liquid crystalline molecules.¹¹

Liquid crystalline polymers, elastomers and dendrimers can be considered high-molar-mass LC.

Liquid-crystalline polymers (LCP) can be formed from the same rigid calamitic or discotic mesogenic groups. Depending on the way these molecules are attached they can form main chain or side chain polymers.²⁰ Many other arrangements can be found as exemplified in Figure 5.

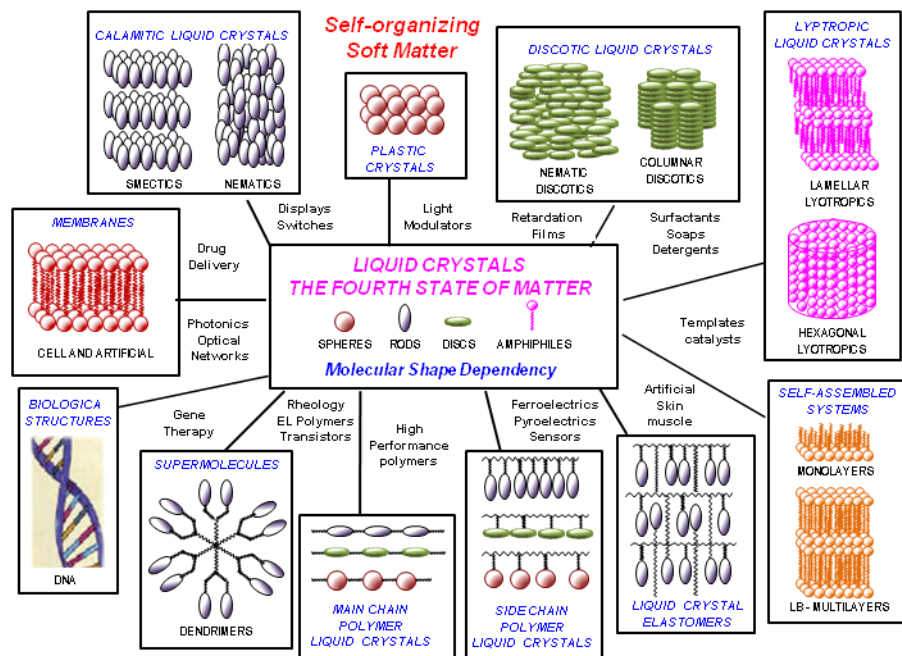


Figure 5: Organization of liquid crystals.²¹

Elastomers are three dimensionally cross-linked polymer networks with elastic properties. These polymer networks can also present LC phases.²²

Dendrimers are highly branched oligomers or polymers of dendritic structure containing mesogenic groups that can display mesophase behaviour; LC Dendrimers are the main focus of Chapter II.

According to the degree of ordering, a series of mesophases can be identified in liquid crystals.

- Nematic phase

The nematic state has the simplest structure of all mesophases, and is characterised by one-dimensional orientational order of the molecules. Although the molecules do not possess any positional order, they tend to align towards a preferred direction as shown in Figure 6. This direction can be denoted by a unit vector called director (\vec{n}).

The nematic phase is formed by a diversity of molecular and supramolecular arrangements, yet the two fundamental molecular shapes are rod-like or disc-like molecules (see Figure 6a) and b), respectively). In order to minimize the excluded volume and maximize the attractive van der Waals interactions, these anisotropic molecules tend to align parallel to each other.²³

This phase is characterised by $D_{\infty h}$ symmetry and it is called uniaxial nematic since there is only one direction in which plane polarized light travels without suffering a

change in its polarization state. This direction is called the optical axis and coincides with the director (\vec{n}).²⁴

The nematic phase is extremely important because of its application in areas like liquid crystal displays (LCDs).

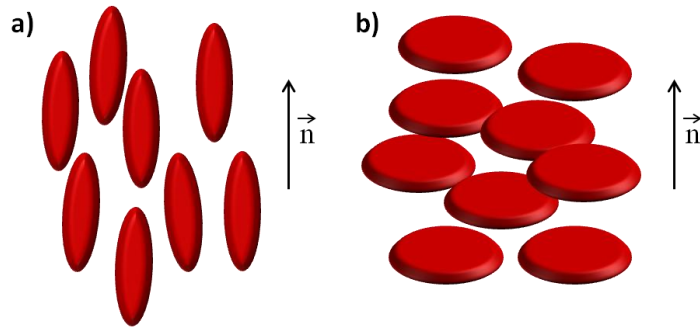


Figure 6: Schematic representation of a uniaxial nematic phase of a) calamitic and b) discotic mesogens.

In 1970, Freiser predicted the existence of a biaxial nematic phase for board-like molecules which assumes the existence of a secondary director, perpendicular to \vec{n} (see Figure 7). Contrary to the uniaxial nematic phase where the molecules rotate freely in a disordered manner around their long axis, in the biaxial nematic state, N_B , the rotation of the molecules about their long axis is restricted leading to a time averaged board-like molecular shape but keeping the liquid like distribution of the centres of gravity.^{24,25}

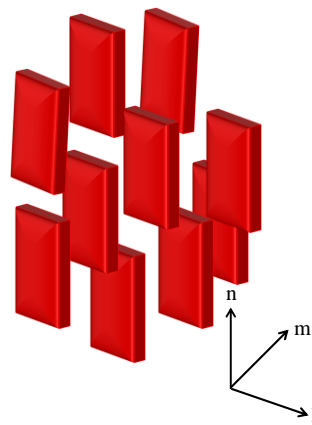


Figure 7: Representation of the biaxial nematic phase (N_B), formed by board-like molecules.

The biaxial nematic phase is also characterised by the presence of two optical axes due to a D_{2h} symmetry.

Theoretical considerations also suggest the existence of the biaxial nematic state in samples of bent core or V-shaped molecules as well as in mixtures of rods and discs, which are discussed in detail in the literature.²³

The N_B phase was first reported for lyotropic systems by Yu and Saupe in 1980.²⁶ Detailed studies on lyotropic micelles presenting uniaxial and biaxial nematic phases were carried out by Gallerne and Neto.²⁷⁻²⁹

More recently, the occurrence of the biaxial nematic phase in concentrated lyotropic liquid crystalline systems of mineral particles was reported, in this case the biaxial nematic phase is observed under external alignment forces such as a magnetic field.³⁰⁻³² The biaxial nematic phase was also identified in polymeric thermotropic systems.³³⁻³⁷ In low molecular weight thermotropic liquid crystals it is proving much more difficult to synthesize materials showing a biaxial nematic phase. Despite the enormous efforts and investigations in this area only one example has been reported in tetrapode systems to have a stable biaxial nematic phase (see Figure 8).^{38, 39}

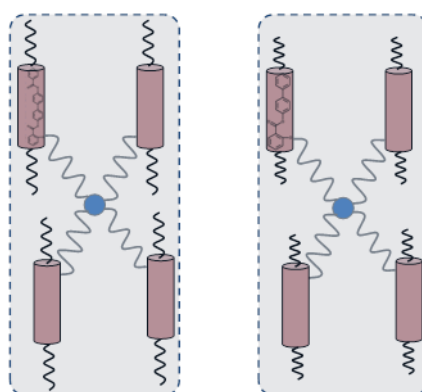


Figure 8: Representation of tetrapode systems that show a biaxial nematic phase (N_B).^{38, 39}

Another situation that can occur in nematic phases is the existence of cybotactic clusters. These are local fluctuations of smectic C-like layers (smectic C phase is described below). This type of nematic phase was found in low molecular weight nematic,⁴⁰⁻⁴² oligomeric, polymeric⁴³⁻⁴⁵ and supermolecular nematics.⁴⁶⁻⁴⁸ They can appear as pretransitional manifestations of the smectic-C phase near the transition temperature between the SmC and the N phases or as a feature of the arrangement of molecules in the nematic phase, where no SmC phases are observed and they persist throughout the entire nematic range.^{47, 48}

The last case of nematic phases that will be discussed is the lamellar nematic phase (LamN) which was identified in bolaamphiphilic compounds.⁴⁹⁻⁵⁴ These T-shaped molecules are formed by an aromatic core, polar lateral groups, such as hydroxyl or amide, and long lateral chains including perfluorinated, siloxane and carbosilane chains, as represented below (Figure 9).

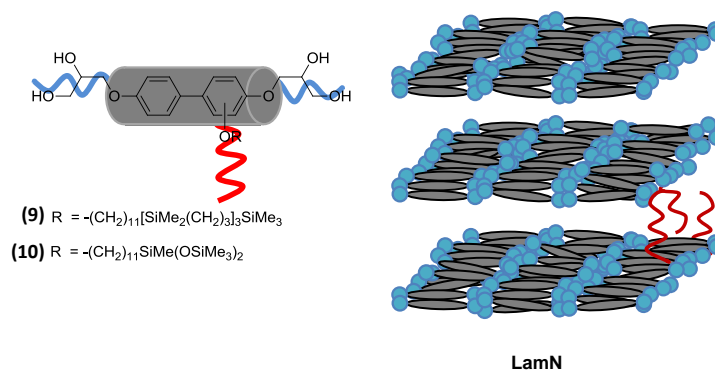


Figure 9: Representation of systems showing lamellar nematic phases.⁴⁹⁻⁵⁴

The laminated state is formed by layers of polar rod-like components separated by disordered long lateral chains; this arrangement in layers is promoted by microsegregation between these two distinct elements. A special characteristic of this nematic state is that the rod-like cores that are π -conjugated orient parallel to the layer plane, whilst in plane nematic order is adopted and orientational correlation between adjoining layers is present. The LamN phase can be regarded as being formed by quasi-2D nematic layers and exhibits D_{2h} symmetry.

Lamellar nematic phases were also reported for rod-like polymers with lateral chains such as the one depicted in Figure 10. In these systems the formation of a layered structure is driven by microsegregation of the rigid backbone, that is arranged in the layer plane, and the lateral alkyl chains.⁵⁵⁻⁵⁸

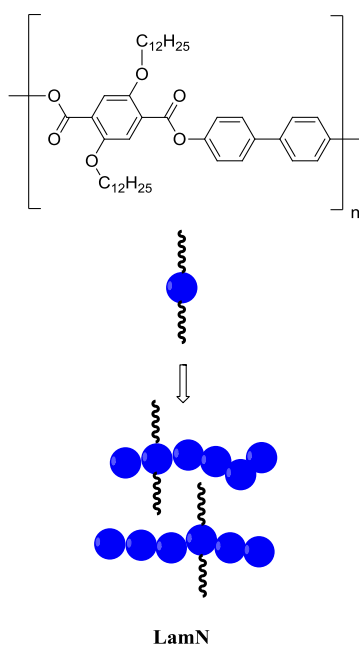


Figure 10: Representation of polymeric system showing lamellar nematic phases.⁵⁵⁻⁵⁸

- Smectic phases

Smectic phases are characterised by equidistant molecular layers. Within layers, molecules are orientated towards a preferred direction (that can be specified by the director) but no in-plane long range positional order is observed.

There are several types of mesophases, characterised by a variety of molecular arrangements within the layers. Examples are: SmA, SmC, SmI, ...⁵⁹

The simplest smectic phase is the smectic A phase (SmA), in which the long molecular axis is oriented on average perpendicular to the layer normal (Figure 11 a)), but with molecules loosely associated into layers. When the molecular director is tilted with respect to the layer normal a smectic C phase is obtained (Figure 11 b)).

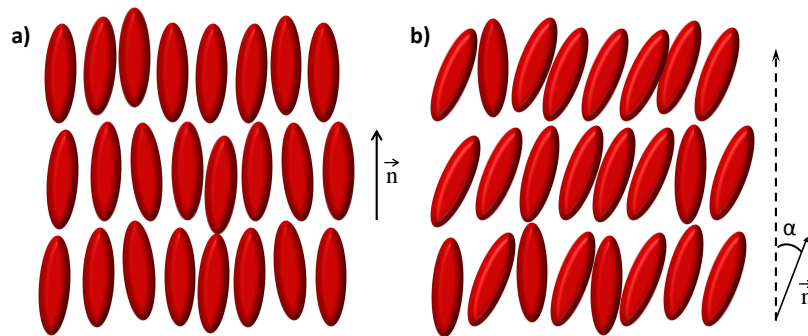


Figure 11: Schematic representation of a) smectic A and b) smectic C phase.

- Columnar Phase

The most common case of the columnar phase is obtained with discotic molecules. In this phase molecules tend to pack with the planes of the molecules broadly parallel in a two-dimensional lattice, but without long-range positional correlations along the columns. They are characterised by the symmetry of this arrangement, and hexagonal (Col_h), rectangular (Col_r), oblique (Col_o) or square (Col_s) columnar phases are formed (Figure 12).

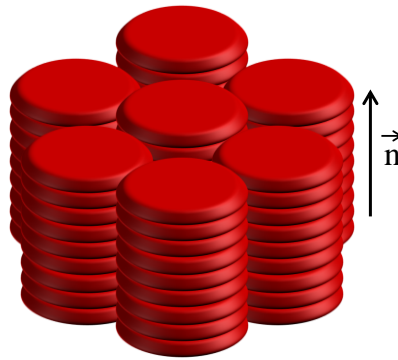


Figure 12: Schematic representation of a discotic columnar phase.

1.4 - Characterisation of liquid crystals

The mesomorphism of liquid crystals can be studied using three main techniques specifically optical polarizing microscopy (OPM), differential scanning calorimetry (DSC), and X-ray diffraction (XRD). Jointly these techniques provide information required to identify the type of mesophase and its molecular structure.

This section will summarize the basic principles of these techniques and an attempt will be made to illustrate how the information individually provided comes together to present a detailed characterization of liquid crystalline materials.

1.4.1 - Optical polarizing microscopy (OPM)

Light is an electromagnetic wave that vibrates equally in all directions. When it encounters a polarizer only the light vibrating in a plane parallel to the polarizer polarization, goes through, becoming linearly or plane polarized light.⁶⁰ If a second polarizer is placed perpendicularly to the first, no light will pass it since light is vibrating in a plane perpendicular to the second polarizer as represented in Figure 13.

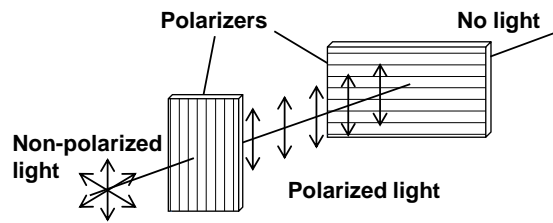


Figure 13: Plane polarized light.

In the same way, optical polarized microscopes such as the one shown in Figure 14 are equipped with a polarizer between the light source and the sample and an analyser before the ocular. The polarizer can rotate 360° however when observing a liquid crystal these should be set perpendicularly to each other.⁶¹

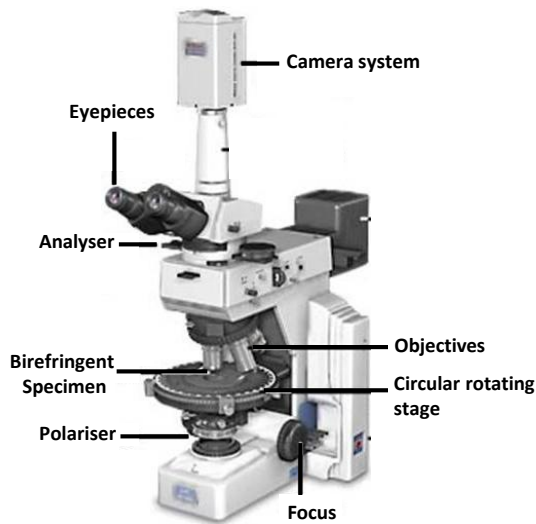


Figure 14: Optical polarizing microscope.⁶¹

The interest in using this technique arises from the fact that liquid crystals are optically anisotropic materials this is, they present different optical properties depending on the direction and polarization of the propagation of light. When light propagates in a anisotropic material it will be refracted by different amounts and will be split into an ordinary ray (n_o) and extraordinary ray (n_e) as represented in Figure 15.⁶²

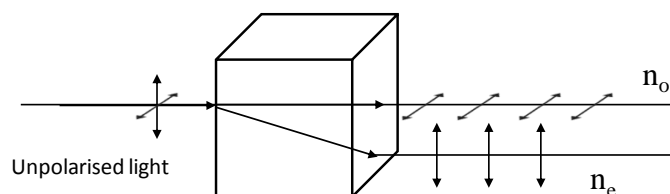


Figure 15: Interaction of unpolarized light with a birefringent medium.

As a consequence light will propagate with different speeds and hence; the materials show different refractive indices in different directions. As a result liquid crystals are birefringent materials where the optical axis is defined by the director. Birefringence is the measure of double refraction in terms of difference in the refractive index⁶³ and can be calculated as shown in (1)

$$\Delta n = n_e - n_o$$

Where Δn is birefringence, n_e is the refractive index of the extraordinary ray (parallel to the director) and n_o is the refractive index of the ordinary ray (perpendicular to the director).

Considering a liquid crystal observed in a polarized optical microscope, plane polarized light that comes through the first polarizer reaches the birefringent sample. Consequently it will be split into the ordinary and the extraordinary rays that propagate with different velocities associated with different refractive indices. The ordinary ray follows Snell's laws of refraction while the extraordinary ray is parallel to the optical axis. Because they travel with different speeds they will emerge from the sample out of phase, therefore elliptically polarized (see Figure 16). Two consequences from this phenomenon are that light emerging from the sample is now able to pass through the analyser (since it has now a component that is parallel to the analyser), and as a consequence that not every wavelength passes through the analyser, liquid crystalline samples will be coloured.⁶⁴

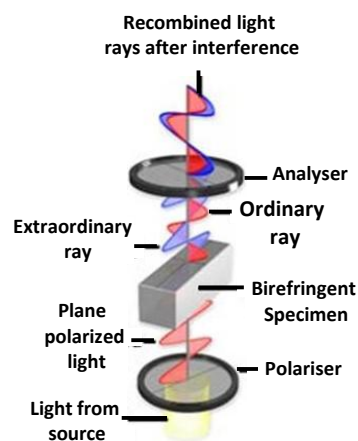


Figure 16: Birefringent specimen between cross polarizers and its interaction with light.⁶¹

In practice, when a liquid crystal sample is observed with OPM a colourful pattern is viewed, and depending both on the preparation of the sample and mesophase displayed by the material, this pattern can vary significantly. If the sample is homeotropic, this is with the director parallel to the direction of propagation of the plane polarized light (Figure 17 a)), there will be no light emerging from the analyser because light

propagating in the direction of the optical axis is, by definition, not affected and will be retained by the analyser.

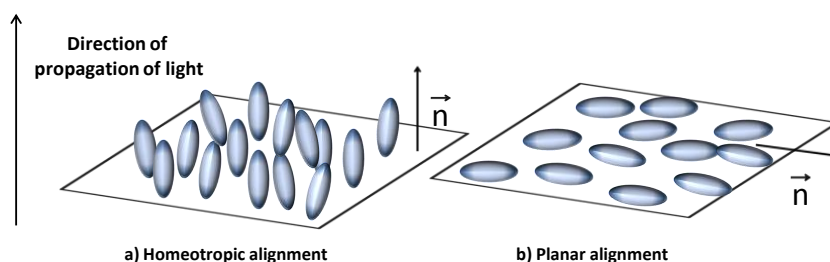


Figure 17: Representation of a) homeotropic alignment and b) planar alignment for calamitic liquid crystal molecules

When the sample is planar (Figure 17 b)), the coloured pattern or texture is then observed. However it was mentioned above that liquid crystals do not possess positional order and depending on the mesophases considered, orientational order can be short or long range. This means that in a microscopic preparation the director of the liquid crystalline sample frequently changes direction (if an orientation is not imposed to the sample), which will influence the birefringence presented by the sample. So considering for example a nematic phase that has neither orientational nor positional order, and a smectic C phase that is characterised by short range positional order, it is expected that light will interact with the two materials in different ways and therefore different textures are expected. In fact it is the different textures observed for each mesophase that make OPM studies so useful in identifying the mesomorphic behaviour of the sample. However the results collected by this technique are far from conclusive since it demands considerable experience and there are literature reports where materials whose mesophase was identified using OPM needed to be reinvestigated and re-classified using a wider range of experimental techniques.^{61, 65-67}

In summary, OPM is an extremely valuable tool for initial assessment of the mesophase type however more detailed studies are needed to fully confirm the mesophase structure.

1.4.2 - Differential scanning calorimetry (DSC)

When materials are heated energy is transferred to the system. This energy input will increase the kinetic energy of the molecules, and when this kinetic energy is high enough intermolecular forces are broken and a phase transition occurs (for example from solid to liquid). Phase transitions are spontaneous conversions, during which the

Gibbs energy is minimized thus these transformations are accompanied by a change in both entropy (S) and enthalpy (H). The temperature at which Gibbs energy is minimal is denominated transition temperature (T_{trs}) and this temperature is pressure dependent.⁶⁸ The differential scanning calorimetry technique measures enthalpy changes associated with phase transitions.

The Gibbs energy is given by

$$G = H - TS \quad (2)$$

At constant pressure, the first derivative of the Gibbs energy with respect to T gives the entropy, equation (3).

$$\left(\frac{dG}{dT}\right)_p = -S \quad (3)$$

The second derivative is related with the heat capacity at constant pressure by equation (4).

$$\left(\frac{d^2G}{dT^2}\right)_p = -\frac{C_p}{T} \quad (4)$$

A phase transition can occur with a discontinuity of the first derivative of the free Gibbs energy therefore entropy and enthalpy, in which case is called first order transition, or with a discontinuity in the second derivative of the free energy, this is the heat capacity, and in this occasion the values of both entropy and enthalpy do not change during the phase transition and it is named second order.

The principle applied in DSC instruments is as follows. Two pans are heated at the same time using the same heating or cooling rate. One of these pans is a reference with a well known heat capacity material (usually gold), the second holds the sample being analysed. During heating this sample will change phase in an endothermic manner. Considering that during phase transitions energy will be used, extra heat has to be supplied to the material so that its temperature is maintained equal to the temperature of reference sample. By contrast in an exothermic process less heat is required given that loss of energy is associated with the phase transition. The temperature control between sample and reference is achieved by altering the power input to the sample. The amount of heat absorbed or released associated with phase transitions are measured by the difference in the heat flow between both sample and reference.

The result is a thermogram in which the heat flow, dq (mW), versus T ($^{\circ}\text{C}$) is plotted allowing the determination of the enthalpy associated with phase transitions and the transition temperature, since they are related by equation (5).

$$\left(\frac{dq}{dT}\right)_p = \frac{dH}{dT} \quad (5)$$

A few considerations should be made when analysing the thermal behaviour of LCs. The phase transitions associated with liquid crystals are mainly first order, meaning that the transition is accompanied by a change in enthalpy or latent heat; LC transitions can have very small enthalpy values. Second order transitions occur with any change in enthalpy though a discontinuity in the heat capacity and are often found for SmA to SmC transition. Usually it is difficult for transitions with small enthalpy values, such as second order transitions, to be detected by DSC. In order to overcome this limitation larger amounts of material can be used to increase the sensitivity of the experiment or by changing heating rates. Glass transitions are another second order discontinuity associated with changes in mobility in polymeric systems however they are not considered formal phase transitions. The associated thermogram involves a change in the base line. The temperature associated with the phase transitions is quoted as the onset temperature since the peak can broaden with changes in heating rates, mass used, viscosity and others, for these reasons the onset temperature is quoted. In the glass transition the quoted temperature corresponds to the middle point of the curve.^{69, 70}

Another important feature when analysing phase transitions is the distinction between thermodynamic and kinetic processes. When a thermodynamically unstable phase persists because the transitions are kinetically hindered, it is called a metastable phase.⁶⁸ When a liquid crystalline sample is supercooled, and it crystallizes in non-equilibrium conditions (due to a kinetic effect), additional mesophases can be observed and are called monotropic phases.⁶⁹

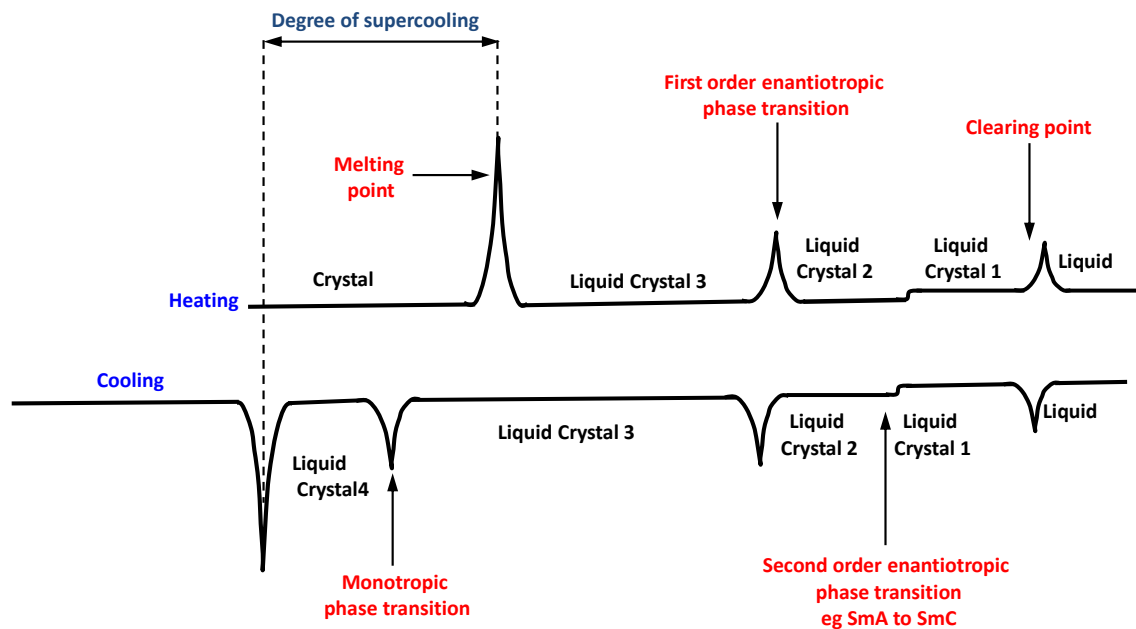


Figure 18: Example of a DSC curve for a liquid crystal with four mesophases.

In Figure 18 a typical DSC curve is shown for a liquid crystal with four mesophases. The heating curve shows a first transition corresponding to the melting of the crystals into a mesophase. This peak is large when compared with the others, since the energy and consequently the enthalpy necessary to break the crystalline network is high. Next a smaller peak related with a mesophase transition, the energy necessary to complete this transition is smaller, and finally the clearing point that corresponds to the transition from a liquid crystalline material to an isotropic liquid. On the cooling curve, it can be initially seen that the transition peaks are at a lower temperature than in the heating curve, corresponding to enantiotropic transitions. A third peak is apparent at lower temperature than the melting temperature; this represents a monotropic liquid crystalline phase, thermodynamically unstable. Finally there is a very small peak (both on heating and cooling curves) corresponding to a second order phase transition, as mentioned above, this transitions have a very small enthalpy value so the peaks are quite small as represented, an example of such transitions are observed for SmA to SmC phases.

1.4.3 - X-Ray diffraction (XRD)

1.4.3.1 - X-Ray diffraction, general concepts

X-ray diffraction is a technique used for characterising the structure of liquid crystals that allows the determination of the molecular arrangements and therefore the full characterisation of a mesophase.

X-rays are electromagnetic waves with wavelengths around 10^{-10} m. An X-ray diffraction experiment typically involves wavelengths of 0.154 nm ($\text{CuK}\alpha$) depending on the X-ray source.

Diffraction occurs when radiation is elastically scattered. In the case of x-ray diffraction the scattering arises from the interaction of the radiation with electrons. The scattered wavelets can experience constructive or destructive interference depending on the wave phase.

Bragg interpreted scattering by a crystal as reflection of a set of planes rather than individual electrons. By doing so he established that for one set of planes constructive interference occurs only between rays reflected by a set of planes so that

$$2d \sin \theta = n\lambda \quad (6)$$

So Bragg's law predicts in which direction rays will be diffracted and states that the smaller the distance d between layers, the larger the diffraction angle 2θ will be. This reveals a reciprocal relation between the layers in the real space and the diffracted angle in the reciprocal space (Figure 19).

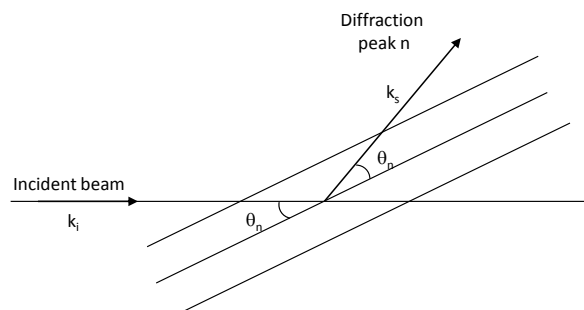


Figure 19: Diffraction from parallel planes.

Bragg's law can also be described as a function of the scattering vector Q (Figure 20), in this case Bragg's law can be written as

$$Q_n = n \left(\frac{2\pi}{d} \right) \quad (7)$$

So for a set of different planes equally spaced $I(Q)$ is always zero except when Bragg's law is fulfilled.

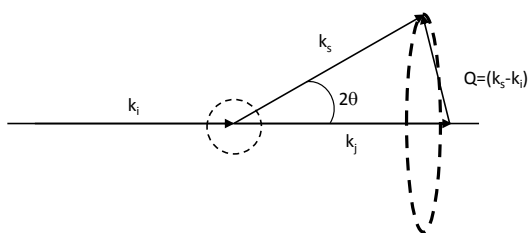


Figure 20: Definition of the scattering vector Q .

A powder sample will be comprised of several microdomains in each of which there will be n number of planes that satisfy Bragg's law originating n number of diffraction peaks. Because there are several microdomains aligned in an angle with the incident beam, instead of spots, the diffraction pattern will be a set of concentric rings or Bragg reflections that arise from different reflection angles⁷¹ (Figure 21).

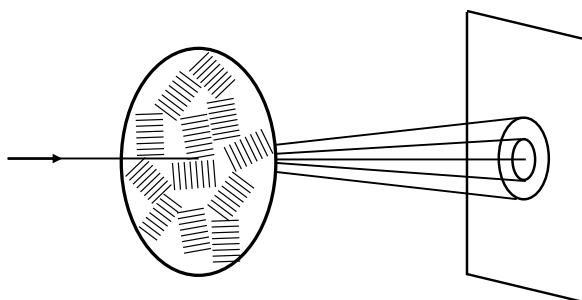


Figure 21: Origin of powder patterns.

A diffraction pattern will then be obtained by plotting $I(Q)$ versus scalar Q since the intensity measured by the detector does not depend on the direction of the scattering vector but varies only with the magnitude of Q or alternatively versus 2θ , where θ is the diffraction angle. The ratio between the positions of the diffraction peaks in the low angle region discloses the long range order of the phase. For example for a smectic phase, the peak ratios will be 1, 2, 3... for a columnar hexagonal phase ratios of $\sqrt{3}$, 2, $\sqrt{7}$, 3...⁷¹

1.4.3.2 - X-ray diffraction of liquid crystals

X-ray diffraction patterns for liquid crystals are quite different from diffraction patterns obtained for single crystals since they do not possess a 3-D lattice. In some ways they are much more similar to those discussed for powder samples due to their lack of long range positional order. However liquid crystals can be oriented by external forces and a

monodomain might be formed. This means that in a well aligned liquid crystalline sample, the diffraction pattern can go from being concentric rings to specific patterns (that will be mentioned later) which are related to degree of order in the sample and therefore the mesophase. The Bragg peaks will be broader because the arrangement of molecules over large distances is lost.

The diffraction patterns are collected using a set up that is equipped with an X-ray source that irradiates the sample enclosed in an electric furnace. A magnet is incorporated in order to align the samples. The radiation emerging from the sample hits a detector (in this work a 2D detector was used) and the 2D diffraction pattern is recorded. The sample is introduced to the furnace in a thin capillary (0.8-1mm in diameter) and should be carefully prepared to obtain a homogeneous sample.

A brief description of the 2D diffraction patterns obtained for the most common liquid crystalline phases and the representative information obtained when analysing XRD data will be made. However, these are generalized patterns and they will vary from sample to sample.

The simplest liquid crystalline phase is the nematic phase, where molecules have orientational order but no positional order.

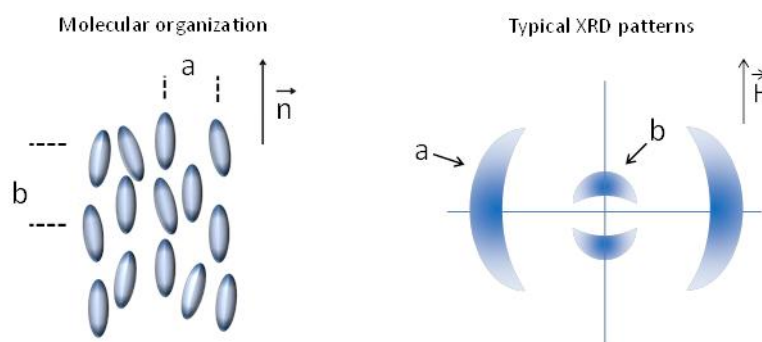


Figure 22: a) Molecular organization of an aligned nematic sample. b) Representation of the diffraction pattern of an aligned nematic sample

The figure represents, on the left, the molecular organization of a calamitic aligned sample and on the right the typical XRD pattern. The intermolecular distances, represented by **a** will correspond to the diffraction peaks in the wide angle region (labeled **a**) in the XRD pattern. The molecular lengths are denominated **b** and will give rise to two reflections above and below the equator.

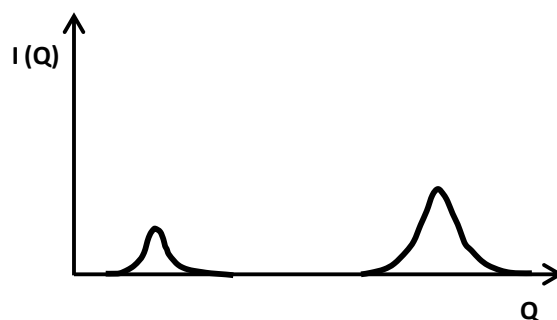


Figure 23: Representation of the radial plot of intensities of a nematic sample.

Cybotactic nematics show, as discussed in previous sections, local SmC arrangements, which will result in a splitting of the reflection in the meridian, when compared with the nematic case presented above. This splitting, (Figure 24) is due to the local SmC-like arrangements as the molecules are locally tilted relative to the director, however the representation of the radial plot of intensities will not suffer any alterations.

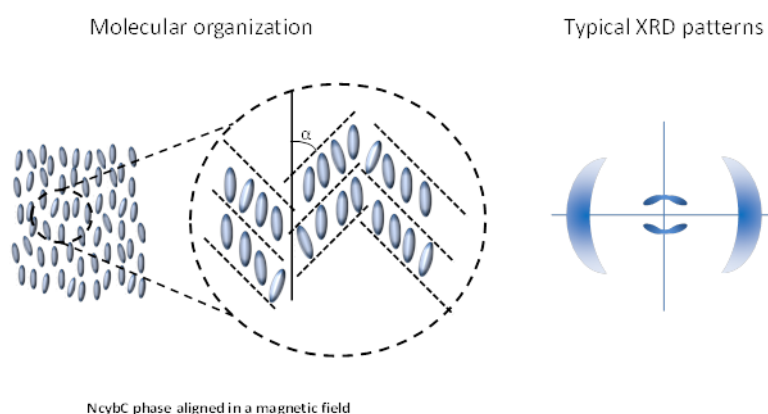


Figure 24: Molecular organization, on the left and representation of the diffraction pattern of an nematic with cybotactic clusters of an aligned sample, on the right.

As mentioned in the previous section, there are few examples of thermotropic liquid crystals showing biaxial nematic phases. It is predicted that the diffraction patterns of aligned samples of board-like compounds would show a splitting in the wide angle region reflection corresponding to two mean distances in l and m direction respectively (see Figure 7).²³

In lyotropic systems there is more information relative to the diffraction pattern of this nematic phase. In 1985,²⁷⁻²⁹ studies of the phase structure of a ternary system of potassium laurate and 1-decanol in D_2O were reported. There are three known nematics for lyotropic systems, two uniaxial nematics (denominated by N_C and N_D) and a biaxial nematic phase N_B . The different nematics arise from fluctuations on the orientation of the micellar aggregates. In the uniaxial cases, the micellar aggregates are allowed to rotate freely around the director, while in the biaxial case, the micellar aggregates

merely oscillate with small angles. It was surprising that the diffraction patterns of monodomains of the three nematic phases were extremely similar. The diffraction pattern obtained is represented in the Figure 25 below.

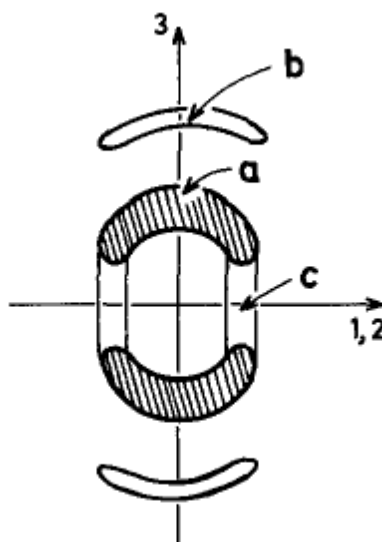


Figure 25: Diffraction pattern obtained for the N_B phase observed in lyotropic systems of potassium laurate and 1-decanol in D_2O , investigated by Gallerne *et al.*²⁷⁻²⁹

Band **a** is attributed to the height of the micelle and has an associated second order band **b** which is related with a lamellar structure shown by this compound. Band **c** was deconvoluted into two diffractions corresponding to length and width of the micelles.

Another example of the diffraction pattern in biaxial nematic systems was reported by van den Pol *et al.*⁷² in lyotropic systems of goethite particles, schematically represented in Figure 26.



Figure 26: Representation of goethite particles shape studied by van den Pol *et al.*⁷²

The advantage of these systems is that it is possible to control the dimensions of the final particles during synthesis, which is extremely useful since it was theoretically predicted that board-like molecules with dimensions $L/W \approx W/T$ would show a biaxial nematic phase. Consequently, particles with the dimensions $L/W = 3.1$ and $W/T = 3.0$ were synthesized and investigated. The XRD pattern is shown in Figure 27.

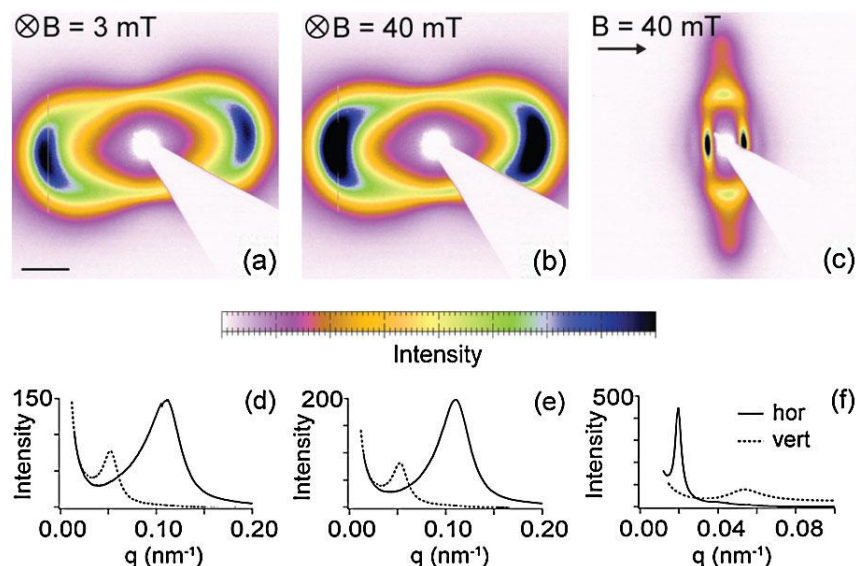


Figure 27: Top-SAXS pattern with magnetic field parallel to x-ray beam and different intensities: a) 3 mT, b) 40 mT and c) magnetic field perpendicular to x-ray beam. Bottom: intensity profiles of a), b) and c) respectively. The horizontal integrations are represented by the solid line and the vertical direction is plotted in dashed line.⁷²

In Figure 27 a) and d) two peaks in the wide angle region and perpendicular to each other (solid and dashed lines) were present associated with the width and thickness correlations. The absence of a small angle diffraction (correlated with the length of the particles) and the perpendicular peaks in the wide angle region suggest the molecular organization represented in the Figure 28 below. Increasing the magnetic field without changing its direction results in similar diffraction patterns with higher intensities suggesting better alignment (Figure 27 b) and e)).

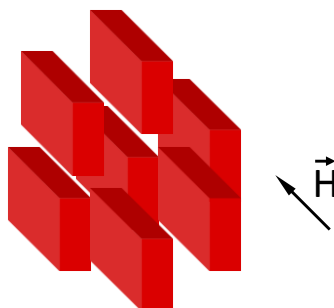


Figure 28: Molecular organization of the biaxial nematic phase in a magnetic field perpendicular to the paper, in the systems studied by van den Pol *et al.*⁷²

By contrast, when the magnetic field was in the direction perpendicular to the X-ray beam (this is parallel to the paper), a distinct diffraction pattern was obtained (Figure 27 c)). In this case, in the horizontal direction a peak in the small angle region is observed corresponding to the length of the molecules. In the vertical direction the width of the

molecules is observed. By changing the direction of the magnetic field, the particles's alignment reoriented and the molecular arrangement is now as represented in Figure 29.

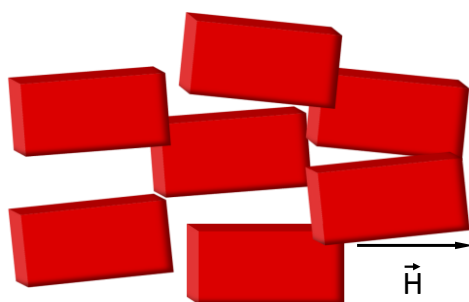


Figure 29: Molecular organization of the biaxial nematic phase in a magnetic field perpendicular to the paper. In systems studied by van den Pol *et al.*⁷²

As discussed previously, lamellar nematic phases were described in polymeric as well as in bolaamphiphilic systems. In order to discuss the XRD patterns of this nematic phase we will focus on the latter type of molecules see Figure 9. The lamellar nematic phase arises mainly from microsegregation between three incompatible regions (aromatic core, glycerol terminal chains and lateral alkyl chains) and formation of hydrogen bonds between the glycerol groups.

The XRD pattern of the molecules studied by Kieffer *et al.*⁴⁹ are represented below (Figure 30).

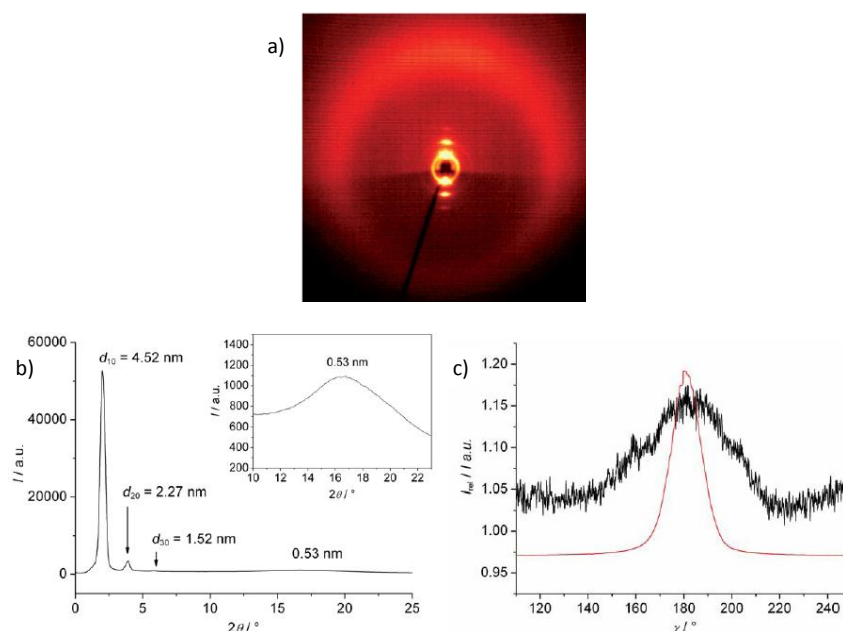


Figure 30: a) diffraction pattern of the LamN phase, b) radial distribution of intensities c) azimuthal distribution of the wide angle scattering.⁴⁹

Considering the diffraction pattern represented in Figure 30 a), the wide angle reflection (0.53 nm, Figure 30 b) associated with the lateral chains) appears as a closed ring, characteristic of the lamellar phases, however the intensity is mainly situated in the

meridian, once the diffraction related with the isotropic state is subtracted, supporting the existence of a layer arrangement. Also in the small angle region three sharp peaks are observed supporting the existence of a layered structure with a layer thickness of 4.52 nm. The lamellar nematic arrangement of the molecules is represented in Figure 31 and is explained by the segregation between the non polar lateral chains and the polar rigid units (aromatic cores and terminal glycerol chains). The layers are formed parallel to the molecules long axis in contrast to what is observed for smectic phases, meaning that the molecules are aligned parallel with the layers. The lateral alkyl chains are situated between the layers formed by the aromatic cores and terminal glycerol chains. Since there is only orientation order in the layers between the polar rigid cores, this phase can be considered as a nematic phase laminated parallel to the long axis of the molecules.⁷³

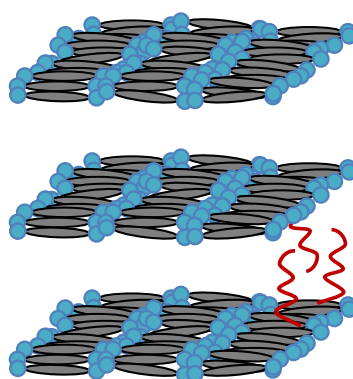


Figure 31: Molecular organization of bolaamphiphilic systems in the lamellar nematic phase.^{49, 73}

For a smectic A phase there is a layered structure, once the molecules orientation order is not perfect, the periodicity of the layers will be slightly smaller than the length of the molecules. In terms of diffraction pattern, the diffuse peaks observed in the small angle region for the nematic phase will become sharp quasi-Bragg peaks (see Figure 22 and Figure 32). Despite having a layered structure smectic phases do not have long-range positional order resulting in a short range organization as a result only the first and second pseudo-Bragg peaks are usually detected. In the wide angle region no significant alterations occur since the lateral packing of the molecules is liquid-like. The expected graphic of the $I(Q)$ versus Q is depicted in Figure 33.⁷¹

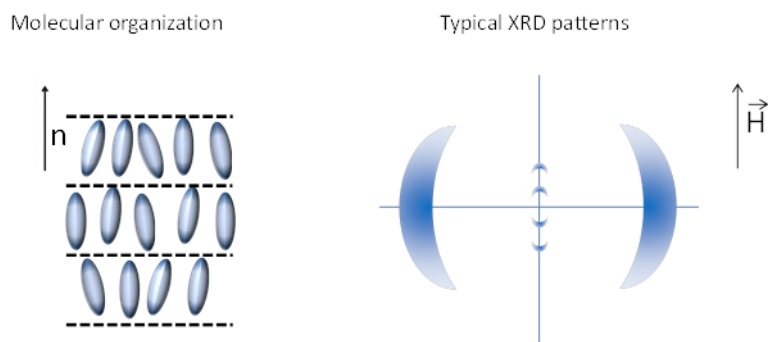


Figure 32: Molecular organization, on the left and representation of the diffraction pattern of aSmA phase.

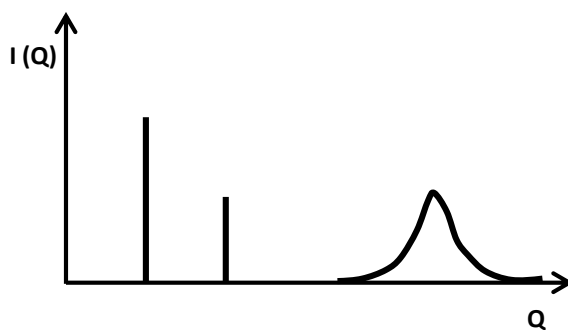


Figure 33: Representation of the radial plot of intensities of a smectic sample.

Several arrangements are possible for the SmC phase resulting in a variety of patterns and sometimes distinguishing it from a SmA phase becomes difficult (see Figure 34).⁷¹ The identification of SmA to SmC transition might be observed by plotting the layer spacing with temperature, as the temperature increases, the layer spacing in the SmC phase increases, stabilizing after the phase transition.⁶⁹ In Figure 34 and Figure 35, are shown some of the diffraction patterns commonly found for the SmC phase of aligned samples.

In Figure 34 the layers are unchanged (comparing to the SmA phase) yet the molecules tilt with no preferential direction of $+\alpha$ or $-\alpha$ angle. When the tilt occurs in different directions over successive layers, the wide angle reflection might split into two peaks above and below the equator however, because this are diffuse peaks, due to the liquid-like structure characteristic of LC mesophases, they are difficult to distinguish and will appear as a large diffuse intensity as shown.

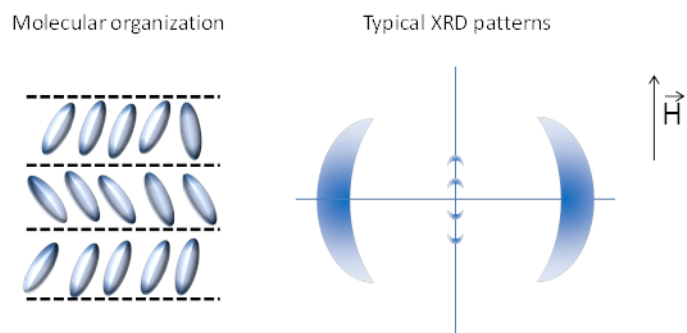


Figure 34: a) Molecular organization of an aligned SmC sample. b) Representation of the diffraction pattern of an aligned SmC sample.

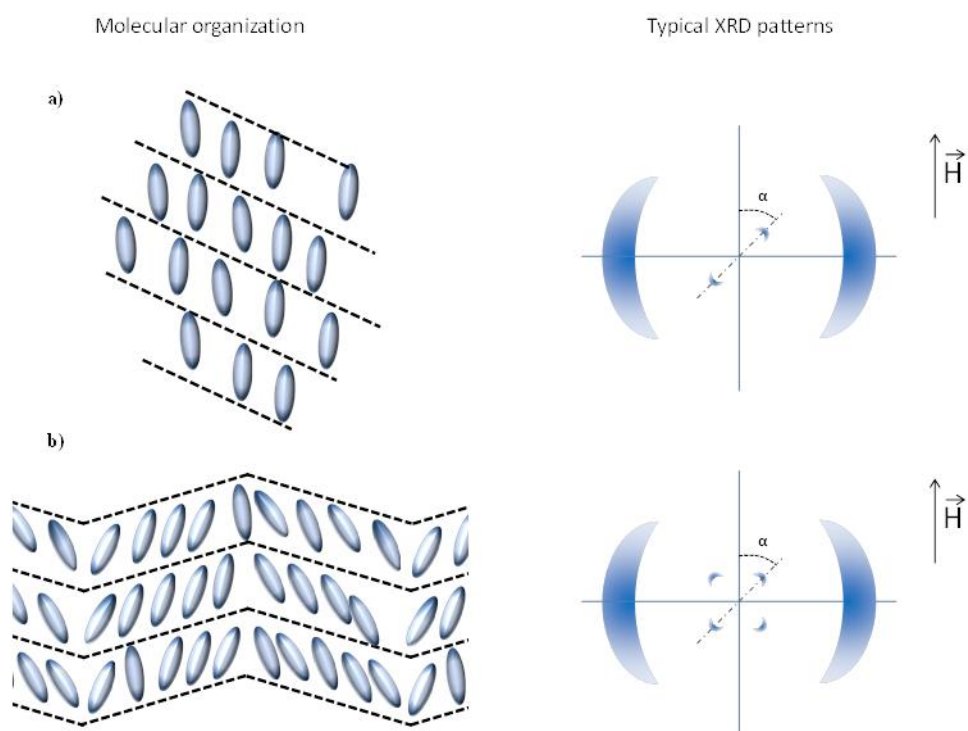


Figure 35: Molecular organization of aligned SmC samples on the right and representation of the corresponding diffraction patterns.

Other possible SmC arrangements are represented in Figure 35. The scenario outlined in Figure 35 a), the layers normal are tilted in one direction $+\alpha$ or $-\alpha$ so the diffraction intensities in the small angle region will be tilted α either to the right or left of the meridian. In Figure 35 b) layers normal are tilted in both directions giving rise simultaneously to pseudo-Bragg peaks both to the right and left of the meridian.

CHAPTER 2: DENDRIMERS

2.1 - General concepts

The word dendrimer comes from the Greek “dendron” meaning tree and “meros” meaning part. These are supermolecules possessing regular three-dimensional hyperbranched architecture.⁷⁴

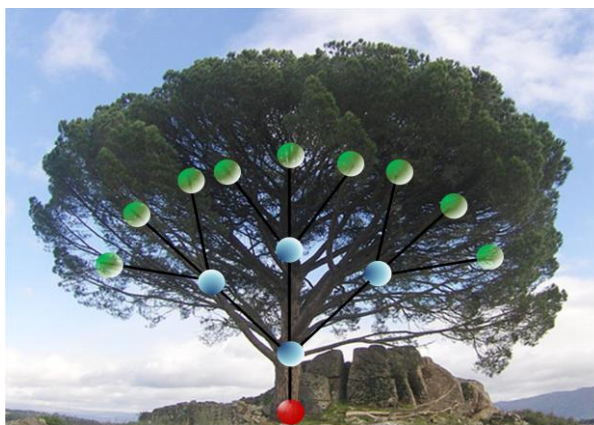


Figure 36: Analogy between architecture and a branching tree, where the name dendrimers took inspiration.

The first reported use of a repetitive addition of monomeric units and activation of the branched molecule for further addition was by Vögtle in 1978 and referred to as “cascade molecules” however, these molecules had low molecular weight⁷⁵. Later in 1980 Tomalia⁷⁶ and Newkome⁷⁷ reported in parallel investigations on synthesis of high molecular weight branched molecules, which determine, in effect, the start of dendrimers as a research area.⁷⁸

Some of the applications foreseen for these materials include targeted drug-delivery, macromolecular carriers, anticancer therapeutics, sensors, light harvesting, surface engineering and others.⁷⁹

The dendritic state can be divided into several groups as depicted in Figure 37 and although this work will focus on dendrimers, a brief description of the sub families will be made.

Dendrimers and dendrons are practically monodisperse and with foreseeable molecular weight since they are perfectly branched.⁸⁰

Hyperbranched polymers are very similar to dendrimers except that they have imperfections in the branching points due to their traditional one-pot synthesis. Since

some control over the structure is lost, this group of molecules is polydisperse.⁸⁰ The subject of hyperbranched polymers has been widely reviewed.^{77, 79}

Dendrigraft polymers, like dendrimers, are synthesised in generations, however the repeating unit is an oligomer or a polymer chain instead of a monomeric unit.⁸⁰

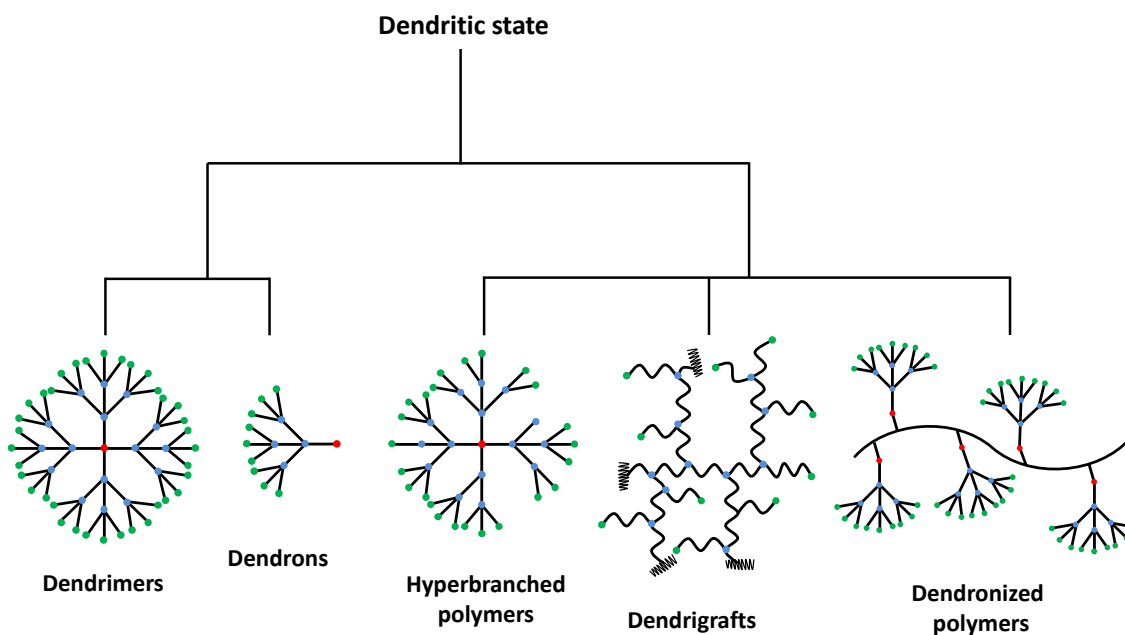


Figure 37: Classification of Dendrimers.⁸⁰

Dendronized polymers are commonly formed by a linear polymer backbone with pendent reactive groups from which dendronic units emerge.⁷⁹ Depending on the density of substitution and size of the dendrons, these macromolecules can have either random-coil or fully stretched out conformation.⁸⁰

2.2 - Dendrimers structure

The dendrimer framework is initiated by a multifunctional core or focal point where the branching units (dendron) emanate from (see Figure 38).

The multiplicity of the inner core is represented by N_c . This core is capped with layers of repeating branched cell units, each of this layers is called generation (G) and the branching multiplicity is denominated by N_b . An outer layer is formed by terminal functional groups (Z) that can be determined by the following equation (8).⁸¹

$$Z = N_c N_b^G \quad (8)$$

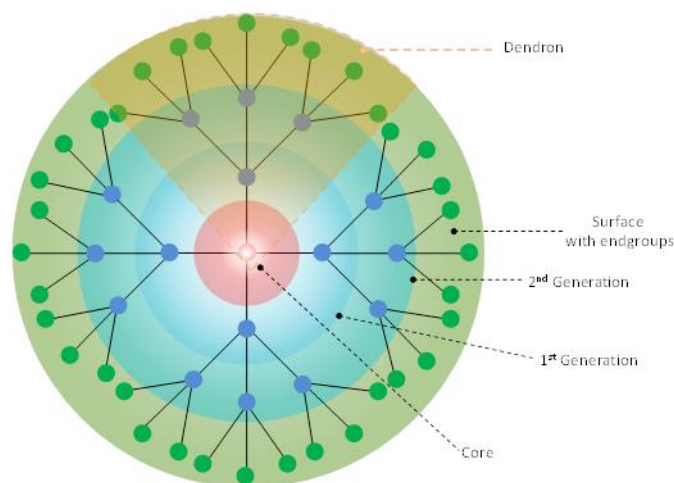


Figure 38: Dendrimers constitution.

Since the radius of the dendrimers increases linearly with (G), whereas the surface cells amplify according to $N_c N_b^G$, there will be a point at which the surface is too crowded with exterior groups that despite having reactive sites, are now sterically constrained preventing further growth of the dendrimer.⁸¹

2.3 - Synthesis of dendrimers

Dendrimers are usually synthesized in a divergent or convergent way. In the divergent way (Figure 39), a monomer with a protected or deactivated functional group (represented by the purple dots in Figure 39), reacts with a core molecule that possess reactive groups. By protecting the functional groups, it is possible to control the growth of the dendrimer. After the first layer of monomers being reacted, the molecules are activated or deprotected and are ready to react with a new set of molecules in the same way. In this manner the dendrimer's generation is increased.⁸²

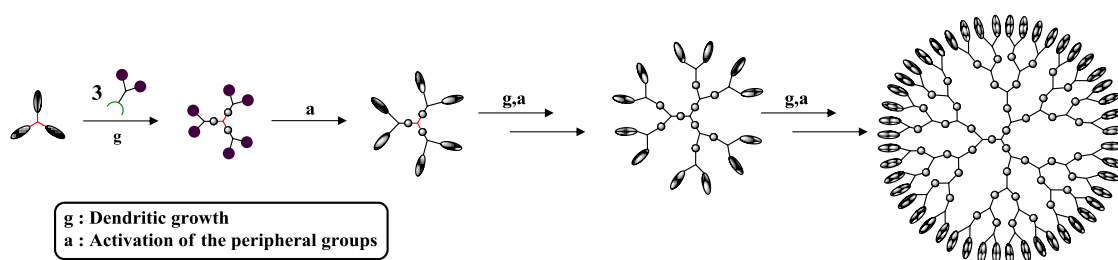


Figure 39: Representation of divergent synthesis of dendrimers.⁸²

In the convergent way dendrons are synthesised individually via activation/deactivation strategy until the appropriated generation is achieved. The core or focal point of the

dendron is finally activated and attached to the central core. In this way dendrons with different functionalities can be connected to the same core (see Figure 40).⁸²

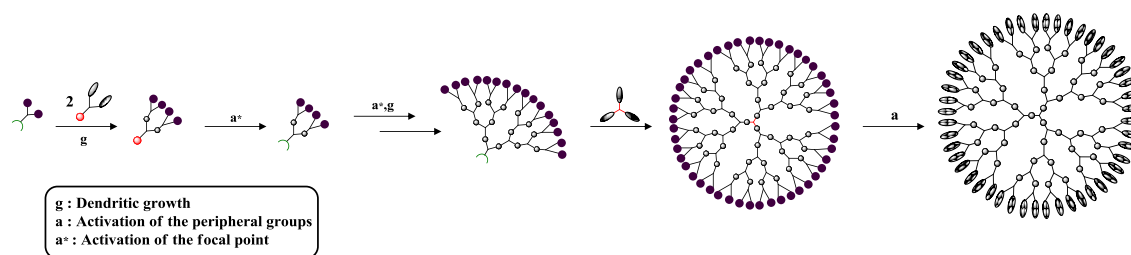


Figure 40: Representation of convergent synthesis of dendrimers.⁸²

2.4 – Liquid crystalline dendrimers

Investigations on LC dendrimers have been reported since the early 90's.⁸³ Generally, the liquid crystalline behaviour is obtained by incorporation of mesogenic units in the dendrimeric structure. In analogy to polymeric systems, LC dendrimers can be denominated by main-chain or side-chain, depending on the location of the anisotropic units. In main-chain LC dendrimers anisotropic molecules are included in the inner dendrimer structure and linked by long alkyl chains (Figure 41 a), while in side-chain LC dendrimers, the mesogenic moieties are linked to the periphery of the dendrimer as a final shell and they can be linked terminally (end-on) or laterally (side-on) as shown in Figure 41 b).⁸⁴

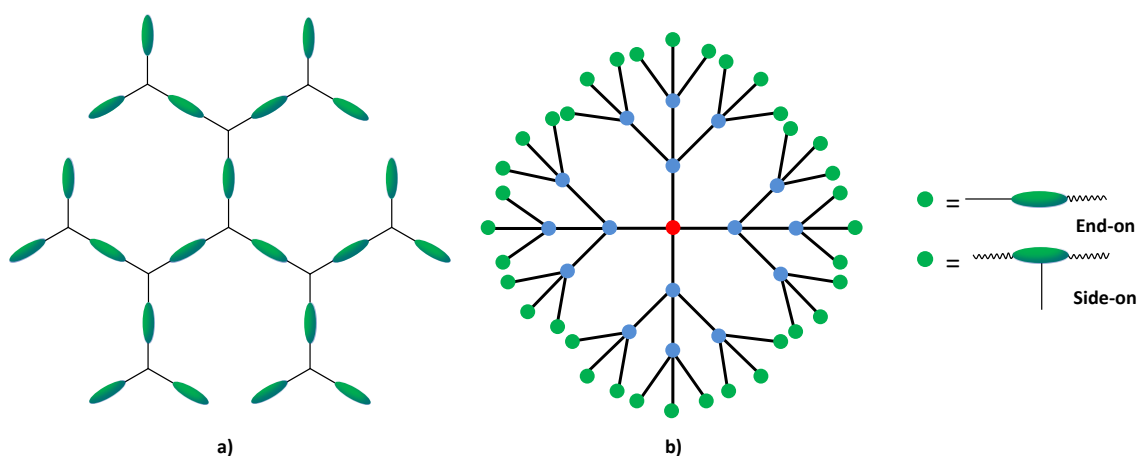


Figure 41: a) Main chain LC dendrimers; b) Side chain LC dendrimers.⁸⁴

Liquid crystal mesomorphism of these supermolecules arises from three main contributions: balance between enthalpy and entropy, formation of domains due to microsegragation and structure and location of the anisotropic units in the dendrimer.⁸⁵

In side-chain LC dendrimers, mesomorphism is promoted by microphase segregation between the chemically different dendritic core and terminal units⁸⁶, moreover the flexible chains that emerge isotropically from the core due to entropic forces⁸⁷, will adjust (as long as it is conformationally and sterically possible⁸⁴ to accommodate the strong anisotropic interactions of the mesogens that are accompanied by a gain in enthalpy. As occurs in conventional LCs this gain in enthalpy promotes mesomorphic behaviour.⁸⁵

As for main-chain LC dendrimers, the mesogenic units are present throughout the dendritic structure which will adopt a more restrained and regular structure due to the gain in enthalpy that emerges from the anisotropic interactions.⁸⁶

Besides side-chain and main-chain liquid crystalline dendrimers there are many other families such as shape persistent LC dendrimers, LC metallodendrimers, LC fullerodendrimers, polypedes and others. More information about the various families of LC dendrimers can be found in the literature.⁸⁶

2.4.1 - Silicon containing dendrimers

Although LC polymers and elastomers containing siloxanes are fairly common, the number of reports on dendrimers built around siloxane cores is very limited. Examples of dendrimeric systems based solely on siloxane cores go back to 1994 when Shibaev *et al.*⁸⁸ published their studies on 1st generation LC dendrimers based on a poly(organo-siloxane) core and six cholesteryl groups attached via undecylene spacers (Figure 42).⁸⁸

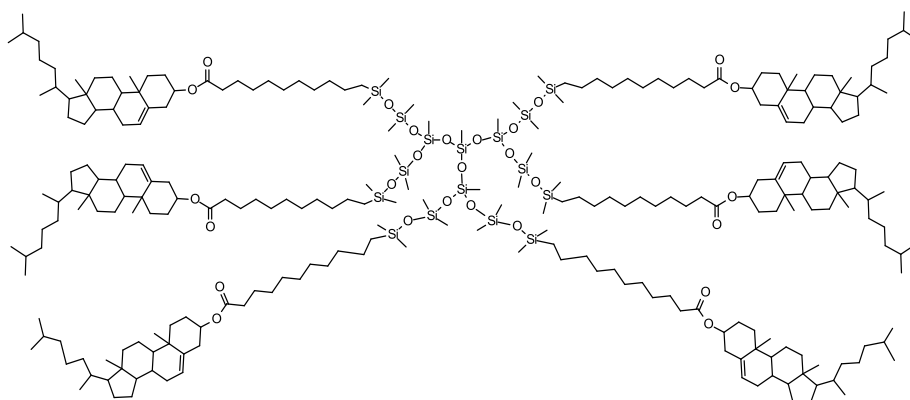


Figure 42: System studied by Shibaev *et al.*⁸⁸

This dendrimeric molecule containing six terminal cholesterol groups showed a very broad SmA phase (T_g -1.5 SmA 120 I). X-ray diffraction results show that the

molecules organize in a single-layer smectic phase where a layer of siloxane cores separates the cholesteryl mesogens that overlap completely Figure 43.^{88, 89}

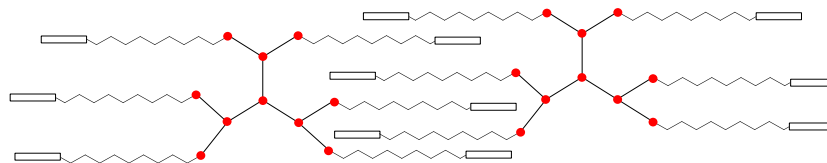


Figure 43: Molecular assembly of the molecules represented in Figure 42 in the SmA phase.^{88, 89}

A zero generation LC dendrimer based on a tetrakis(dimethoxy)siloxane core containing four cyanobiphenyl groups was prepared by Mehl *et al.*⁹⁰

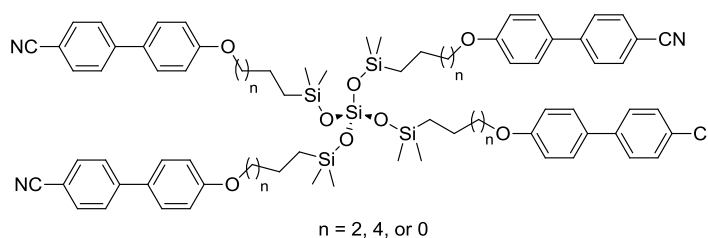


Figure 44: System studied by Mehl *et al.*⁹⁰

These materials exhibited smectic phases and variation of the aliphatic spacer from 4 to 11 methylene units increased the clearing temperature and mesophase stability. For the longer spacer both SmA and SmC phases were found.

Other siloxane cores were investigated while keeping identical mesogenic units, revealing that the structure of the siloxane core has minimal influence on the LC properties of these dendrimers.⁸⁹ The introduction of nematic phases in these systems was achieved by adding side-on mesogens to the siloxane cores.⁹¹

Despite siloxane cores being rarely used as scaffold for LC dendrimers, the use of oligo(siloxane) units is frequently employed to form oligomers, to decrease transition temperatures and stabilize mesophases such as reported in recent examples.⁹²

The introduction of oligo(siloxanes) in LC mesogens has other effects than the ones mentioned above. When these units are attached to bent-core mesogens they are able to change ferroelectric to antiferroelectric material, as well as induce “dark conglomerate phases”. Tschierske *et al.*^{93, 94} used oligo(siloxanes) attached to chiral bent-core mesogens to study the effect of combining molecular chirality and superstructural chirality in LC phases.

Kieffer *et al.*⁴⁹ used oligo(siloxanes) and oligo(carbosilanes), for their stabilizing effect on mesophases, which allow them to carry structural studies on lamellar phases presented by T-shaped bolaamphiphilic LC molecules as shown in Figure 45.

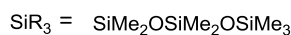
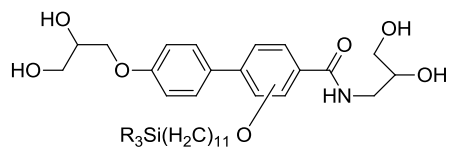


Figure 45: System studied by Kieffer and co-workers.⁴⁹

These examples reflect how oligo(siloxanes) are frequently used in the investigation of LC systems. However, they are far from the dendrimeric structures previously discussed. Siloxane units can exist in many different shapes: linear, as mentioned above, cyclic, or cage-like structures. In fact, the last one of these seems to be the most successful and widely used siloxane core for the synthesis of LC dendrimers, it is also the building block chosen in the work we presented here to synthesize LC dendrimers, hence, these systems, their applications and LC properties will be discussed in detail in the next section.

2.5 - Polyhedral octa(dimethylsiloxy)octasilsesquioxanes (POSS)

Silsesquioxanes are compounds with the empirical formula $\text{RSiO}_{3/2}$ and are described as having “hybrid” properties between the chemical inert and thermally stable inorganic Si-O-Si fragment and some from the potentially reactive and readily modified R-Si fragment.⁹⁵ They can have various structures (Figure 46) from random to ladder polymers and even highly ordered discrete molecular species with the formula $(\text{RSiO}_{3/2})_n$.⁹⁶

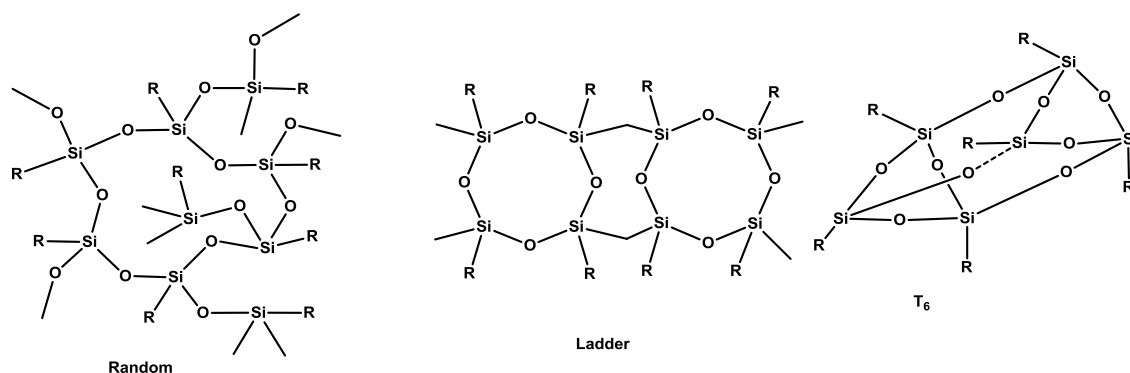


Figure 46: Chemical structures of different types of silsesquioxanes.⁹⁶

This report will focus on structures of the type $(\text{RSiO}_{3/2})_8$, polyhedral oligosilsesquioxanes which are generally referred to as POSS (see Figure 47). Previously dendrimers were described as molecules that possess branching units emanating from a central core. In each layer added to the central core, the number of functional groups increases. Structures of the type $(\text{RSiO}_{3/2})_8$, or silsesquioxanes, can be regarded as an inorganic central core, from where eight functional groups emanate radially, providing the possibility to be derivatized right at G0 level. This means that a first generation silsesquioxanes can already have 16 functional groups. The fact that a large number of functional groups can be achieved at low generation numbers, contrary to the dendrimers described in previous sections, anticipates that the number of synthetic steps necessary to achieve a certain number of functional groups is much smaller. At the same time due to their structure, the silsesquioxane core provides an immediate globular shape. Another advantage of these compounds as scaffolds for the synthesis of dendrimeric structures is the ease with which they are prepared, when compared with previous cores, since they are mainly functionalized via hydrosilylation reactions. In the following sections all these aspects regarding their structure, synthesis, functionalization and liquid crystalline properties will be discussed in detail.

2.5.1 - Nomenclature and structure of POSS

In the literature, silicon polymer nomenclature is commonly adopted, for example a silicon atom bearing three oxygen atoms also connected to silicon is denoted by T, so the structure a) in Figure 47 can be denoted by T_8R_8 . A different nomenclature is used when the silicon atom is connected to four oxygen atoms (as seen in Figure 47 b) and in

this case the molecule is denoted by Q_8R_8 ⁹⁷ the introduction of the spacer–OSiMe₂– detaches the substituent groups R from the core.

The POSS crystalline silica-like core posses a cage structure with 0.5 nanometres in diameter and after being functionalized, they might have a diameter of 1.2-1.4 nanometres. Its eight Si atoms are placed at cube vertices providing eight radial primary branches, which can be derivatized giving organic-inorganic hybrid structures at the G0 level⁹⁸ Figure 47, oxygen atoms interspersed along the edges.⁹⁹

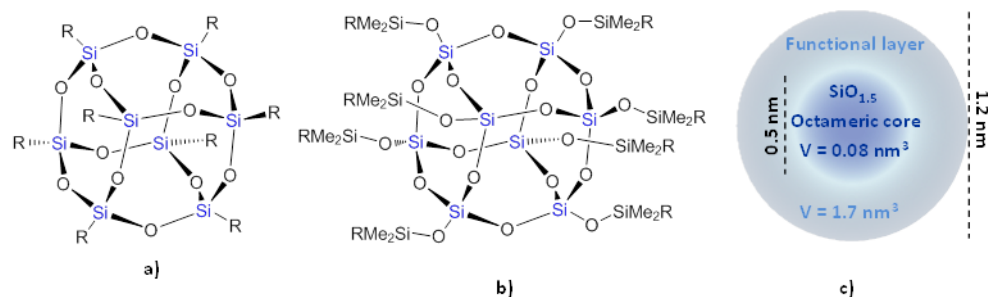


Figure 47: Cubic silsesquioxanes. a) T_8R_8 (T = carbon-SiO_{1.5}). b) Q_8 (Q = SiO₄). c) Typical sizes/volumes.⁹⁶

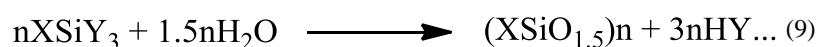
Polyhedral silsesquioxanes have many diverse applications including modelling catalytic surfaces,¹⁰⁰⁻¹⁰² substrates for new catalysts¹⁰³⁻¹⁰⁵ and novel porous media,¹⁰⁶ they are used as NMR standards,¹⁰⁷ encapsulators,^{108, 109} biomaterials,¹¹⁰ dental fillings¹¹¹ and building blocks for nanostructured materials and alignment of liquid crystals.⁹⁸ They are also largely used in composite materials or incorporated in polymers to improve their macroscopic properties such as processability, toughness and thermal and oxidative stability.⁹⁶

2.5.2 - Synthesis of POSS cages

A brief overview on strategies employed to synthesise silsesquioxanes containing materials will follow in an attempt to show how versatile the silsesquioxane building block can be, however the topic of synthesis of silsesquioxane core is vast and out of the scope of this thesis. Many reports and patents in the literature can be consulted for more information on this subject.^{96, 97}

Early work carried out on cubic silsesquioxanes relied on its spontaneous formation from hydrolysis and condensation reactions of chloro and alkoxy-silanes over T10 or T12 species due to the stability of the Si₄O₄ ring structure.⁹⁵

Although polyhedral silsesquioxanes were synthesized using a hydrolysis and condensation method from monomers of $XSiY_3$, where X is a chemically stable substituent (CH_3 , vinyl, phenyl), Y is a highly reactive group (Cl, OH or OR), problems existed related to long reaction times and low yields due to formation of other siloxane species as linear, cyclic, polycyclic.⁹⁵



Equation 9: Equation for the formation of polyhedral silsesquioxanes.

For example the synthesis of octahydrosilisesquioxane (T_8H) by hydrolysis and condensation of $HSiCl_3$ originated the product in low yields (15-20 %).⁹⁶ Despite being very useful precursors for the synthesis of POSS derivatives, the synthesis of molecules such as T_8H_8 and T_8Me_8 occurs with very low yields and attempts to improve it are still ongoing. To date the best yield achieved is 23%.⁹⁵

In order to overcome the low yields and byproducts resulting from these reactions, improvements related with reaction conditions were attempted by introducing changes in solvent systems used, type of hydrolysis and addition of other substances to reactions.⁹⁵

Hoebbel *et al.*¹¹² developed octameric silicate anion systems from hydrolysis and polycondensation of tetraalkoxysilane in the presence of tetramethylammonium ions that lead to the formation of a double four membered ring. Hasegawa *et al.*^{113, 114} followed this concept and identified a route to synthesise POSS cubes (of Q_8 type) by silylation of a silicate anion solution (see Figure 48).

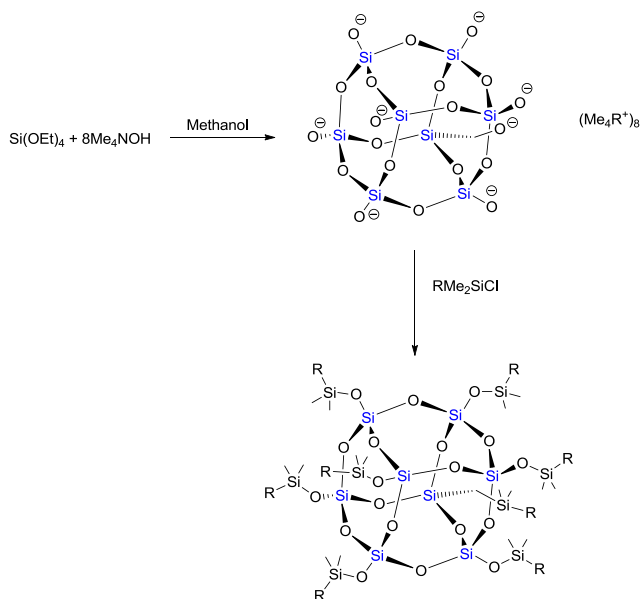


Figure 48: Synthesis of POSS cubes (Q_8 type) Hasegawa and co-workers.^{113, 114}

Of significant importance was the realisation that this cubic silsesquioxane formation depended of the existence of ammonium counter ions as well as water, but also that when the concentrations of ammonium counter ion, for example Me_4N , relatively to the concentration of silicates was higher than 0.5M, the formation of Q8 species was almost complete.⁹⁷

Synthesis of systems having Si-H or vinyl bonds is very important since they can be easily functionalized via hydrosilylation in the presence of a Pt catalyst, as will be discussed later, allowing the formation of very diverse building blocks such as the ones represented in Figure 49.

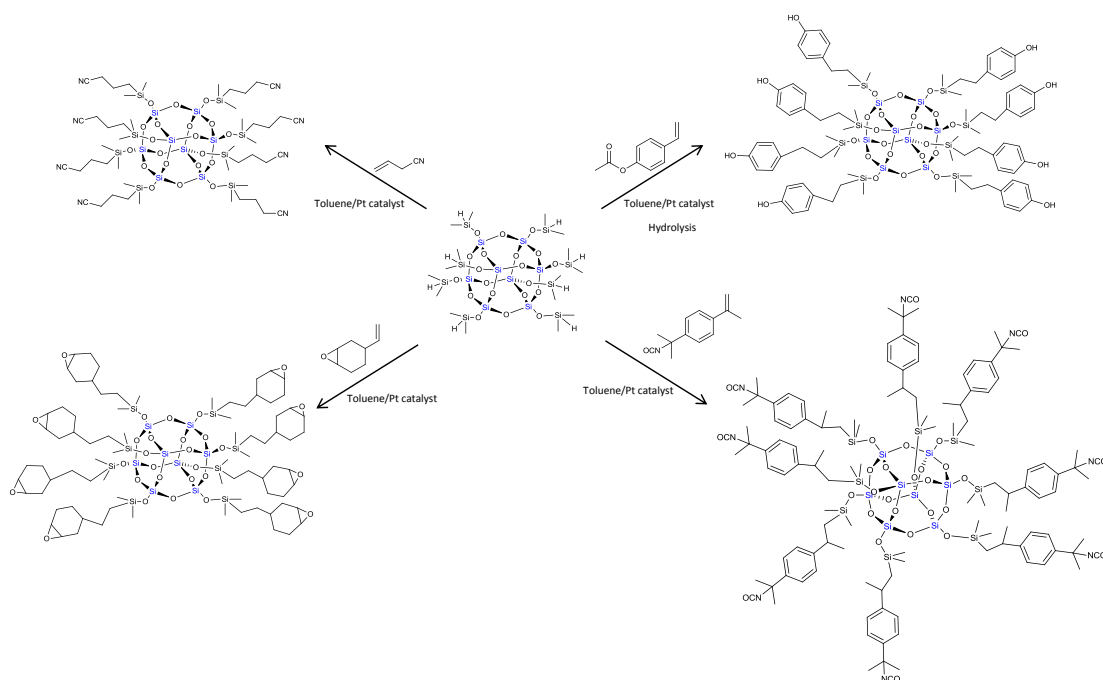


Figure 49: Examples of functionalization of POSS cores through hydrosilylation.⁹⁶

The functionalization of T_8 systems is also possible for example, T_8Ph_8 that can be prepared and further functionalized as shown in Figure 50. The functionalization of materials like POSS with alkyl or phenyl chains, Expls $\text{T}_8[(\text{CH}_2)_3\text{NH}_2]_8$ and T_8Ph_8 , is attractive because the yield of the reactions is higher and there are a variety of reactions that they can tolerate such as the ones represented in Figure 50.

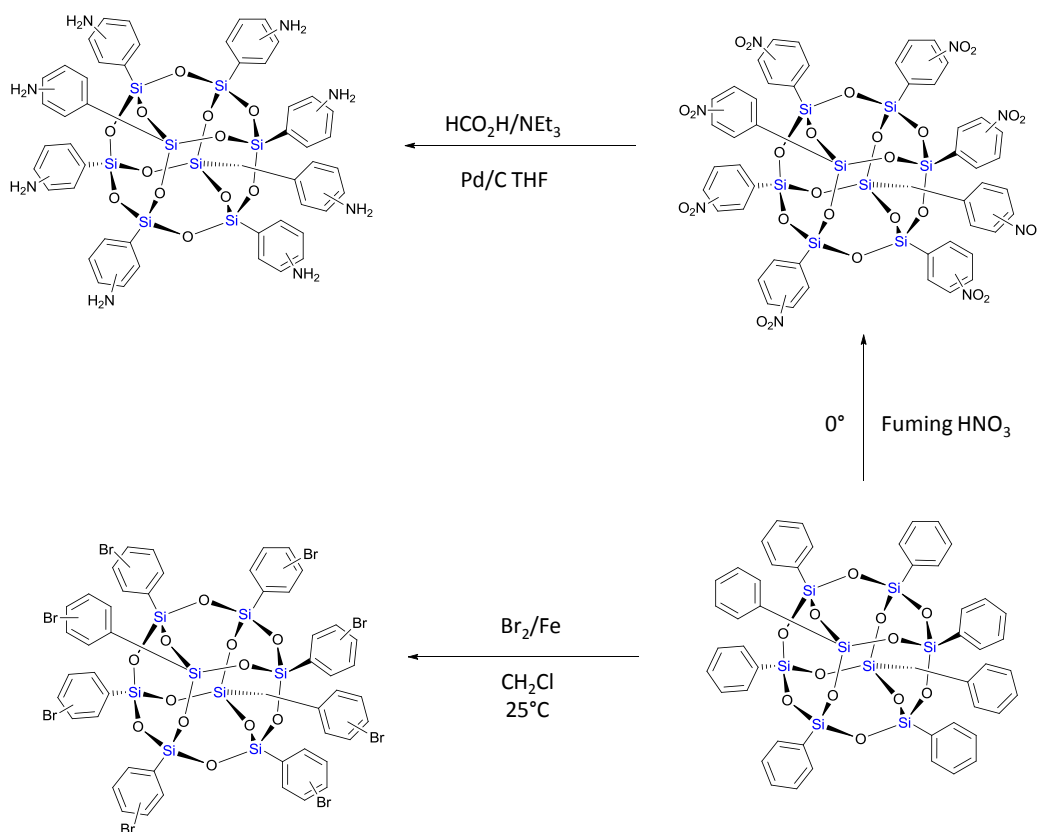


Figure 50: Synthesis of POSS derivatives by nitration, iodination, bromination.⁹⁶

A different approach is to start from partially condensed silsesquioxanes and add a new functionality in one of its corners following the same general reaction (Figure 51). This route was explored by many authors¹¹⁵⁻¹²² but this will not be described any further here.

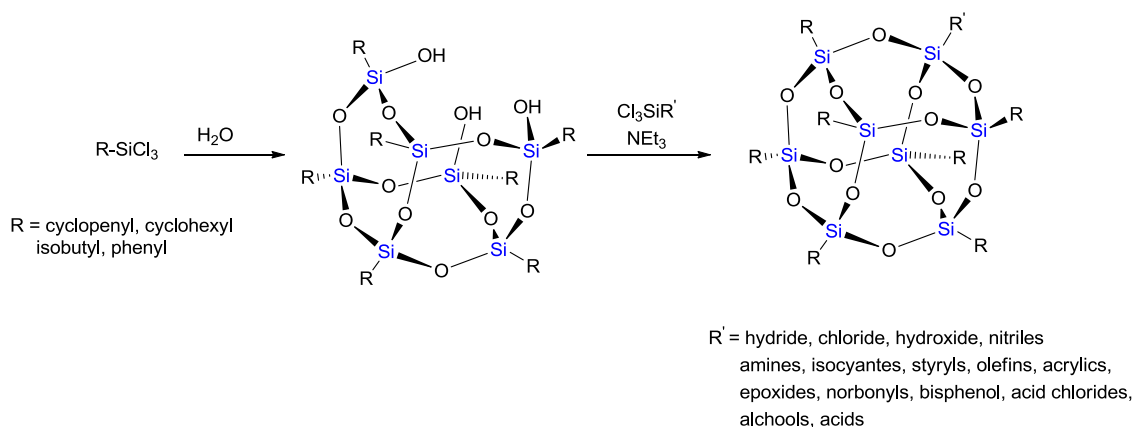


Figure 51: Synthesis of a POSS derivative starting with a partial condensed silsesquioxane.¹¹⁵

2.5.3 - Functionalization of POSS by hydrosilylation

Hydrosilylation is frequently used to prepare organosilicon compounds and involves the addition of Si-H bonds, in this case from materials such as T_8H_8 or $T_8(OSiMe_2H)_8$, across unsaturated bonds such as alkenes and alkynes. It can occur in one of two ways: a) hydrosilylation of a mesogen containing a terminal alkene with hydrosilsesquioxane core; or b) hydrosilylation of an alkenylsilesquioxane with a mesogen that possesses terminal hydrosilicon functionality (see Figure 52).¹²³

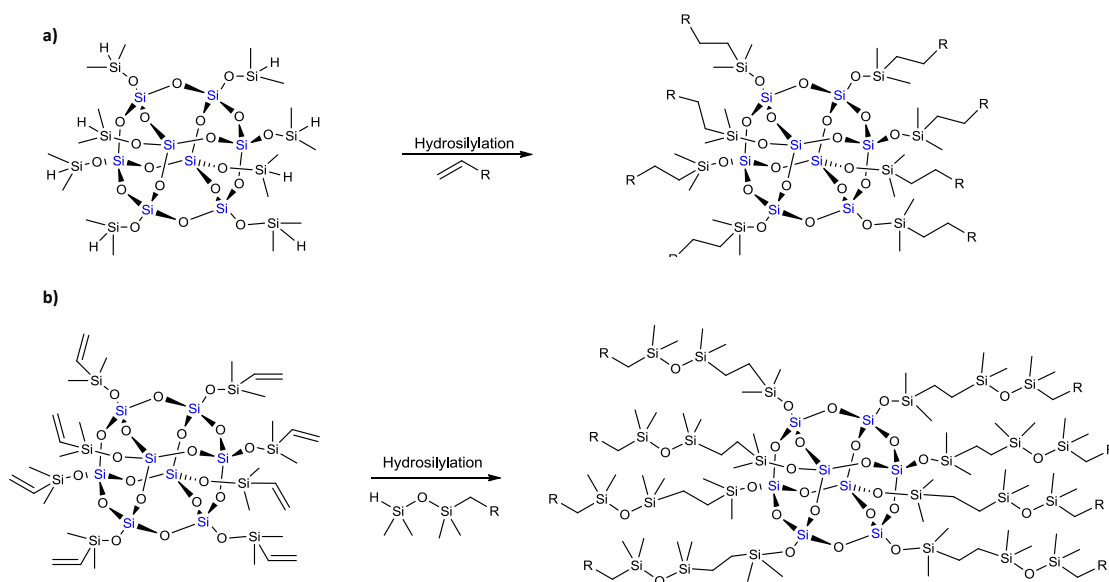


Figure 52: Hydrosilylation of silsesquioxanes.

In order to achieve the connection of the silsesquioxane core to the mesogenic unit, a Pt catalyst is usually used.

Although the reaction yields are fairly high, there are two potential problems. The first being the possibility of β -addition to the double bond (see Figure 53), however due to the strong directing effect of the silicon, this is not usually a problem and the sole product of the reaction is the α -product.

Secondly if alcohols, aldehydes or ketones are present, the reaction of the silicon atoms with the oxygen may occur, forming silylethers.

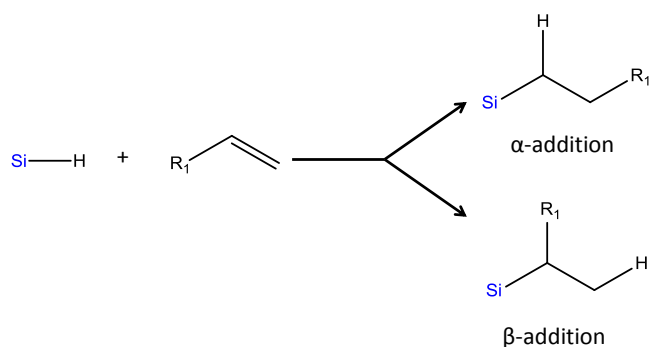


Figure 53: α - and β - addition in hydrosilylation reactions.¹²³

Syntheses of polyhedral silsesquioxane based LCs is mostly carried out via hydrosilylation using an excess of the mesogenic unit in order to ensure complete reaction of all the available sites on the silsesquioxane core. However, for other applications several other synthetic procedures using the silicon atom are employed such as chloride/alkoxide exchange,¹²⁴ exchange of protons,¹²⁵ introduction of di-trimethylsilyl species¹²⁶ etc. Besides using the silicon functionality, POSS derivatives can be prepared by using common organic reactions in the organic substituents of the silsesquioxane cores. This possibility expands extensively the number of materials that can be synthesised. Within organic reactions used examples of nucleophilic substitutions,¹²⁷ Heck reactions,¹²⁸ Suzuki reactions,^{129, 130} Sonogashira reaction,¹³¹ nitrations,¹³² and substitutions at an aromatic ring,¹³³ and many others have been reported.¹³⁴ Despite the flexibility of these materials towards organic reactions the integrity of the POSS core has to be assured and reactions that might jeopardize it should be avoided such as the use of strong bases that can cleave Si-O bonds in the POSS core.

2.6 - Liquid crystalline silsesquioxanes: Synthesis and applications

Polyhedral liquid crystal dendrimers are mainly synthesized in a convergent way; the silsesquioxane core and LC chains are prepared separately and fused in the last step, although a divergent synthesis is also possible, this strategy is employed to synthesize the majority of LC POSS reported in the literature such as the ones discussed below. Generally a liquid-crystalline silsesquioxane has four components (Figure 54).

- Silsesquioxane core (**A**)
- Attachment linking the inorganic core to the spacer, usually $-\text{SiMe}_2\text{O}-$ unit (**B**)
- A hydrocarbon spacer (**C**)
- Mesogenic unit (**D**)

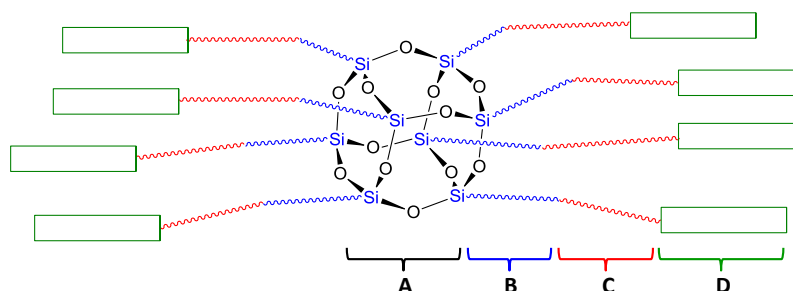


Figure 54: In this figure, the general components of a silsesquioxane core dendrimer.¹²³

Taking into account the variety of POSS cores, mesogens, and attachments (end- or side-on) that might be used, is not surprising that a vast number of LC POSS can be synthesised, in order to achieve specific properties that are suitable for desired applications.

A series of papers were reported on the investigation of liquid crystalline POSS possessing cyanobiphenyl derivatives (see Figure 55).¹³⁵ These mesogenic units were attached end-on to the silsesquioxane core, through an alkyl chain as shown in Figure 55. Different chain lengths were used and the liquid crystalline properties studied using OPM, DSC and X-ray.

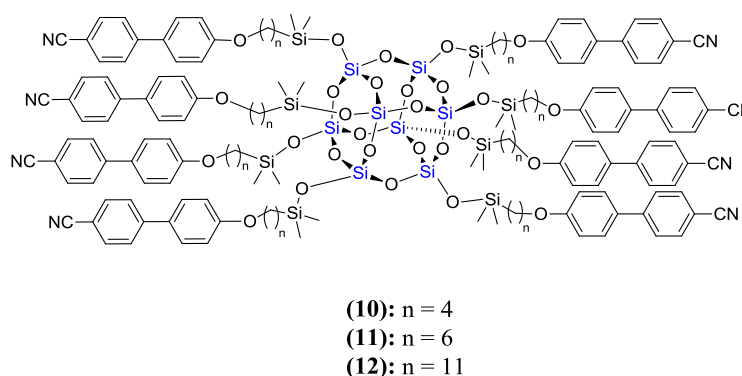


Figure 55: System studied by Mehl *et al.*¹³⁵

A first attempt to synthesise compounds **10** to **12** was made using Spier's catalysts (H_2PtCl_6) yet complete substitution of the cubic core was not achieved and Karstedt's catalyst, which is stronger and allows reactions to be carried at room temperature, was employed.¹³⁵ The result was complete α -addition of the terminal alkene to the silicon groups on the core. Compounds **10** to **12** exhibit SmA phases and the increase of the

number of alkyl units, increases the isotropization temperatures from 93.9 °C to 128.5 °C, which could be explained by the decoupling of the mesogenic units from the central core, promoting intermolecular interactions among cyanobiphenyl groups, increasing the order of the molecules and the transition temperatures. On the other end the glass transition temperatures diminish from 11 °C in compound **10** to -7 °C in compound **12**. The X-ray studies suggest that the siloxane cores are in the middle of the layers and the mesogenic groups interdigitate as represented in Figure 56.

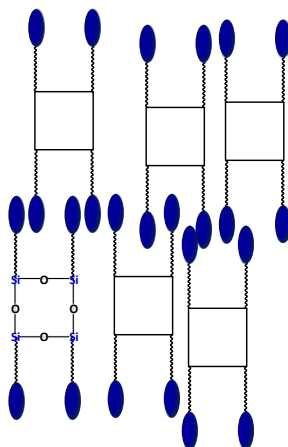


Figure 56: Representation of interdigitation of molecules represented in Figure 55.

Saez *et al.*¹³⁶ took this work further by synthesising a LC dendrimer of the 1st generation, containing 16 cyanobiphenyl mesogenic units attached to a octasilsesquioxane core via undecylene aliphatic chains.¹³⁶ In order to prepare this compound, the core was derivatized with HSiMeCl₂ followed by reaction with vinyl magnesium bromide, which increased the number of positions that could be further functionalized. The mesogenic units were prepared separately and hydrosilylation with Karstedt's catalyst in toluene at room temperature, result in compound **16** see Figure 57.

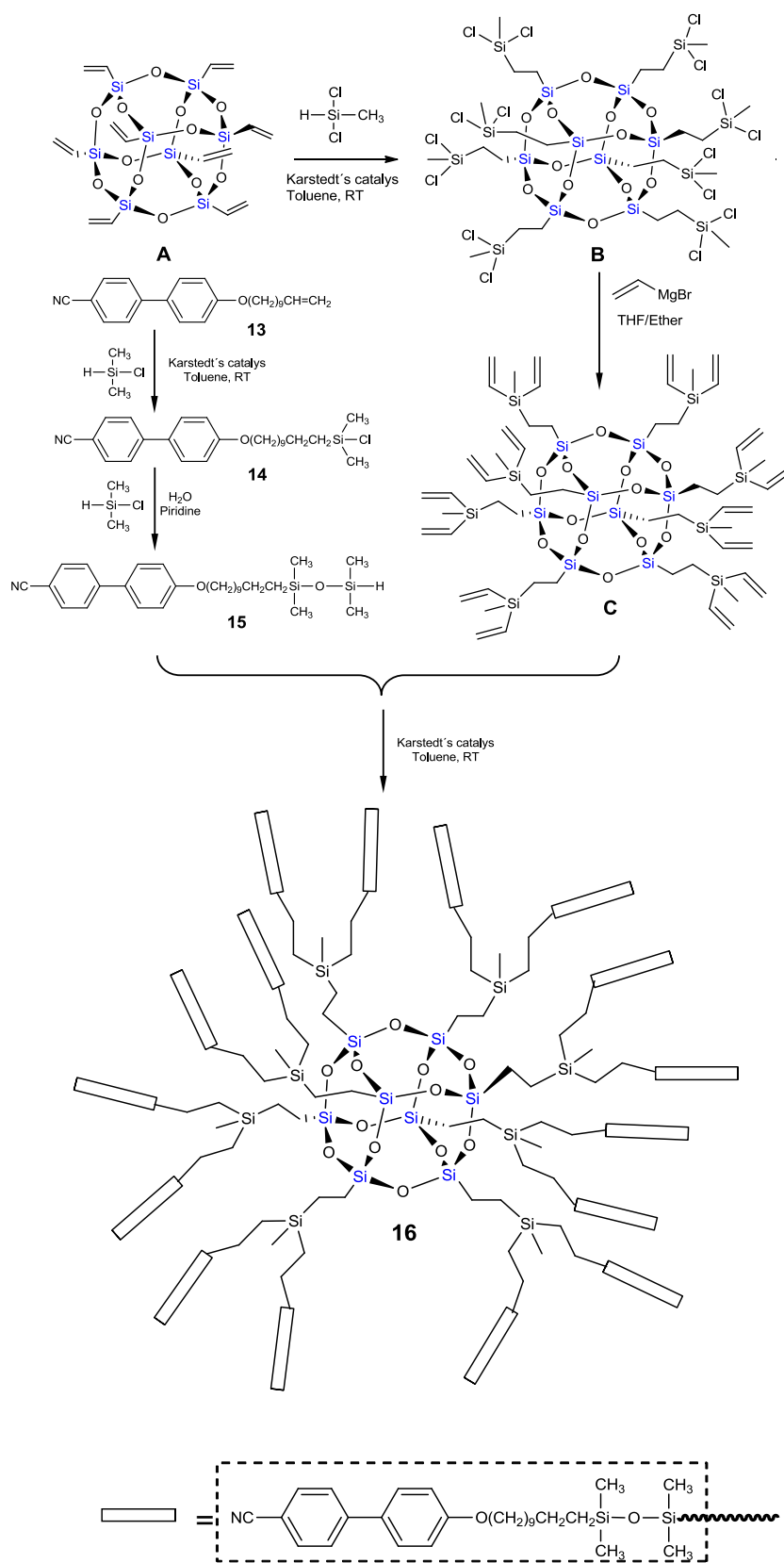


Figure 57: System studied by Saez and co-workers.¹³⁶

The authors expected that increasing the numbers of mesogenic groups would force the molecules to adopt a spherical shape able to compete with the deformation of the system in order to fit in with its mesogenic environment and obtained columnar or cubic

phases. However, compound **16** showed solely smectic phases and the transition temperatures were found to be $T_g -17.5$ SmC 63.1°C SmA 91.7°C I. In order to explain these results was suggested that this 1st generation dendrimer adopted a rod-like conformation where the mesogenic arms stayed above and below the octasilsesquioxane core (as exemplified in Figure 58), making it possible to pack in layers consisting of a quasi-bilayer of the mesogens and a monolayer structure for core C.

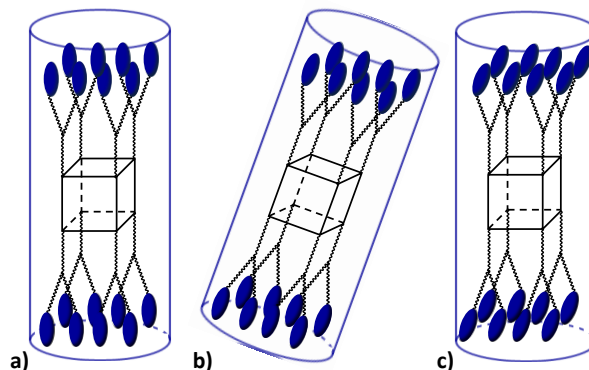


Figure 58: Representation of possible organization of molecules in Sm phases.¹³⁶

The synthesis of LC POSS derivatives showing nematic behaviour has been achieved by one of two manners: lateral attachment of mesogens or incomplete substitution of the cubic core. As shown in the work reported by Sellinger¹³⁷ (Figure 59) and Zhang¹³⁸ (Figure 60), where the authors wished to polymerize LC POSS derivatives. With this in mind they partially functionalized the octasilsesquioxane core having on average 4-5 pre-mesogenic molecules and leaving 3-4 “open” corners that could be substituted with polymerizable groups to afford compounds with low transition temperatures required for biological applications such as dental fillings.¹¹¹

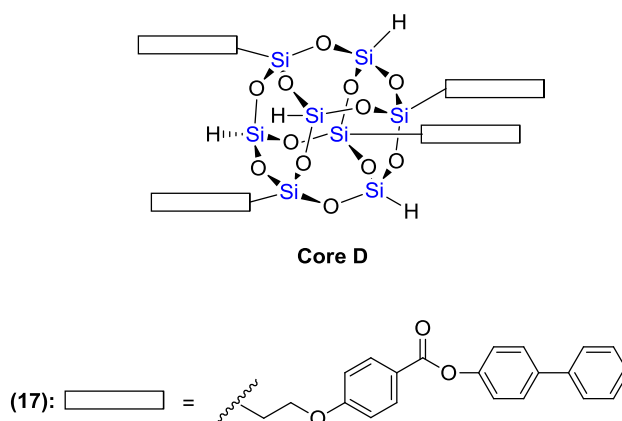


Figure 59: System studied by Sellinger *et al.*¹³⁷

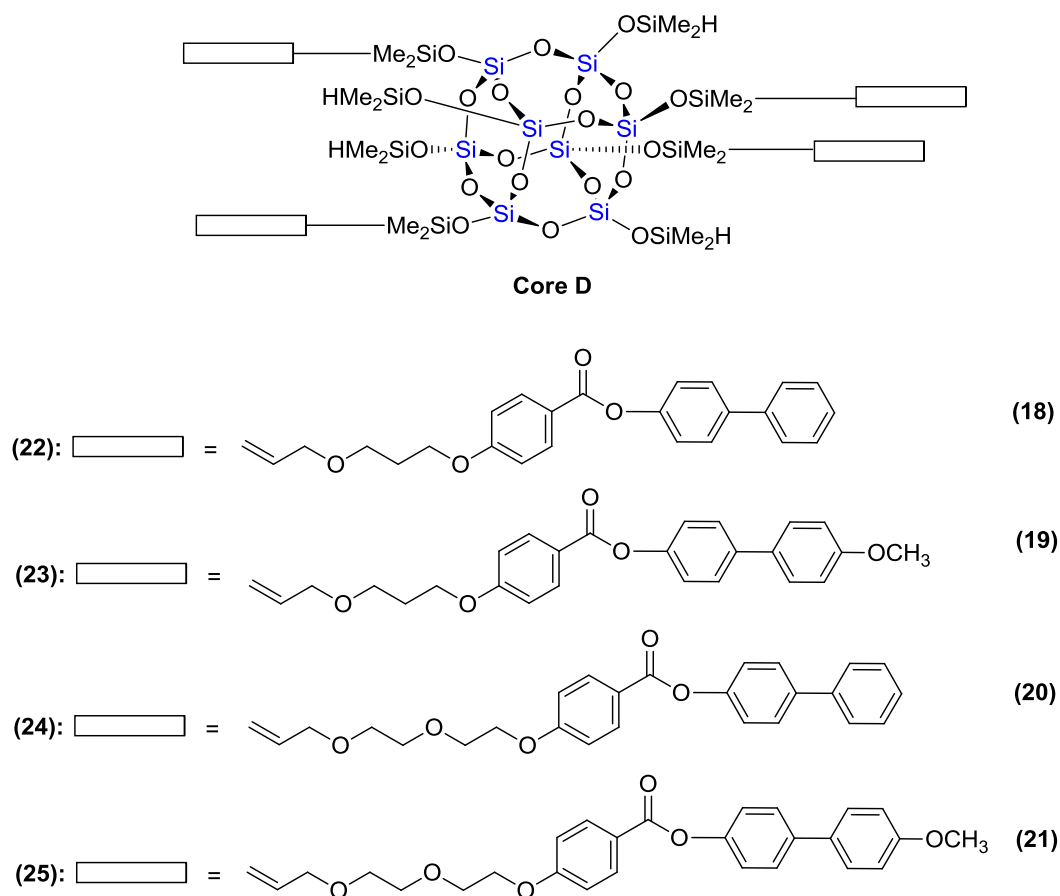


Figure 60: System studied by Zang *et al.*¹³⁸

The initial work by Sellinger reported that compound **17** showed a nematic phase between 134 - 178 °C. Following this work, the LC-silsesquioxane synthesised by Zhang are on average penta-substituted (results confirmed by EA and NMR). Very narrow polydispersity values (1.03-1.06) were reported, which did not seem to agree with the statistical distribution of the products (mono-, di-, tri-, etc.). The similarities in the hydrodynamic radii of these species due to their rigid 3D structure might result in narrow polydispersities. Thermal studies verified that the compounds are stable up to 280°C/N₂ (typical for organic compounds) and that ceramic yields are in agreement with theoretical calculations considering average degree of substitution.

The LC behaviour was checked by POM, DSC and confirmed by XRD experiments and mesophase behaviour is depicted in the Table 1. Despite the liquid-crystalline behaviour of the monomers all POSS derivatives except **22** exhibited LC behaviour.

Table 1: Phase transitions for compounds studied by Zhang et al.¹³⁸

Mesogen	Phase transitions (°C)	POSS derivative	Phase transitions (°C)
18	Cr 103 Iso	22	Cr 138 Iso
19	Cr 67 N 205 Iso	23	Cr 148 SmA 177 N 189 Iso
20	Cr 63 Iso	24	Cr 90 SmA 113 Iso
21	Cr 121 Iso	25	Cr 123 SmA 156 N 158 Iso

Following previous work,¹³⁷ flexible ethylenoxy spacers were introduced to decrease transition temperatures from 143 °C for mesogen in compound **17** to 63 °C (in the best case, for compound **20**). POSS derivatives were prepared by hydrosilylation using a Pt catalyst with α -addition being favoured. The terminal alkene compounds **18**, **20** and **21** (Figure 60 and Table 1) showed no liquid crystalline properties, explained by an increase in the flexibility of the spacer. The introduction of polar methoxy groups increases the thermal transition temperatures of the corresponding LC cubes as denoted in Table 1 for compounds **22** and **23** and for compounds **24** and **25**. The phases observed by POM were confirmed by XRD studies.

As mentioned previously, nematic LC POSS can be obtained by lateral attachment of mesogenic molecules as first reported by Kreuzer *et al.*¹³⁹ This methodology was also used by Elsäßer *et al.*¹⁴⁰ to induce nematic phases in silsesquioxanes. The systems studied are shown in Figure 61. Another objective in this study was to understand whether the dictating effect on phase behaviour was microphase segregation (between organic mesogens and inorganic core) or the size of the bulky methyl groups of the siloxane units. For this reason, molecules **26** and **27** were attached to cores **F**, **G** and **H** through hydrosilylation using Karstedt's catalyst.

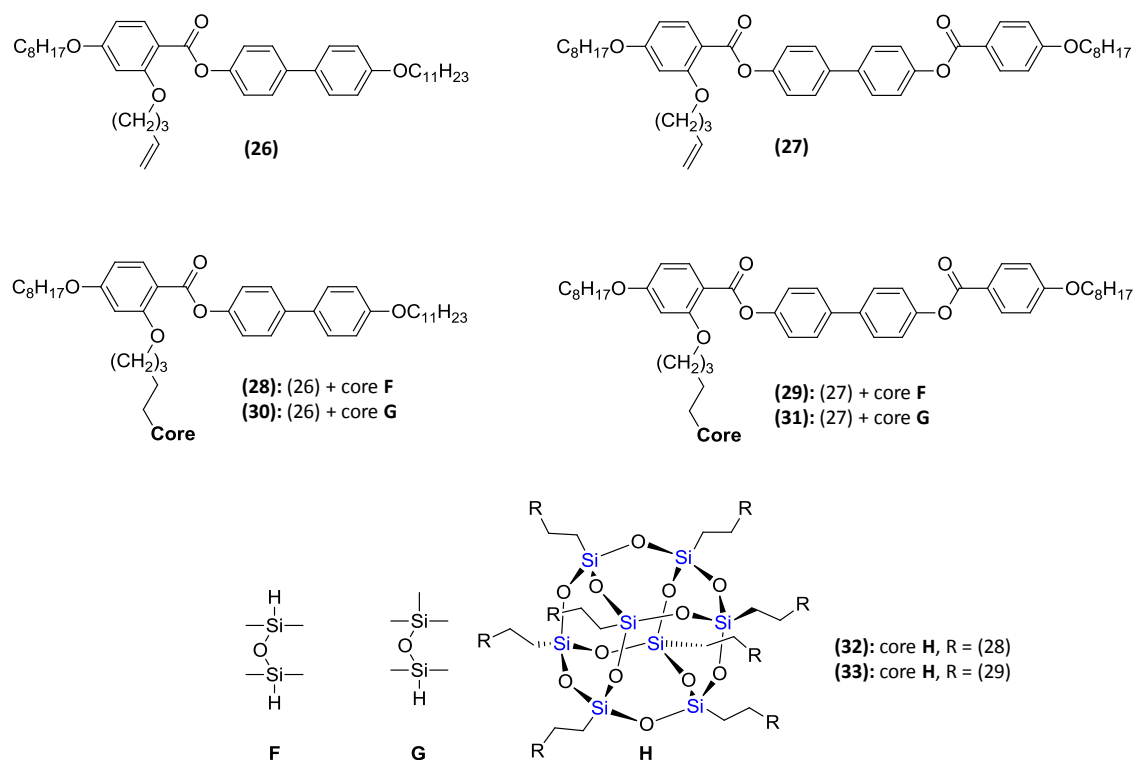


Figure 61: System studied by Elsässer and co-workers.¹⁴⁰

The liquid-crystalline behaviour described by the authors is depicted in Table 2. From the observation of the transition temperatures, it is clear that the introduction of siloxane units decreases substantially both melting and isotropization temperatures (compare compounds **26** with **28** or **30**, for example). However compounds **28** and **30** as well as **29** and **31**, having different siloxane cores, show very similar transition temperatures suggesting that the phase behaviour is not related with the mesogen groups, but with microphase separation. The observation of an unidentified phase is mentioned by the authors.

Table 2: Phase transitions for compounds studied by Elsässer et al.¹⁴⁰

Compound	Phase transitions (°C)
26	Cr 53.8 N 72.7 Iso
27	Cr 99.4 N 173.2 Iso
28	Cr 18.0 N 39.1 Iso
29	Cr 67.1[SmC 51.3] N 123.8 Iso
30	Cr 24.8 N 39.5 Iso
31	Cr 76.6 [SmC 58.2] N 122.0 Iso
32	G -19.3 SmX 37.6 N 50.5 Iso
33	Cr 59.5 [SmX 33.1] SmC 111.3 N 145.8 Iso

Following the findings of columnar phases in dendritic materials with similar mesogens prompted the above systems to be revisited and the nature of the unidentified phase was identified as a columnar hexagonal phase.⁴⁸ The recent reports on these systems will be discussed next.

The material studied by Karahaliou *et al.*⁴⁷ has a 4 aromatic ring mesogen as shown in Figure 62 and it is attached to a silsesquioxane core by a longer spacer than compounds **25** and **26** in Figure 61.

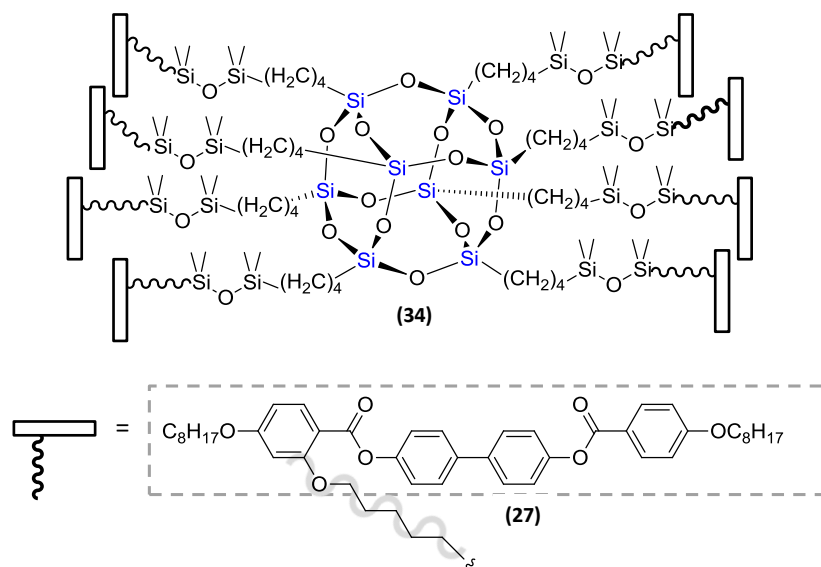


Figure 62: System studied by Karahaliou *et al.*⁴⁷

Compound **27** was investigated as well as a series of mixtures of compounds, **27** and **34**, the increase in the amount of **27** destabilizes higher order liquid-crystalline phases such as columnar rectangular and columnar hexagonal phases, culminating in their suppression when the amount of monomer **27** is 0.44 and 0.69 respectively. The XRD experiments carried out revealed some interesting features such as the existence of cybotactic clusters that were persistent throughout the entire mesophase range. Models for both columnar hexagonal and rectangular phases were suggested.

In the Col_h phase, column formation arises from microsegregation between the cubic inorganic cores and the organic mesogens. The interior of the columns is formed by the core and spacers, while the calamitic mesogens surround them in a uniform manner with the long axis positioned on average along the columns. Within each column, the mesogens of adjacent cubes will interdigitate, since the distance between two siloxane cores (14 Å) is smaller than the length of the mesogen **27** approximately 23 Å. In the Col_r phase mesogens are no longer evenly distributed around the column axis, however the mesogens of adjacent columns will orientate in such a way that a more uniform

mesogen density is achieved. Interdigitation of mesogens belonging to adjacent cubes within a column is also present.

The reassessment of mesomorphic behaviour attributed to compound **32** (Figure 61, pag. 46) was carried by Karahaliou *et al.*⁴⁸ in 2006, where extensive XRD studies were reported. As described above they confirmed the presence of cybotatic clusters throughout the entire range of temperatures. The existence of a Col_h phase in which the inorganic cubes are stacked in the centre of the columns surrounded by mesogens with their long axes parallel to the column axis, promotes the interdigitation of the end chains of the mesogenic units (since the length of the extended mesogen (41 Å) is bigger than the silsesquioxane cores (≈ 14 Å)). This results in slices of tilted bilayers formed by the mesogenic units.

The use of lateral attachment of mesogenic units to a silsesquioxane core to obtain nematic phases, was extended to the chiral mesogens in an attempt to obtain chiral nematic systems by Saez *et al.*¹⁴¹

The strategy used was based on the functionalization of hexadecaviny dendrimer with a chiral mesogen (Figure 63).

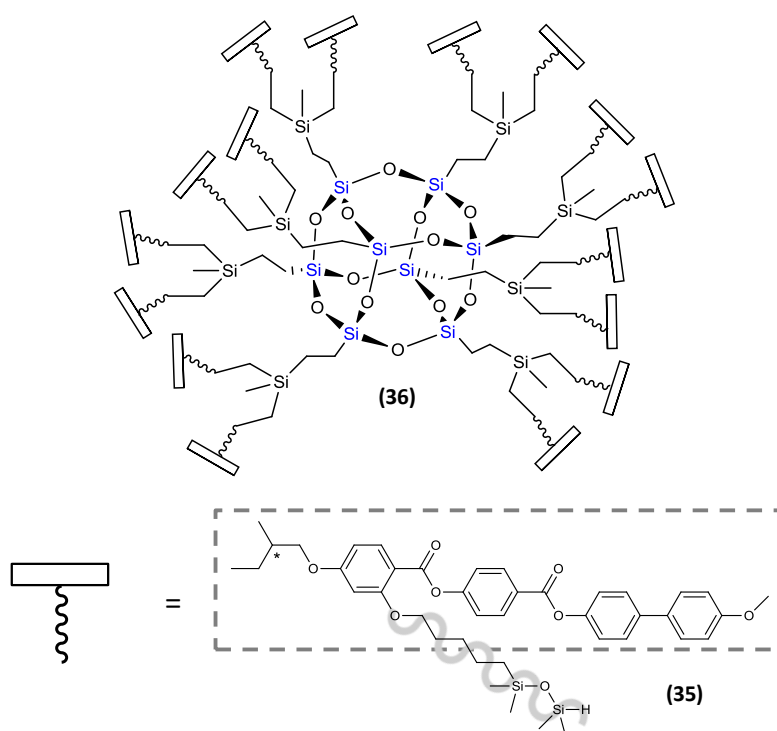


Figure 63: System studied by Saez *et al.*¹⁴¹

The liquid crystalline properties of the monomer **35** and octapode system **36** were studied by POM, DSC and X-ray diffraction. The monomer **35** showed only a chiral

nematic phase (Cr 73.6 °C N* 88.2 °C Iso). Calorimetric studies for the POSS derivative **35** showed, on cooling, only two peaks corresponding to a chiral nematic (107.7 °C) and a columnar hexagonal mesophases. However, both polarizing optical microscopy and XRD pointed to the existence of a further columnar rectangular phase at approximately 30 °C. The data suggested that on cooling the hexagonal columnar phase becomes distorted, culminating in the formation of rectangular columnar phase. A model for the molecular organization of the mesophases was proposed for the columnar hexagonal phase. The authors suggested that the dendrimer assumed a cylindrical shape, with similar width and height, surrounded by mesogens with their major axis parallel to the rotational axis of the cubes, stacked into columns, similar to that previously discussed for the systems studied by Karahaliou *et al.*^{47, 48} Relative to the chiral nematic phase they foresee two possibilities: that the dendritic cylindrical entities self-organize into a chiral nematic discotic phase, or that they assume an oval shape organizing themselves in a calamitic chiral nematic phase.

LC hybrid polymers based on functionalised silsesquioxanes are expected to show enhanced properties by combining properties between organic LC and inorganic silsesquioxane materials. With this in mind in 2001, Chujo *et al.*¹⁴² reported the synthesis of a liquid-crystalline hybrid polymer with organic (methacrylate derivative) and inorganic (functionalised POSS) side chain monomers Figure 64. Variation of the amount of POSS modified the LC behaviour as well as thermal stability of the copolymer.

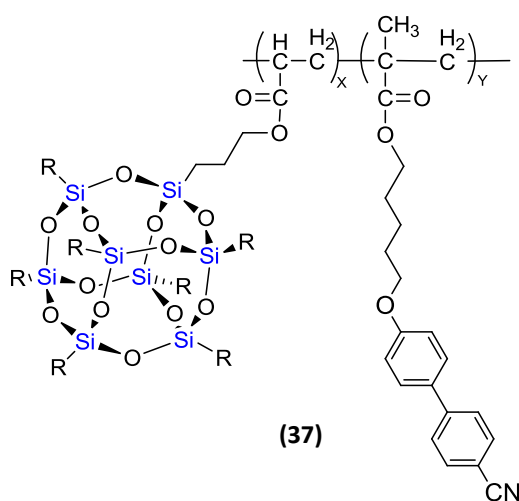


Figure 64: System studied by Chujo *et al.*¹⁴²

An interesting observation was that there appeared to be a maximum value of POSS that could be incorporated in the polymer. Additionally, the POSS homopolymer showed

lower molecular weight than the rest of this series of materials. This was explained by the steric hindrance caused by the bulkiness of the POSS macromonomer.

Surprisingly the addition of more than 10% of POSS into the hybrid polymer suppressed the existence of LC phases. One explanation is the fact that the rigidity and bulkiness of POSS prevented the appearance of LC phases resulting from the orientation of the methacrylate derivative mesogen, reducing the mobility of LC hybrid polymers. TGA analyses showed an increase in the 10% decomposition temperature from 316 °C to 385 °C which occurred when the amount of POSS in the polymer was raised.

In the same year Chujo *et al.* reported the study of LC behaviour of some mesogens and their POSS counterparts (Figure 65).¹⁴³

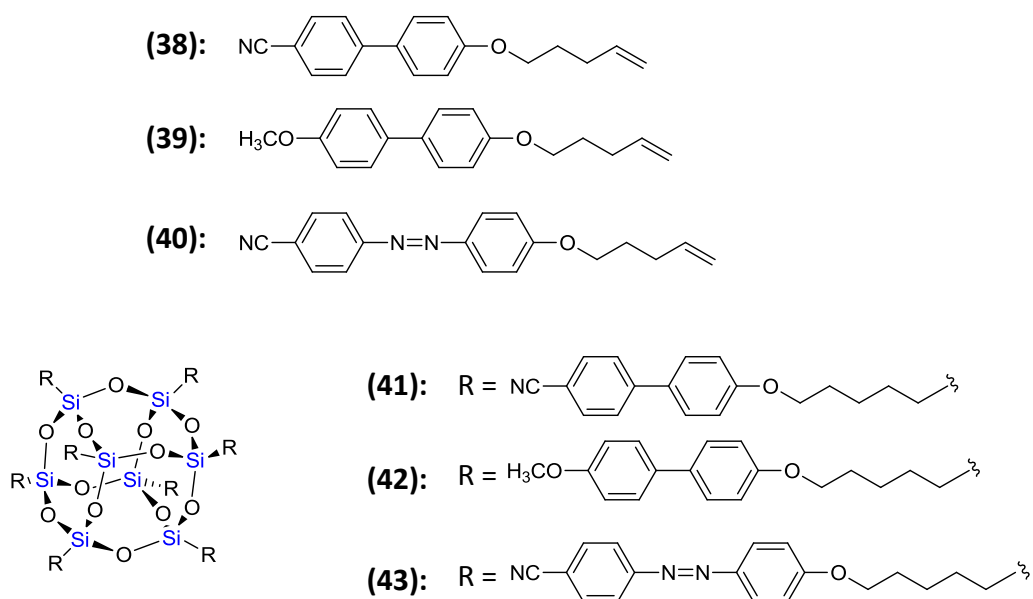


Figure 65: System studied by Chujo *et al.*¹⁴³

The reaction of the mesogens with the silsesquioxane shown in Figure 65 was made via hydrosilylation using hexachloroplatinic acid as a catalyst, with yields around 50%. NMR showed full substitution of the silsesquioxane core (this is eight mesogens per cube) and their LC behaviour was studied by DSC and OPM.

Although compounds **38** to **43** were described as monotropic liquid crystals, the authors refer the observation of liquid crystalline textures both on heating and cooling for the POSS derivatives, **41** to **43**. The authors present transition temperatures for the compounds (see Table 3) obtained by OPM. At the same time transition temperatures obtained by DSC and referred to by the authors as melting temperatures are quoted, for compounds **38** to **40** these temperatures are higher than the temperature reported for the

Iso to N transition, agreeing with monotropic behaviour. For compounds **41** to **43** the temperatures quoted seem to correspond to the clearing temperatures, since they concur with the temperatures reported for the N to Iso transition. Although this suggests that the POSS derivatives might be enantiotropic liquid crystals, the authors mention that the transition temperatures observed by OPM “are nearly consistent with that observed by DSC”¹⁴³ but unfortunately this is not discussed further. The authors suggest that the increase in the local concentration of mesogens caused by the fixed directionality of the silsesquioxanes facilitates the orientation of the mesogenic units, stabilizing the LC phase.

Table 3: Phase transitions for the systems studied by Chujo *et al.*¹⁴³

Mesogen	Phase transition (°C)	POSS derivative	Phase transition (°C)
38	Iso 109 N 102 Cr	41	Cr 166 N 215 Iso
39	Iso 65 N 48 Cr	42	Cr 70 N 139 Iso
40	Iso 113 N 101 Cr	43	Cr 140 N 173 Iso

So far, this report has focused on several examples of calamitic mesogens connected to silsesquioxane cubes but the synthesis of POSS dendrimers is not limited to calamitic mesogens. Some examples have been reported where discotic 99 or bent-core LCs were used.

In 2008, Pan *et al.*¹⁴⁴ studied how the number of bent core mesogenic LCs attached to a silsesquioxane core as well as the size of the silsesquioxane core influenced the liquid crystalline behaviour.

The octapodes were synthesized by hydrosilylation of the POSS cores **I** or **J** with the mesogenic unit (**44**) depicted in Figure 66. The materials using core **I** were synthesized to have an average of 3.5, 5, and 8 mesogenic units connected (compounds **46**, **47** and **45** respectively), while core **J** was full substituted with mesogen **44** (see Figure 66). DSC, XRD, and electrooptic studies were performed in order to characterise the liquid crystalline behaviour which is summarized in Table 4.

see Figure 67. The pre-mesogenic units used varied in the number of methylenic units and are also represented in Figure 67. Thermal stability studies showed that cyclic oligosiloxanes are thermally not as stable as the silsesquioxane series although for both systems, degradation began at 150 - 200 °C above isotropization temperatures hence not affecting the mesophases.

With regards to the liquid crystalline behaviour, neither of the series showed LC behaviour for the mesogens with the shorter spacer **49**. For the **K** series all the compounds showed LC behaviour (see Table 5) and increasing the chain length decouples the organic moieties from the siloxane core increasing the range and thermal stability of the mesophases. In the silsesquioxane series, the need for much longer spacers seems to be required for the existence of LC phases, since only **62** and **63** show LC behaviour. The variation of the melting temperatures does not follow a particular trend, yet the clearing temperatures increase with the increase of the chain length, and as a result a increase in the thermal stability of the LC phases is observed.

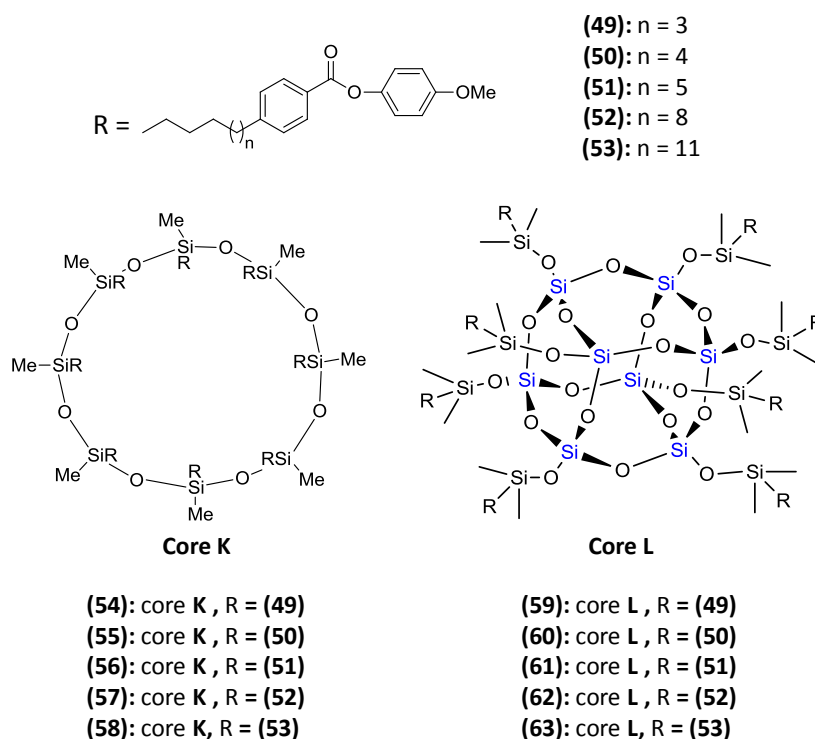


Figure 67: System studied by Soltysiak *et al.*¹⁴⁵

Table 5: Phase transitions for the systems studied by Soltysiak et al.¹⁴⁵

Compound	Phase transitions (° C)	POSS derivatives	Phase transitions (° C)
54	Cr 42 Iso	59	Cr ₁ 49 Cr ₂ 79 Iso
55	Cr 55 N 74 Iso	60	Cr ₁ 50 Cr ₂ 69 Iso
56	Cr 51 N 103 Iso	61	Cr ₁ 50 Cr ₂ 57 S ₁ 111 Iso
57	Cr 45 N 94 SmA 107 Iso	62	Cr ₁ 38 S ₁ 58 SmA 123 Iso
58	Cr 38 SmA 118 Iso	63	Cr 59 SmA 133 Iso

A series of biphenyl derivatives with different number and length of terminal alkoxy chains were synthesized (see Figure 68) by Wang *et al.* with the intent of studying their influence in the formation of LC phases in POSS derivatives.¹⁴⁶

The first main observation on this work was the fact that only compounds bearing one terminal alkoxy chain in the mesogen (compounds **64** to **67**) exhibited liquid crystalline phases. The thermal behaviour for this series of compounds obtained by DSC measurements is depicted in Table 6.

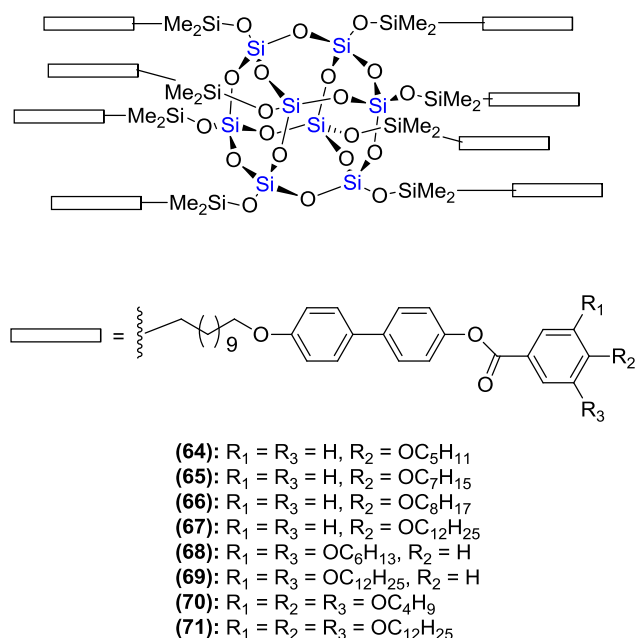


Figure 68: System studied by Wang *et al.*¹⁴⁶

Derivatives with only one flexible chain **64** to **67** from Figure 68, show LC phase behaviour while when more than one was present, regardless of their length no LC phases were formed. To explain the results, the concept of FGD “flexible group density” (defined as the number of the CH₂ groups per unit volume in the periphery of

the POSS molecule) was introduced. The high FGD exhibited by di- and tri-substituted mesogens explains the absence of LC phases.

Table 6: Phase transitions for the systems studied by Wang et al.¹⁴⁶

POSS derivative	Phase transitions (°C)
64	Cr 124 Sm 220 Iso
65	Cr 122 SmA 233 Iso
66	Cr 127 Sm 232 Iso
67	Cr 119 Sm 211 Iso
68	Cr -8.5 Iso
69	Cr -0.9 Iso
70	Cr 39.7 Iso
71	Cr 25 Iso

CHAPTER 3: PHOTOCROMIC AZOBENZENE CONTAINING MATERIALS

3.1 - Photochromism: general concepts

According to IUPAC, photochromism is a reversible transformation of a chemical species in one or both directions by absorption of electromagnetic radiation between two forms A and B, having different absorption behaviour (Figure 69).

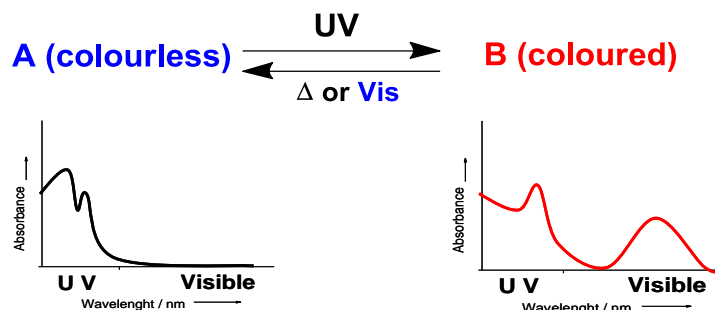


Figure 69: Representation of absorption spectra of a photochromic system.

Considering the figure above, irradiation (UV, vis or IR irradiation) of stable form A gives product B. When the reverse process or back reaction occurs thermally it is denominated photochromism of type T while when the back reaction occurs photochemically it is said to be of type P.¹⁴⁷

Photochromic reactions are commonly unimolecular but they can also be bimolecular and if $\lambda_{\max}(A) > \lambda_{\max}(B)$, the photochromism is assigned of positive, if the reverse is observed then it is negative photochromism.¹⁴⁷

3.2 – Azobenzenes

Azobenzenes are chemical compounds composed of two benzene rings which may or may not be substituted, linked by a N=N double bond (Figure 70). They were first described in 1856 and were initially used as dyes or organic pigments. Azobenzenes colour can be adjusted by changes in ring substitution, varying the absorption maxima anywhere from UV to the visible red region.¹⁴⁸

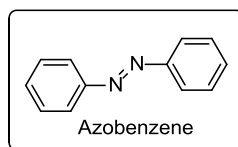


Figure70: Molecular structure of azobenzenes

The double bond of azobenzenes permits them to photoisomerise between a *trans* and a *cis* form as shown in Figure 71. This isomerisation process between the thermally stable *trans* and the metastable *cis* configuration is completely reversible and occurs without side reactions. The first report of a photochromic effect in these compounds dates back to 1937.¹⁴⁹

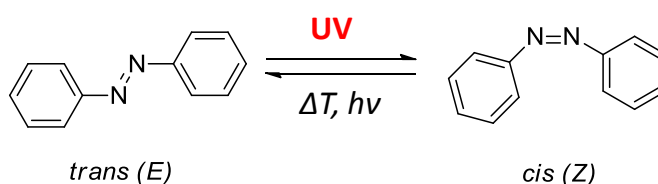


Figure 71: Azobenzene *trans* isomer can be converted into its *cis* form by irradiation with UV light. Back isomerisation to the *trans* form is accomplished thermally or by irradiation with a distinct wavelength of light.

When the *trans* form is irradiated with the appropriate wavelength (this is in the *trans* absorption band), it will isomerize to the *cis* form with high quantum yield. The reverse transformation can be achieved by further irradiation within the absorption band of the *cis* isomer (Figure 72). Thermodynamically, the *trans* isomer is usually more favored than the *cis* isomer, being approximately 50 kJ/mol more stable. Due to the energy barrier of the photo-excited state being around 200 kJ/mol, azobenzenes will predominantly exist as the *trans* isomer.

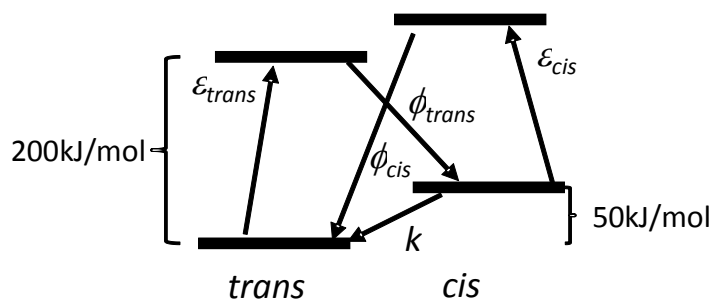


Figure 72: Simplified state model for azobenzene chromophores where ϵ denotes the extinction coefficients, ϕ denotes the photoisomerisation quantum yields and k represents the rate of thermal relaxation.¹⁵⁰

These isomerisation reactions are in the order of picoseconds. However, even without illumination, the *cis* isomers will slowly revert in solution back to the more stable

trans state, with a time-scale from seconds to hours, depending on the substitution pattern.

The isomerisation mechanism for azobenzenes is not yet clear and it has been subject to many investigations. The two possible pathways are inversion that takes place via a semilinear and hybridized transition state, and rotation that demands rupture of the π bond. Both hypotheses seem to be supported by experimental evidence, and it has been suggested that the path followed depends mainly on the compound. Despite not being understood yet, it seems that the inversion mechanism is generally more accepted and that some rotational motion, in early stages of isomerisation, is involved. The thermal back reaction is agreed to occur via rotation¹⁴⁷ (see Figure 73).

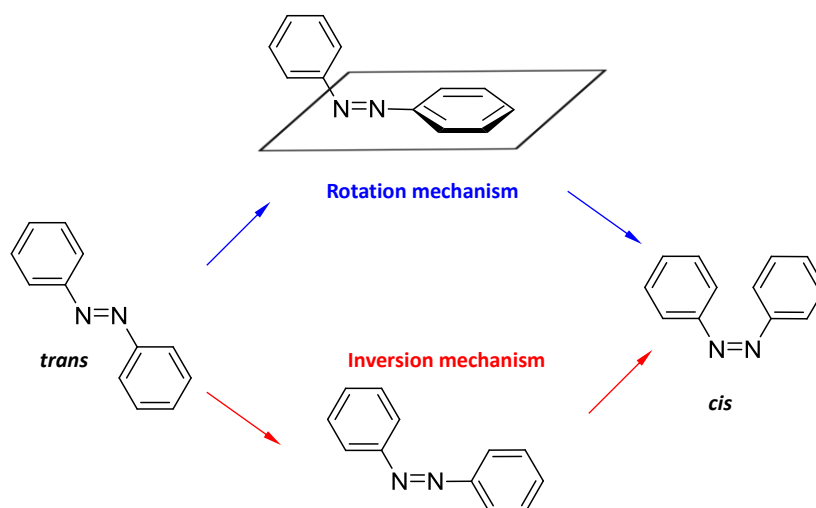


Figure 73: Representation of isomerisation mechanisms.¹⁴⁷

3.3 - Changes induced by photoisomerism of azobenzenes, from molecular level to macroscale

Isomerisation of azobenzenes and the associated molecular changes are very attractive for numerous applications in fields such as: photonic applications, photoalignment, displays and optical recording.

Several types of stimuli can be used to trigger actions in a material but light possesses a particular feature: it approaches materials in a “non-contact” manner and with great accuracy. Light can be modulated in terms of intensity, energy, polarisation coherency etc, therefore, assemblies of photochromic molecules will be sensitive to any changes of light properties mentioned above.¹⁵¹

The photochromic unit most commonly incorporated in molecular assemblies and organized polymeric systems is the azobenzene moiety.¹⁵² Its advantages are:

- The materials and their derivatives are usually synthesised easily
- They are highly sensitive to photoisomerisation
- Generally photofatigue is negligible
- The molecule has a rod-like shape and is symmetrical which makes their incorporation into molecular assemblies, especially liquid crystalline systems, favourable.¹⁵²

Azobenzenes have been incorporated into many different types of materials which can be hierarchically organized in terms of feature size as shown in Figure 74 and motion scales. However it is impossible to describe these phenomena in a compartmentalised way as suggested by the figure since motions on all scale sizes are related and are mutually affected. In the next section an attempt to describe how azobenzene isomerization, a motion at the molecular level, is related with higher size motions will be made. The discussion will follow on three levels of motion: 1) the chromophore; 2) domain and 3) macroscopic motions, a concept which has been introduced by Natansohn *et al*¹⁵³ and Stumpe *et al*.¹⁵⁴

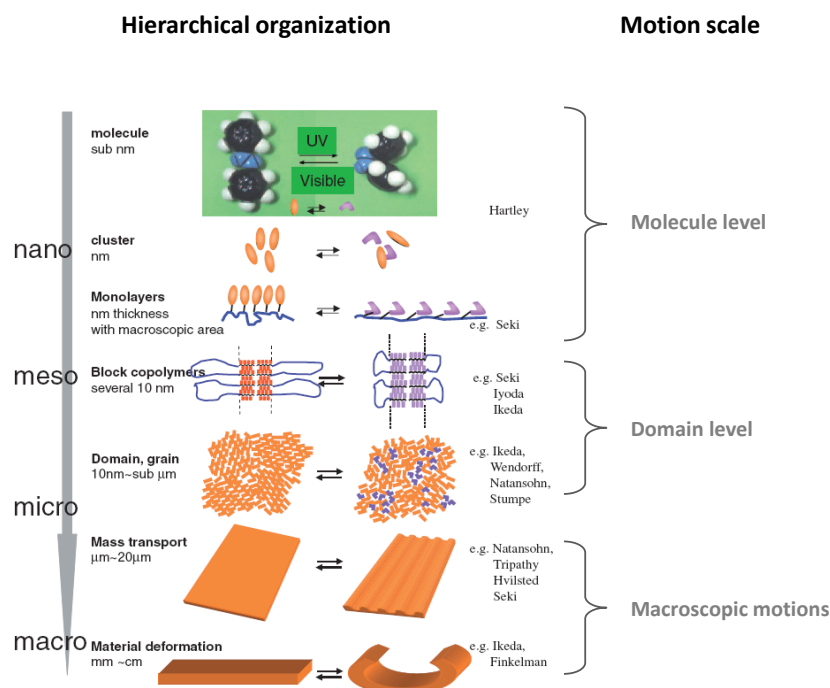


Figure 74: Scheme of hierarchical organization from molecule to materials of azobenzene containing materials and some representative research targets for each hierarchy.¹⁵⁵

Photoisomerisation of azobenzene induces a conformational change on the molecular level which manifests itself as a change in a material property on a macroscopic level.¹⁵³ Starting at the chromophore level, *trans-cis* isomerisation results in a change in shape that will be discussed in detail below (molecular motion) however it is important to mention that azobenzene in the *trans* form is a pro-mesogenic molecule, and when adequately substituted may show liquid-crystalline properties. This feature was discovered by Winogradow *et al.* in 1908 who recognized liquid-crystalline properties in 4-4' substituted azobenzenes with short alkyl chains.¹⁵⁶ To this day, studies of liquid crystalline properties of 4-4' substituted azobenzenes are still ongoing.^{157,158}

Monolayers at interfaces can be thought of as a bridge between molecules and materials. Although their thickness is approximately one molecular unit in size, their area can be extended to a macroscopic size. Hence a photoinduced change of molecular shape manifests itself macroscopically on the monolayer properties.

Relative to micrometer size materials, domains formed by molecular assemblies in LC materials can be mentioned. On a practical level, to be able to orientate and align molecules is extremely important.

In 1995, the discovery of the formation of relief structures by mass migration took research in azobenzene containing materials to the micro level. Finally on a macroscopic level, photo-driven materials can be found which are visible to the naked eye.¹⁵⁵

The subject of azobenzene polymers either in the main chain or side chain is vast, as are their applications and the subject has been extensively reviewed; Barret in 2006¹⁵², reviewed photo-switching materials containing azobenzene, Seki reviewed in 2004 and again in 2007 photoresponsive azobenzene containing polymers^{151, 155}, photoinduced motions were reviewed by Rochon in 2002¹⁵², Ichimura reviewed photoalignment¹⁵⁹ and Ikeda photoorientation for photonic applications.¹⁶⁰ These are only the most important examples, the literature is extensive and only the most relevant work for this thesis will be referred to in more detail.

3.3.1 - Molecular motion

At a molecular level, azobenzene isomerisation leads to large changes in the conformation and size of the molecule. The *trans* isomer has a more linear shape while the *cis* form possess a bent shape (Figure 71). The distance between the 4- and 4'-carbons decreases from 9.0 Å in the *trans* form to 5.5 Å in the *cis* form.¹⁶¹ Another characteristic that changes with photoisomerization is the dipole moment which changes from less than 0.5D in the *trans* form to 3.1D in the *cis* form.¹⁶²

When azobenzenes are irradiated with linearly polarised light of the correct wavelength, the molecules aligned along the polarisation direction will absorb and subsequently reorient. Specifically, *trans* azobenzenes with their long axis parallel to the direction of polarisation of the incident light are promoted to their excited states and then isomerise to the *cis* (*Z*) isomer. Upon relaxation back to the more stable *trans* isomer, the molecules take on a new random orientation. The ones that lie perpendicular to the polarisation direction cannot absorb and remain fixed in this orientation. The rest will reabsorb and undergo a repeat cycle of *trans-cis-trans* isomerisation which, after several cycles, will lead to a net population of azobenzene molecules aligned perpendicular to the direction of polarisation, resulting in a photoinduced alignment and conferring anisotropy on the material. This process is reversible and irradiation with circularly polarised light will restore the isotropic state (Figure 75). Additionally, further irradiation with light polarised in a different direction can initiate another photoreorientation of the molecules.^{150, 160} This process gives rise to strong birefringence (anisotropy in refractive index) and dichroism (anisotropy in absorption spectra).

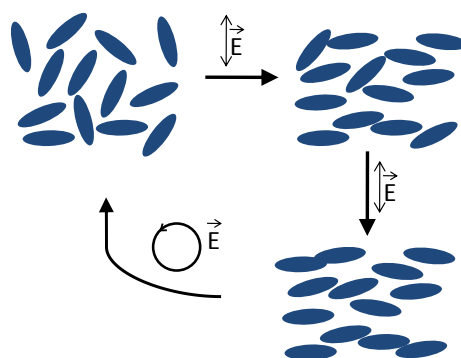


Figure 75: Schematic representation of statistical photoorientation. An isotropic distribution of chromophers aligns when irradiated with polarised light. Isotropic state is recovered by irradiation with circularly polarized light.¹⁵⁰

When considering the photoisomerism of solely one molecule, the process alone is not of great importance; however when looking at a group of molecules such as monolayers or domains, the process described above suddenly has a much bigger impact because the consequences are on larger scale making it more interesting in terms of possible applications. So the description of azobenzene behaviour, motions and materials is not trivial, and the practical demonstration of the above phenomenon falls in the second type of motion.

3.3.2 - Motions at Domain level

Liquid crystal copolymer systems containing both azobenzene and mesogen groups in the side chains have been studied with regard to photoalignment.^{163, 164} When irradiated, azobenzenes photoalign and this induces a concomitant alignment of the mesogens even if they are non photoactive. Above T_g this has been explained by cooperative motion and below T_g dipole-dipole interaction strongly affect this process.

It was mentioned previously that azobenzenes were pro-mesogenic molecules which together with the ability to isomerise; it means they can be used to disturb or induce order in LCs.

In LC systems, photoisomerization of azobenzene groups allows control of LC phases and furthermore the photoorientation can reorientate the liquid crystal director. A small amount of azobenzene can orientate an entire sample Figure 76 For instance; the addition of only 1% of azobenzene was shown to induce the nematic-isotropic transition under irradiation at temperatures below the “normal” transition temperature.¹⁶⁵ The isomerization to the *cis* form destroys the normal packing of mesogens, permitting a photo-activated phase change. This phenomenon has been shown to be applicable to polymeric systems as well.¹⁶⁶⁻¹⁶⁸

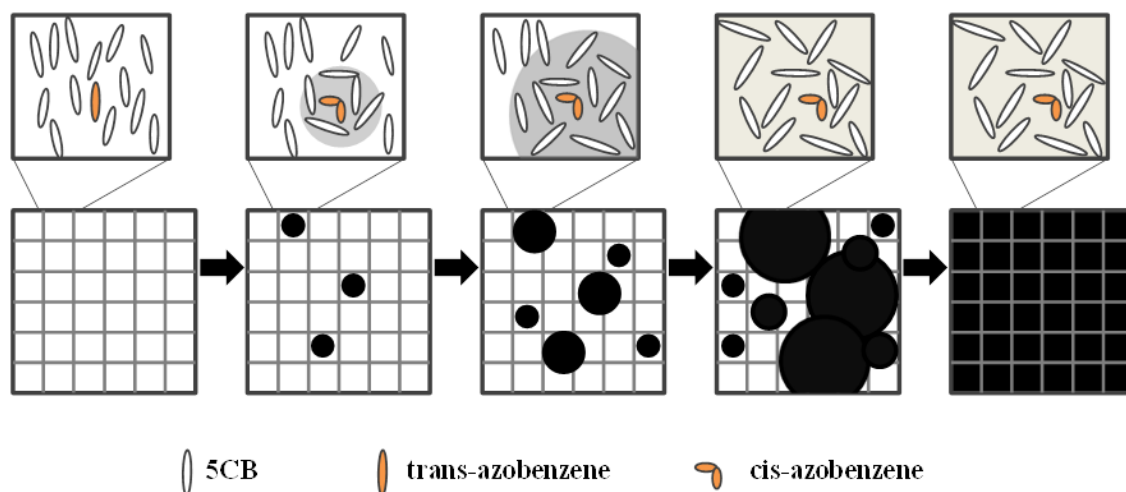


Figure 76: Representation of the effect of trans-cis isomerization in N-Iso transition in guest-host liquid crystals. The liquid crystal used is 4-cyano-4'-pentylbiphenyl (5CB).¹⁶⁰

If a photochromic molecule (azobenzene) is added to a LC, a guest/host mixture is obtained. The irradiation of this mixture with UV light instigates photochemical reactions which lead to a thermally isotropic phase transition. The result arises from the photoisomerism induced by the azobenzene group. As discussed above, in the *trans* state azobenzene is a rod-like shape that stabilizes LC phases. When irradiated, the shape changes to the bent form that will introduce some disorder in the LC phase inducing a decrease in temperature of the LC isotropic phase transition of the mixture.¹⁶⁰

Ikeda reported a reversible photochemical induced isothermal phase transition of a series of polyacrylates containing azo and ester containing mesogens. Under irradiation with 366 nm, a N-Iso phase transition was observed (*trans-cis* photoisomerization) whilst with subsequent irradiation at 525 nm, an Iso-N transition occurred (*cis-trans* photoisomerisation).¹⁶⁵

When an LC homopolymer (as well as copolymers) was irradiated with a pulsed laser and time-resolved analyses response to it were used, a fast response to the 10 ns laser pulse was obtained and the change was completed in about 200 ms. These results lead to a possible application in optical switching and image storage for this photoinduced phase transition.¹⁶⁹⁻¹⁷¹

An even lower response time (200 μ s) was obtained when the concentration of azobenzenes was increased to one per unit. Although the recovering of the nematic phase was problematic, it was improved with the introduction of donor-acceptor substituted azobenzenes. The stabilization of the LC phase due to the polar mesogen permitted the transition Iso-N in 300 μ s while the recovery (Iso-N) was accomplished in milliseconds at high temperatures.¹⁷²

One possible application for these materials using the photoinduced phase transition is formation of surface relief gratings¹⁷³⁻¹⁷⁶ which will be discussed in the section dedicated to macroscopic size motions and discussed in more detail in Chapter 4.

The pitch of cholesteric liquid crystalline systems can be changed by incorporation of photochromic units such as azobenzenes whether these units are part of the helical structure or mixed into the LC systems. When photochromic units isomerise, the pitch changes are accompanied by a color variation. The induction of chiral domains in optically inactive LC or pre-oriented amorphous polymers is accomplished by irradiation with circular polarized light. This effect arises from the interaction of CPL (circularly polarized light) with the material. After interacting with the first layer CPL becomes EPL (elliptically polarized light) which will orient photoactive units that are deeper in the sample and the ellipticity of light is changed resulting in domains becoming chirally distributed.

Molecular or polymeric thin films, with a surface modified with photochromic groups such as azobenzenes can be used to photoalign liquid crystals, and this alignment can be reversed by changing radiation. These surfaces are usually called command surfaces since each photochromic unit can align around 10^4 LC molecules and they were first described by Ichimura *et al.*¹⁷⁷ using a cell in which the surface was treated with a monolayer of azobenzenes and homeotropic alignment of nematic LC was favored. When the cell was irradiated, *trans-cis* isomerisation occurred and the liquid crystal adopted a planar alignment in a reversible way.

In liquid crystalline systems, when azobenzenes isomerise and align perpendicular to light polarization, they will force non photochromic molecules to align in the same direction, this is called cooperative motion and it is a consequence of the restriction imposed by isomerisation of azobenzenes when irradiated. Because they change shape and liquid crystals have a thermodynamic tendency to align along a preferred director, adjacent mesogens will be forced to follow the direction induced by polarized light. The orientation forced upon the azobenzene due to irradiation with light is extended to the entire material and is said to be an amplification phenomenon. This phenomenon was observed above T_g and also below T_g in amorphous samples where dipole interactions are very important.

3.3.3 - Macroscopic motions

Monolayers of polymeric azobenzenes, as mentioned before, are very useful to bridge the molecular changes occurring during *trans*-*cis* isomerisation to macroscopic motions that occur in materials. Since they (molecular changes) can be directly related with changes in film properties such as area and surface pressure.

The first observation of a contraction in a main-chain azo monolayer was reported by Blair.^{178, 179} When the monolayer was irradiated with UV light, a decrease in stress in the air/water surface was observed. When left in the dark, the stress in the interface increased and this process could be repeated. The contraction phenomenon could be explained because the azobenzene molecules laid flat on the water surface and when isomerized, the *cis* form occupied a smaller area, resulting in a contraction of the materials.

Menzel and Seki¹⁸⁰ observed the reverse result in monolayers with azobenzene molecules as side-chains. In this case, the expansion of the monolayers, when irradiated with UV light and contraction when exposed to visible light was related with changes in the dipole moment. As already mentioned, the *cis* form has a higher dipole moment than the *trans* isomer and consequently more affinity to the water surface. The monolayer was therefore forced to expand when irradiated with UV light. In the system explored by Seki up to three fold expansion was observed and changes in the monolayer thickness in the order of 0.2-0.3 nm were observed.

Contraction of several polymer networks cross linked with azobenzenes were reported although these contractions were very small (aprox 5%). More interesting results were found for LCEs (liquid crystalline elastomers) where contractions of 20% were observed.

Liquid crystalline elastomers (LCEs) combine the anisotropic character of liquid crystalline phases with the elasticity of polymer networks. The application of external stimuli such as temperature, light or electric fields can modify mesogenic alignment causing LCE deformations.

The introduction of a photochromic compound like azobenzene molecules in such materials may amplify the “motion” existent in these molecules. Upon irradiation the photoisomerization of the azobenzene moiety causes a cooperative change in alignment of the mesogens, as mentioned previously. The advantage of this phenomenon is that only a small amount of energy is needed to change the alignment of all LC molecules.

In 2001, Finkelmann *et al.*¹⁸¹ reported a contraction in the order of 20% of an azobenzene containing LCE, after its exposure to UV light. The system used is in the Figure 77. The system used, together with small amounts of photochromic units as side chain, and non liquid crystal molecules in order to influence the glass temperature. Two linking agents were then used to form the network. An important aspect is that a subtle change in the nematic order due to photoisomerism, causes a significant uniaxial deformation of the LCs along the director axis when the LC molecules are strongly associated by covalent cross-linking to form a 3D polymer network.¹⁸¹

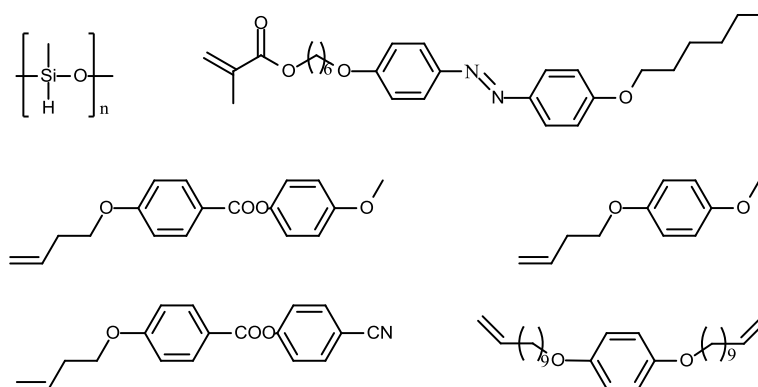


Figure 77: System studied by Finkelmann *et al.*¹⁸¹

Terentjev *et al.* studied the deformation behaviour of LCEs with a range of azobenzene derivatives when exposed to UV light.¹⁸²

In 2003, Li *et al.*¹⁸³ reported a fast contraction of about 18% size of a thin liquid-crystalline elastomeric film containing azobenzene molecules (Figure 78) when irradiated by UV light. These films were produced from nematic azobenzene side-on elastomers by photopolymerization which was induced in aligned nematic azobenzene monomers in a conventional liquid crystal cell. The contraction process was reversible by thermal back reaction, in the absence of light.¹⁸³

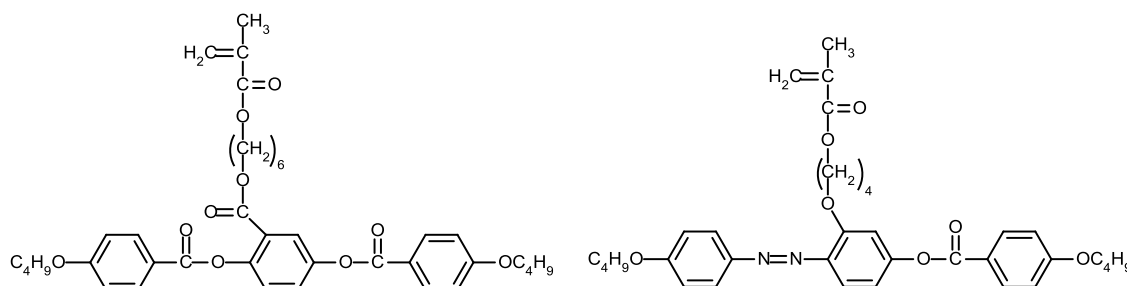


Figure 78: System used by Li *et al.*¹⁸³

An important step forward was achieved when 3D movements were attained. This effect was apparent in both, LC gels and LC elastomers containing azobenzenes.^{161, 184, 185}

Ikeda *et al.*^{161, 186} studied the bending of a monodomain LCE film. The film bending occurred along the rubbing direction and towards the UV light. Additionally, when irradiated with visible light, the bending was reversed and the initial flat film was obtained. This reversible process could be controlled by simply varying the irradiation wavelength. The fact that the observed bending was always along the rubbing direction, even when the film was rotated by 90°, clarified that this result was anisotropically induced.

The irradiation only induced photoisomerization of azobenzene molecules at the surface of the 20µm film. In the bulk, the photochromic molecules were not affected meaning that the volume contraction was only felt in the surface, forcing the film to bend in the direction of the incident light.^{161, 186}

Studies about the influence of the amount of crosslinking agent on the bending processes were also carried out by Ikeda *et al.*¹⁸⁴ By increasing cross-link concentration, the order of the film was also increased, consequently, when irradiated with UV light, the decrease in the alignment order of azobenzenes, gave rise to a larger contraction along the rubbing direction and towards the incident radiation.

The direction of bending could be controlled by selective absorption of linearly polarized light in polydomain LCE films. The film bent towards the irradiation source parallel to the polarization light.¹⁸⁶

A larger deformation was induced in an LCE sample doped with azobenzene, by a non uniform illumination by visible light, in a system studied by Palffy-Muhory.¹⁸⁷

Tabryan *et al.*¹⁸⁸ developed a strong LCE film that showed a fast response to laser beam illumination. The direction of bending or twisting of the film could be reversed by changing the direction of polarization of the laser beam.

In 2009 Jiang *et al.*¹⁸⁹ reported the synthesis of an LCE containing azobenzene moieties. Anisotropic networks were prepared through cross-linking polymerization of monoacrylate and diacrylate (Figure 79).

3.4 - Dendrimers containing azobenzene groups

Functional liquid-crystalline polymers have several applications. Main-chain polymers are being used as the active component in electroluminescent display devices, and as non-linear optical materials. Side-chain LCPs find commercial use as passive optical films with carefully tailored optical properties.

The advantage of such electro-active polymeric LC is that the functionality of small molecules is achieved without the existence of liquid phases in the cell. Side-chain materials keep their low viscosity due to the polymer backbone while having some liquid phase mobility due to the side-chain mesogens. Thus LCPs optical properties can be tailored to enhance the performance of a small molecule.

As discussed earlier, irradiation of an azobenzene group induces its photoisomerization to the surrounding matrix which leads to a change of its geometry, dimensions and dipolar moment. This molecular motion promotes large-scale motion and even macroscopic switches of material properties. A common research theme has involved the photoalignment of azobenzene containing materials and hence, the photochromic azobenzene moiety has been incorporated into a variety of systems in order to photoinduce new properties.

Systems studied include mixtures of azobenzene with small molecules, doped and covalently linked polymeric systems, supramolecular assemblies and liquid crystals.^{152, 153} Even in amorphous samples, below T_g , the process occurs and is facilitated by mesogen-like cooperative motion of azobenzenes.^{192, 193}

Synthesis of dendrimeric materials containing azobenzenes has attracted considerable interest as several possible applications were anticipated for these materials. The addition of photochromic units to a dendrimer, means that the small molecular changes that occur in azobenzenes during isomerisation can be enlarged to the three-dimensional architecture. The low viscosity of dendrimers suggests that a fast optical response and reorientation of the branched structure under the presence of external fields such as light can be achieved. As a consequence they can be applied as fast-acting photoresponsive materials as well as in holography,¹⁹⁴ and other applications to trap/release guest molecules or drug delivery materials by cleavage of the N=N bond.¹⁹⁵ Presently the area of photochromic dendrimers is very large and has been reviewed extensively.¹⁹⁶⁻¹⁹⁸

In order to synthesise dendrimers containing azobenzenes, these molecules have to be carefully designed. Whether they have one functionality, two different functionalities or the same functionality in different ends of the azo molecule, dictates if they are attached

to the periphery of the dendrimer, incorporated in the layers or used as the central core respectively. Generally, when positioned on the periphery, the generation of the dendrimer does not affect the *trans-cis* or the *cis-trans* isomerisation. For dendrimers with one azobenzene in the core a relation between generation number and *trans-cis* isomerisation has been observed. In the case of azobenzenes being part of the layers an increase in steric hindrance with the generation number has an effect on the isomerisation process. The detailed discussion of this effect is beyond the scope of this work and more can be found in the literature.¹⁹⁵ The first dendrimer reported using azobenzenes was by Vögtle and co-workers¹⁹⁹ and is shown in Figure 80.

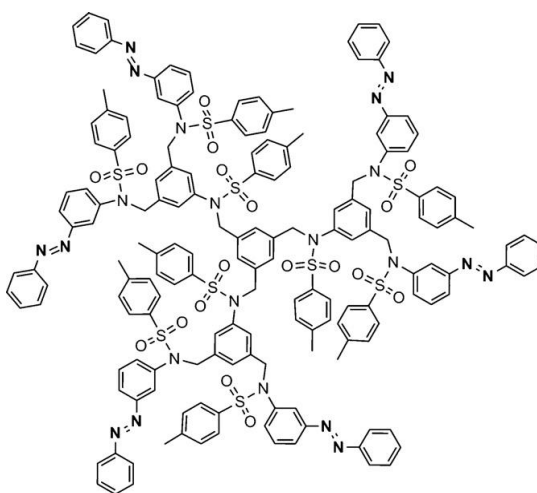


Figure 80: First photochromic dendrimer reported.¹⁹⁹

The possibility of using dendrimers with terminal azobenzene groups for holographic data recording was demonstrated by Balzani *et al.* in 1998.²⁰⁰

The synthesis of liquid crystalline photoactive dendrimer was reported for the first time by Shibaev *et al.*²⁰¹ in 2001. The LC carbosilane dendrimer of the first generation having cinnamoyl groups as photosensitive units showed a SmA mesophase from -28 to 58 °C. The photochromic mesogen used besides undergoing *E-Z* photoisomerization could also participate in [2+2] photocycloadditions.

In 2002 Shibaev¹⁹⁴ studied the photochemical and photooptical properties of a first generation LC dendrimer (Figure 81) which forms SmA phases over a wide temperature range.

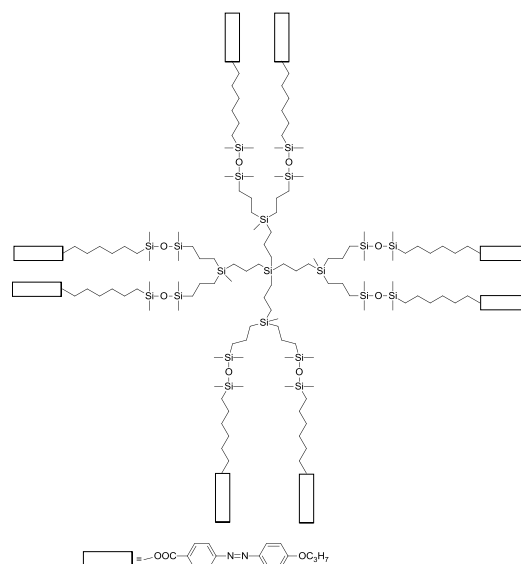


Figure 81: Structural formula of the dendrimer used by Shibaev.¹⁹⁴

The LC carbosilane dendrimer possessed terminal propoxyazobenzene mesogenic units which like all azobenzene groups can undergo E-Z photoisomerism. In this system, the azobenzene units have two distinct functions: due to their rod-like shape, it was expected that LC behaviour would be induced and due to its photochromic properties the materials would be sensitive to light. Studies on the photooptical behaviour of the photochromic LC dendrimer in solution and in an amorphous or LC film were carried out.¹⁹⁴

3.5 - POSS in azobenzene moieties

Despite star shaped dendrimers and dendrons being extensively studied, the literature related to silsesquioxanes is far less extensive.

The incorporation of POSS in azobenzenes LC polymers combines their individual features. On one hand the photoresponse behaviour from azobenzene groups is preserved and the introduction of POSS results in enhanced thermal, mechanical, dielectric properties of the polymer but also stabilizes LC phases.

Considering these factors, Xie *et al.*²⁰² synthesised a side-chain azobenzene copolymer containing pendant polyhedral oligomeric silsesquioxanes, Figure 82.

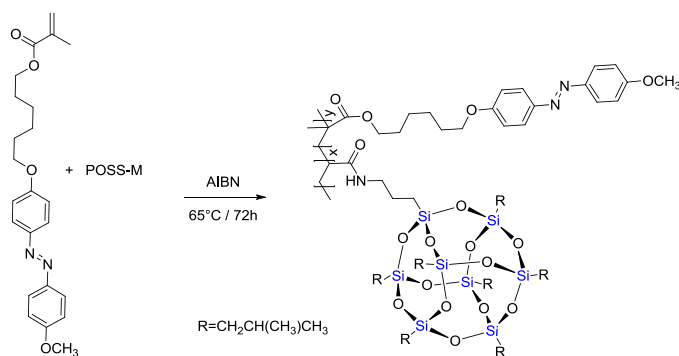


Figure 82: System studied by Xie *et al.*²⁰²

When compared to the homopolymer of an acrylate monomer, LCP-POSS exhibits higher glass-transition temperature and thermal stability. Transition temperatures showed by the LCP are raised on the LCP-POSS, and the nematic phase range is increased by 10 °C.

The development of laser technology resulted in a growing need for optical limiting materials for protection of optical sensors and human eyes, from laser damage.

Su *et al.*²⁰³ studied optical limiting properties of POSS-based functional hybrid nanocomposites with different architectures achieved by changing the feed ratio of the monomers and POSS molecules (Figure 83 and Table 7).

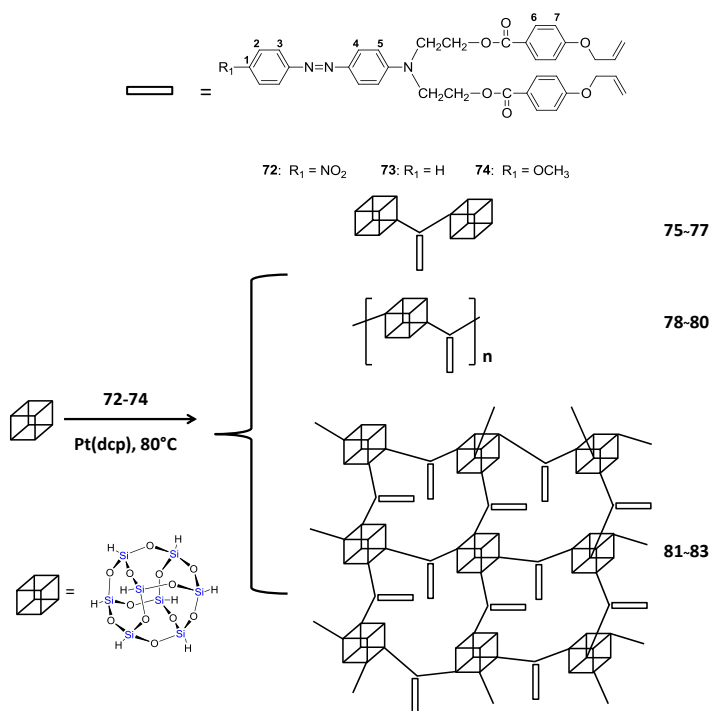


Figure 83: System studied by Su *et al.*²⁰³

When compared to the monomer, POSS derivatives showed an increase in the thermal decomposition temperatures (thermal decomposition with 5wt % loss) between 65 - 85 °C. This showed that incorporation of POSS into NLO chromophres increased their

thermal stability. The nitro-substituted hybrid showed the lowest thermal decomposition and, from all the different structural hybrids, the bead-type showed higher thermal stability. NLO properties and OL properties were retained with the incorporation of POSS and the solubility of the systems increased, improving their film-forming ability which is very often a limiting factor for the application of fast response materials in devices as limiters.

Table 7: Composition of the POSS derivatives studied by Su *et al.*²⁰³

Feed ratio Mesogen : POSS (1:2)	
Mesogen	POSS derivative
72	75
73	76
74	77
Feed ratio Mesogen : POSS (1:1)	
72	78
73	79
74	80
Feed ratio Mesogen : POSS (2:1)	
72	81
73	82
74	83

Continuing this line of work a new set of materials was prepared. This new series of hybrids also displayed good optical limiting properties, large non-linear optic response and high thermal stability, initiating a new route for designing new optical limiting materials with high thermal stability and good processability.²⁰³

In 2011 Bialecka-Florjanczyk *et al.*²⁰⁴ and co-workers studied a series of silsesquioxanes having two different mesogens attached, in which one of them was a photochromic azo molecule and the other was blind to light (it did not absorb or isomerize in the presence of light), see Figure 84. The silsesquioxane derivatives were synthesized via hydrosilylation using a Karstedt's catalyst.

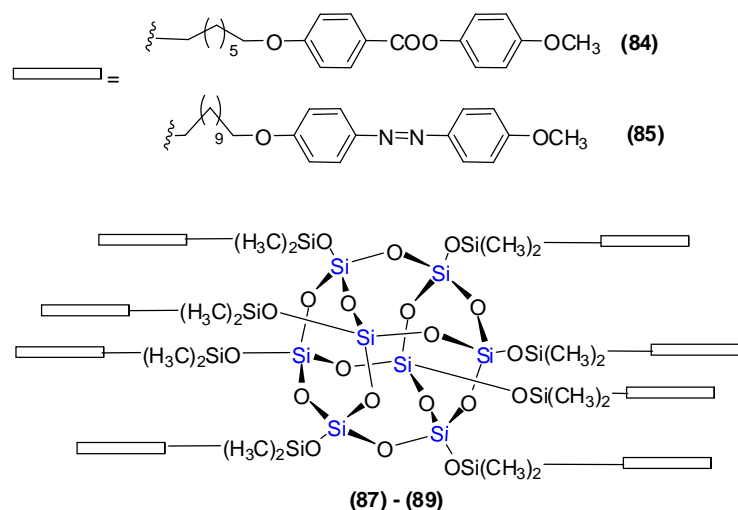


Figure 84: System studied by Bialecka-Florjanczyk *et al.*²⁰⁴

The liquid crystalline properties were studied by DSC and OPM and are summarized in the table below (Table 8). It was observed that all the silsesquioxane derivatives synthesized were liquid crystalline and only exhibited a nematic phase. As the content of co-mesogen **85** increased, the clearing temperature diminished from 112 °C (100% azobenzene) to 79 °C (12 % of azobenzene) in compound **89**. The thermal stability of the compounds was studied by thermogravimetric analysis and it showed that the decomposition temperature increased for materials with lower content of azobenzene mesogen, from 268 °C in **86** to 310 °C for **89**.

Table 8: Transition temperatures and ratio of compounds **84** to **85** in the systems studied by Bialecka-Florjanczyk *et al.*²⁰⁴

POSS derivatives	Transition Temperatures (°C)	Calculated ratio 84/85
86	Cr 93 N 112 Iso	0/100
87	Cr 72 N 102 Iso	12.5/87.5
88	Cr 51 N 84 Iso	50/50
89	Cr 44 N 79 Iso	87.5/12.5

The photochromic properties of the materials were investigated; UV-Vis spectra were recorded in solutions of CHCl₃. The spectra recorded show a maximum intensity at 355 nm attributed to $\pi-\pi^*$ electron transition for the *trans* isomer and a low intensity band at 400 nm related with $n-\pi^*$ electron transition of the *cis* form. The samples were irradiated at $\lambda = 365$ nm for 20 min which resulted in an increase of the band at 440 nm and a decrease of the band at 355 nm, corresponding to the *cis* rich state. The back

isomerization process was slower and the initial state was reformed after the samples being kept in the dark for periods varying between 36 – 48 h.

CHAPTER 4: PHOTOORIENTATION OF AZOBENZENE CONTAINING MATERIALS

4.1 – Photoorientation: general concepts

In a sample containing azobenzene molecules, irradiation with linearly polarized light will induce *trans-cis* isomerisation of the molecules with their transition dipole axis (long axis of the azo molecule) parallel to the polarisation of incident light. After back isomerisation to the *cis* form, some molecules will orient perpendicularly to this direction so they will no longer absorb and hence, isomerise, while molecules with any other orientation will continue this process. A preferential orientation of the azo groups perpendicular to light polarisation will be eventually achieved and this process is known as the “Weigert effect”.²⁰⁵ A consequence of the induced photoorientation is the generation of optical anisotropy and hence dichroism and birefringence arising from a difference in absorption and refractive indices in the directions parallel and perpendicular to the light polarization.²⁰⁶

This photoorientation process occurs also in amorphous polymers in the glassy state, where the cooperative motion between the azo mesogen-like molecules makes this process especially effective below T_g .¹⁶³

When irradiation is interrupted the molecules will isomerise back and the initial state will be recovered. However, if materials exhibit a glassy state, the photo induced orientation will be retained, and the initial state will only be re-established if the materials are irradiated with circularly polarized light or heated above the glass transition temperature. As a result induced optical anisotropy is reversible.²⁰⁷

Some of the applications arising from the photoorientation process were already described in the previous chapter including the use as alignment layers, command surfaces, being the origin of the macroscopic motions such as expansion and contraction as well as bending in polymeric and elastomeric films. Additionally, interesting applications are suggested based on the induced birefringence including: formation of wave-plates²⁰⁸ and polarization filters,²⁰⁹ channel waveguides,^{210, 211} all optical-switches,²¹² optical data storage and holography.²¹³ The latter is a method of recording information based on optical changes in a material, such as birefringence, that are induced by irradiation of an interference pattern and will be described in detail later in

this chapter. Optically induced anisotropy in azobenzene containing materials will be discussed followed by a brief discussion focused on holography and surface relief gratings.

4.2 – Optically induced anisotropy in azobenzene containing materials.

Photoorientation of azobenzenes occurs in solutions, LCs and glassy polymers yet the stability of the induced anisotropy depends on the dynamics of the matrix.¹⁵⁴

Todorov and co-workers^{191, 214} reported induced optical dichroism derived from an anisotropic realignment of azobenzene molecules when irradiated with linearly polarised light. Their system contained methyl red and methyl orange (azo dyes) dispersed in a poly(vinyl alcohol) matrix as shown in Figure 85.

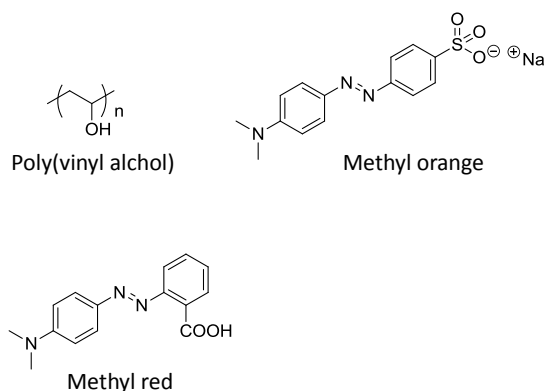


Figure 85: System studied by Todorov *et al.*²¹⁴

Irradiation of the polymer matrix with a linearly polarized laser beam (488 nm) caused the optical transmittance of light polarized parallel to the polarization direction of the laser to increase. Transmittance of light polarised perpendicular to this direction was decreased and hence dichroism was induced in the system. The drawback of this guest-host system was that the stability of the induced anisotropy would decrease after a short period of time, even when the sample was kept in the dark. Despite the induced anisotropy not being stable it proved in principle the potential for azo containing polymers to be used as an optical recording medium.^{191, 214}

Natansohn and others²¹⁵⁻²¹⁹ developed an amorphous azobenzene polymer where the stability of the birefringence induced at room temperature below T_g was accomplished by covalently bonding the azobenzene molecules to the polymer. The induced alignment

could be erased thermally and photochemically, and re-induced by irradiation with linearly polarized light.

Tredgold *et al.*²²⁰ studied induced birefringence in copolymeric systems of styrene and maleic acid functionalized with azobenzene molecules. Depending on the content of azobenzene in the polymers, they were either amorphous (when the amount of azobenzene was 30% and 50%) or crystalline (for systems with 90% azo units) and the authors observed that the birefringence value was higher in the ordered systems. They were also the first to note an amplification phenomenon, an increase in the value of birefringence after heating the samples following irradiation.²²⁰

A visual representation of the orientation process was introduced by Anderle *et al.*^{221, 222} and an example of it is shown in Figure 86. In the graphic absorbance is plotted as a function of the angle between the light plane of polarization and the director of the nematic sample.²²¹

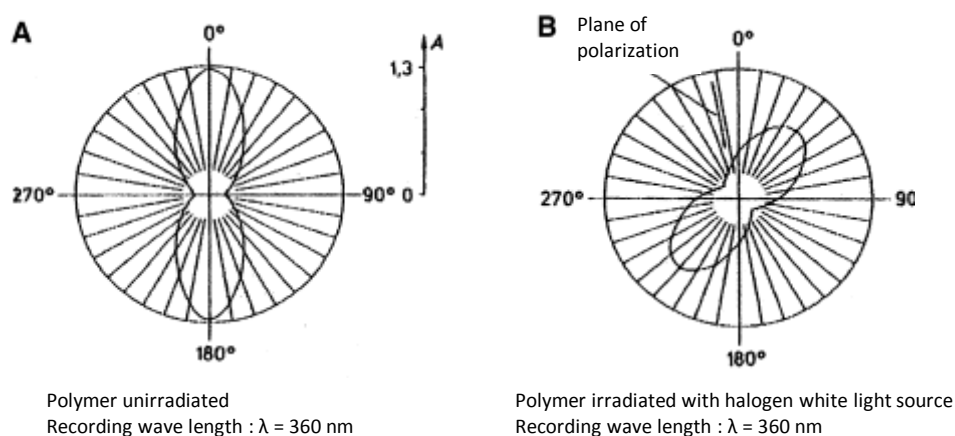


Figure 86: Example of the polar graphics introduced by Anderle *et al.*²²¹

The concept of molecular addressing was introduced by Anderle *et al.*²²² to explain the interaction between azo groups and non photochromic groups in LC copolymers, both above or above and below the glass transition temperature^{161, 223}. In contrast to the observations made by other authors,^{161, 223} they suggested that only azobenzene groups were addressed below the T_g. More recent explanations for the results obtained involve the concept of cooperative motion in studies published concerning amorphous polymers and liquid crystalline materials above the T_g.²¹⁵ This means that isomerisation of azobenzenes imposes an alignment of non-photochromic groups as discussed in Chapter III. Recently it has been shown that the cooperative motion is affected by dipole-dipole interactions and that these are, in fact, vital in the reorientation process.^{215, 224}

Several aspects regarding the induced photoorientation of azobenzene containing materials have been widely studied, such as the amount and nature of the azo

chromophore,¹⁶⁴ morphology of the sample before irradiation,²²⁵ intensity of incident actinic light,²²⁶ spacer length of the side chains in liquid crystalline polymers and others.²²⁷⁻²³⁰ Changing these parameters can improve the photo-induced alignment behaviour.

While the photo-induced anisotropy by irradiation with linearly polarized light in guest-host systems was not stable, in amorphous polymers, where the azobenzene molecules were covalently attached, the induced birefringence was stable in the glassy state and could be erased as mentioned above.^{231, 232} Due to the amorphous character of the materials, the value of the induced birefringence was fairly small and did not meet the necessary requirements for photonic applications.²³³

The addition of a co-mesogen showed an improvement of birefringence values due to the cooperative motion.²³⁴

The situation encountered in azobenzene containing LCP is different since it is possible to manipulate the alignment of liquid crystalline moieties to achieve higher birefringence values. Wendorff *et al.* reported on photoinduced dichroism in liquid crystalline polymers containing azobenzene groups in 1987, where the mesogenic groups were also time photochromic.^{235, 236} Birefringence values of about 0.7 were obtained for the azotolane polymer shown in Figure 87.²³⁷⁻²⁴⁰

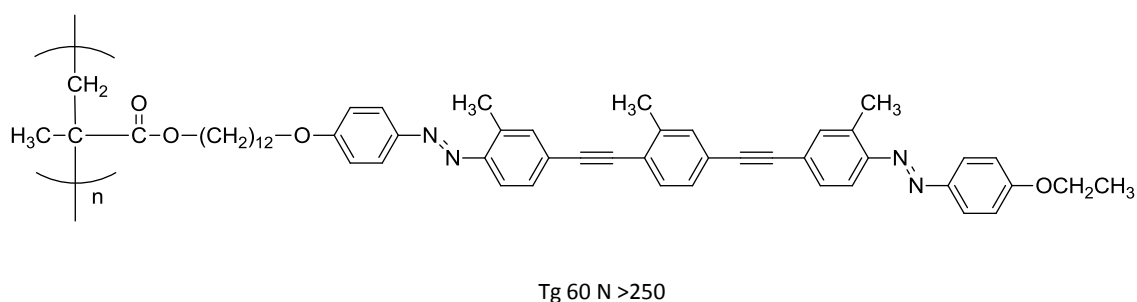


Figure 87: Azotolane polymers studied by Okano *et al.*²³⁷

Cooperative motion below the glass transition temperature was also observed in systems studied by Stumpe *et al.*¹⁶⁴, but most surprisingly, amplification of the birefringence as a consequence of annealing the liquid crystalline polymer was observed and was superior to the results obtained for the amorphous equivalent.

The thermal treatment of liquid crystalline polymeric films with pendant azo molecules enhanced the order parameter even though exposures times were shorter than those necessary to obtain maximum values of optical anisotropy were used.^{164, 211} This property is attributed to a seeding effect where the aggregation of liquid crystalline groups allows the formation of liquid crystalline domains.²⁴² It should be noted that

these systems are usually prepared by a spin coating technique, where the fast removal of the solvent is part of the process. Consequently, the prepared films have a random orientation of molecules and are amorphous. When irradiated below T_g with polarized light, birefringence is induced, suggesting photoorientation of nonphotochromic groups instigated by the photo alignment of the azobenzene molecules. For materials with a low content of azo groups (around 10 %), photo induced anisotropy was observed^{223, 243} and amplification of optical anisotropy verified.^{242, 244-247}

For liquid crystalline polymeric systems, induced birefringence was observed in films with homeotropic alignment, and a homogeneous orientation occurred even below T_g .²⁴³ Temperature effects in the photoinduced birefringence were not very noticeable below the T_g , in contrast to what has been shown above T_g , where increasing temperature can increase the value of the induced birefringence by as much as one order of magnitude, though near the clearing temperature the photoinduced birefringence disappeared.¹⁶⁴

The possibility of photoorientation of azobenzene containing materials and consequently the inducement of optical anisotropy is very important, as it shows that these materials can be used for holographic data storage. Despite being outside the scope of this thesis, this subject will be briefly discussed as the holographic recording method is used in the formation of surface relief gratings, a phenomenon associated with holographic recording of azobenzene containing materials.

4.3. - Holographic data storage (HDS): history and general concepts.

For a material to be suitable for HDS an optical property has to change when interacting with an interference pattern, for instance the birefringence. Since the photoorientation of azobenzenes is a reversible process, these materials are suitable for rewritable holography.

The use of azobenzene materials as HDS is based on photo-induced orientation of the chromophores, which is usually achieved by several cycles of *trans-cis-trans* isomerisations. This is a time consuming process and the problem is overcome by overlapping, as much as possible, the absorption bands for the *trans* and *cis* form, making the photoorientation process quicker.²⁴⁸

Holography was first discovered by Dennis Gabor in 1948 when investigating electron microscopes.²⁵¹ The term holography comes from the greek “holos” that means whole and “gramma” meaning message, implying the whole message alluding to the possibility of capture the entire information of an image. Gabor received the Nobel Prize in 1971 for “invention and development of the holographic method”. In a hologram, both phase and amplitude of the light reflected from an object are retained. This means that not only the intensity but also the phase length of the light deriving from all the points of the object are perceived. Since the phase measures the distance between all the points to the viewer, a three dimensional image can be captured. This information is recorded as the interference pattern between the waves emitted from the object and the coherent beam waves (the reference beam). The recording of the interference field occurs preferentially as modulation of the refractive index in the medium.

Volume holograms, where the data is stored throughout the volume of the material, may be used for holographic data storage; but this is only possible when the material responds to the interference pattern that is being recorded by changing some properties. In photoanisotropic materials the variations in phase and amplitude of light waves are recorded in the material by periodic variations of the optical properties of the materials. A change in the absorption coefficient gives an amplitude hologram, whereas a change in the refractive index gives a phase hologram.¹⁶⁰

Since azobenzene containing liquid crystalline materials are sensitive to intensity, polarization, phase interference etc of the incident light, holograms can be recorded in these materials by photoinducing an orientation change in LC materials in a periodic pattern, obtained as described above from interference of two coherent beams.

Currently there is a high demand for storing great amounts of information with fast rates of recording and reading of the data. Optical data storage emerged in early 1980s with the commercialization of CDs wherein reading and recording of the digital data is made in a non contact manner, and durability of the data prolonged.²⁵⁰ New optical data storage methods that use the full volume of the recording media are pursued as the upper limit of planar recording and have already been achieved with the Blue-ray disc format. Three-dimensional based storage methods such as optical holography are being developed.²⁵¹

Materials suitable for optical data storage must possess high optical sensitivity, high storage densities, short switching and access time, reversibility and high signal-to-noise-ratio after many write-erase cycles. Materials studied for HDS include photorefractive

polymers, photoaddressable polymers; polymer dispersed liquid crystals and photopolymers.

The work on optically induced orientation in doped systems by Todorov *et al.*,^{191, 214} was extremely important, despite the low stability of the induced anisotropy, since it suggested the possibility of using azobenzene containing materials as optical recording media.²⁵² Wendorff and co-workers, reported in 1987 the first use of a liquid crystalline polymer with azobenzene groups as side-chains for optical data storage.²³⁵ Liquid crystals were at the time being investigated for optical data storage using a thermorecording processes. Wendorff's group proposed a different approach in which the materials were pre-aligned by an electric field to form monodomains and after irradiating using linearly polarized green light (514 nm, 100 mW/cm²), stable gratings with diffraction efficiencies of 4% were obtained. Despite the inscription being related with *trans-cis* isomerisations the gratings were stable without illumination suggesting that the photochromic molecules were not sensitive to the thermal back reaction of the azobenzene.^{235, 236} This phenomenon was explained by a photoselection process as found in LC systems, isomerisation of the azobenzene forcing an orientation upon the mesogenic groups (as discussed in previous chapter) and consequently the recovery of the *trans* isomer was held up by the orientation of the liquid crystalline molecules. By heating above isotropization temperature, the gratings were erased.¹⁵³ It is important to mention that these were the first reversible holographic gratings inscribed in liquid crystalline polymeric materials.^{235, 236}

4.4- Surface relief gratings

Surface mass transport can be described as a micron scale photophysical motion on the surface of a film that appears as a consequence of exposure to spatially modulated light. The topological surface modifications or surface relief gratings (SRG) observed are a consequence of surface mass migration and reproduce the sinusoidal interference pattern of incident light (see Figure 88).

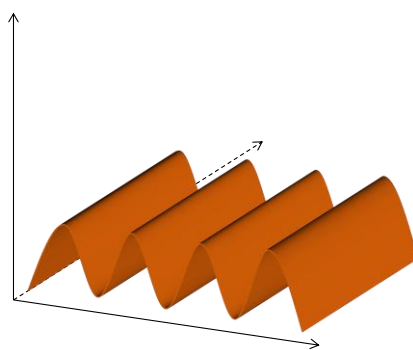


Figure 88: Representation of a Surface relief grating in azobenzene containing materials.

The grating depth (therefore the diffraction efficiency) depends on the polarization of the incident beam²⁵³ and can be as high as $1\mu\text{m}$. This change in the material from nano to micro length scales occurs at temperatures below T_g . The process requires the presence of azobenzene moieties and the occurrence of *trans-cis* isomerisation.²⁵⁴ The phenomenon is reversible, and a flat surface and original thickness can be recovered by irradiating the sample with circularly polarized light or heating it above the glass transition temperature.

Contrary to photoorientation, SRGs are only induced below the glass transition temperature and are thermally reversible. Although the driving force of this feature is not yet understood, it involves a mass migration in the direction of the modulation of the electric field vector.

It seems that *trans-cis* isomerisation is essential for the inscription of SRGs, and that the surrounding environment is important in determining the stability of the recorded gratings.¹⁵⁴

Usually experiments for SRG inscriptions are performed in spin-cast films between 10 to 1000 nm but they can also be carried out in films produced by a doctor blade, layer-by-layer (LbL) technique and in Langmuir-Blodgett films.¹⁵⁴ Typical experiments for recording SRGs use the same set up as the one used to holographic recording. The experimental set up involves an Ar^+ laser beam and the typical recording wavelength is 488 or 515 nm. The laser is spatially filtered before being collimated and split by a beam splitter (BS), producing two beams of equal intensity that are reflected from the mirrors and finally recombined in the recording medium, forming an interference pattern. The angle between the interference beams can be adjusted to form gratings with a desired periodicity.^{154, 206, 254} The formation of SRGs is followed in real time and the diffraction efficiency measured by monitoring the diffraction of a He-Ne laser (1 mW, 633nm) from the spot in the material where the two beams interfere. Changes in the

grating spacing and the intensity profile spacing are achieved by varying the incidence angle of the writing beam.²¹³

Surface relief grating applications envisage diffractive optical elements,²⁵⁵ wave guide coupler,^{256, 257} lasing²⁵⁸ and optical storage.¹⁵⁴

4.4.1- Surface relief gratings inscription in azobenzene containing materials.

In 1995, for the first time, Natansohn *et al.*²⁵⁹ and Tripathy and co-workers²⁶⁰ reported at the same time and independently, the inscription of surface relief gratings (SRGs) in azo containing polymeric films as well as the inscription of volume gratings.

4.4.1.1- Guest-host systems

Azo doped systems are in principle good materials for the recording of SRGs, as they are easy to prepare and chromophore concentration is easily controlled. After mixing azobenzene molecules into the polymeric matrix, the solvent is evaporated in a vacuum oven, and the film prepared over a glass substrate by casting or spin coating.²⁰⁶ Despite the advantages of guest-host systems, there are restrictions on the solubility of azobenzene units, phase separation and molecular aggregation induced by π - π stacking of the aromatic groups.¹⁵⁴

Surprisingly, the recorded SRGs have very weak diffraction efficiencies, even though isomerisation of azobenzenes occurs freely (since they are not hindered by polymeric chains). It seems that the molecular motion is not transferred to the matrix, and therefore migration of polymer chains does not occur.²⁰⁶ Azo doped systems include the work reported by Todorov discussed previously.^{191, 214} In attempts to increase birefringence, addition of liquid crystalline molecules was carried out. Efforts to pursue these doped systems involved the fabrication of low molecular weight glasses where stable amorphous or homogeneous films with no light scattering were accomplished.^{261, 262} Increased diffraction efficiency gratings in systems with nematic LCs were achieved by annealing the films after recording of SRGs. One of the most important results from investigations in guest-host systems was that it seemed to be essential that azobenzenes were covalently bound to the polymeric systems for SRGs formation to be possible.

4.4.1.2 - Azobenzene functionalized systems

Though low molecular weight azo materials are superior in terms of their mobility, this becomes a problem because it brings difficulties in recording holographic gratings with high resolution and it affects their stability. In contrast to observations made in azobenzene functionalized polymers.

In 1995 Nathanshon *et al.*²⁵⁹ and Tripathy *et al.*²⁶⁰ reported as mentioned previously, at the same time and independently the inscription of surface relief gratings in amorphous azo functionalized polymeric films. These gratings appeared when a sample was irradiated (in a typical holographic inscription setup) for longer than the time necessary to induce photoorientation. This modification of the film surface was associated with a motion of the material at room temperature well below T_g . The gratings could be erased with a polarised beam.

Experimental work developed over the years showed the following conclusions:

Inscription of SRGs is only possible in azo containing systems. Studies compared the inscription of SRGs between systems containing azobenzenes, stilbene and imine groups (see Figure 89). The inscription of SRGs was only successful for azo containing polymers while the gratings produced in stilbene as well as imines polymers were not evident, despite the fact that they can also undergo *trans-cis* isomerisation. The advanced explanation for these observations was related with the free volume required by stilbene and imine (aprox 224 Å) for the photoisomerization when compared to the smaller volume required by azobenzenes (127 Å).²⁶³

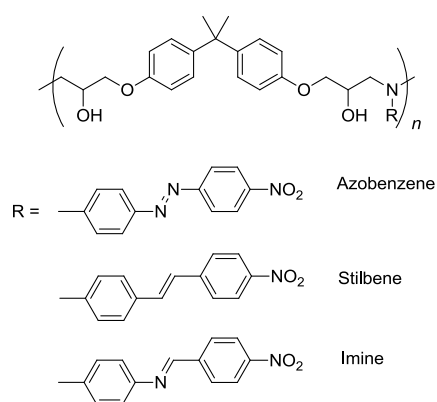


Figure 89: Systems studied by Victor *et al.*²⁶³

Not only a *trans-cis* isomerisation of azobenzenes is required but also *trans-cis-trans* cycles need to occur as shown in systems where the absorption for both forms does not overlap and are in the blue and red region of the spectra. In this case recording of

gratings only occurs if both irradiations corresponding to both wavelengths takes place.^{264, 265}

When azo groups are not covalently attached to polymeric chains (this is in guest-host systems) the surface relief structures produced are very small. It seems that in these systems polymer chain migration is hindered reducing the occurrence of mass migration.²⁰⁴

It appears that SRGs inscription is strongly dependent on polarization and intensity of the recording beams.²⁶⁸ By varying the polarization of the recording beams, Azo containing polymers presented SRGs with different diffraction efficiencies as well as modulation depths. Variation of light intensities and resultant electric field gradient in the direction of the grating vector²⁶⁸ seems to be fundamental for the appearance of surface relief gratings and are a consequence of alteration of the polarization recording conditions.²⁰⁶ Yet some SRGs were recorded in experiments in which the light intensity was uniform through the film surface.²⁶⁷

For the majority of azo containing polymers, the result is a phase relation between the incident light field and the resulting SRGs. The light intensity maxima will correspond to a valley in the surface relief pattern, while the light intensity minima correspond to the peaks, data suggests that mass moves away from light.²⁶⁸⁻²⁷⁰ However for liquid crystalline polymeric systems, it seems that this phase is inverted, the recording interference pattern minima will correspond to the valleys while the maxima corresponds to the surface relief peaks, that is, mass moves towards the light.

When high power ($> 300 \text{ mW/cm}^2$) is used in the recording experiments, amorphous azo containing polymers, showed an inversion of the phase relation or in-phase grating.²⁶⁶ These were found to be stable against erasure suggesting a destructive process, contrary to gratings inscribed with moderate intensities (minor 100 mW/cm^2) where a flat film with the original thickness is recovered after erasing (by heating to T_g or specific polarization conditions for both the writing and the erasing beam).²⁷¹

Grating efficiencies and thus the amplitude of SRGs, depend on the inscription angle, revealing a maximum when $\theta = 15^\circ$.

Grating height increases with the irradiation time until the saturation point is achieved, a non-linear relation between the recording intensity, which can be as low as 1 mW/cm^2 , and the SRGs height was also observed.²⁷²

It was reported that the efficiency of SRGs recording depends on the molecular weight of the materials, the optimal value being of approximately 10^3 g/mol . When the

molecular weight of the polymers is too large, it is possible that some entanglement between the polymeric chains occurs, working as a cross-linking, and preventing the migration of the polymer backbone. However some counter-examples in materials such as azo-cellulose of MW around 10^7 g/mol were also reported.^{273, 274}

When an azobenzene containing material is irradiated with two coherent beams, there are several phenomena occurring at the same time and as a consequence of *cis-trans-cis* isomerisation (see Figure 90), a chemical grating is created, since the material will have areas where it is *cis* rich and others where it will be *trans* rich. A photo induced orientation of the photochromic groups occurs and consequently a stable birefringence grating that contributes to the overall diffraction efficiency is recorded. If a spatial variation of the polarization or intensity is present, a stable and large surface relief grating (that can overpower the other gratings) is formed due to a mass migration process. A density grating is formed (under appropriate conditions) underneath and this also leads to a periodic change of the refractive index. When a material is heated, the SRGs are erased, and density gratings start to emerge, where the SRGs were previously formed. Analytical evaluations of the contributions into the diffraction efficiency have been carried out.

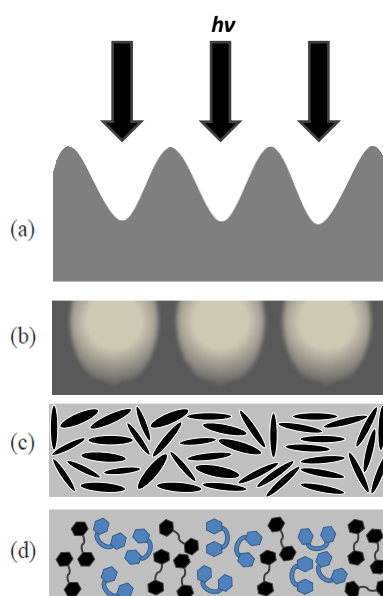


Figure 90: Different processes that occur during SRG inscription. a) SRGS gratings, b) density grating, c) photoorientation of the molecules irradiated and c) *trans-cis* isomerization.²⁷⁵

For example in some liquid crystalline materials the contribution of the birefringence gratings to the diffraction efficiency is larger than the contribution of the inscribed SRGs, however SRGs have been successfully recorded in LC materials and some of the most relevant work will be discussed in detail later.

Finally it is important to note that experimental evidence indicates that the mass migration phenomenon occurs on the surface and then expands to the bulk of the sample contrary to the birefringence gratings that are a bulk phenomenon. If the surface of a sample is restricted, the surface initiated movement will not occur and the formation of SRGs is almost inhibited and birefringence gratings will be the predominant phenomenon.²⁰⁶

Complex topological surfaces can be recorded by superimposition of SRG achieved by rotation of the material after recording followed by new SRG inscription (see Figure 91).^{206, 276} Kulikovska recorded 2D gratings consisting of up to 13 linear gratings.²⁷⁷



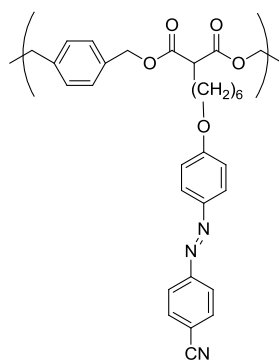
Figure 91: Multiple SRGs recorded by rotation of the azobenzene containing film.²⁷⁸

In addition to guest-host polymeric systems, side chain azo polymers, main chain azo polymers, polymers with π conjugated backbone, ionic complex materials and many others have been investigated and detailed description can be found in the literature.¹⁵⁶

The next paragraphs will focus on liquid crystalline materials.

It was discussed before that LC azobenzene containing materials are prone to large induced birefringence when irradiated with linearly polarized light, a consequence of the “Weigert effect”.²⁰⁵ If the material is subject to irradiation with two coherent beams (that result in an interference pattern) a large modulation of the refractive index can be achieved. This is particularly important since it is related with the diffraction efficiency, one of the most important parameters in holographic recording.¹⁶⁰

Eich *et al.*^{235, 236} reported the first optically induced birefringence in a LC azopolymer film represented in Figure 92. In this case the mesogens are also the photochromic units and the polymeric material showed SmA and N mesophases. Cells of 7-10 μm were filled with the polymer and they were subject to preorientation by an electric field to form a monodomain. This treatment was carried out above the glass transition temperature. After this, the sample was irradiated with linearly polarized light and the formation of very stable gratings with diffraction efficiencies of 4% were obtained. By heating the sample above the clearing point, the inscribed gratings were erased.



Tg 34 S_A 84 N 104 Iso

Figure 92: System studied by Eich *et al.* First liquid crystalline polymer where birefringence and dichroism were induced.²²⁷

Among liquid crystalline materials, polyester and polymetacrylates polymers were used very successfully for SRGs recording. The addition of LCs in polymeric materials for the inscription of SRGs can increase the change in birefringence. The alignment of these materials can produce a high modulation of birefringence that results in high diffraction efficiency in relief gratings. Diffraction efficiencies of around 40% were achieved in azobenzene containing LC polyesters.

Wendorf *et al.*²²⁹ studied the inscription of surface relief gratings in thin films (0.4- 2 μm) of low molecular liquid crystals (Iso 239 N 221 Sm 32 Tg) quenched into the amorphous state. They observed that besides the photoorientation in the LC phase there was a strong tendency for the formation of surface relief gratings as well as their enhancement during thermal annealing. This process occurred above the glass transition temperature and it is reported as a consequence of the tendency of the mesogens to self-organize as well as the suppression of the mesophase in the glassy state.

In 2003, Zettsu *et al.*²⁸⁰ studied the formation of photoinduced relief gratings in liquid crystalline azobenzene polymer films. The recording process was carried out after irradiation of the film with UV light creating a *cis*-rich sample. In the systems studied, the *trans-cis* and *cis-trans* isomerization bands overlapped. The pre exposure of the system to UV light proved fundamental to the recording of SRGs using low intensity exposure. It seems that the recording of surface reliefs was related to the phase transition (from isotropic state to mesophase) induced by *cis-trans* isomerization.¹⁷³ In this work different polarization states were used to induce SRGs. After irradiation at low intensities (5 mW/cm²) for 10 s the relief gratings recorded show a diffraction efficiency of 3% and a modulation depth of \approx 200 nm. However when orthogonally

polarized beams were used, no considerable diffraction exposure was observed even when light of higher intensity was used (100 mJ/cm^2). To understand this phenomenon better, an experiment using nonpolarized incoherent light ($\lambda = 436 \text{ nm}$) was carried out, with the use of a grid type photo mask. As a result SRGs were recorded and mass migration occurred from the bright areas to the dark regions within the plane. This set of experiments suggests that SRGs are induced by intensity modulations independently of the polarization used, contrary to observations on amorphous polymers. The authors suggest that due to the soft nature of the film, secondary effects resulting from dewetting of the polymeric films, isomerization of the azobenzenes and self organized motion of the LC polymer are responsible for the rapid formation of SRG. This process is stopped once the film becomes liquid crystalline.

In 2006 Morikawa *et al.*²⁸¹ reported the use of SRG inscription to promote alignment of a diblock copolymer formed by a photochromic azobenzene and a poly(ethylene oxide) chain in-plane and out-of-plane. Based on previous work,²⁸² the authors expected that the mass migration (due to inscription of SRGs) would modulate the orientation of the PEO cylinders. The addition of pentyl cyanobiphenyl (5CB) to the polymer allowed the inscription of SRG, explained by the fact that this softens the material and mass migration becomes possible. After pre-irradiation with UV light (365 nm), the films were subject to holographic irradiation and subsequent annealing and films with thickness between 30 and 70 nm were obtained. It was possible to see that when the thickness of the valleys and crests was higher or lower than 70 nm, alignment out of plane and in plane, respectively, was achieved and the latter is ruled by selecting the polarization of the beam used for the holographic recording procedure.

Yu *et al.*²⁸³ studied the enhancement of surface relief gratings in liquid crystalline copolymers shown in the figure below.

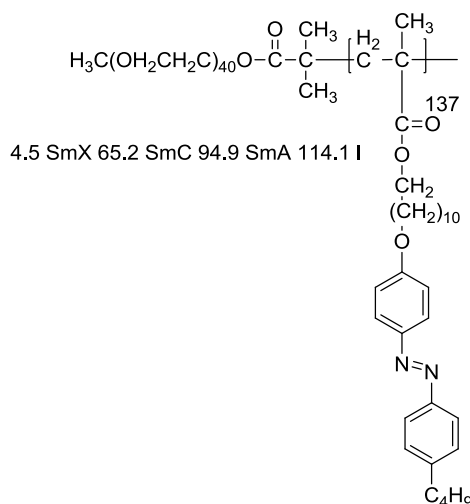


Figure 93: System studied by Yu *et al.*²³²

Prior to irradiation in holographic set up, the materials were irradiated with UV light to create a *cis*-rich material, and therefore an isotropic material, as in this state the molecular mobility is increased. The irradiation using a holography set up promotes *cis-trans* isomerization in the bright area of the interference pattern and as a result a phase transition from isotropic to nematic is achieved in these regions. By contrast this is not observed in the dark regions of the interference pattern, still *cis*-rich. As a result of this phase modulation, a refractive index grating is formed. A preferential alignment of the *trans* azobenzene isomer perpendicularly to the polarization of the writing beams is induced. After annealing, the refractive index gratings are still present, yet their amplitude decreased significantly as a consequence of the partial disorganization induced by this procedure. A nanoscale phase separation phenomenon induces a mass transfer and disturbs the LC alignment in the gratings. The SRGs formed showed a surface modulation almost one order of magnitude higher than the ones observed prior to the occurrence of the nanoscale phase separation, and an increase of the diffraction efficiency accompanied this process. The driving force for these results was attributed to the pressure gradient induced by the interference writing beams.

Recently photoorientation and SRG inscriptions in dendrimeric systems have been studied. When compared to polymers, dendrimers have lower viscosity that envisages fast response to optical modulation.

The liquid crystalline dendrimer studied is shown in Figure 93 and shows the following thermal behaviour: Tg -15 SmX 9 SmA 51 Iso. The SmX phase was described as a smectic phase with unknown structure. Photoorientation studies were undertaken in thin films of less than 1 μ m. When the samples were irradiated with an Ar⁺ laser (488nm)

linear dichroism was induced and maximum values of $D = 0.16$ were obtained. However this induced anisotropy disappeared after the irradiation process finished. Thermal annealing, which was seen to increase the dichroism values in PLCP, erased the induced optical anisotropy. When a film of the dendrimer in the SmA phase was irradiated with linearly polarized light at room temperature, no linear dichroism was reported, suggesting that the SmA phase hinders the photoorientation process of the azobenzene.^{256, 257}

Recently, Tomczyk *et al.*²⁸⁴ studied photoorientation in dendritic structures such as the ones shown in Figure 94 by means of induced dichroism and SRG inscription.

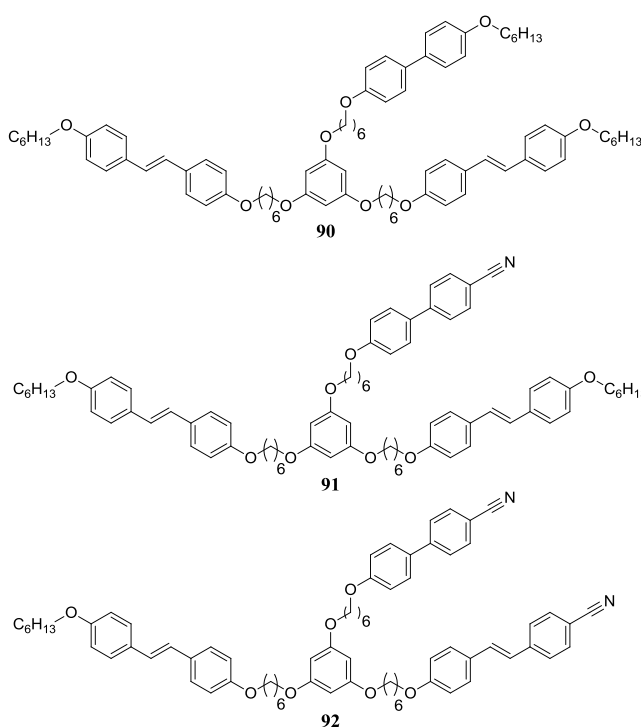


Figure 94: Systems studied by Tomczyk *et al.*²⁸⁴

Solutions of compounds **90**, **91** and **92** in chloroform were prepared and it was observed that scattering in solutions of **91** and **92** was decreased by irradiation with UV light, due to the inhibition of crystallization. Photoinduced anisotropy (irradiation with $\lambda = 633\text{nm}$) in spin-cast films was studied and photoinduced dichroism of compound **90** was observed with no prior UV exposure. In contrast, anisotropy in compound **91** was not induced while this procedure was successful for compound **92** (dichroism of 0.77 was measured) after UV exposure. The induced anisotropy was achieved due to the preferential orientation of the azobenzene molecules perpendicularly to the electric field of the incident light. The pre-treatment with UV light promotes a decrease in the

number of molecules parallel to the electric field vector and an increase of the number of molecules perpendicular to the field vector (as a consequence of the Weigert effect), contributing to high dichroic value found. After the photoinduced anisotropy (by different exposure times) the samples were annealed for periods ranging from 10 min to 24 h, in the mesophase. Samples **90** and **91** did not show an increase in dichroism and in fact for compound **90** this value decreased. A dewetting process occurred for **91** and **92** and for the latter one a clear difference between non-irradiated areas and irradiated areas was observed, suggesting that the irradiation process influences the self-organization of the molecules in the film.

Another experiment was performed where the absorption spectrum was recorded at different temperatures. For compounds **91** and **92** the dewetting process prevented the realization of these experiments. Compound **90** showed an increased absorption at 316 nm therefore the dichroism values for these experiments were measured using $\lambda = 410$ nm. For this wavelength, an increase in dichroic value from 0.05 to 0.43 was achieved after annealing at 75 °C, corresponding to maximum dichroic value. After these observations, the authors attempted to measure the photo induced anisotropy at 366 nm by preparing a thinner sample. In this case, no change was observed. The number of chromophores oriented parallel to the direction of the electric field vector increased, while no variation was observed in the perpendicular direction. Indicating that the orientation process at room temperature leads to out of plane orientation while at 75 °C the orientation is in-plane. An increase in dichroism from 0.13 to 0.3 was observed.

Gratings were recorded for compounds **91** and **92** and this process showed that the diffraction efficiency increased quickly at the beginning of the recording and diminished as the recording process continued. Gratings with diffraction efficiencies of 14% were obtained. The gratings are characterised by contributions from changes of the absorption coefficient, changes in the refractive index and variations on the thickness of the sample, these are amplitude gratings, phase gratings and surface relief gratings respectively. After annealing the sample the gratings were erased, indicating a low long term stability.

CHAPTER 5 - MOTIVATION AND AIMS

This work was driven by the current interest in photochromic liquid crystalline materials with a focus on optical applications, being part of a wider collaboration in a multidisciplinary and highly interactive European Marie-Curie Research Project.

The overall aim was to synthesise and characterize novel photoactive liquid crystalline organic/inorganic hybrids showing nematic phase behaviour and a glassy state at room temperature, having in view materials which are sophisticated in design, simple in structure and with the ability to achieve high photodichroic ratios.

In practical terms the aim was to design and synthesize a laterally connected azobenzene containing mesogen, characterize it chemically, investigate its photochromic as well as its liquid crystal properties and connect it to a silsesquioxane core resulting in a photochromic liquid crystalline organic-inorganic hybrid system.

The target was to optimize the liquid crystal properties of the materials in systematic iterative steps by introducing co-mesogens based on a cyanobiphenyl core, where the size of the core and the length of spacer connecting the mesogens and silsesquioxane core was varied systematically.

The optimization steps were to be achieved by gaining a clear understanding of the structure of the liquid phase behaviour of the materials, based on detailed optical polarizing microscopy, differential scanning calorimetry and extensive and detailed X-ray diffraction studies of magnetically and mechanically aligned samples over the whole liquid crystal temperature.

CHAPTER 6 - EXPERIMENTAL

All starting materials were purchased from Lancaster Synthesis, Acros Chemicals or Sigma Aldrich.

NMR spectra were obtained from a Jeol JNM-ECP 400 MHz FT-NMR spectrometer, with chemical shifts reported in ppm relative to a tetramethylsilane standard.

Analytical TLC was carried out using aluminium backed silica gel 60 F254 and visualised using UV light (254 / 365 nm). Column chromatography was performed using ICN silica 32-63, 60Å.

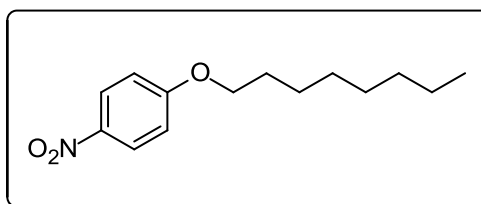
Phase transition temperatures were determined using a Perkin-Elmer DSC7 under nitrogen atmosphere against an indium standard. Transition temperatures quoted correspond to the onset of the endotherm except for glass transition temperatures, where the mid-point is quoted. Different heating and cooling rates were used as necessary.

The mesophases were studied using an Olympus BX51 equipped with a Mettler FP52 heating stage controller. The microscope was equipped with an Infinity light camera and the micrographs were collected using the Mettler Studio capture software.

XRD experiments were performed to study the phase structure of the liquid crystalline materials synthesised. The XRD equipment used consisted of a Mar345 diffractometer and a 2D image-plate detector (CuK α radiation, graphite monochromator, $\lambda = 1.54 \text{ \AA}$). The samples were heated in the presence of a magnetic field using a home-built capillary furnace. The data was analysed using "Datasqueeze" software and OriginPro 8.6 software package from OriginLab.

UV/Vis studies were made using an Agilent 8453 diode array spectrometer and a Varian Cary 50 spectrophotometer. Irradiation was carried out using a Thermo Oriel monochromator connected to an Oriel arc lamp supply.

6.1 - Synthesis of 1-nitro-4-(octyloxy)benzene (**93**)²⁸⁵

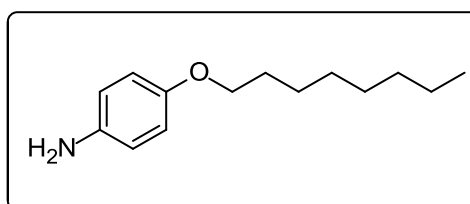


Potassium carbonate (10 g, 0.18 mol) was added to a solution of 4-nitrophenol (10.0 g, 0.07 mol) in Dimethylformamide (245 mL) at 80 °C. This mixture was left to stir for 2 h 40 min at 80 °C and 1-bromooctane (14.0 g, 0.072 mol) was added dropwise. After 17 h the reaction mixture was filtered and washed with dichloromethane. The filtrate was evaporated under reduced pressure and the product recrystallised from MeOH.

The product was obtained as a white solid, (13.17 g, 75 %)

¹H NMR (400 MHz, CDCl₃): δ 8.19 (d, 2H, ³J = 9.4 Hz); 6.94 (d, 2H, ³J=9.4 Hz); 4.05 (t, 2H, ³J=6.6 Hz); 1.78/1.86 (m, 2H); 1.41/1.51 (m, 2H); 1.24/1.40 (m, 8H); 0.89 (t, 3H, ³J = 7.2 Hz).

6.2 - Synthesis of 4-(octyloxy)aniline (**94**)²⁸⁶

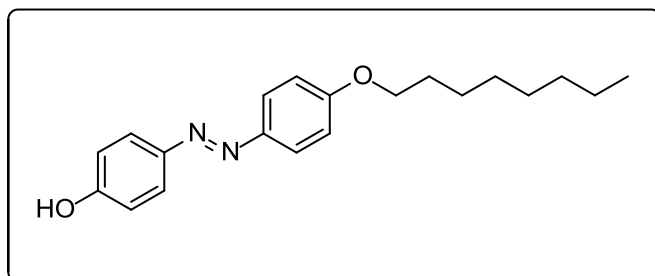


To a solution of **93** (2.5 g, 0.01 mol) in tetrahydrofuran (50 mL) was added Pd/C (0.1 g, 5 % wt/wt) and hydrogen bubbled through the stirred mixture. After 3h, the reaction was complete as shown by TLC (DCM). The reaction mixture was filtered through Celite and the solvent removed under reduced pressure. The title compound was isolated by column chromatography on silica gel (hexane/dichloromethane; gradient 0 % to 20 % hexane).

Compound **94** was obtained as an off white solid (1.81 g, 80 %).

$^1\text{H NMR}$ (400 MHz, CDCl_3): δ 6.74 (d, 2H, $^3J = 8.8$ Hz); 6.64 (d, 2H, $^3J=8.8$ Hz); 3.87 (t, 2H, $^3J= 6.6$ Hz); 1.69/1.78 (m, 2H); 1.38/1.47 (m, 2H); 1.24/1.37 (m, 8H); 0.88 (t, 3H, $^3J = 7.0$ Hz).

6.3 - Synthesis of 4-((4-(octyloxy)phenyl)diazenyl)phenol (**95**)²⁸⁷



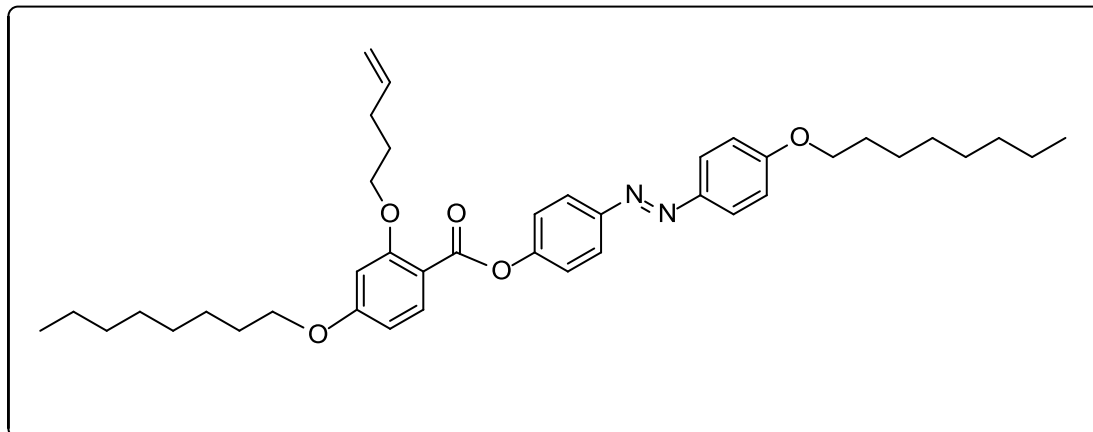
To a stirred solution of compound **94** (5.35 g, 24.2 mmol) in water (4.84 mL) and acetone, concentrated HCl (5.6 mL) was added slowly. Ice was added to the reaction mixture in order to maintain temperature under 5 °C and an ice salt bath was used. After 1 hour, a mixture of NaNO_2 (1.7 g, 24.2 mmol) and water (2.6 mL) was added to the reaction mixture. Finally phenol (2.54 g, 26.62 mmol) was added and the reaction was left to stir at room temperature until finished. The reaction was followed by TLC (dichloromethane).

The product was isolated by column chromatography on silica gel (Hexane/Dichloromethane; gradient 90 % to 100 % hexane).

Compound **95** was obtained (6.43 g, 81 %).

$^1\text{H NMR}$ (400 MHz, CDCl_3): δ 7.86 (d, 2H, $^3J = 9.0$ Hz); 7.83 (d, 2H, $^3J=9.0$ Hz); 6.99 (d, 2H, $^3J=9.0$ Hz); 6.93 (d, 2H, $^3J = 9.0$ Hz); 5.13 (br s, 1H); 4.03 (t, 2H, $^3J = 6.6$ Hz); 1.78/1.85 (m, 2H); 1.42/1.52 (m, 2H); 1.24/1.40 (m, 8H); 0.89 (t, 3H, $^3J = 7.2$ Hz).

6.4 - Synthesis of 4-((4-(octyloxy)phenyl)diazenyl)phenyl 4-(octyloxy)-2-(pent-4-enyloxy)benzoate (**96**)²⁸⁸



To a solution of 4-(octyloxy)-2-(pent-4-enyloxy)benzoyl chloride (1 g, 3 mmol) in anhydrous dichloromethane (3 mL) was added compound **95** (2.97 g, 9.1 mmol) and dimethylaminopyridine (0.31 g, 2.5 mmol). The mixture was stirred and the flask cooled to 0 °C in an ice bath. DCC (0.68 g, 3.3 mmol) was then added and the cooled solution stirred for another 10min. Finally the ice bath was removed and the mixture was left stirring at room temperature overnight. The mixture was filtered and washed with DCM. The filtrate was extracted with HCl (aq) (0.5 N, 25 mL) followed by a saturated solution of sodium bicarbonate (25 mL).

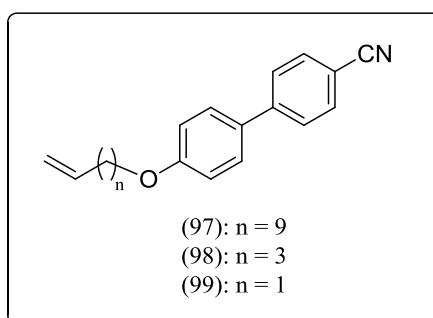
After removal of the solvent, compound **96** was purified by column chromatography (dichloromethane).

Compound obtained in yield 78 % (4.54 g)

¹H NMR (400 MHz, CDCl₃): δ 8.05 (d, 1H, ³J = 8.8 Hz); 7.94 (d, 2H, ³J=9.0 Hz); 7.91 (d, 2H, ³J=9.0 Hz); 7.33 (d, 2H, ³J = 9.0 Hz); 7.00 (d, 2H, ³J = 9.0 Hz); 6.49/6.56 (m, 2H); 5.77/5.88 (m, 1H); 4.99/5.06 (m, 1H); 4.94/4.99 (m, 1H); 4.00/4.09 (m, 6H); 2.25/2.33 (m, 2H); 1.92/1.99 (m, 2H); 1.77/1.87 (m, 2H); 1.53/1.24 (m, 20H); 0.83/0.93 (m, 6H)

¹³C NMR (100 MHz, CDCl₃): δ 164.56, 163.73, 161.66, 161.61, 152.77, 150.18, 146.79, 137.69, 134.52, 124.70, 123.66, 122.48, 115.27, 114.68, 110.96, 105.36, 100.21, 68.36, 87.99, 31.79, 30.00, 29.34, 229.32, 29.21, 29.17 29.11, 28.25, 26.01, 25.98, 22.65, 14.09

6.5 - Synthesis of Cyanobiphenil derivatives (97 – 99)²⁸⁹



General procedure:

A solution of 4'-hydroxy-[1,1'-biphenyl]-4-carbonitrile (1 equivalent) and K_2CO_3 (1.5 equivalents) in butanone was heated at 50 °C for 30 min. R-Br (1equivalent) was added dropwise and the reaction left under reflux for 8 hours.

Compound	R-Br	Yield
97	11-bromoundec-1-ene	66%
98	5-bromopent-1-ene	72%
99	3-bromoprop-1-ene	68%

Compound 97

1H NMR (400 MHz, $CDCl_3$): δ 7.69 (d, 2H, $^3J = 8.6$ Hz); 7.64 (d, 2H, $^3J=8.4$ Hz); 7.53 (d, 2H, $^3J= 8.8$ Hz); 6.99 (d, 2H, $^3J = 9.0$ Hz); 5.76-5.78 (m, 1H); 4.91-5.03 (m, 2H); 4.00 (t, 2H, $^3J= 6.6$ Hz); 2.1-2.08 (m, 2H); 1.77-1.85 (m, 2H); 1.27-1.50 (m, 12H).

Compound 98

1H NMR (400 MHz, $CDCl_3$): δ 7.70 (d, 2H, $^3J = 8.1$ Hz); 7.64 (d, 2H, $^3J=8.8$ Hz); 7.53 (d, 2H, $^3J= 9.0$ Hz); 7.00 (d, 2H, $^3J = 8.8$ Hz); 5.81-5.92 (m, 1H); 4.99-5.11 (m, 2H); 4.02 (t, 2H, $^3J= 6.4$ Hz); 2.23-2.30 (m, 2H); 1.88-1.96 (m, 2H).

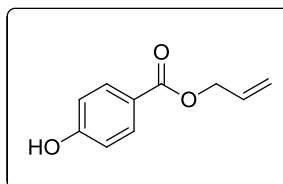
MS(CI) m/z 2841.1 (M+H)⁺

Compound 99

$^1\text{H NMR}$ (400 MHz, CDCl_3): δ 7.70 (d, 2H, $^3\text{J} = 8.6\text{Hz}$); 7.64 (d, 2H, $^3\text{J}=8.6\text{ Hz}$); 7.53 (d, 2H, $^3\text{J}= 8.8\text{ Hz}$); 7.02 (d, 2H, $^3\text{J} = 9.0\text{ Hz}$); 6.03-6.13 (m, 1H); 5.30-5.48 (m, 2H); 4.58-4.62 (m, 2H).

MS(CI) m/z 253.1 ($\text{M}+\text{NH}_4$) $^+$

6.6 - Synthesis of allyl 4-hydroxybenzoate (100)²⁹⁰



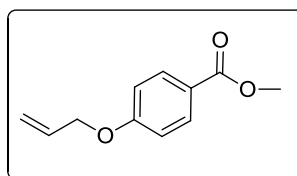
To a solution of 4-hydroxybenzoic acid (2.16 g, 15.6 mmol) and 40% aq tetrabutylphosphonium hydroxide (9 ml, 32.2 mmol) in THF (31 mL), was added allyl bromide (1.35 mL, 15.6 mmol) at 0 °C. The resulting reaction mixture was allowed to warm to ambient temperature. The reaction was stirred at this temperature until it was determined to be complete by TLC. The solvent (THF) was removed and product obtained by column chromatography with silica gel, solvent used was hexane/ethyl acetate, gradient.

$^1\text{H NMR}$: (400 MHz, CDCl_3): δ 7.97 (d, 2H, $^3\text{J} = 8.8\text{ Hz}$); 7.76 (bs, 1H); 6.92 (d, 2H, $^3\text{J}= 8.8\text{ Hz}$); 5.97-6.08 (m, 2H); 5.40 (dd, 1H, $^3\text{J}_{trans}= 17.2\text{ Hz}$, 1H, $^2\text{J} = 1.3\text{Hz}$); 5.29 (dd, 1H, $^3\text{J}_{cis} = 10.5\text{ Hz}$, 1H, $^2\text{J} = 1.1\text{Hz}$); 4.80-4.83 (m, 2H).

MS(EI) m/z 196.01 ($\text{M}+\text{NH}_4$) $^+$

HRMS: Calculated for $\text{C}_{10}\text{H}_{14}\text{NO}_3$: 196.0968, found 196.0968.

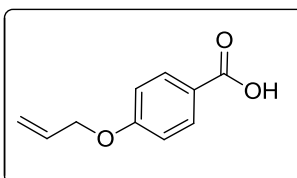
6.7 - Synthesis of methyl 4-(allyloxy)benzoate (101)



A solution of methyl 4-hydroxybenzoate (5.26 g, 34.5 mmol), potassium carbonate (7.74 g, 55.9 mmol) and allyl bromide (3.25 ml, 37.6 mmol) in butanone was heated under reflux over night and a drying tube was added. The reaction was followed by TLC. After removal of solvent under reduced pressure, a yellow oil was obtained and a white powder (6.11g, 92 % yield) was obtained after precipitation from hexane.

¹H NMR: (400 MHz, CDCl₃): δ 8.06 (d, 2H, ³J = 9.1 Hz); 6.96 (d, 2H, ³J = 8.8Hz); 6.01-6.12 (m, 1H); 5.41-5.47 (m, 1H); 5.31-5.35 (m, 1H); 4.60-4.63 (m, 2H).

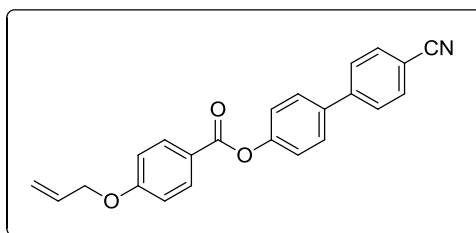
6.8 - Synthesis of 4-(allyloxy)benzoic acid (102)²⁸⁸



A solution of potassium hydroxide (22.65 g, 0.4 mol) in water was added to a solution of methyl 4-(allyloxy)benzoate (5.85 g, 30.4 mmol) in THF (35 ml) and MeOH (195 ml). The reaction was left stirring over night and completed by refluxing for 2 h. After removal of solvents under reduced pressure, a mixture of ice and water were added. The solution was acidified with conc. HCl and extracted with ethyl acetate and finally recrystallised from methanol. A white powder was obtained in 3.66 g, 68 % yield (first recrystallisation)

¹H NMR (400 MHz, CDCl₃): δ 8.06 (d, 2 H, ³J = 9.07 Hz); 6.96 (d, 2 H, ³J = 8.76 Hz); 6.01-6.11 (m, 1H); 5.47-5.40 (m, 1H); 5.36-5.31 (m, 1H), 4.64-4.60 (m, 2H).

6.9 - Synthesis of 4'-cyano-[1,1'-biphenyl]-4-yl 4-(allyloxy)benzoate (**103**)²⁸⁸



A solution of compound **102** (3.66 g, 20.54 mmol), dimethylaminopyridine (2.48 g, 20 mmol), 4'-hydroxy-[1,1'-biphenyl]-4-carbonitrile (12.03 g, 61.6 mmol) in THF was stirred in a water and ice bath. Dicyclohexylcarbodiimide (7.68 g, 37 mmol) was added over a period of 5 min. After the addition was complete the reaction mixture was left to stir for another 10 min and the water and bath was removed. The mixture was stirred at room temperature over night and followed by TLC (hexane: ethyl acetate; 7:3). The reaction mixture was evaporated under reduced pressure and the crude reaction mixture was separated by chromatographic column (hexane: dichloromethane: 97:3). Compound **103** was obtained as a white solid (1.46 g, 20 %; yield results from first column).

¹H NMR (400 MHz, CDCl₃): δ 8.06 (d, 2H, ³J = 8.8 Hz); 7.74 (d, 2H, ³J = 8.4 Hz); 7.69 (d, 2H, ³J = 8.1 Hz); 7.64 (d, 2H, ³J = 8.4 Hz); 7.33 (d, 2H, ³J = 8.4 Hz); 7.02 (d, 2H, ³J = 9 Hz); 6.03-6.13 (m, 1H); 5.43-5.50 (m, 1H); 5.33-5.38 (m, 1H); 4.63-4.67 (m, 2H).

MS(EI) *m/z* 356.1 (M+H)⁺

HRMS: Calculated for C₂₃H₁₈NO₃: 356.1281, found 356.1276

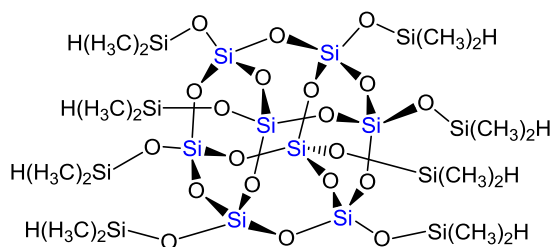
6.10 - Synthesis of POSS derivatives¹²³

POSS derivatives were synthesised according to the procedure described in the literature.¹²³

Example procedure for the synthesis of compound **104**.

A solution of toluene (40 mL), compound **96** (1.3 g, 2.03 mmol) and 25 μL of a 3.0–3.5 % solution of Karstedt's catalyst dissolved in xylene was gently aerated for 20 s. A solution of *octakis* (hydrodimethylsiloxy)octasilsesquioxane (0.12 g, 0.12 mmol) dissolved in dry toluene (20 ml) was added dropwise at room temperature over a period of 1 h. The reactions were left stirring in the dark and at room temperature over night.

The silsesquioxane core used is shown in Figure 95.

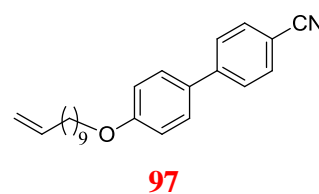
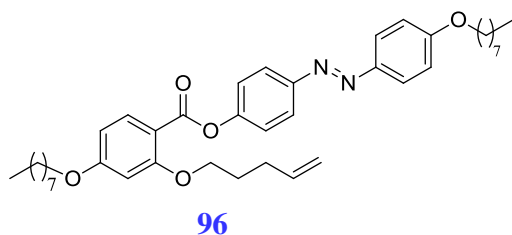


Core I

Figure 95: Silsesquioxane core used in the synthesis of compounds 104 – 116.

The tables below summarize, for the four series synthesized, the amounts of the different mesogens used, yields and final proportion of mesogens in the silsesquioxane derivatives, determined by ^1H NMR.

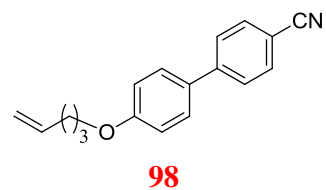
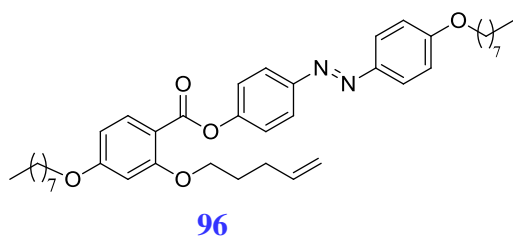
Series I



Compound	Amount of POSS (mol)	Mesogens used and amount (mol)		Yield (%)	Proportion of mesogens (%)*	
		96	97		96	97
104	1.19 E ⁻⁴	2.03 E ⁻³	-	8	100	-
105	9.85 E ⁻⁵	2.03 E ⁻³	8.26 E ⁻⁴	55	39	61
106	3.87 E ⁻⁵	7.32 E ⁻⁴	3.21 E ⁻⁴	63	52	48
107	1.02 E ⁻⁴	1.01 E ⁻⁴	5.62 E ⁻⁴	63	51	49
108	0.10 E ⁻³	-	1.58 E ⁻³	70	-	100

* Proportion of mesogens determined by ^1H NMR

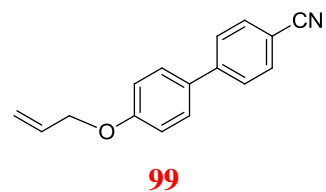
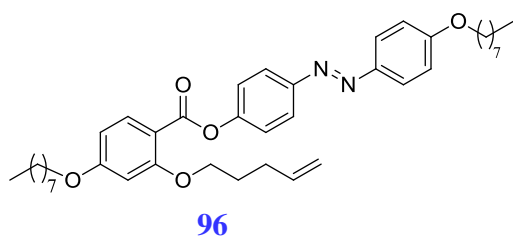
Series II



Compound	Amount of POSS (mol)	Mesogens used and amount (mol)		Yield (%)	Proportion of mesogens (%)*	
		96	98		96	98
109	6.06 E ⁻⁵	6.49 E ⁻⁴	3.22 E ⁻⁴	50	64	36
110	9.79 E ⁻⁵	5.26 E ⁻⁴	1.05 E ⁻³	60	25	75
111	9.29 E ⁻⁵	-	1.42 E ⁻³	64	-	100

* Proportion of mesogens determined by ¹H NMR

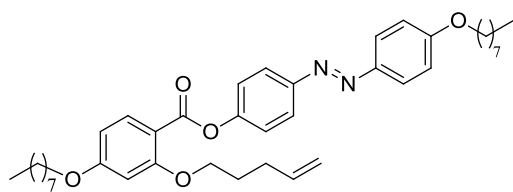
Series III



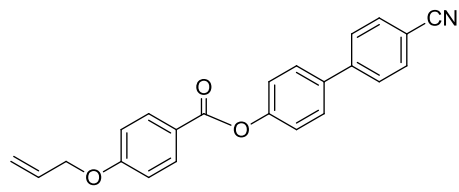
Compound	Amount of POSS (mol)	Mesogens used and amount (mol)		Yield (%)	Proportion of mesogens (%)*	
		96	99		96	99
112	8.14 E ⁻⁵	6.71 E ⁻⁴	6.66 E ⁻⁴	67	43	56
113	6.36 E ⁻⁵	8.25 E ⁻⁴	4.30 E ⁻⁴	61	45	55
114	9.27 E ⁻⁵	-	1.58 E ⁻³	52	-	100

* Proportion of mesogens determined by ¹H NMR

Series IV



96



100

Compound	Amount of POSS (mol)	Mesogens used and amount (mol)		Yield (%)	Proportion of mesogens (%)*	
		96	100		96	100
115	7.68 E ⁻⁵	6.53 E ⁻⁴	6.24 E ⁻⁴	66	50	50
116	7.74 E ⁻⁵	-	1.25 E ⁻³	58	-	100

* Proportion of mesogens determined by ¹H NMR

CHAPTER 7 – DISCUSSION

This discussion will be divided in three parts. Part I will discuss the synthesis, thermal and photochromic behaviour of liquid crystal materials synthesized, starting with low molecular weight materials followed by silsesquioxane derivatives. A discussion of the phase structure for the novel liquid crystalline materials will form Part II. The last part (Part III) will be dedicated to the discussion of photoinduced alignment and SRGS inscription of compound **115**.

DISCUSSION PART I-

7.1 Synthesis and characterization of low molar mass mesogens

The general synthetic scheme used for the synthesis of compound **96** is given below.

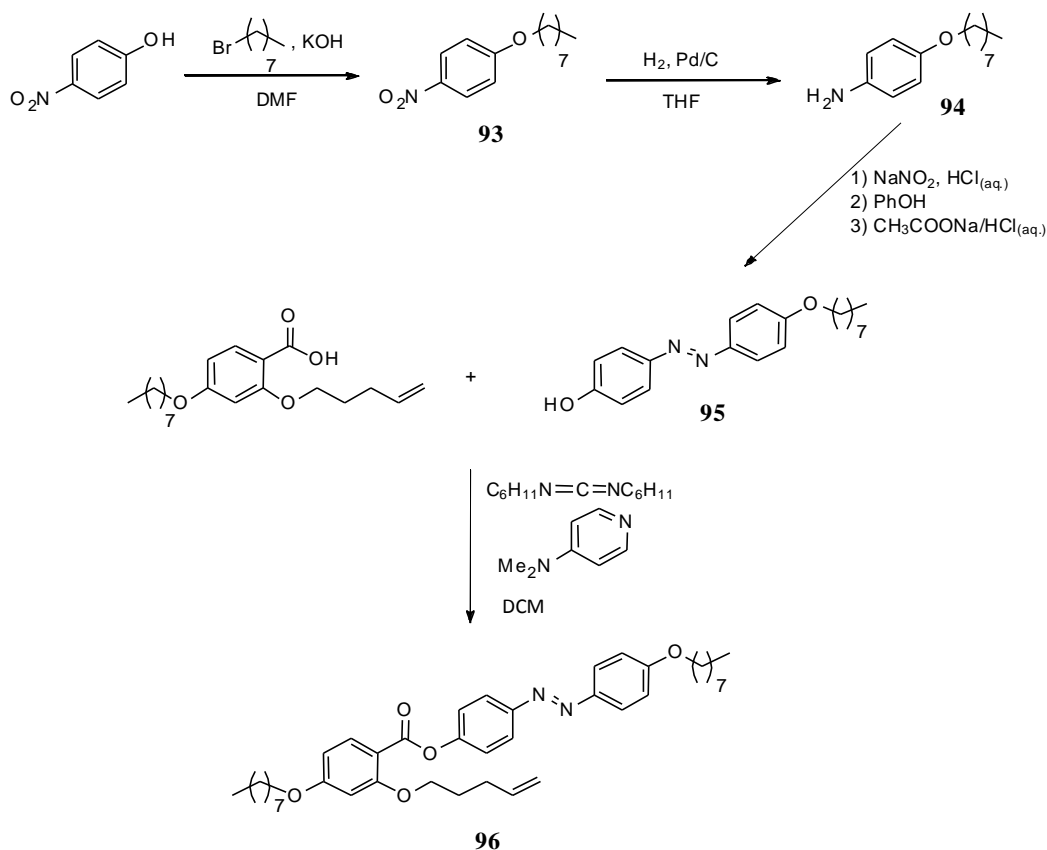


Figure 96: Synthesis of mesogen **96**.

The first step of this (Figure 96) synthesis, the Williamson etherification, occurred as expected and a yield of 75% was obtained. Although compound **93** is easily recrystallised from methanol, its melting point is very close to room temperature therefore the filtration process was carried out using a cold suspension ($\cong 4\text{ }^{\circ}\text{C}$) and as quickly as possible. When these conditions were followed the product was obtained without problems and in good yields.

Compound **94** was obtained by reduction of the nitro group by hydrogenation, using Pd on carbon (5% wt/wt). Initially two methods were used that diverged mainly on the pressure used. The first method used a hydrogenator apparatus where pressure conditions were close to atmospheric pressure. The reaction was followed by TLC and after 8 hours, a small amount of product was formed, however after another 24 hour period no further progress had occurred. The second method was based on a high pressure equipment where precise control of pressure used is possible. The reaction was carried using 2.5 bar. After a reaction time of 8 hours, the reaction was monitored by TLC, yet no product was formed.

Since none of the above methods were successful, the reaction was repeated by simply bubbling hydrogen through the reaction mixture for a 9 hour period and then monitored by TLC. In this case the reaction was almost complete by TLC and product **93** was obtained in 80% yield. The purification process of this compound proved to be challenging and will be discussed next.

A classical work up for amines involves protonation and extraction with an organic solvent. Yet when the reaction crude was washed with (HCl (aq) (0.5 N)) there was not a clear phase separation between organic and aqueous layers. It seemed that when protonated, compound **94** acted as a surfactant making it very difficult to extract. To ensure that the material was recovered, a ^1H NMR was collected and is depicted below (see Figure 97). The spectrum showed the peaks corresponding to the aromatic group with the expected chemical shifts but with poorly resolved peaks. To recover **94**, the crude material was washed with a saturated solution of Na_2CO_3 , a ^1H NMR was collected showing a very well resolved signals as expected. This compound was then isolated by column chromatography. However because this compound is an important intermediate for the synthesis of the liquid crystalline materials, an effort to simplify the purification process was tried. The crude material was usually filtered through Celite, for the removal of the (Pd/C) catalyst and a ^1H NMR of the material after this process was made and the difference between the spectra before and after the chromatographic separation was minimal, allowing this material to be used with no further purification.

Figure 97 shows the ^1H NMR of **94** when filtered through Celite (spectrum A) and after being purified by chromatography, Spectrum B.

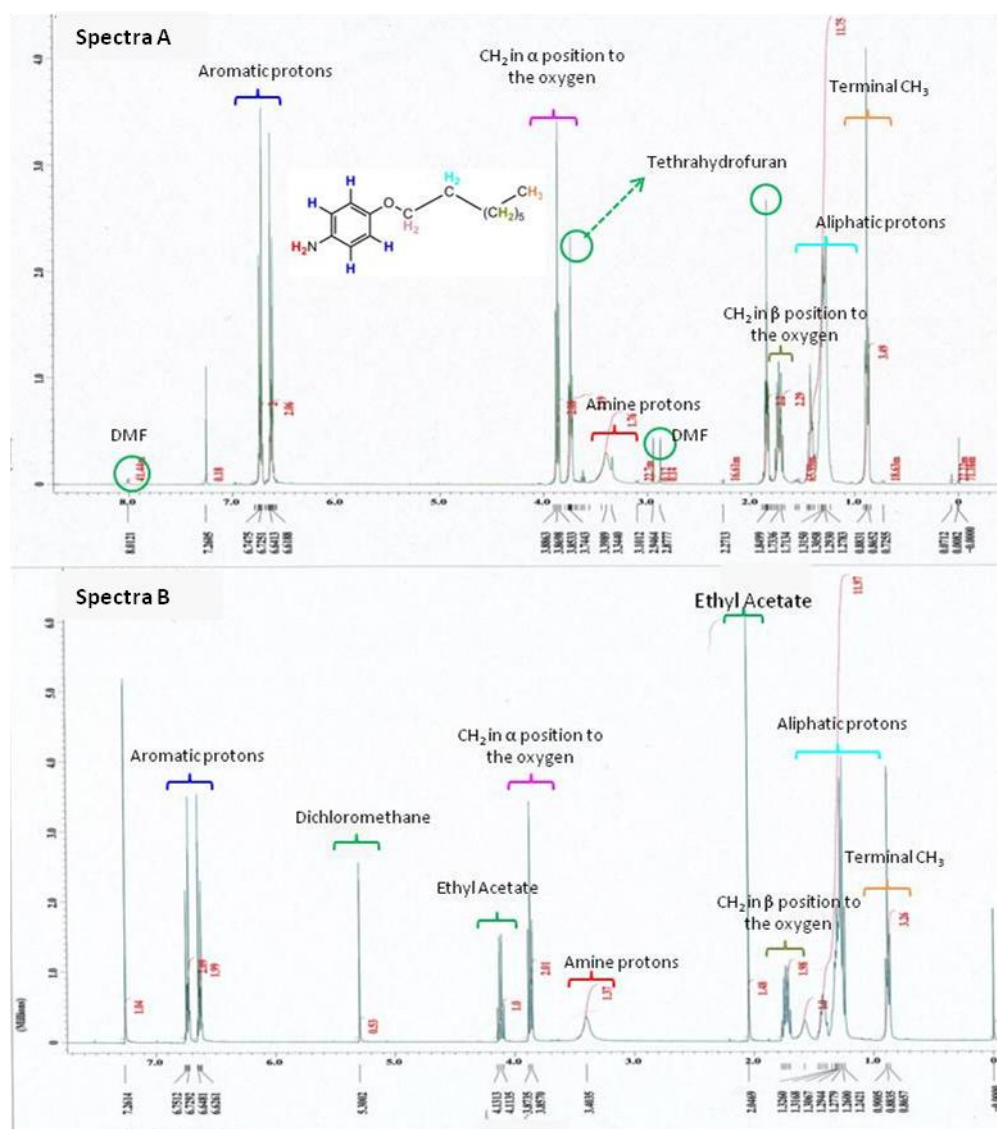


Figure 97: ^1H NMR spectra of compound **94**; before (Spectrum A) and after (Spectrum B) being purified by chromatography.

In spectra A the characteristic peaks of **94** are observed as well as solvent peaks, apart from that no other relevant peaks can be observed. After purification of **94** by chromatography, a pure compound (by ^1H NMR) was obtained. Some peaks present in Spectrum A (Figure 97) disappeared although their amounts were already very small. Since there was not a major improvement by carrying this extra purification step (compare with Spectrum B Figure 97), compound **94** was used in the next reaction without being purified by column chromatography.

Because **94** was an important intermediate for the synthesis of the first mesogen, attempts of scaling up this reaction were carried out. When the reaction was carried out

on a 6 g scale, the reaction time increased and the reaction was not completed after a week. Initially it was thought this could be a consequence of an old catalyst; to make sure this was not the case, a new catalyst was used, and the same result was obtained, this dismissing the possibility of scaling up this reaction without alterations to the procedure used.

One problem found in the synthesis of **95** was the process of extracting the compound from the aqueous reaction media. Initially a large amount (more than 2.5 L) of dichloromethane was required to extract the product, so efforts were made to extract the product using other solvents such as ethyl acetate, ether and chloroform. None of these solvents proved to be an improvement over dichloromethane. Using a mixture of dichloromethane/methanol (96 : 4 %) was extremely efficient, there was a significant decrease of the amount of solvent required, but despite this improvement, a yellow coloration in the water layer was still present. Considering that the reaction media was pH 11 there was the possibility of the existence of phenoxide ion which would explain the persistence of the yellow colour in the water layer. By acidifying the water layer to pH 5 and extracting it with dichloromethane/methanol the yellow colour disappeared. These changes lead to a very efficient way of extracting compound **95**. The amounts of solvent used were reduced to 400 mL (2 x 200 mL). Observation of the water layer under UV light showed that no product was left and the overall process was much faster. The product was further purified by column chromatography as described in the experimental section. It is possible that the same effect mentioned for the extraction of **94** occurred where due to the long alkyl chain, **95** also acts as a surfactant being soluble in water. By converting the water layer to an alkaline pH the compound should now be neutral and the mixture of dichloromethane and methanol, which is a very polar solvent, allows the extraction of the compound from the water layer fairly easily.

Purification of **96** was initially achieved by column chromatography and two fractions were obtained. The ^1H NMR spectrum showed peaks corresponding to product **95** and two extra peaks in the aromatic region with chemical shifts of approximately 7.6 and 7.5 ppm. In the literature^{291, 292} there are references of protonation of azobenzenes. To verify if this was the case, the first fraction (showing two extra signals) was washed initially with potassium carbonate and afterwards with NaOH (0.1 M), ^1H NMR of both attempts showed no change in these two signals.

Both ^1H NMR and TLC suggested that this compound was not pure. Yet after further purification by column chromatography and recrystallization, it seemed that the compound was still impure. Thus the question arose whether the compound was

degrading or if the spot seen in the TLC was just due to isomerisation of the azobenzene group. A simple experiment was made to try to clarify this aspect. A ^1H NMR sample was prepared and a spectrum was recorded. This NMR tube was left on a windowsill for approximately 1 hour, and another ^1H NMR spectrum was recorded. Finally, this sample was left in the dark over night and after this period one more ^1H NMR spectrum was recorded. The results obtained are shown in Figure 98. This set of spectra shows that in spectrum A peaks in the aromatic region, consistent with impure compound, are present. In spectrum B, after exposure to light for one hour, the peaks that initially seem a small impurity were now much sharper and much more intense and are pointed out in the spectra of Figure 98 by the red dashed circles. The evident change in these peaks makes their attribution to a simple impurity unlikely yet degradation of **96** in the presence of light was still a possibility. In order to clarify whether the changes in the ^1H NMR spectrum were a consequence of degradation or isomerization, the sample was stored in the dark over night. It was expected that the isomerization process would restore the original spectrum and degradation process would result in a spectra identical to spectrum B. The data is presented in Figure 98, spectrum C and the absence of the peaks in question is clear, more when compared with the initial state, this spectrum reflects a pure sample by ^1H NMR, suggesting that a small amount of the *cis* isomer was present in the initial sample which is in agreement to the existence of two spots in the TLC. The possibility of quantifying the proportions of each of the isomers is demonstrated and will be explored in Part II of this discussion.

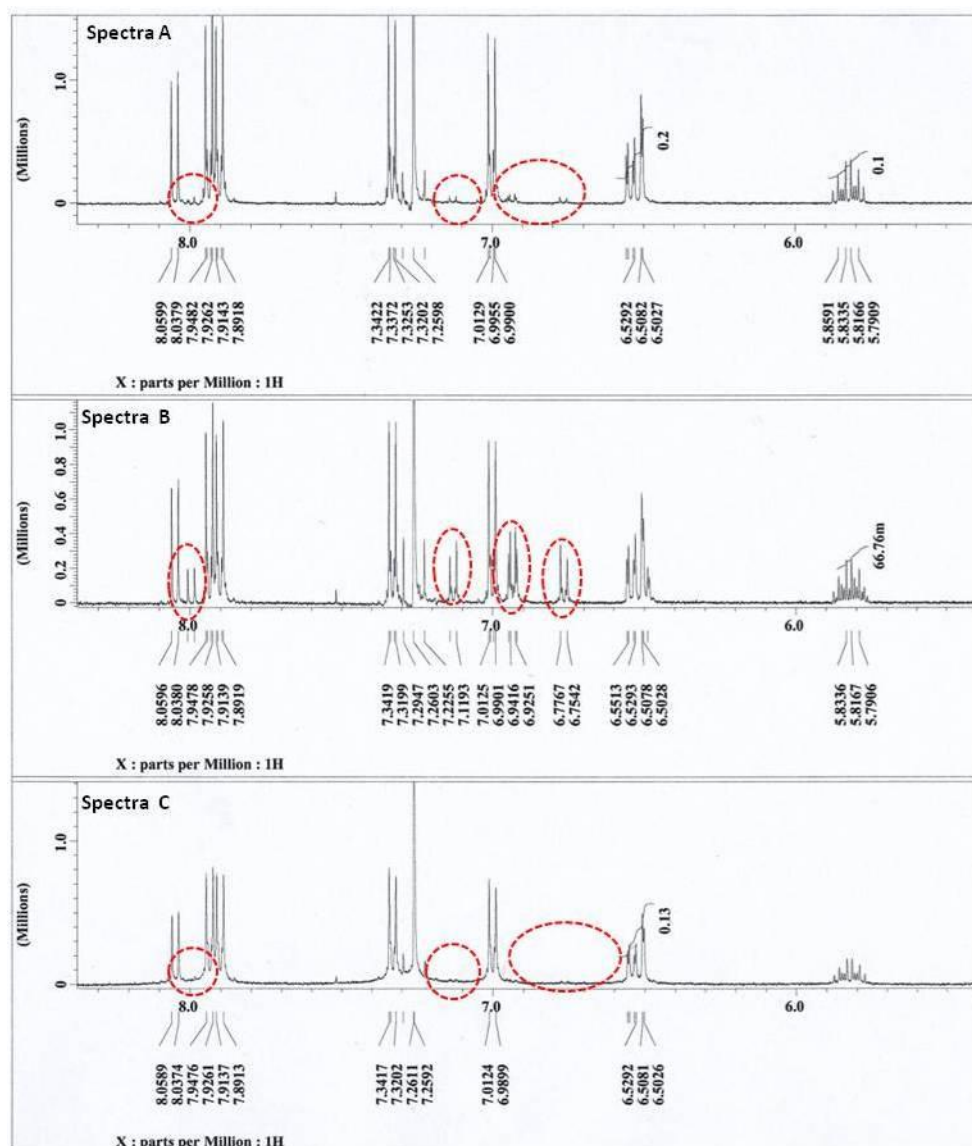


Figure 98: ^1H NMR spectra of compound 96. Spectrum A, first spectrum carried; Spectrum B was carried after 1 hour in light and Spectrum C was performed after the sample has been kept in the dark.

The synthesis of the cyanobiphenyl derivatives **97-99** (Figure 99) was carried out in line with literature reports.

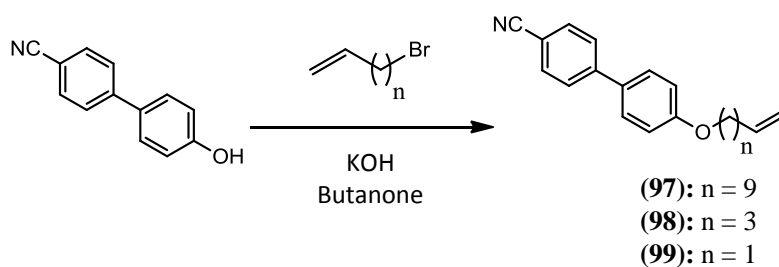


Figure 99: Scheme of synthesis of compounds 97 –99.

The synthesis of mesogen **103** was surprisingly difficult. A selective alkylation of alcohols described by Liu *et al.*²⁹⁰ indicated the synthesis of molecule **102** in 91% yield was possible (Figure 100).

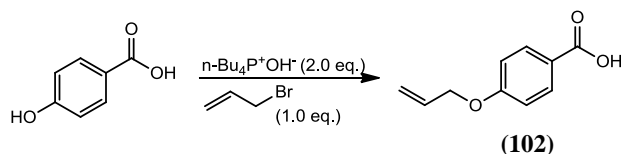


Figure 100: Reaction scheme for the synthesis of compound **102**.²⁹⁰

When this procedure was repeated the result obtained did not correspond to the one described in the literature. Although proton and carbon NMR appeared to justify the expected structure **100** (Figure 101), when the resulting product was used in the next step (esterification), none of the synthetic routes used (acyl chloride or DCC coupling) was successful. The lack of reactivity of this compound lead to the view that the molecule obtained was in fact **100** (Figure 101).

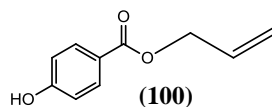


Figure 101: Compound **100**.

That would explain the similarity of the proton and carbon NMR. In order to clarify this point some literature research for the NMR of these two molecules was carried out. The results in the literature seem to suggest a slight difference in the chemical shift of the CH_2 adjacent to the oxygen of the ether and the ester.

Comparing the ^1H NMR data obtained Figure 102 we can see this difference in the chemical shift of these CH_2 protons. For molecule **100**, spectrum B, the chemical shift of the protons next to the oxygen of the ether is 4.85 ppm while for the expected molecule **102** the chemical shift is 4.62 ppm.

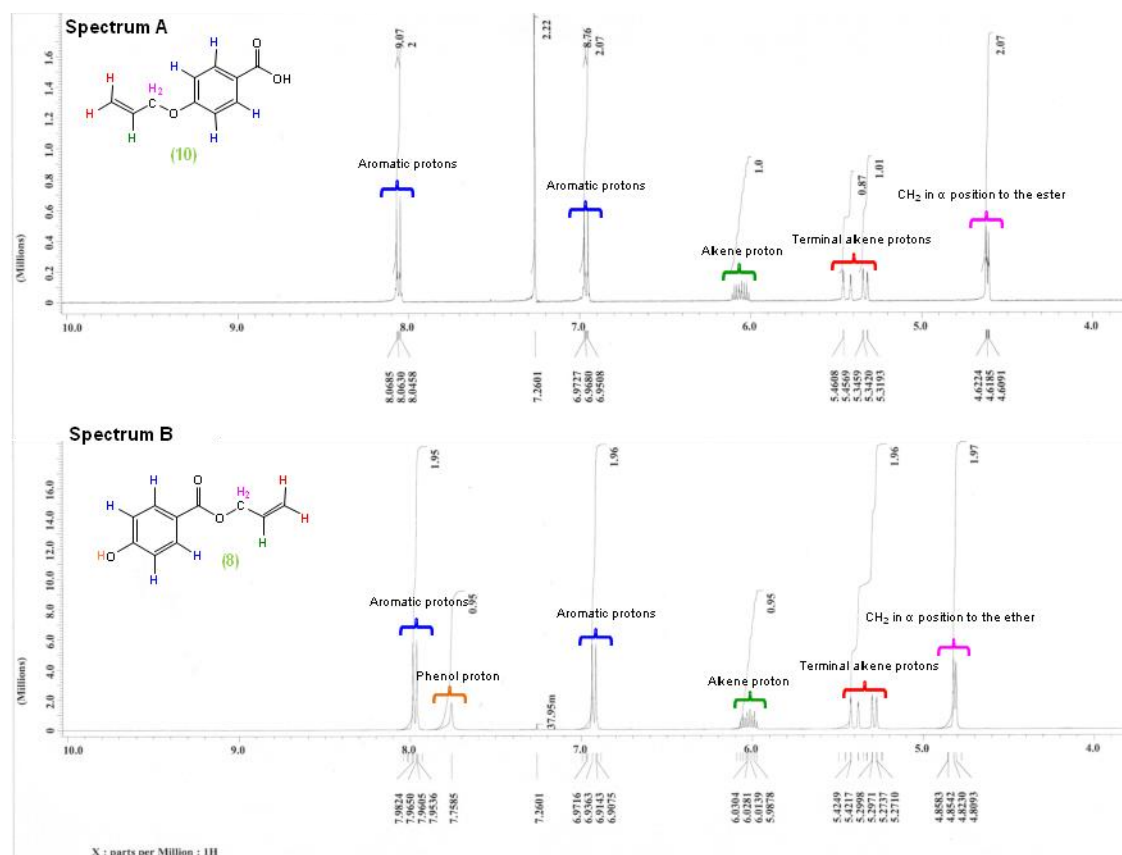


Figure 102: ¹H NMR spectra of compound 102 (Spectrum A) and compound 100 (Spectrum B).

Considering that the molecule obtained was not the molecule desired, a protection/deprotection synthetic strategy (Figure 103) was used to obtain compound 103.

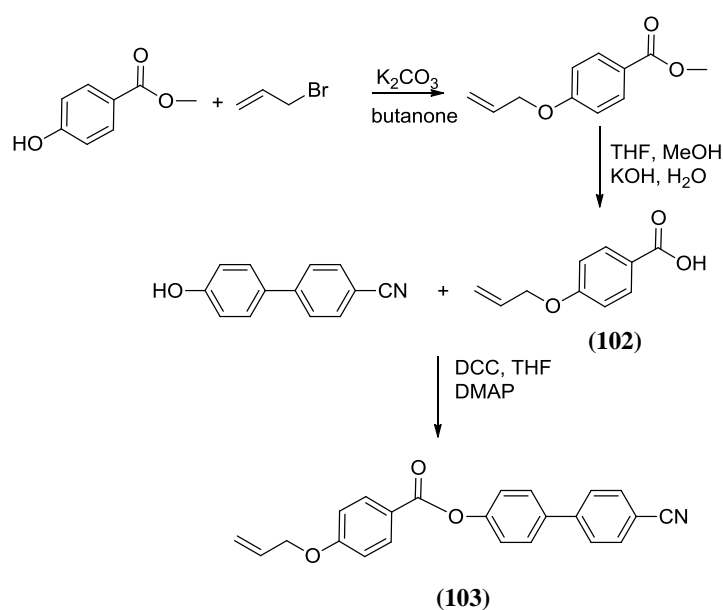


Figure 103: Scheme of the strategy used to synthesise compound 103.

7.2 Synthesis and characterization of POSS derivatives

One of the main aims of this work was to synthesise a dendritic material containing azobenzene groups which exhibit a nematic phase and a glass transition at room temperature.

The dendritic core chosen was a polyhedral silsesquioxane (POSS) represented in Figure 95. This cubic core can be used to prepare robust materials and it can be handled easily.

POSS derivatives were synthesised via the hydrosilylation reaction of core **I** and mesogens **96** to **99** and **103** (Figure 104) using Karstedt's catalyst at room temperature. The reaction times reported in the literature when this method was followed are on the scale of a few minutes. When the synthesis of the first POSS derivative **104** was attempted, it was surprising that the reaction was not completed after 25 minutes; the Si-H signal characteristic of core **I** at 4.7ppm was still present in the ^1H NMR spectra. The reaction was left over night and the amount of catalyst used was increased from 10 μL reported in the literature to 25 μL used in all the following synthesis.

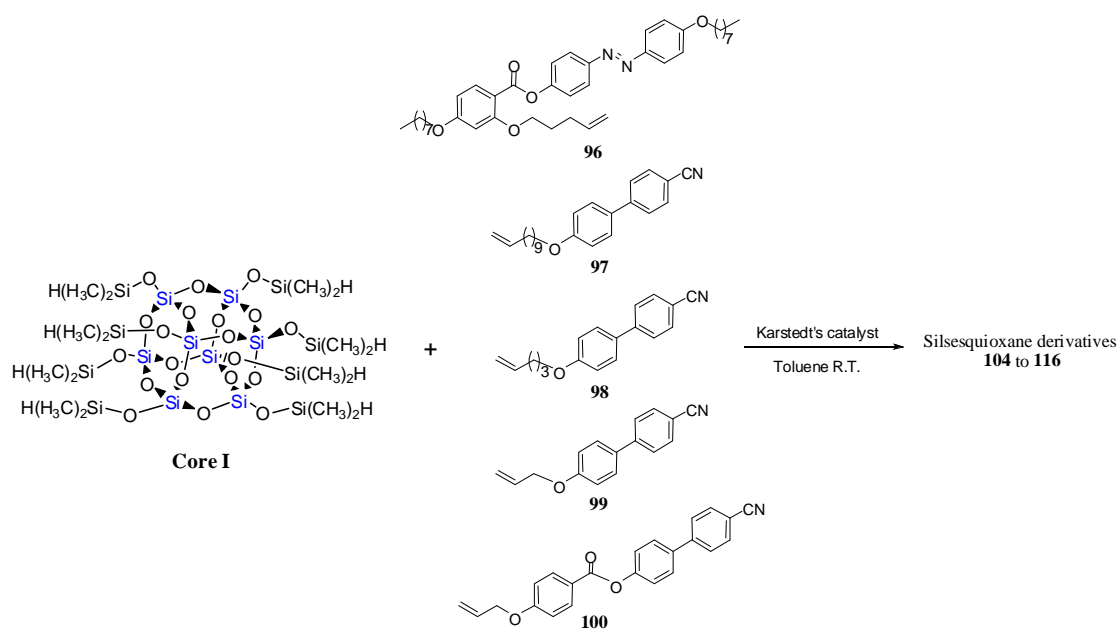


Figure 104: Siloxane core I and mesogens used in the synthesis of compounds 104 to 116.

After eight hours and a significant decrease of the Si-H signal, the reaction was stopped by addition of triphenylphosphine. A suggestion for the apparent lack of reactivity of mesogen **96** could be attributed to its larger size compared to that for the molecules

reported in the literature. This could lead to some steric crowding at the reactive centres, close to the POSS core, resulting in longer reaction times and incomplete reactions.

The existence of the *cis* isomer in the reaction media, due to photoisomerization of the azobenzene group, could also have an effect on its reactivity. To prevent any possible effect of *cis-trans* isomerisation in the reactivity of mesogen **96**, the compound was stored in the dark and ^1H NMR analysis before reaction (to ensure that no *cis* isomer was present) were carried out.

Compounds **104** to **116** were purified by precipitation of the reaction mixture with methanol. This process was repeated until no further mesogen was observed by TLC, and the results confirmed by the disappearance of the signals characteristic to terminal alkenes in the ^1H NMR spectra.

^1H NMR spectra gives information about the purity of the synthesised compounds, the existence of any Si-H unreacted positions, and therefore the degree of substitution of the POSS cube. An estimation of the ratio of the mesogens attached to the POSS core can also be made (Figure 105). A broadening of the signals is observed, as expected for this type of system.

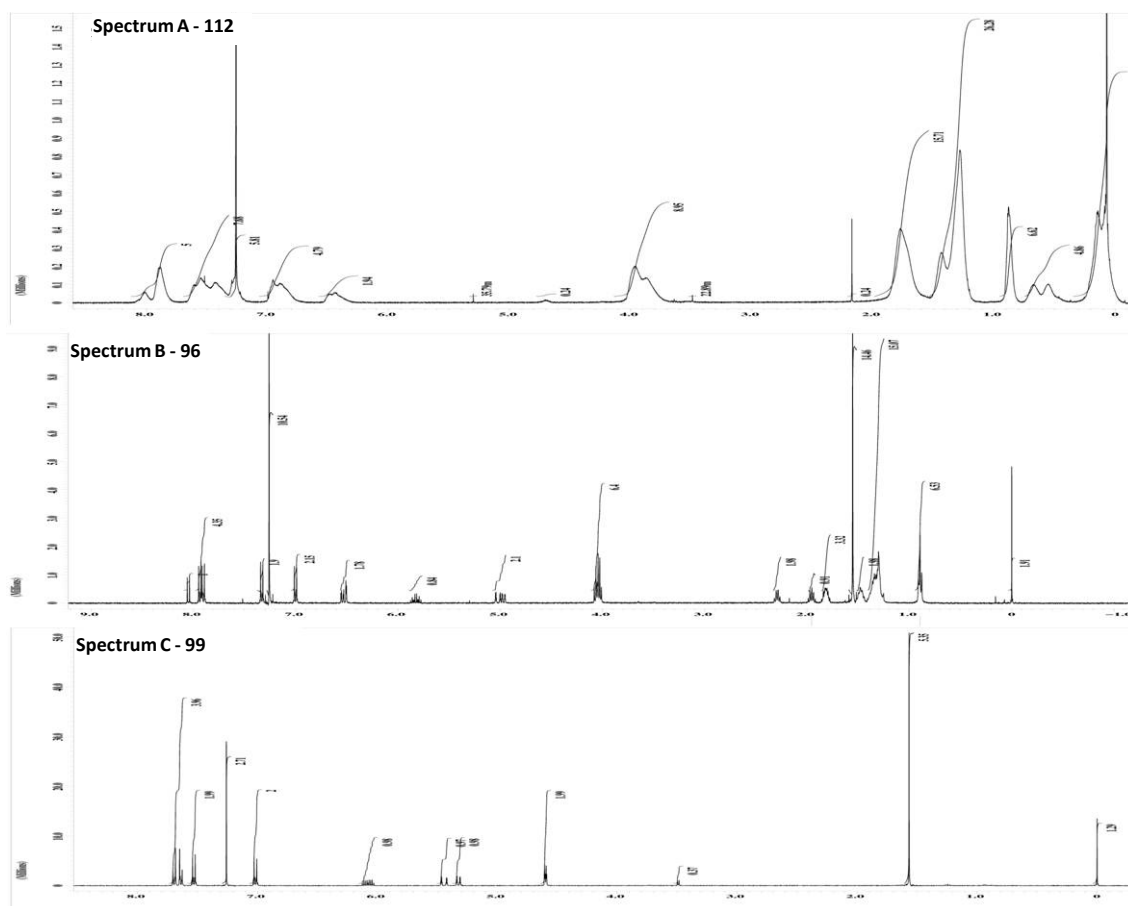


Figure 105: ^1H NMR spectra of compound **112** in Spectrum A and mesogens **96** and **99** in Spectrum B and C.

Figure 105 shows the ^1H NMR spectra of compound **112** in Spectrum A and mesogens **96** and **99** in Spectrum B and C respectively. In spectrum A a broadening of the peaks is noticeable, the existence of a small amount of Si-H signal at 4.7 ppm (see Table 9) and the disappearance of the peaks characteristic for the terminal alkene groups. Comparing these three spectra, an estimation of the proportion of both mesogens is possible.

Purity measurement of the POSS derivatives by gel permeation chromatography (GPC) was also attempted. The GPC system used was calibrated using an external polystyrene standard that has a helicoidal structure very different from the globular shape of POSS derivatives. Therefore some caution has to be applied when analyzing these results and using the absolute molecular weight values obtained from the GPC instrument. For example, compound **116** is according to ^1H NMR spectroscopy, completely substituted, so only one peak should be expected by GPC instead, two peaks appear, with molecular weights of 7832 and 3474. Since the possibility of dimerization reactions is very low, an explanation could be that there is an aggregation of POSS derivatives in the column, in which two POSS derivatives travel together giving a molecular weight that is roughly twice the molecular weight of only one molecule.

When unreacted Si-H signals are found in the ^1H NMR the existence of a mixture can be expected, some cores might have eight substituents, some can have seven or maybe less thus polydisperse peaks were expected. The GPC results obtained show mainly the existence of monodisperse peaks (1.02-1.17) that can be explained by the similarity of hydrodynamic radii of these compounds due to their rigid 3D structure. Compounds **106** and **113** show extremely high polydispersity indices (PDIs) and three to four different species with similar retention volumes, therefore the calculation of the PDIs might not be accurate.

Table 9: Summary of characterization of compounds 104 to 116.

	POSS derivative	Percentage of mesogens used		Yield (%)	Proportion of mesogens in POSS derivative*		Existence of unreacted Si-H bonds
		96	97		96	97	
	104	100	-	60	100	-	Yes ^Y
	105	53	47	55	39	61	Yes ^{YY}
Series I	106	68	32	63	52	48	Yes ^{YY}
	107	66	34	63	51	49	Yes ^{YY}
	108	-	100	70	-	100	No
		96	98		96	98	
	109	95	5	52	64	36	Yes ^{YY}
Series II	110	32	68	60	25	75	Yes ^{YY}
	111	-	100	64	-	100	No
		96	99		96	99	
	112	50	50	67	43	56	Yes ^{YY}
Series III	113	65	35	61	45	55	Yes ^Y
	114	-	100	52	-	100	No
		96	103		96	103	
Series IV	115	50	50	66	50	50	Yes ^Y
	116	-	100	58	-	100	No

* Percentage determined by ^1H NMR. ^Y Less than $\times 10^{-3}$. ^{YY} less than $\times 10^{-1}$.

One aspect to consider with respect to the synthesis of POSS derivatives is related to the effort of synthesising compounds with different mesogen ratios. In Table 9 the

percentage of mesogens used and the percentage found (by ^1H NMR) in the final products is depicted.

Compound **105** was synthesised in an attempt at trying to achieve 50% of each mesogen attached to core **I**. It was surprising to notice that only 40% of **96** was found to react. When **96** and **97** were used in a 2:1 proportion (compounds **106** and **107**) a 1:1 mixture was obtained. In both cases the results obtained were identical suggesting that the results are reproducible.

When 95% of **96** was used, the amount attached to silicon core was found to be 64%, compound **109**. Together with the results discussed above it seems that different mesogens have different reactivities in the hydrosilylation reaction.

Compounds **112** and **115** were both synthesised using a mixture of 50% of **96** and **97** and **103** respectively. In both compounds a 1:1 ratio of mesogen **96** to **97** for compound **112** and **96** to **103** in compound **115** was found, showing that the results are in agreement with the projected ratio.

The increase in the ratio of azobenzene is not reflected in the proportion of the mesogens attached to the siloxane core **I**. There seems to exist a threshold amount above which the attachment of azobenzene groups to the POSS cube is difficult to obtain. In order to overcome this, the excess of azobenzene used have to be extremely high as observed to compound **109**.

The observation that the stoichiometric ratio of the starting materials is not entirely reflected in the products composition makes the design of co-mesogenic POSS derivatives with specific ratios difficult.

Finally it seems that the use of azobenzene **96** in the hydrosilylation reaction makes it difficult to obtain complete reaction (fully substituted POSS derivatives) even when the reaction time is as long as 8h.

7.3 Liquid crystalline properties of low molar mass mesogens

The liquid crystalline behaviour of the synthesized materials was initially studied by polarized optical microscopy and calorimetry. These results will be discussed next. The initially proposed mesophase was confirmed by X-ray experiments the results obtained will be discussed in detail in Part II.

In Figure 106 a micrograph obtained by POM from **96** shows a marbled texture which is characteristic for nematic samples that have not been rubbed or suffered any treatment.

The change in color can be attributed to changes in birefringence associated with variations of the thickness of the sample as well as changes in the direction of the director. The transition temperatures Cr 58 N 91 Iso were collected from the DSC data (see Table 10).

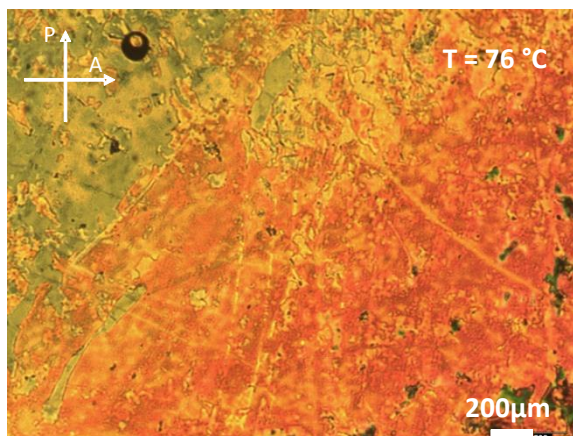


Figure 106: Texture obtained by OPM for compound 96.

The liquid crystalline behaviour of the cyanobiphenyl series, compounds **97** to **99** and **103**, will be discussed based on the information obtained by DSC and OPM.

The DSC data shown in Figure 107 shows that compounds **98** and **99** are monotropic liquid crystals. The transition temperatures and enthalpy values from the second heating curves, for compounds **96** to **99** and **103** are summarized in Table 10.

Table 10: Liquid crystalline properties of compounds 96 to 99 and 103.

Compound	Phase transitions <i>T</i> / °C (ΔH /Jg ⁻¹)
96	Cr 58 (64.1) N 91 (3.4) Iso
97	Cr 56 (99.3) SmA 71 (2.2) N 74 (5.3) Iso
98	Cr 89 (N 71(-2.3)) Iso
99	[N 71(-3.9)] Iso
103	Cr 122 (68,1) mesophase 267 (6.2) Iso

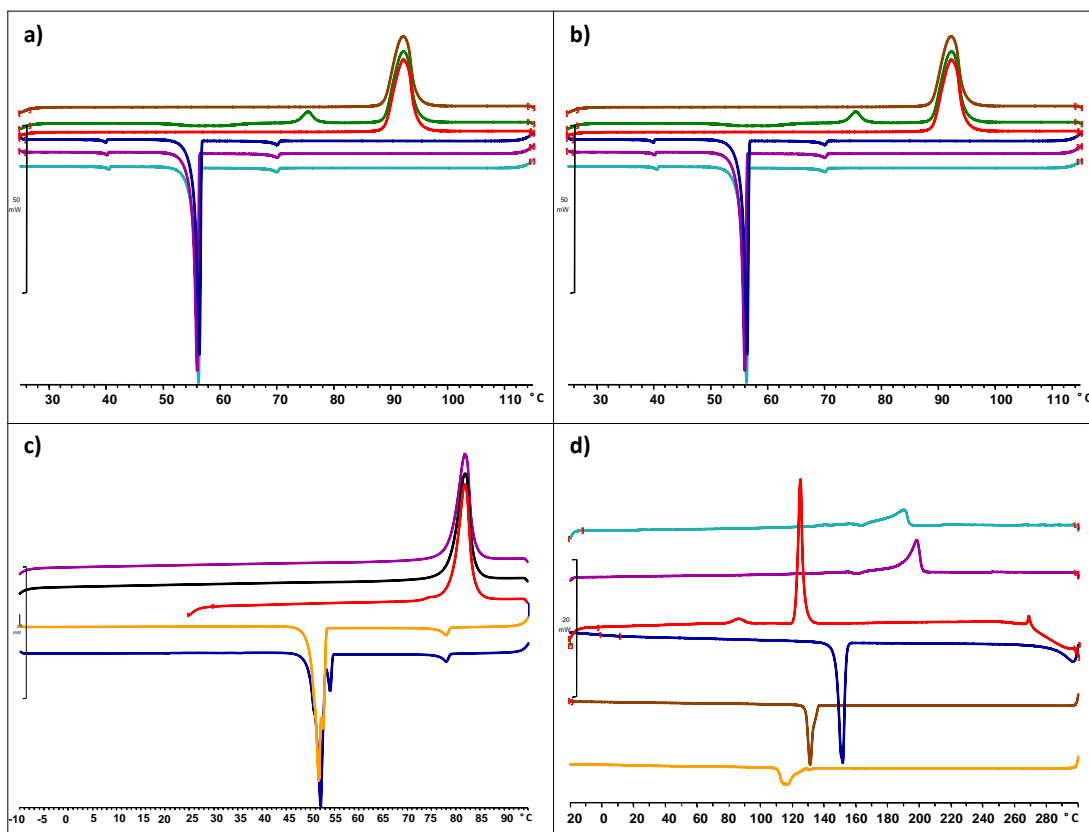


Figure 107: DSC curves a) 97, b) 98, c) 99 and d) 103.

All DSC curves were recorded at 10 °C/ min and it can be observed that compounds **97** and **103** have enantiotropic liquid crystalline behaviour. The phase transition temperatures and associated enthalpies are depicted in Table 10. The textures obtained by OPM are shown in Figure 108 a) broken-fan texture associated with a Sm phase and Figure 108 b) Schlieren texture associated with the nematic phase.

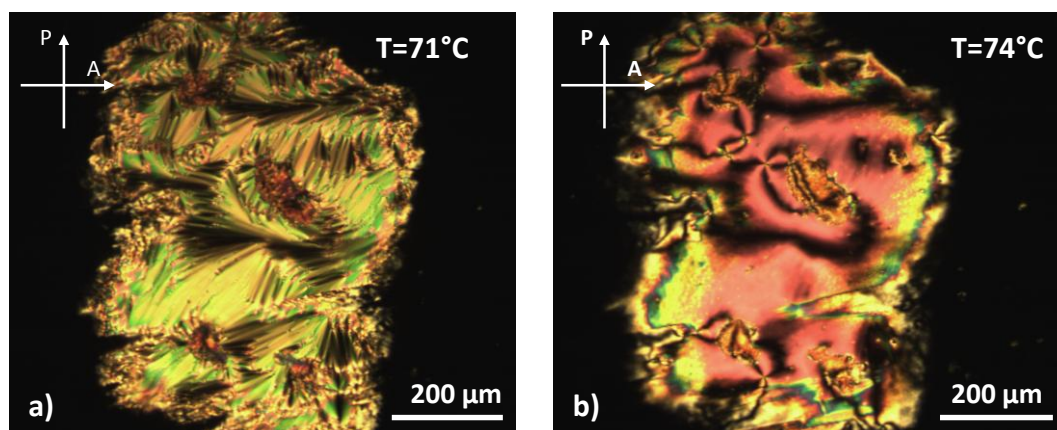


Figure 108: Textures of compound 97 obtained by OPM.

When observed under crossed polarizers, compound **97** showed some birefringent areas in a black surface. This homeotropic alignment together with Figure 108 a) suggests the

existence of a SmA phase. The existence of the long alkenyl chain in compound **97** allows the molecules to have more freedom, favouring the existence of the nematic phase, albeit over a narrow temperature range.

Compounds **98** and **99**, with shorter alkenyl chains have monotropic mesophases, assigned by OPM as being nematic, as shown in Figure 109 and Figure 110, respectively.

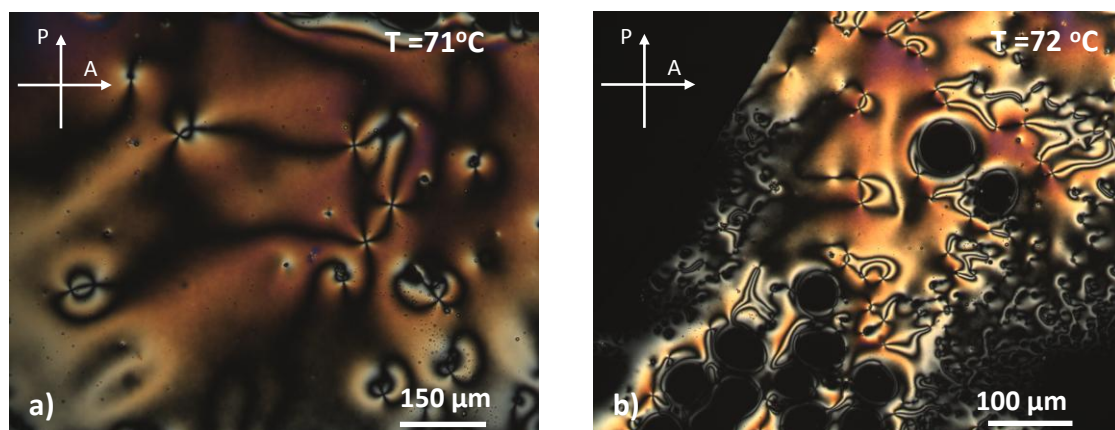


Figure 109: Schlieren texture obtained by OPM for **98**.

The texture obtained for compound **98** and shown in Figure 109 were identified as a Schlieren texture, indicating the existence of a nematic phase. Relatively to compound **99** the texture shown in Figure 110 a) is a marbled texture with Schlieren features and Figure 110 b) shows nematic droplets associated with the appearance of the nematic phase.

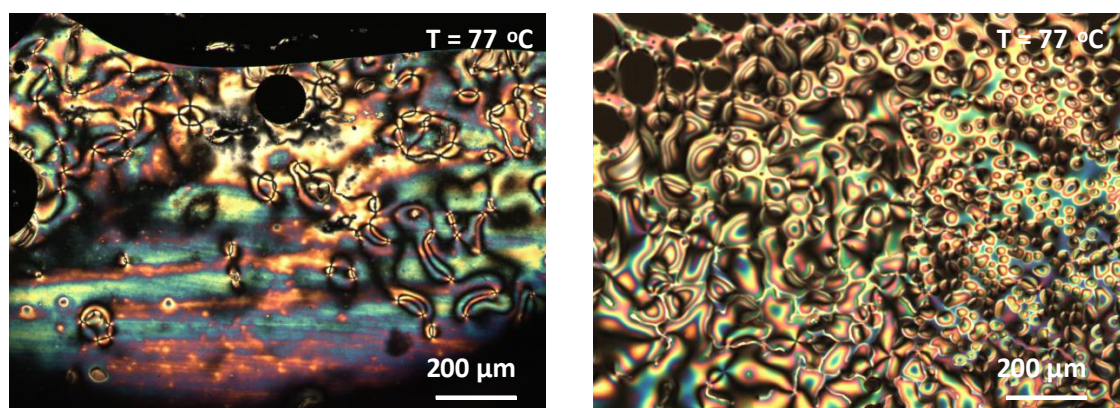


Figure 110: OPM textures of compound **99**.

Compound **103**, that has a similar alkenyl chain as **99** but an extra benzyl ester unit, shows an extremely wide mesophase (see Figure 111 - 1st heating curve). This could be due to the fact that the extra benzoate group disturbs the packing of the molecules, allowing the formation of a mesophase. Compound **103** shows an N-Iso transition at

267 °C. DSC curves show a decrease of almost 100 °C of the peak corresponding to the N-Iso transition together with a broadening of the peak.

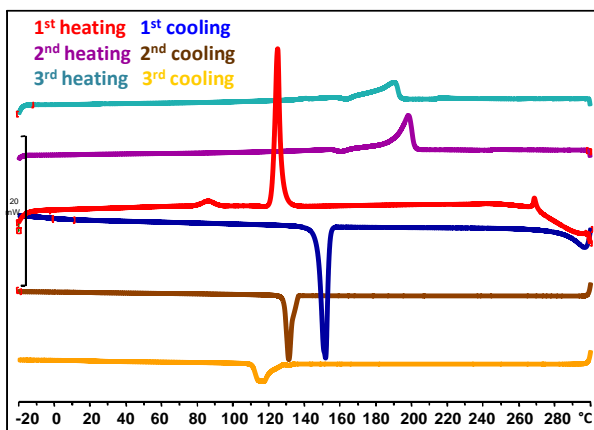


Figure 111: DSC curves for compound 103.

Considering that the N-Iso transition occurs at 267 °C, degradation of the molecule is likely to occur. When observed under OPM, a nematic phase was observed characterised by the marbled texture shown in Figure 112 a) and b)

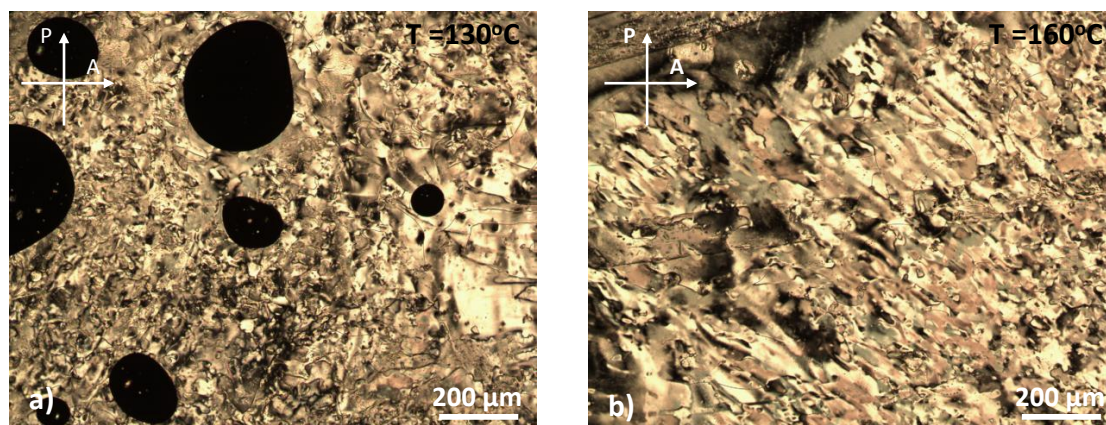


Figure 112: Texture obtained by OPM for compound 103. a) Marbled texture at 130°C. b) Marbled texture at 160 °C.

In terms of liquid crystalline properties of this series of biphenyl molecules, long chains favour enantiotropic LC behaviour. The fact that **98** and **99** did not show smectic behaviour was surprising; however they do show monotropic nematic phases.

7.4 Liquid crystalline properties of POSS derivatives

The liquid crystalline properties of POSS derivatives will be discussed on the basis of the textures obtained by OPM and the transition temperatures obtained by DSC. The effect on liquid crystalline properties between POSS derivatives with a single mesogen and the materials synthesized using a co-mesogen approach will be investigated, furthermore the influence on the liquid crystalline behaviour of the ratio between co-mesogens will be discussed.

SERIES I

Comparing **104** with the pure mesogen, compound **96**, it is evident that the nematic mesophase is retained. It is known that siloxane units decrease transition temperatures and in this case, this was confirmed as the clearing point decreased by approximately 40 °C. However instead of a crystalline phase at low temperatures a glass transition occurred. DSC studies were performed on this material, and some of the results obtained are shown in Figure 113. The first and second DSC curves were collected using a heating rate of 10 °C/ min. and the 3rd curve was collected at a heating rate of 2 °C/min.

The curves shown in graph b) were collected with a heating and cooling rate of 10 °C/min, but they appear quite different than the ones referred to above. This difference could be related with the amount of sample used since in the plots Figure 113 a) the amount of sample used was 5.37 mg and in the plots in Figure 113 b) was 3.6 mg.

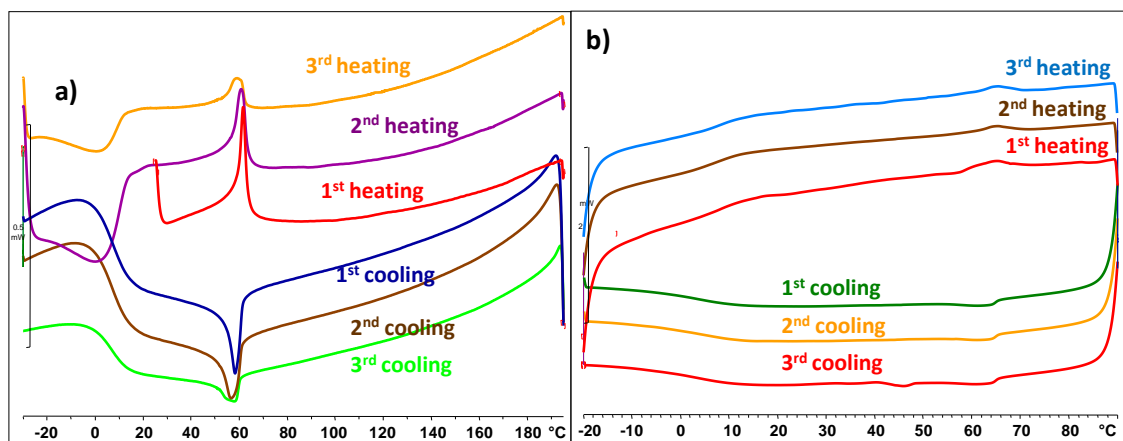


Figure 113: DSC curves of 104: a) sample weight 5.37 mg, and heating/cooling rates of 10 °C/ min for curves 1 and 2 and 5 °/min in curve 3. b) sample weight 3.6 mg, and heating/cooling rates of 10 °C/ min for all the curves.

In Figure 114 plots a) to c) are the DSC curves collected for open pan systems, varying the heating/cooling rates from 2 °C min⁻¹ in plot a); 10 °C min⁻¹ in plot b) and 20 °C min⁻¹ in plot c). The first observation is that the glass transition is much better defined in plot b). In plot a), the base line has an angle that seems to decrease with the increase in the heating rate. Regarding the clearing point, in this plot on the heating cycles it seems that there is a splitting in the peaks related with N-Iso transitions yet this feature is not observed in the cooling cycles or in fact in any of the other experiments (plots b) and c)). In the latter ones the shape of the peak associated with Iso-N transition resembles a glass transition however this is attributed to the fact that the baseline is not levelled, as discussed before. This is not uncommon for high molecular weight materials such as polymers and elastomers, as the silsesquioxane derivatives have much higher molecular weight than the average liquid crystalline mesogen, this observation as well as a broadening of the peaks was not surprising. Taking into consideration that there is the possibility of polydispersity of the materials, which increases with the synthetic approach of making use of co-mesogens, it is not surprising that in terms of thermal behaviour these compounds will resemble polymeric systems.

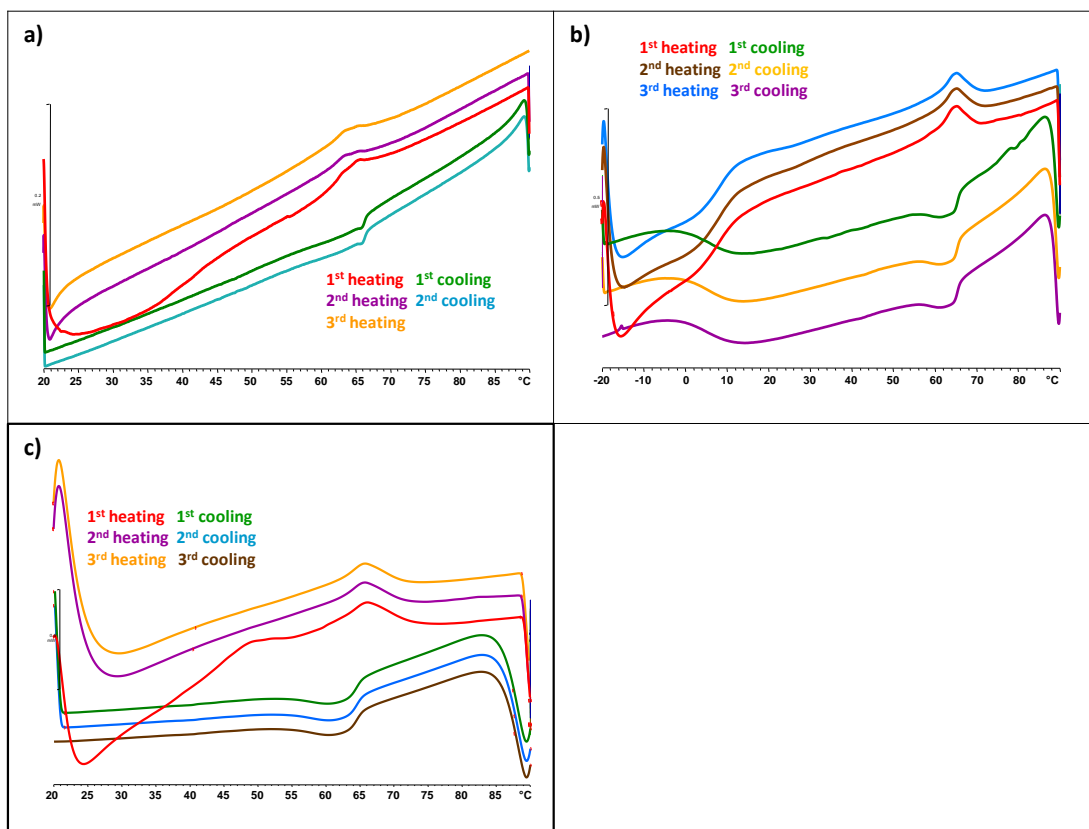


Figure 114: DSC curves for 104. The same sample was subject to different cooling rates. a) 2 °/min, b) 10 °C/min and c) 20 °C/min.

In order to investigate if the DSC curves obtained previously could be improved; the experiments described above were repeated using closed pan systems, the results are depicted below.

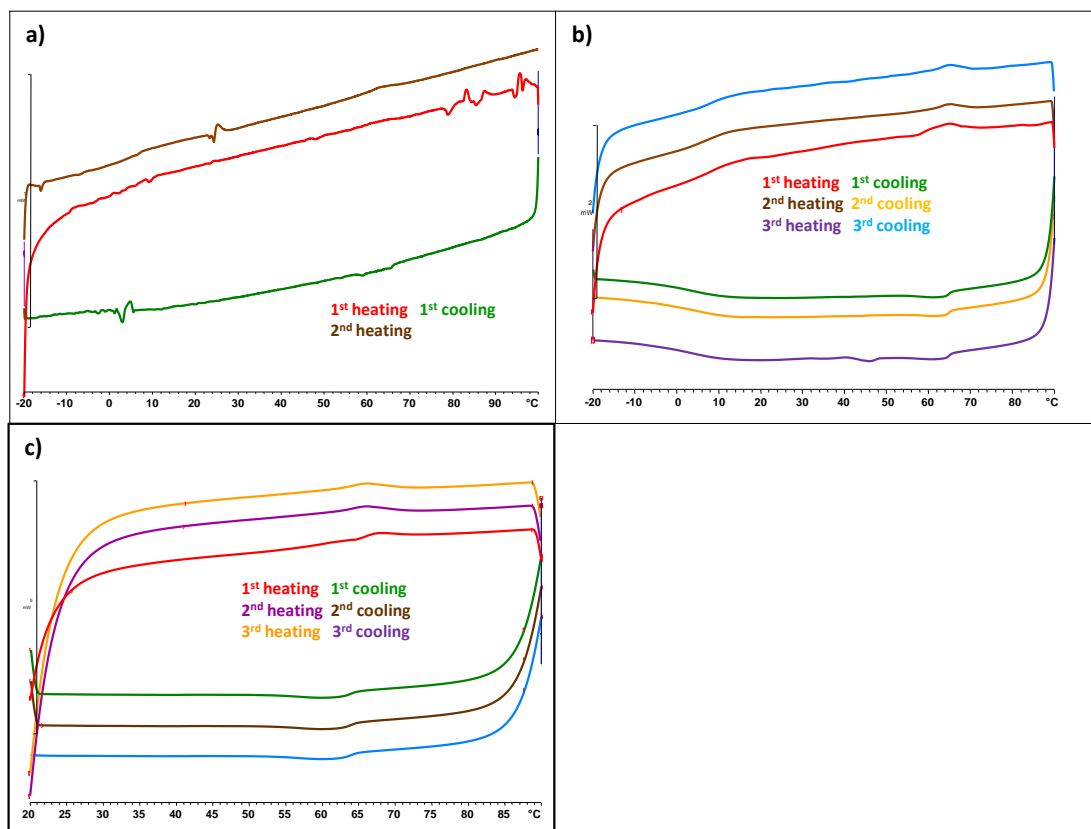


Figure 115: DSC curves for 104. Experiments made using a open pan system and different heating/cooling rates were used. a) 2 °/min, b) 10 °C/min and c) 20 °C/min.

Initial observations are that the base line seems to be more horizontal and that as before the best heating/cooling rate seems to be 10 °C min⁻¹. In plot, Figure 115 a), the two heating curves are quite different and not very smooth, several peaks can be observed but it is difficult to relate them with the transition temperatures observed by OPM. Yet considering all the data discussed so far, and especially the curves shown in Figure 115, these peaks are much more likely to be artifacts from the slow heating/cooling rate used. The enthalpy values as well as the transition temperatures are depicted in Table 10 and the values are from the second heating.

OPM micrographs in Figure 116 show a marbled texture and thread features. Figure 116 c) and d) show the texture of this compound after shearing. These materials, contrary to low molecular mass mesogens are very viscous.

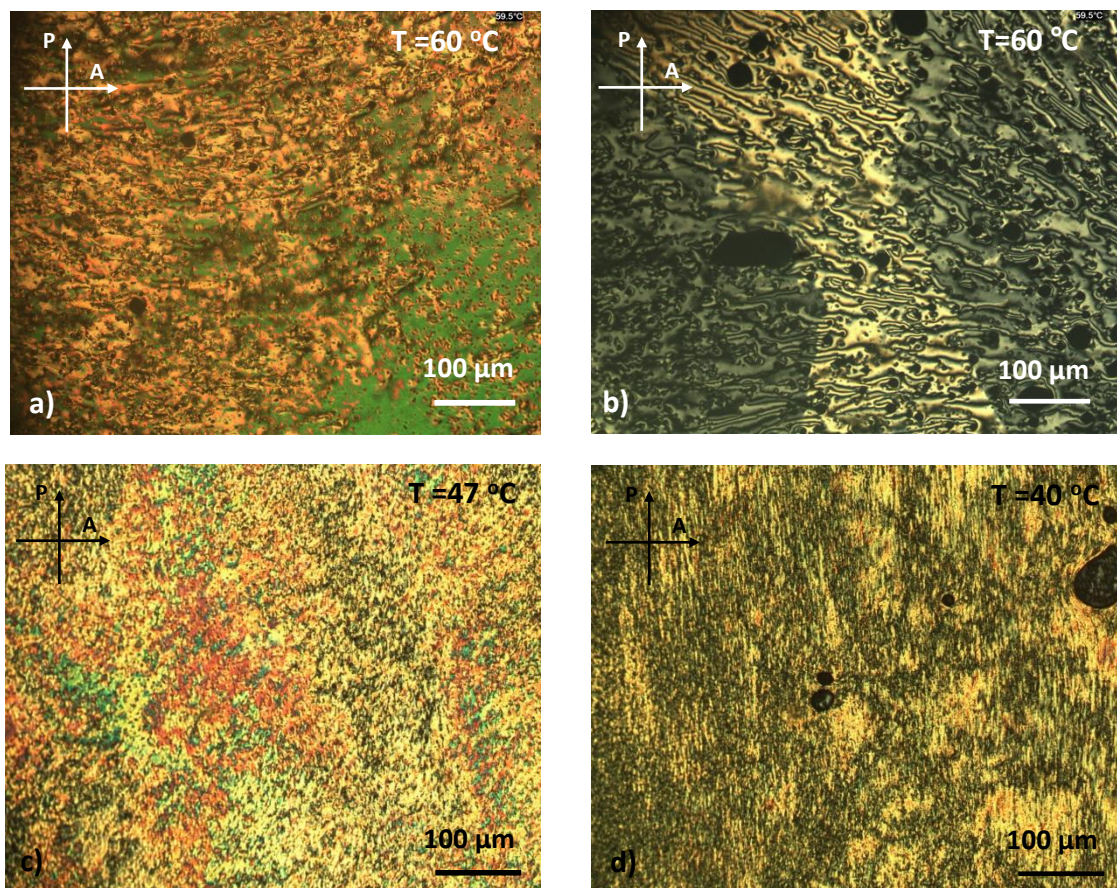


Figure 116: Micrographs of the nematic phase of **104**. a) marbled texture; b) marbled texture with Schlieren features; c) and d) marbled texture after shearing.

Compounds **106** and **107** have the same composition as described before, two co-mesogens in a ratio of approximately 4:4 of **96** and **97**. These compounds show similar liquid crystalline properties therefore, only **106** will be discussed in detail. The DSC and POM are described next.

Figure 107 shows the nematic phase of **106**, in a) a marbled texture with some Schlieren-like features on the edge of the sample. b) A marbled texture with some thread features can be observed, c) after the sample being sheared, the marbled texture is still visible, and finally d) was taken at a lower temperature and we can see the total recovery from the marbled texture.

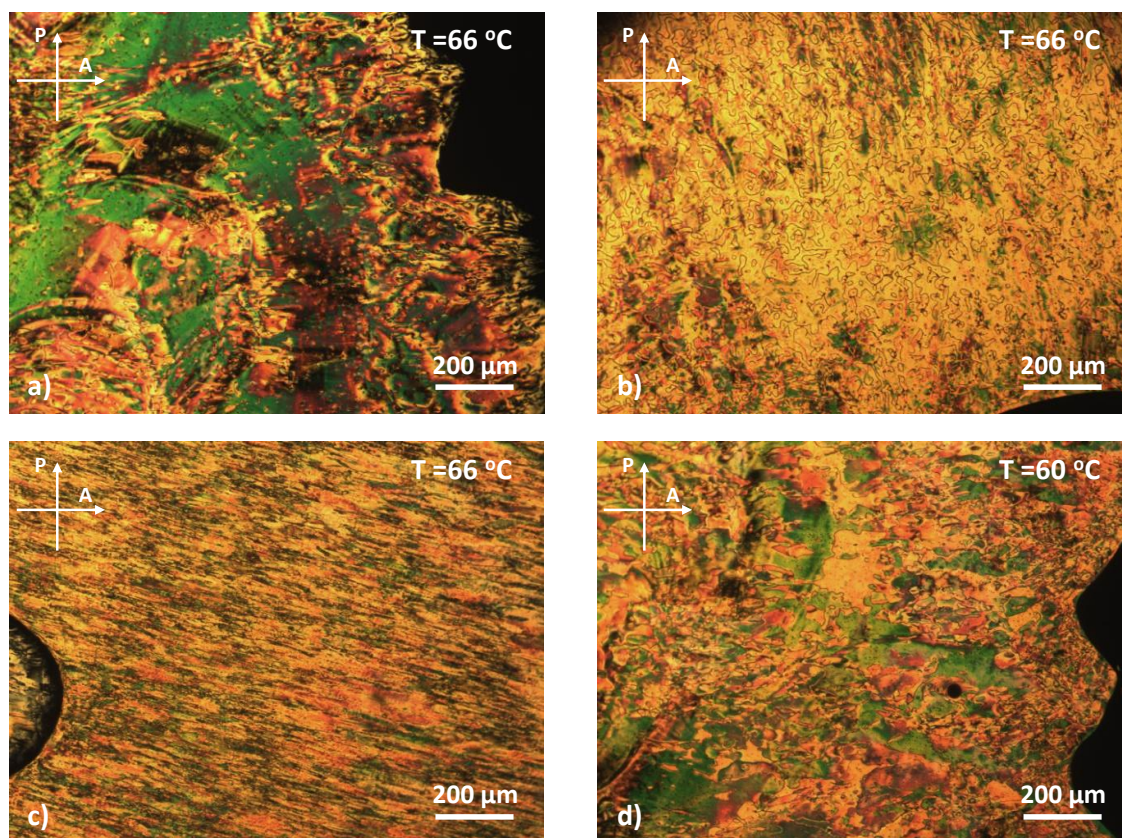


Figure 117: Micrographs of the nematic phase of 106.

The DSC results are presented in the Figure 118 below. The curve shows that isotropization occurs at 62.3 °C and the associated $\Delta H = 1.61 \text{ Jg}^{-1}$, is typical of the values for a nematic isotropic transition. The glass transition temperature decreased, when compared to **104**, with the addition of cyanobiphenyl **97**. Despite the sharp peak present in the DSC curve, when observed using POM the mesophase is observed above the transition temperature associated with the N-Iso transition, a marbled texture was observed at temperatures 10 °C above this temperature.

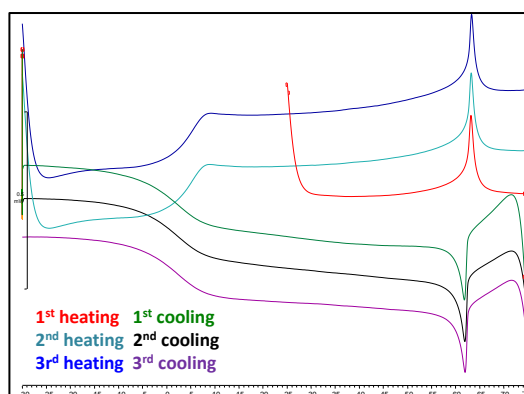


Figure 118: DSC curves of compound 106.

For **105** the amount of cyanobiphenyl was increased and the proportion of the mesogens was approximately 3:5 (mesogen **96**: mesogen **97**). POM studies reveal a marbled texture. The textures were observed well above the isotropization temperatures when very slow cooling rates (between 0.2 and 1 °C) were used. It should also be mentioned that there is a difference between the values obtained by DSC for the transition temperatures on heating and cooling where the latter is higher (≈ 68 °C on cooling vs. 61 °C on heating). So despite being unexpected, the observation of liquid crystalline textures above the clearing temperature considered by DSC seems to be a feature of these systems. It was also observed that the clearing points of the materials observed by POM are usually 10 °C higher than the ones collected by DSC. This could be related with the viscosity associated with these materials so even though the isotropization begins, this process is not immediately complete taking a few degrees for this to be observed in the entire sample. Another surprise was the fact that even though isotropization of the samples was achieved, no birefringence is observed using polarized optical microscopy with cross polarizers. If the light was switched off and the materials left annealing for approximately 10 min a birefringent marbled texture appeared. This observation, despite being surprising, can be explained by the *cis-trans* isomerization that will occur when the light is switched off. When this occurs, the disorder induced by the *cis* isomers decreases and together with a cooperative motion effect promotes the appearance of the mesophase. The effect of the *trans-cis* isomerization on the N-Iso transition will be discussed in the next section.

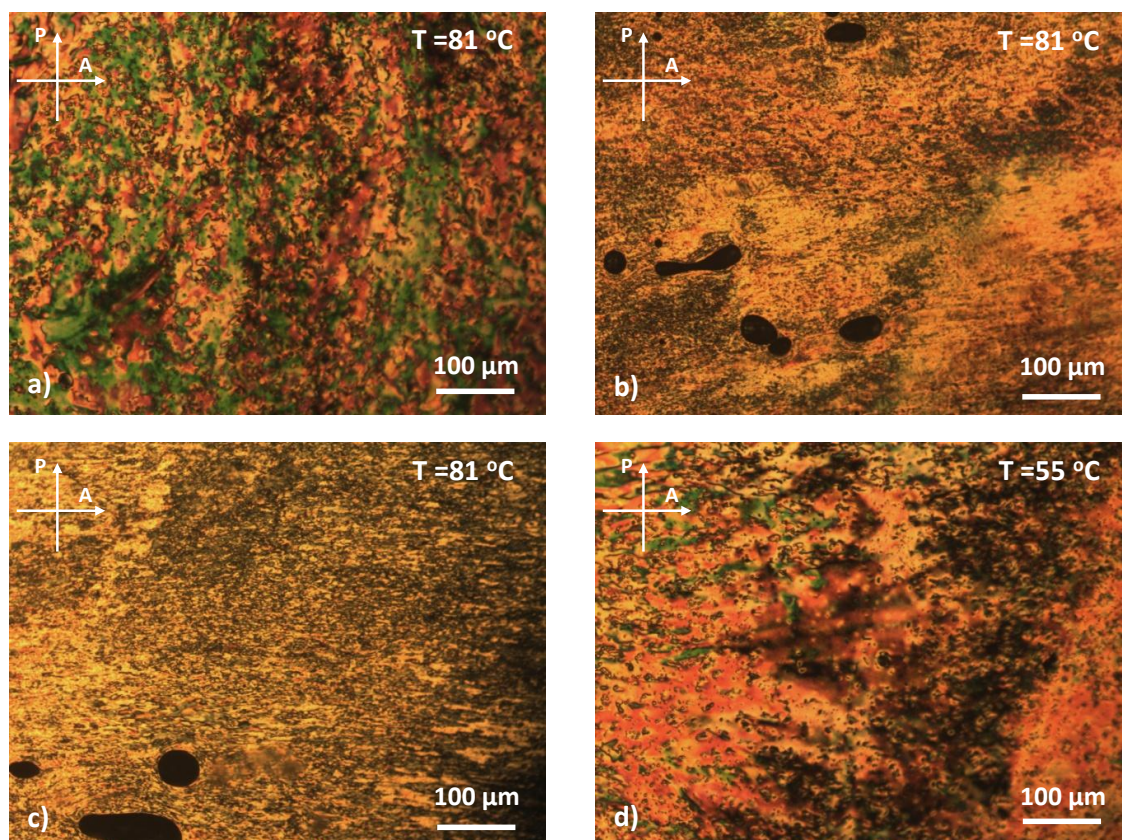


Figure 119: Micrographs of the nematic phase of 105.

In Figure 119 a) a marbled texture can be observed at 81 °C. As discussed before, the samples were left annealing and the appearance of a texture occurred during this annealing procedure. Micrographs b) and c) show the sample after shearing; it is possible to see the direction of shearing by a stretch observed in the texture. Micrograph c) shows signs of isotropization. Figure 119 d) shows once more, a marbled texture obtained after annealing the sample at 55 °C, clearly in the mesophase, considering the transition temperatures for the Iso-N transition collected by DSC.

Finally in this series of materials the liquid crystalline behaviour of compound **108** where the silsesquioxane core is fully substituted by mesogen **97** will be discussed.

The absence of azobenzene mesogen changes drastically the liquid crystalline behaviour, although a glass transition is still present, only a smectic phase is observed.

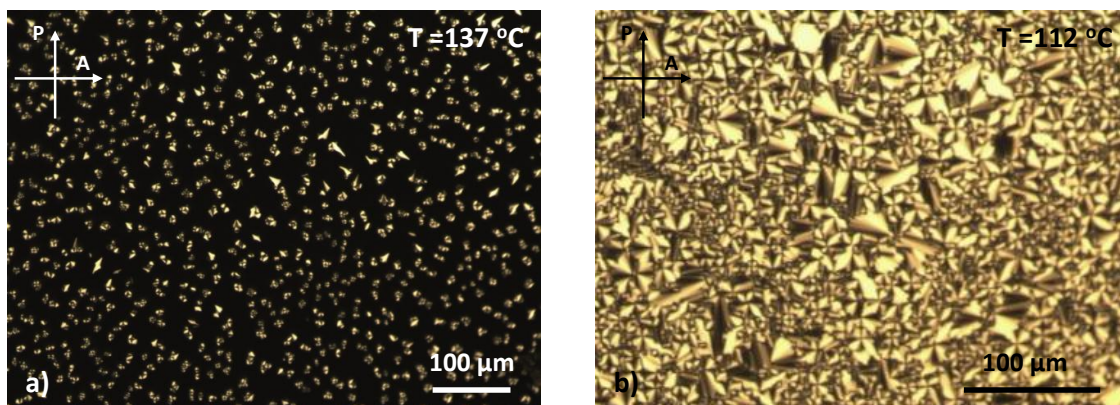


Figure 120: Micrographs of the smectic phase of 108.

In Figure 120 a) the appearance of bâtonnetes in the isotropic melt and b) a mixture of fan-shaped and focal conics can be observed. The temperatures for the phase transition obtained by DSC experiments are 127 °C and the associated enthalpy is 9.25 Jg^{-1} .

SERIES II

OPM studies for compound **109** were carried out and the same marbled texture was obtained. In Figure 121 some micrographs taken in the mesophase are shown.

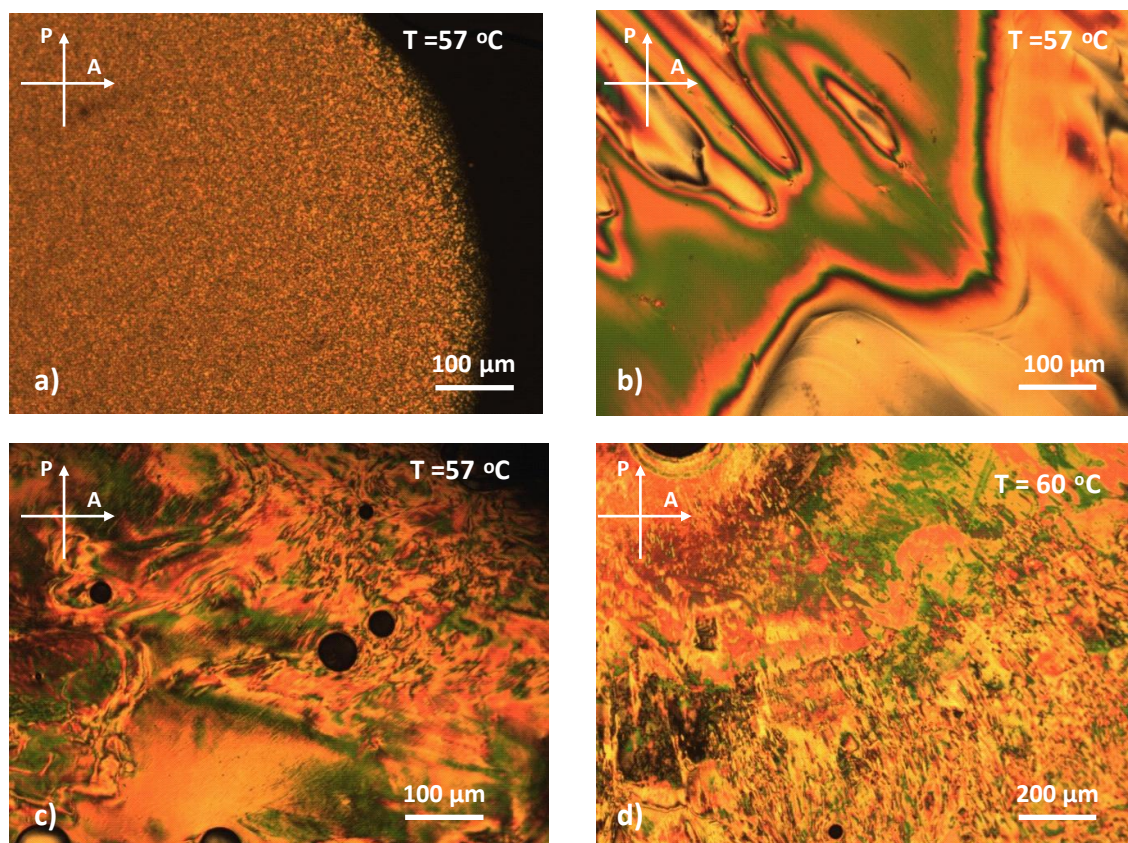


Figure 121: Micrographs of the nematic phase of compound 109.

Micrograph a) was collected on cooling just below the Iso-N transition and it shows a birefringent texture for compound **109**. The texture is very small and therefore difficult to identify. However after shearing the sample, plates b) and c) were collected. In both pictures we can see a marbled texture, characteristic of the nematic phase. Plate D) shows also a marbled texture with thread-like features.

The DSC curve for this compound resembles the one shown for **106** (Figure 118) and the transition temperatures collected from the second heating are for the glass 10 °C and for the N-Iso transition 50 °C. The enthalpy value associated with this transition is 1.34 Jg⁻¹ which is within the range of N-Iso transition enthalpies.

OPM studies of compound **110** were carried out. The compound showed a marbled texture as shown in Figure 122 a). In Figure 122 b) a marbled texture after shearing can be observed, characteristic of the nematic phase.

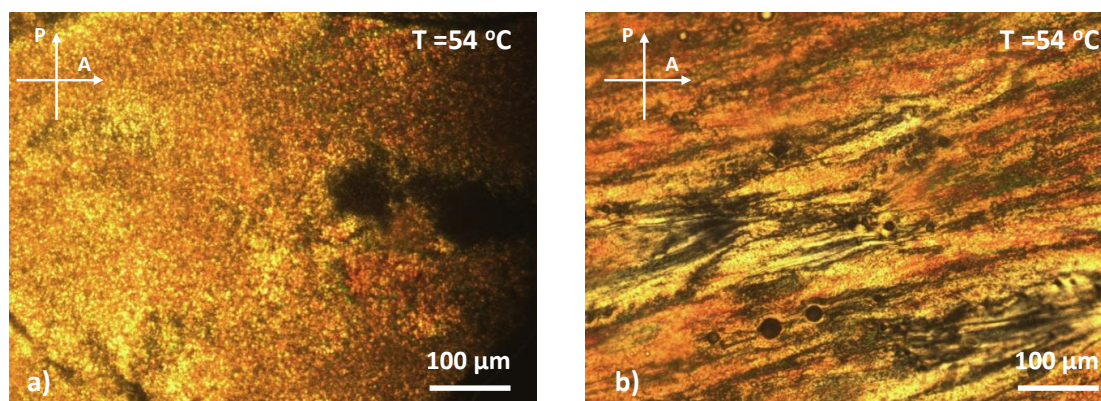


Figure 122: Micrographs of the nematic phase of **110**.

The DSC results show a mesophase between 18 °C and 57 °C the enthalpy for the N to I transition is 0.57 Jg⁻¹), characteristic of the nematic to isotropic transition.

The final compound of this series, compound **111**, corresponds to the silsesquioxane which is fully substituted with cyanobiphephenyl having a pentyl spacer.

This compound shows monotropic liquid crystalline behaviour as shown in the DSC curves (Figure 123). The melting occurs at 140.8 °C ($\Delta H_{\text{trans}} = 8.15 \text{ Jg}^{-1}$). On cooling the transition temperature from the isotropic to the mesophase is 127.9 °C and the enthalpy measured for the transition is 5 Jg⁻¹.

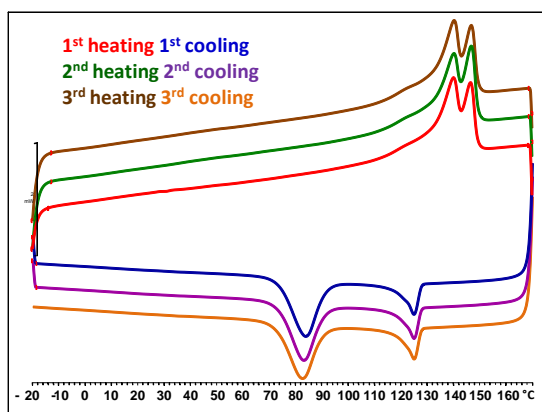


Figure 123: DSC curves of 111. Heating/cooling rate is 10 °C/min.

OPM studies were carried out and in Figure 124 the textures obtained are shown. Micrograph a) shows the formation of focal conics, in micrograph b) a fan-shape focal conics texture can be observed. The assignment of the mesophase by means of OPM and DSC is not conclusive since the focal conic texture can be present in both SmA and SmC phases. XRD experiments were necessary to confirm the phase structure of these compounds and this will be discussed in detail.

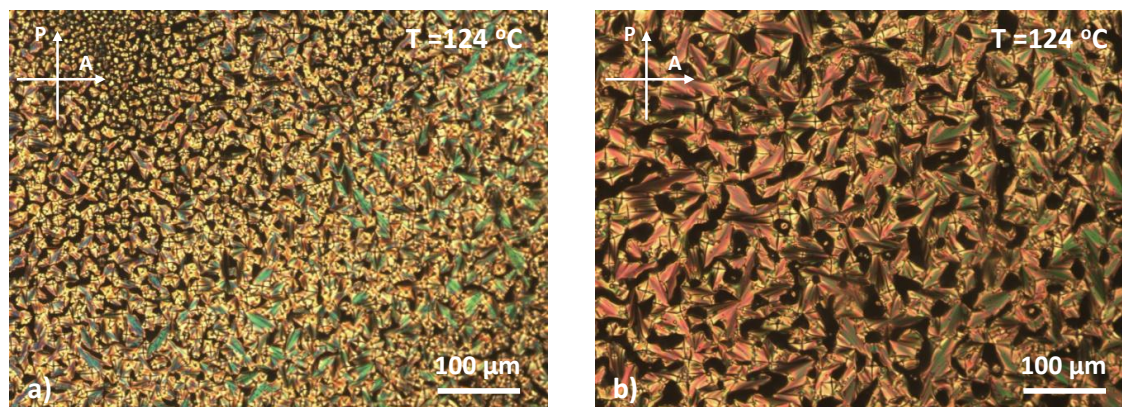


Figure 124: Micrographs for 111.

SERIES III

The polarized optical microscopy studies carried out on compound **112** were surprising. After heating the compound past the clearing point and cooling into the mesophase this compound showed homeotropic alignment, as shown in Figure 125 a). In this image some birefringence mainly at the air interface can be seen, in the bulk of the sample a black texture is present. In order to try to acquire more information about this mesophase texture, the sample was sheared. The marbled texture formed is depicted in

Figure 125 b). Due to the existence of a glassy state and viscosity of the materials, this texture remained. Figure 125 c) and d) show also marbled textures. This texture is retained until the material is heated again past the isotropization temperature.

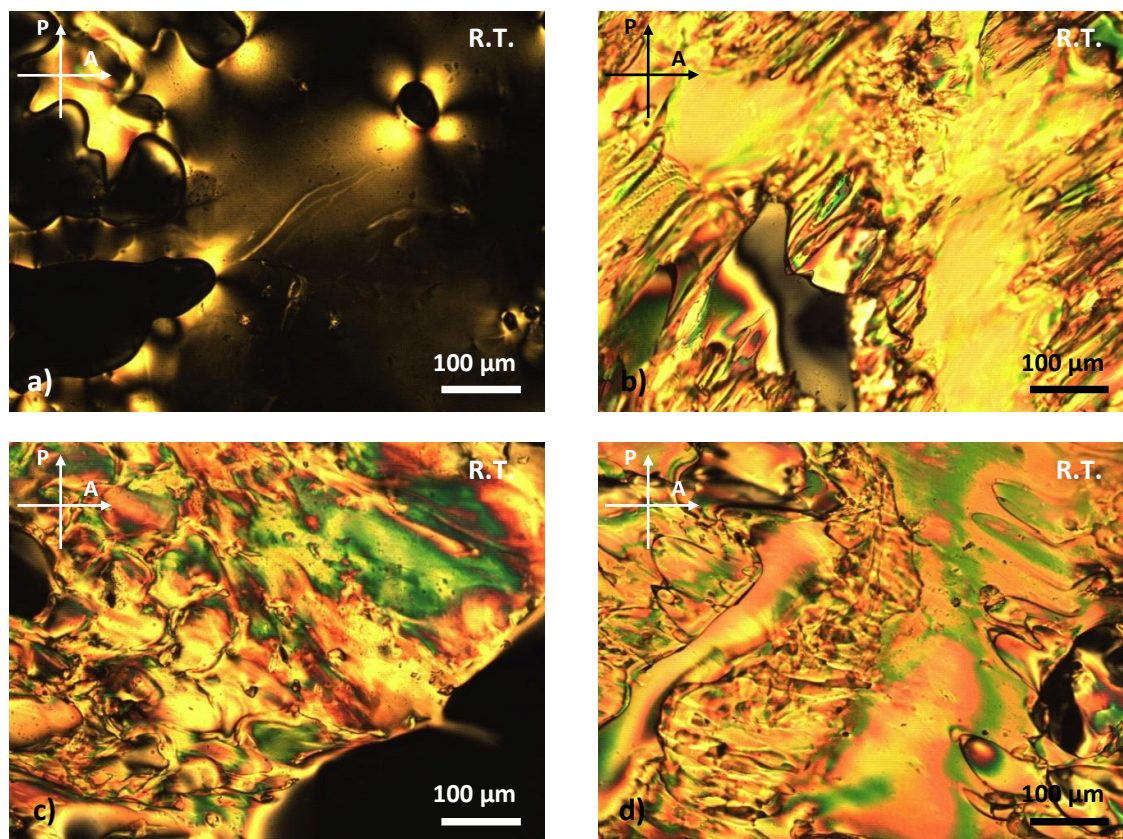


Figure 125: OPM textures for compound 112.

The DSC curves are shown in Figure 126. When compared with those collected for compound **106** and depicted in Figure 118, the main difference is the size of the peak corresponding to N-Iso transition. The temperature associated with this phase transition is 37.0 °C and $\Delta H_{\text{trans}} = 0.43 \text{ Jg}^{-1}$. The glass transition temperature is 19.5 °C.

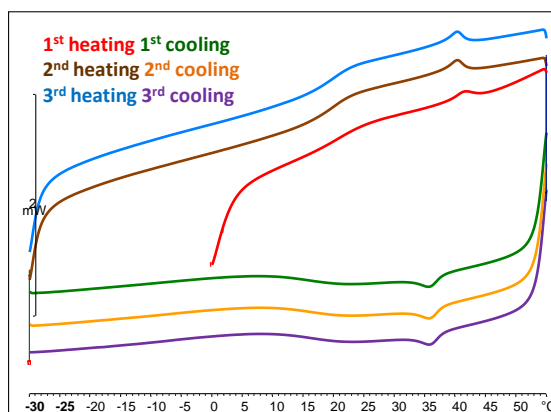


Figure 126: DSC curves for compound 112.

The micrographs obtained for **113** during OPM studies are shown in Figure 127. In micrograph a) a homeotropic alignment can be seen with birefringence only in the air-liquid crystal interfaces. When the sample was sheared, birefringence in the bulk of the sample was observed as shown in Figure 127 b), supporting the existence of a mesophase.

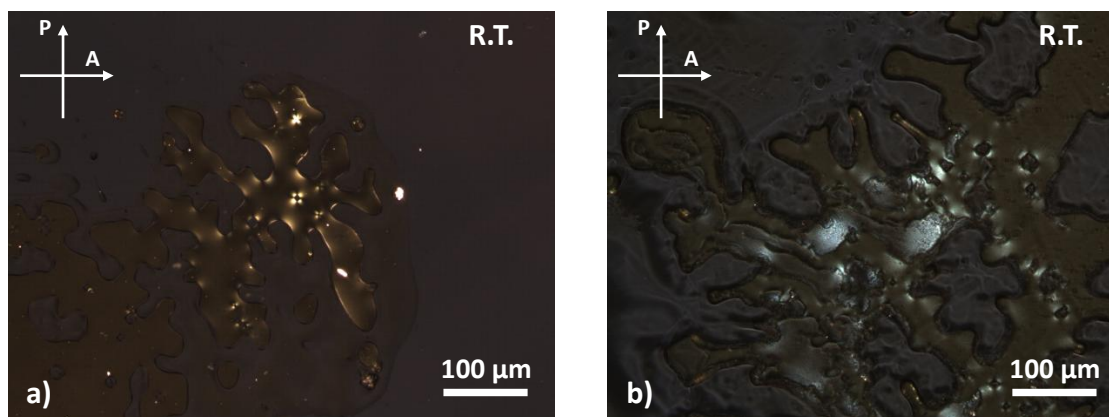


Figure 127: Micrographs obtained for 113 during OPM studies.

The DSC curves were collected until 170 °C and no peaks corresponding to a phase transition were observed, see Figure 128. The liquid crystalline properties of this material are not fully understood and investigations in order to clarify it are ongoing.

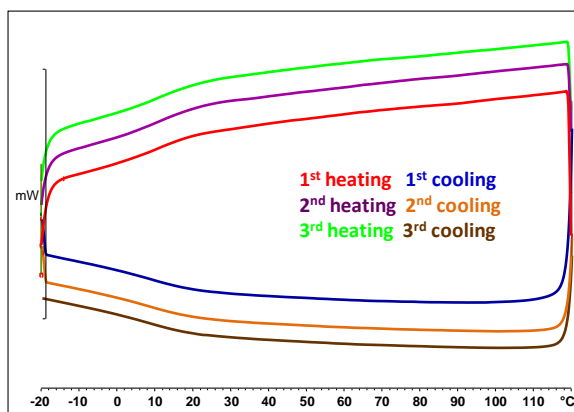


Figure 128: DSC curves for 113.

Compound **114** liquid crystalline behaviour was studied using OPM and DSC. The fan-shape texture shown in Figure 129 suggests that this material forms a SmA phase. The transition temperatures obtained by calorimetry experiments show a melting at 27.5 °C ($\Delta H_{\text{trans}} = 3.22 \text{ Jg}^{-1}$) and a clearing point at 117.4 °C ($\Delta H_{\text{trans}} = 2.99 \text{ Jg}^{-1}$). Surprisingly the peak corresponding to the isotropization is very broad and microscopy studies reveal that the complete extinction of birefringence occurs around 160°C. Considering the high viscosity of these materials, it is not unexpected that the isotropization range is quite large.

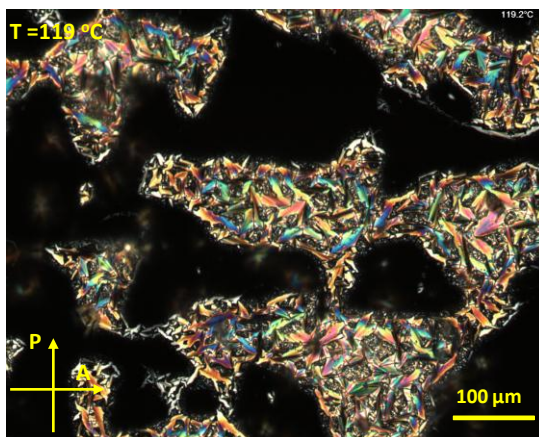


Figure 129: Texture observed with polarized optical microscope of compound 114.

As the clearing point is relatively high, it can be anticipated that some degradation starts to occur at high temperatures. This view is supported by a decrease in the transition temperatures in subsequent runs in which the transition temperatures corresponding to Iso-SmA phase are shifted to lower temperatures as shown in Figure 130.

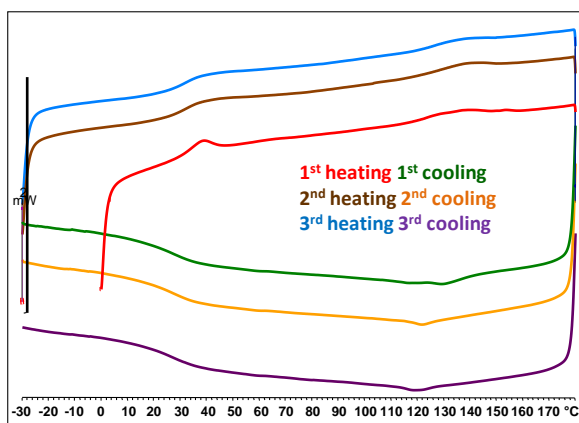


Figure 130: DSC curves for compound 114.

SERIES IV

In this series the main change is the increase in length of the aromatic core, as discussed in the synthesis section.

The textures observed for **115** using OPM, are presented in Figure 131. Micrograph a) and b) show a marbled texture and some thread-like features can be observed in micrograph a). In micrograph c) a stretched marbled texture can be observed, since these compounds are extremely viscous, the alignment induced by shearing is preserved and is shown in micrograph c). The micrograph shown in micrograph d) was taken at 87 °C after shearing. It is possible to see that the marbled texture is recovered after the sample was subject to shearing, yet some signs of the shearing direction are still present.

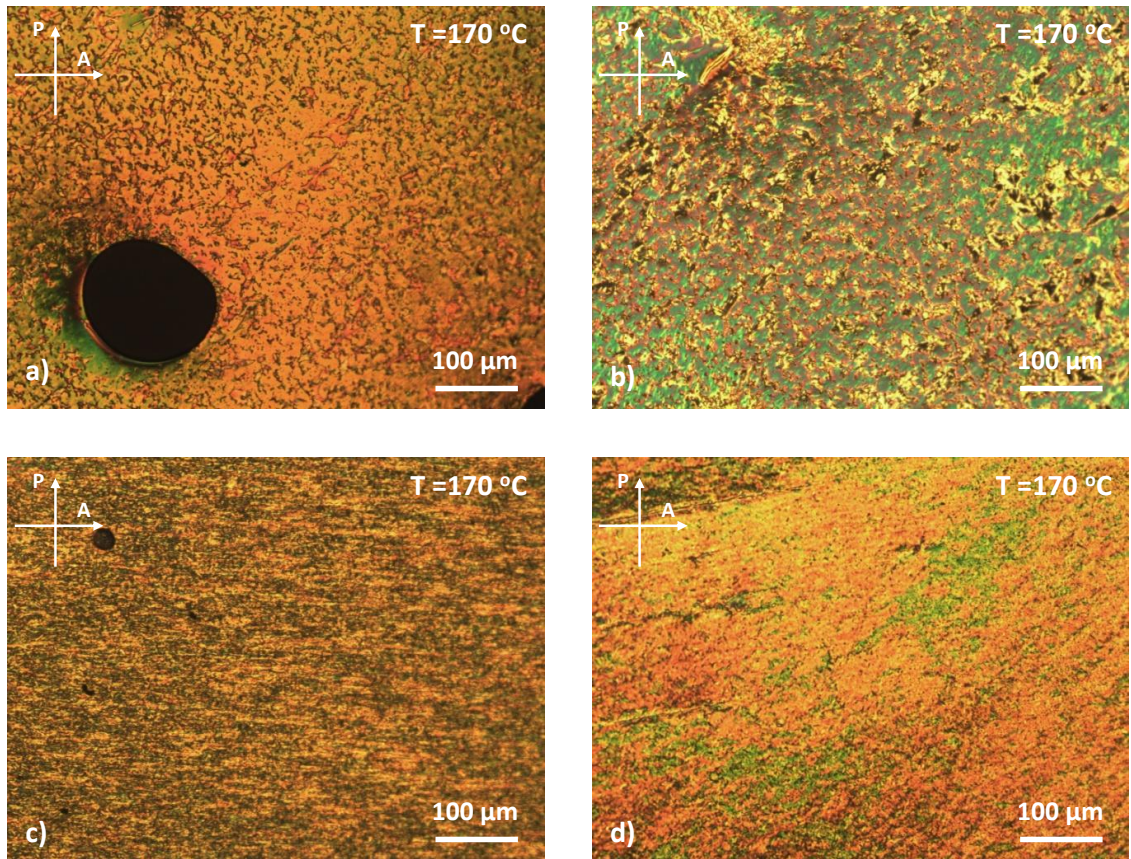


Figure 131: Micrographs obtained for 115 during OPM studies.

A notable result of the OPM studies is that the biphasic region is extremely wide. The material was heated up to 264 °C and even at that temperature some birefringence could still be observed as shown in the sequence of micrographs in Figure 132.

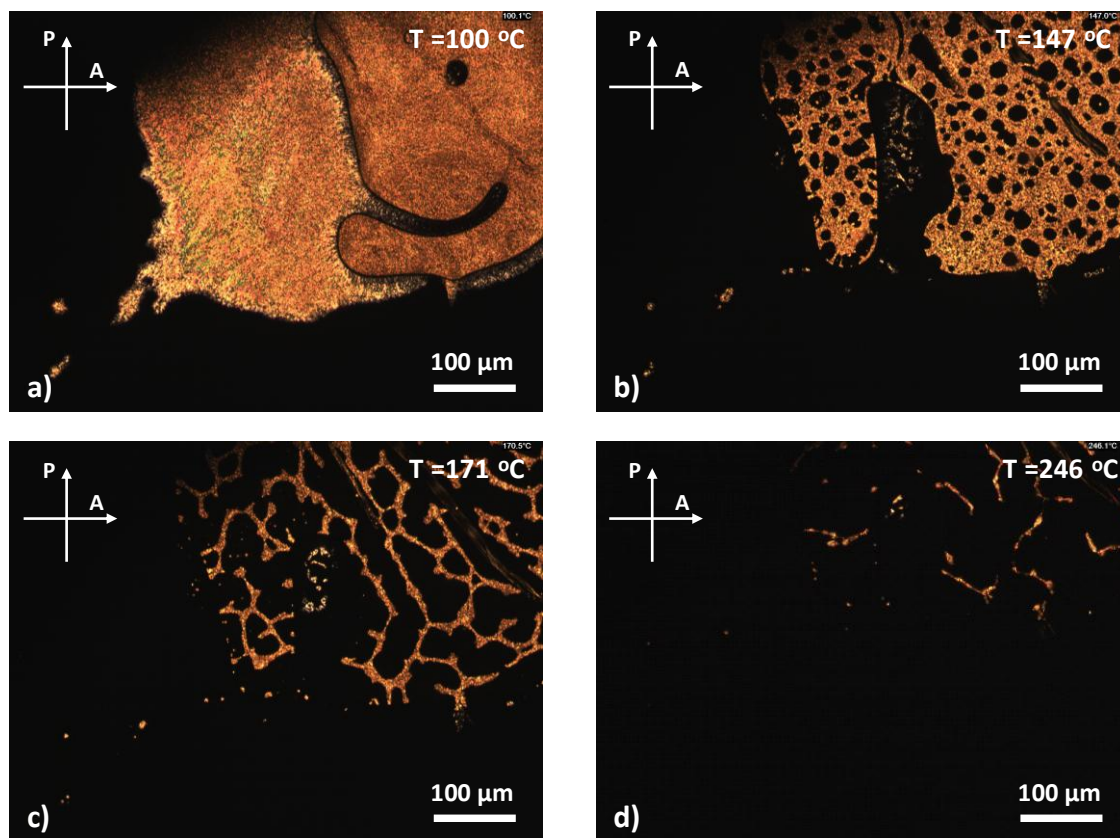


Figure 132: Micrographs of N-Iso transition 115.

Surprisingly, the DSC curves showed no peak associated with a transition temperature. Different heating/cooling rates from 10 °C min^{-1} to 30 °C min^{-1} were used, yet a transition peak could not be detected. The data collected with a heating/cooling rate of 10 °C min^{-1} is shown in Figure 133.

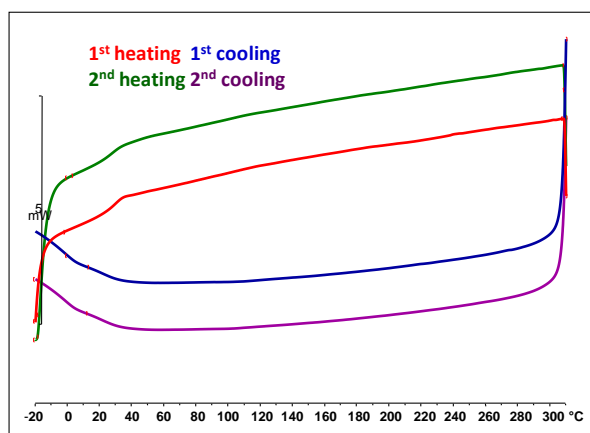


Figure 133: DSC curves of 115.

Compound **116** is characterised as being extremely viscous. In Figure 134, the texture of the mesophase is shown, at this temperature it is not possible to see the material flowing, as expected for liquid crystals, however the existence of birefringence points to

the existence of a mesophase. The compound was sheared and although this process was difficult, it is possible to see a change in texture and the shearing direction is very clear, plate b) Figure 134, supporting the existence of a very viscous birefringent fluid as in a liquid crystalline material. Initially the material was heated at very high temperatures but no isotropization was observed (contrary to what was described for **115** see Figure 132). The calorimetric experiments did not show the existence of a peak up to 190 °C. However it is possible that the clearing point of this material is out of the temperature range that could be investigated in the available equipment.

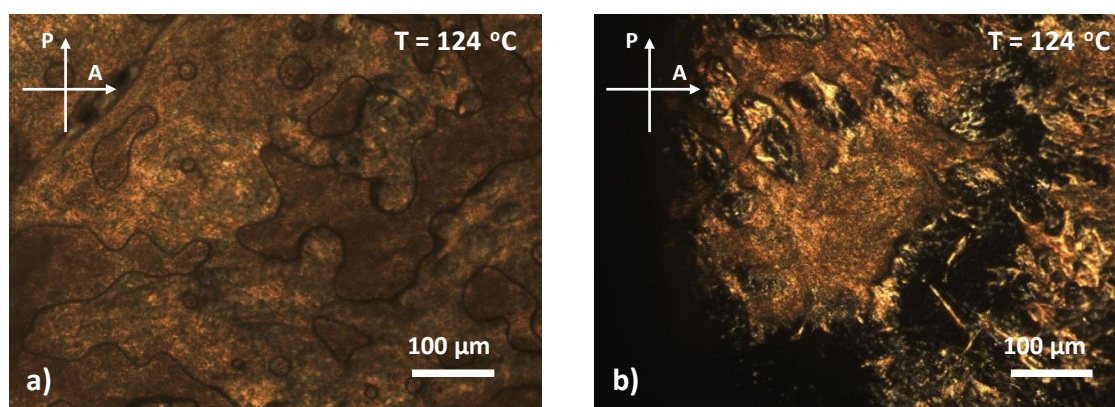


Figure 134: Micrographs obtained for 116.

The fact that the material is extremely viscous and the clearing temperature is very high made it impossible to obtain textures that would elucidate more information about the possible mesophase of this compound.

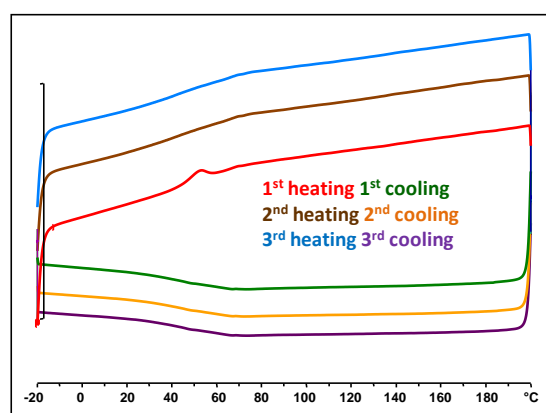


Figure 135: DSC curves obtained for 116.

Considering the above discussion on the liquid crystalline properties of these four series of compounds, some conclusions can be drawn. The table below (Table 11) summarizes the liquid crystalline behaviour of the materials discussed.

Table 11: Summary of the liquid crystalline properties of silsesquioxene derivatives 104-116.

	POSS derivative	Percentage of mesogens		Phase transition temperatures (°C)
		96	97	
	104	100	-	g (9) N (56) Iso
	105	39	61	g (2) N (63) Iso
Series I	106	52	48	g (4) N (62) Iso
	107	51	49	g (4) N (62) Iso
	108	-	100	g (-2) Sm (127) Iso
		96	98	
	109	64	36	g (8) N (52) Iso
Series II	110	25	75	g (17) N (58) Iso
	111	-	100	Iso (130) Sm (85) Cr
		96	99	
	112	43	56	g (20) N (37) Iso
Series III	113	45	55	g (10) N (310)* Iso
	114	-	100	g (31) Sm (121) Iso
		96	103	
Series IV	116	50	50	g (23) N (147)* Iso
	116	-	100	g 41

*Data obtained by microscopy since no other transitions were observed in DSC curves.

An initial aim of this work was to be able to synthesize LC materials which were photochromic, which had nematic mesophase with a glassy state at room temperature. These three characteristics, envision their investigation in terms of photoorientation and recording of surface relief gratings that will be discussed Part III of this discussion.

The four series of compounds discussed were synthesized in order to achieve a material that would combine the three properties mentioned above.

The first step was to synthesise a photochromic material, azobenzenes are very well known pro-mesogenic materials and are widely explored.

The design of compound **96** took into account the introduction of alkyl chains (Figure 136) that are essential to promote LC behaviour between 30 °C and 90 °C. The pentyl spacer used has two main features; the existence of a terminal alkene that enables the connection of this mesogen to the siloxane core **I** via a hydrosilylation reaction, and it also allows the decoupling of the mesogen from the central core preventing the formation of smectic phases. The attachment of laterally linked mesogens to the POSS core is known to induce nematic phases to organic-inorganic hybrid systems.

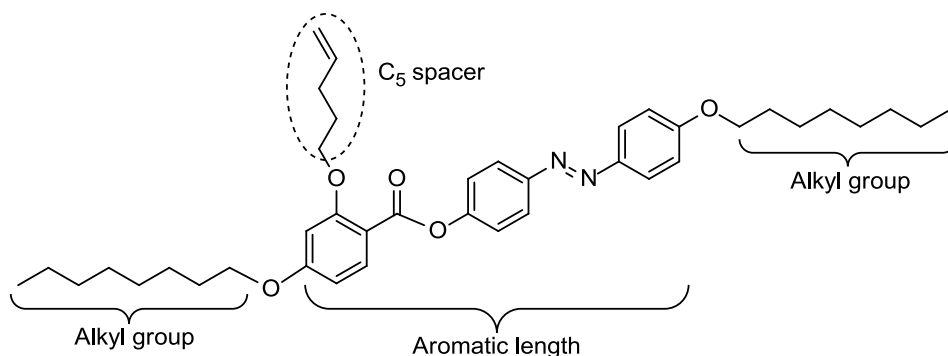


Figure 136: Compound **96**.

The silsesquioxane core chosen has the possibility of being substituted with eight azobenzene molecules in one single synthetic step, so in one molecule it is possible to have eight photochromic groups which suggests a fast response to light modulation. Silsesquioxane derivatives are also known by to have glassy states which become fundamental to record light induced changes.

The first organic-inorganic hybrid compound synthesised showed nematic behaviour, however the glass transition temperature was very low. In order to increase the glass transition temperature, cyanobiphenyl mesogens were also attached to the siloxane core. In POSS systems, cyanobiphenyls are known to show smectic phases due to their large terminal dipole, as reported by Mehl *et al.*,¹³⁶ where POSS derivatives using cyanobiphenyls with butyl, hexyl and undecyl spacers were reported.

The idea of adding a co-mesogenic group, resembling the synthesis of co-polymeric materials, combines the properties of both materials. Using this approach, it was expected that the addition of the cyanobiphenyl would increase the transition temperatures. Compound **108** was synthesized and used as a control. The results described in this thesis are in full agreement with the results previously reported. The undecyl spacer was initially chosen to prevent the formation of higher order liquid crystalline phases

Compounds with different proportions of **96** and cyanobiphenyl **97** were synthesised. The increase of the amount of **97** (compounds **105** and **107**) raises the nematic to isotropic transition temperature from 56 °C to 62 °C. The glass transition temperatures decreased with the introduction of mesogen **97**, from 9 °C in compound **104** to 2 °C in compound **105**. But if **105** and **106** (or **107**) are compared the increase in the glass transition temperature from 2 °C to 4 °C it is evident see Table 11.

Surprisingly, even with as much as 61 % of **96** attached to the POSS core (compound **105**), no smectic phases were found. This might suggest that the laterally linked mesogen **96** prevents the formation of higher ordered phases.

The introduction of mesogen **97** to increase the glass transition temperature was not successful. The decrease of the alkenyl chain length seemed to be a better way to increase the glass transition temperature; therefore the same methodology was used with mesogen **98**.

As observed for compound **108** the absence of azobenzene **96** leads to the appearance of smectic phases. Compound **111**, in contrast to all the other POSS derivatives synthesised has monotropic LC behaviour

Compounds **112** and **113** show very different liquid-crystalline properties even though the proportion of mesogens seems to be identical. Compound **112** shows a glass transition at 20 °C and an N to Iso transition temperature at 37 °C, while for compound **113** the glass transition temperature is at 10 °C and a extremely wide range mesophase is observed. At first glance these results seem to be inconsistent. GPC results for compound **113** show four different species, while compound **112** exhibits only two, which appears to demonstrate that these two compounds are in effect different mixtures. Finally, mesogen **103** was synthesised with an extra aromatic ring incorporated to give more rigidity to the molecule and promote higher transition temperatures. When only mesogen **103** was attached to the siloxane core, a glass transition of 42 °C was observed and no other phase transitions were observed. A 1:1 mixture of **96** and **103** exhibited the desired properties. A glass transition at 24 °C and an N to Iso transition temperature at 147 °C determined by microscopy was recorded. No endothermic peaks were observed in DSC curves even when the compound was heated up to 310 °C. This suggests a very low ordering of the nematic phase.

Contrary to what was expected, none of the POSS derivatives synthesised where azobenzene **96** was present showed higher ordered liquid crystalline phases. Apart from **113** where so far the mesophase exhibited was not identified, only nematic phase behaviour was detected.

In order to learn more about the thermal stability of these compounds, thermal gravimetric analysis (TGA) was undertaken.

TGA showed that the decomposition of compound **115** occurs in two regimes. The first one at 150 °C with 5% loss and a second one at 350 with 20% loss shown in Figure 137.

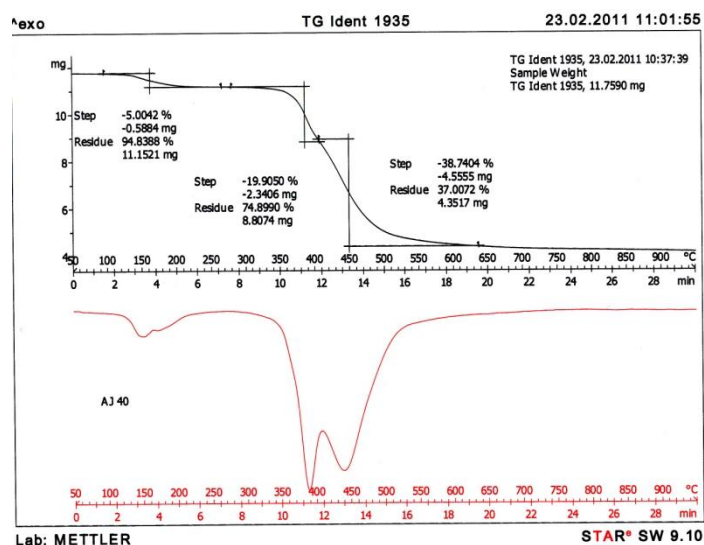


Figure 137: Thermal gravimetric spectra of compound 115. Analysis carried under N₂.

DSC samples were prepared using a solution in dichloromethane because the materials are very sensitive to static electricity. This involves evaporation of the solvent which was made using a hot stage. The samples were left at 70 °C for at least ten minutes. The 5% weight loss occurring at 150 °C could be due to degradation of N=N bonds although in polymers the correspondent temperature is of the order of 260 °C²⁹³. The ester bonds combined with aliphatic chains in polymers is described to be 370 °C.²⁹³ The results presented show that at 350 °C there is 20 % loss, leaving the siloxane core.

TGA results are not completely understood yet and further investigation has to be made.

7.5 Photochromic studies of the materials synthesized.

Isomerization of azobenzenes and their characteristics were described in the introduction. Since the materials synthesized are azobenzene derivatives, their photochromic behaviour was studied.

The first results discussed come from OPM studies. It was mentioned before how *cis-trans* isomerization could influence the Iso-N transition temperatures. With this set of experiments we wanted to quantify how much it was possible to decrease the N-Iso transition temperature. With this purpose in mind three compounds were investigated: **96** a low molecular weight azobenzene derivative, **104** silsesquioxane derivative fully substituted with **96** and finally **106** a co-mesogenic silsesquioxane derivative.

The samples were left annealing just below their clearing points, so that a good texture could be obtained. The sample was irradiated with the microscope light at maximum intensity. The irradiation period varied and lasted until the isotropic state was achieved or until no changes were recorded during a reasonable (≈ 1 h) period of time.

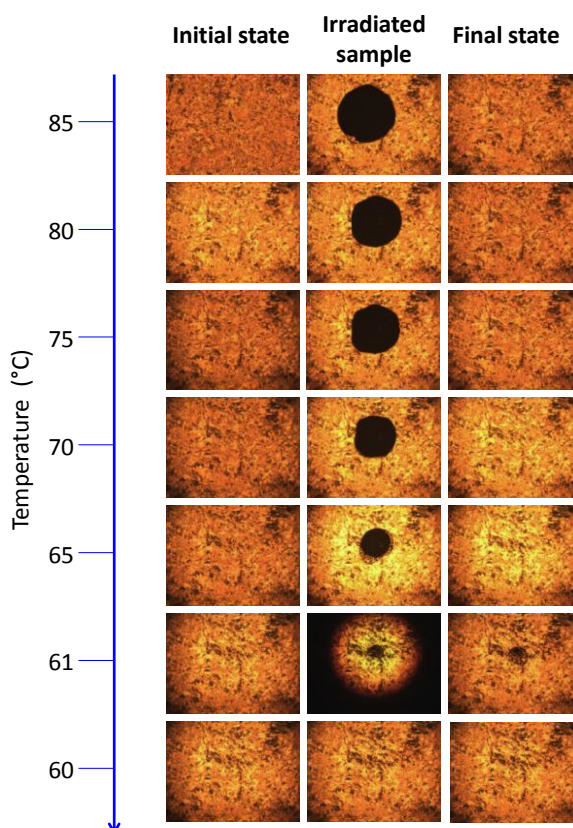


Figure 138: OPM images for irradiation of 96 with light.

In Figure 138 the results obtained for irradiation of **96** with the microscope light are presented. The initial state assumes that the nematic phase has completely recovered. The irradiation times, as mentioned before, differ according to temperature and the materials.

For the experiment related to the results shown in Figure 138, the average irradiation times for temperatures between 85 °C and 70 °C was 4 min. The recovery of the nematic phase, as demonstrated in the column final state, Figure 138, was approximately 7 min, for this temperature interval. Below 70 °C the isomerization of the sample becomes increasingly more difficult. At 65 °C and 61 °C the irradiation times were 17 min and 22 min respectively. The irradiation at 60 °C occurred for 1h 10 min and no isomerization occurred.

The N-Iso transition temperature was then decreased, for **96**, to 61 °C, this is 30 °C below the transition obtained in calorimetry experiments.

The same experiment was repeated for **104**. Because this compound has eight photochromic groups it was expected that the effect of *trans-cis* irradiation to be quite pronounced.

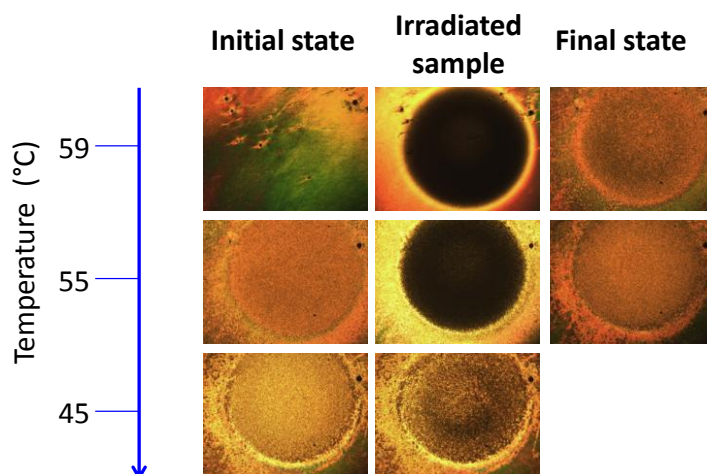


Figure 139: OPM images for irradiation of **104** with light.

The results obtained for **104** are shown in Figure 139. Isotropization at 55 °C is very clear yet at 45 °C this does not seem to be so prominent. There is a degree of *trans-cis* isomerization occurring thus the irradiated sample is more isotropic than the initial state. The irradiation at 45 °C occurred during 1h showing that the isomerization process at this temperature is rather difficult.

Despite the amount of photochromic groups, it was only possible to decrease the N-Iso transition by approximately 10 °C. This difficulty in isomerization of azobenzene

groups, could be associated with the high viscosity of these materials, despite being in the liquid crystalline state at 45 °C and isomerization occurring, the induction of isomerization by molecules in the *cis* state is hindered due to the lack of mobility, preventing cooperative motion and therefore, isomerization of a wider region of the sample.

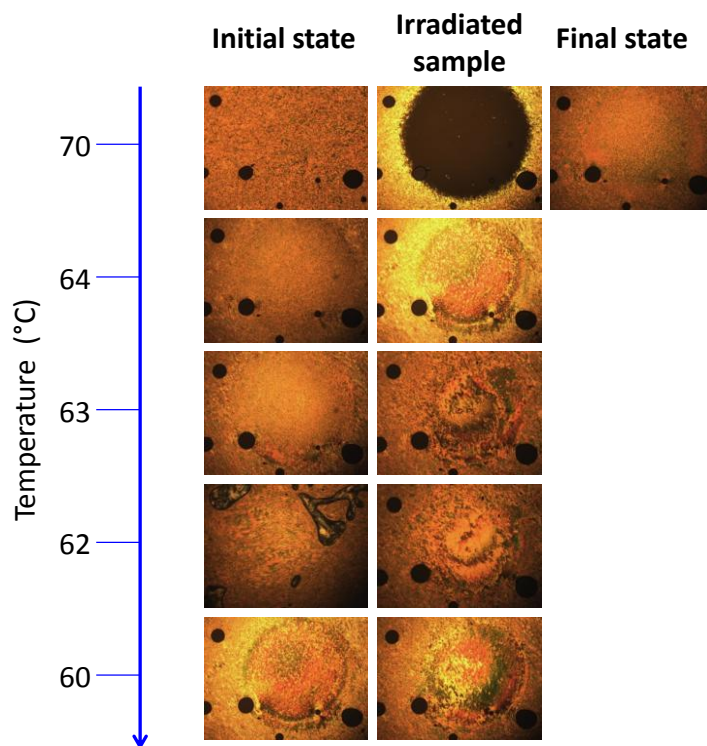


Figure 140: OPM images for irradiation of 106 with light.

Compound **106** has mesogens **96** and **103** in a 1:1 ratio, and the irradiation studies are shown in Figure 140. For this compound isotropization due to *trans-cis* isomerization becomes more difficult than the systems discussed before.

In fact in both silsesquioxane derivatives the N-Iso transition with light seems to occur for temperatures above the N-Iso transition temperatures detected by DSC. According to the DSC data, the clearing point of **106** is at 62 °C. Irradiation at this temperature seems to change the texture of the compound but not enough for isotropization to occur. The irradiation times for **106** varied from 3 min at 70 °C to 40 min at 62 °C. For the irradiation time minor changes are observed and no significant decrease in N-Iso transition temperatures could be observed.

To summarize, for silsesquioxane derivatives investigated the effect of viscosity suppresses the cooperative motion induced by *trans-cis* isomerization. Probably better

results would have been obtained if UV light of appropriate wavelength was used instead of actinic light.

The UV/Vis spectra for compounds **96**, **104** and **115** were recorded and will be discussed next.

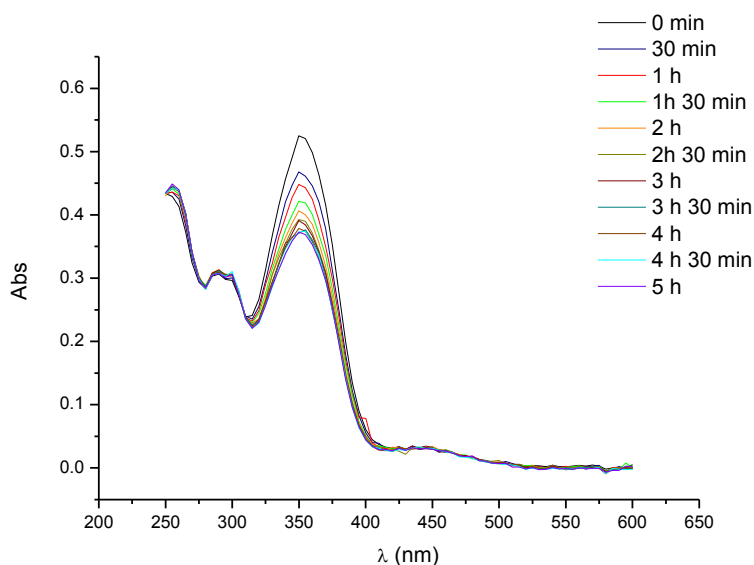


Figure 141: UV/Vis spectra of a solution of **96** in DCM, conc. $1.56 \times 10^{-4} \text{ mol dm}^{-3}$.

The samples were irradiated at 313 nm as this corresponds to the maximum intensity of the light source. The spectrum of compound **96** shows at $\approx 365 \text{ nm}$ the absorption band corresponding to $\pi\text{-}\pi^*$ electron transitions of the *trans* isomer which decreases with irradiation time as shown in Figure 141. The photostationary state is achieved after 3h 30 min. At $\lambda \approx 450 \text{ nm}$ there is a small band corresponding to the $n\text{-}\pi^*$ of the *cis* azobenzene chromophore. The initial state is recovered after the sample is stored in the dark for ≈ 48 hours.

The UV –Vis spectrum for **104** is shown in Figure 142 and is very similar to the one obtained for **96** as expected. The absorption maximum decreased slightly as the concentration of this solution is ten times smaller. The photostationary state is achieved after irradiation for ≈ 2 hours.

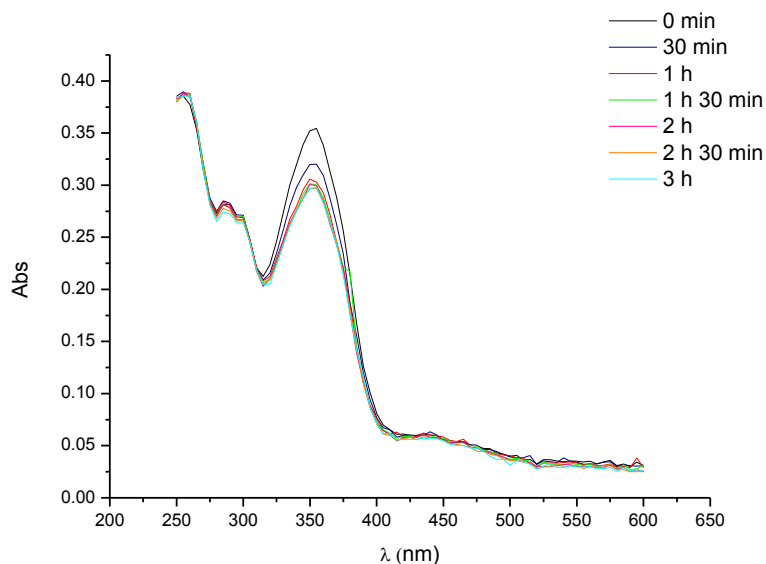


Figure 142: UV-Vis spectra of 104 in solution Under UV irradiation (313nm).

The spectrum obtained for **115** is quite different see Figure 143. The absorption of the band with maximum absorption at ≈ 275 nm is much higher. And the absorption corresponding to the π - π^* band is slightly less intense than the ones above. Which is related to the fact that molecule has only a 50% content of azobenzene materials.

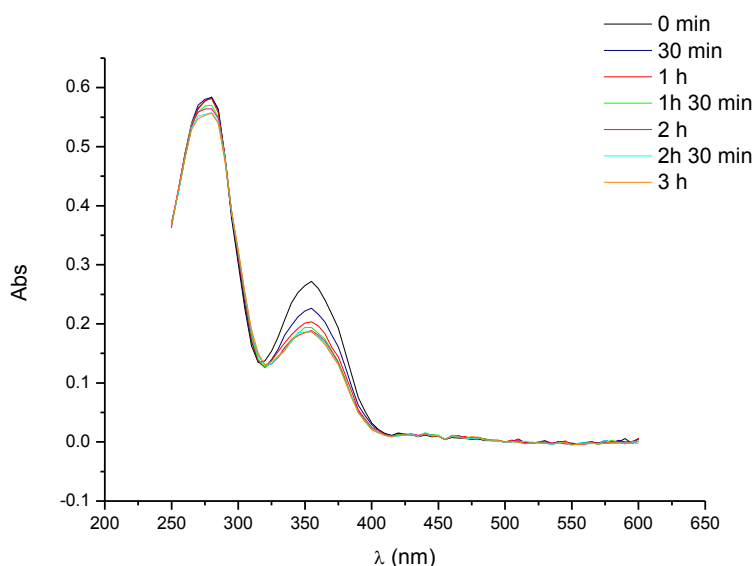


Figure 143: UV-Vis spectra of 115 in solution under UV irradiation (313nm).

The process of back isomerization is fairly slow in all the compounds taking on average 48h to be achieved.

In order to calculate the conversion from the *trans* to the *cis* form, ^1H NMR spectra were recorded of a sample that had been irradiated until the photostationary state was achieved (Figure 144).

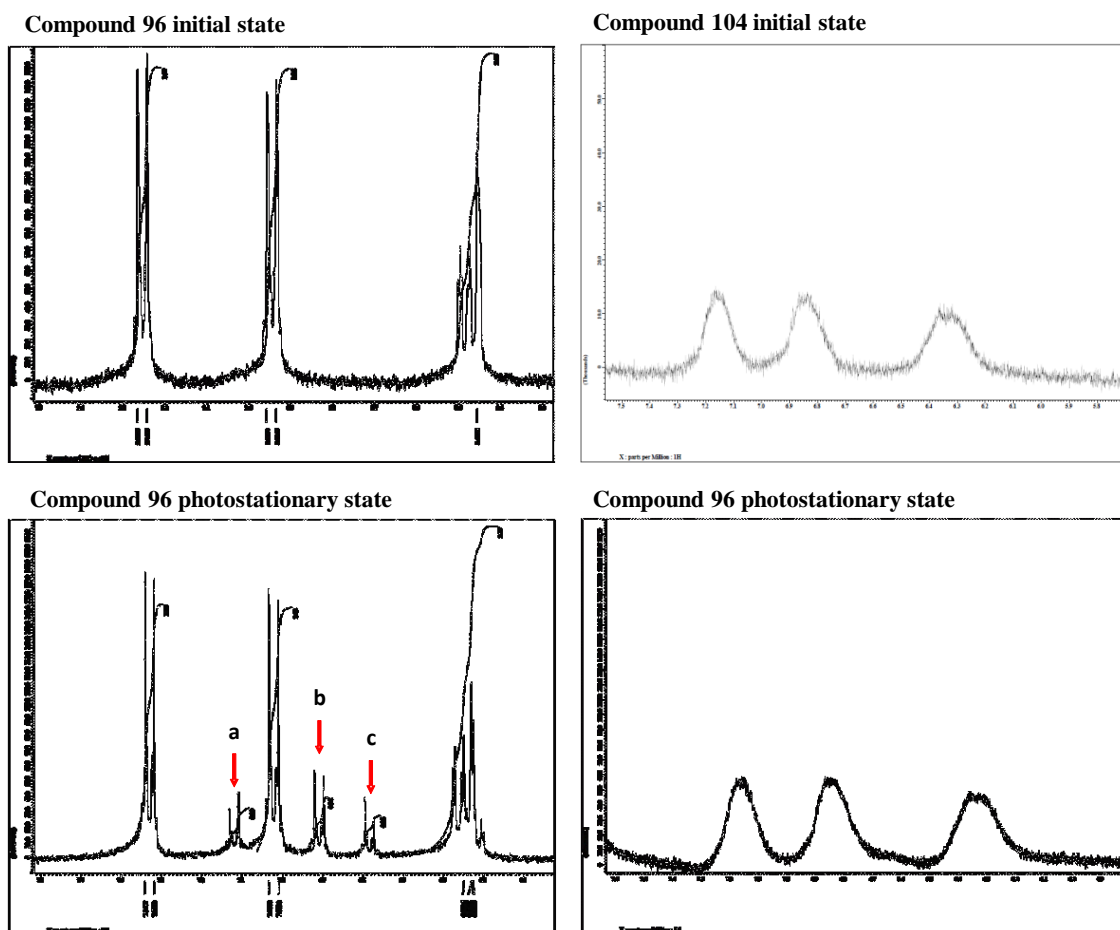


Figure 144: ^1H NMR spectra for compounds **96** and **104** in the *trans* form and in the photostationary state.

As shown in Figure 144, the peaks correlated to the *cis* form appear and in the pure *cis* isomer they should integrate to two protons.

For compound **96** the calculated conversion varies between 12% and 18% for peaks **a** to **c** in the spectrum of the photostationary state. The calculation of the conversion for peak **b** is shown below.

$$\text{Integration of peak } \mathbf{b} = 0.36$$

In the pure form this peak should integrate to two protons, therefore: $0.36/2 \times 100 = 18\%$.

For the silsesquioxane derivatives such as **104** the conversion values could not be calculated from ^1H NMR due to overlapping of *trans* and *cis* peaks (see Figure 144).

DISCUSSION PART II-

7.6 - Phase structure assignment based on XRD studies

In this section the phase structure and self-assembly arrangement for the synthesized materials will be discussed based on X-Ray data.

The discussion will follow the structure used for the discussion of both the synthesis (section 7.1 and 7.2) and the liquid crystalline properties (section 7.3 and 7.4). The novel low molar mass liquid crystal **96** will be discussed initially followed by four series of silsesquioxane derivatives, where the spacer of the cyanobiphenyl units varies from an undecyl to a propyl unit (Series I to III) and finally series IV where the length of the aromatic core was increased.

The diffraction patterns show some asymmetry between the left and the right sides. The azimuthally integrated plots show also an asymmetry between 2θ values 0° - 180° and 180° - 360° . This could be, in some cases, related with the position of the beam stop and will be discussed when appropriate. For these reasons the half from 180° - 360° of the χ -scans will not be taken into account when analyzing the phase structure.

7.6.1 - Low molecular weight mesogen

The diffraction studies of **96** were carried out on samples prepared by flow filled capillaries. The material is characterised by the phase sequence Cr 53 N 98 Iso as determined by OPM and DSC.

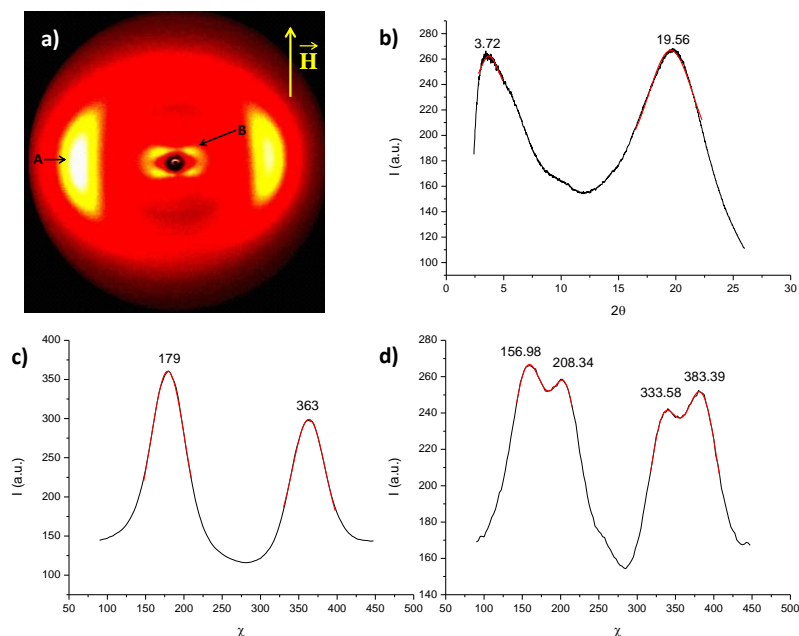


Figure 145: X-ray diffraction data from compound 96. a) 2D diffraction pattern, b) radially integrated scans, c) and d) azimuthally integrated scans of peaks A and B, respectively.

Table 12: Calculated distances for compound 96.

	Peak A	Peak B
2θ	19.56	3.72
d (Å)	4.54	23.75

The diffraction pattern of compound **96** was recorded in the nematic phase at 70 °C. The diffraction pattern depicted in Figure 145 a) shows typical features of low ordered liquid crystals. In the wide angle region, diffuse diffractions associated with the intermolecular distances of the oriented mesogens ($2\theta = 19.58$) 4.54 Å are observed. In the small angle region, four off-meridian pseudo Bragg reflections can be observed. These features in the nematic phase are attributed to the formation of SmC-like cybotactic clusters and in this particular case a tilt angle of approximately 63° was calculated from the azimuthal scan of the small angle reflections Figure 145 d).

7.6.2 - High molecular weight materials

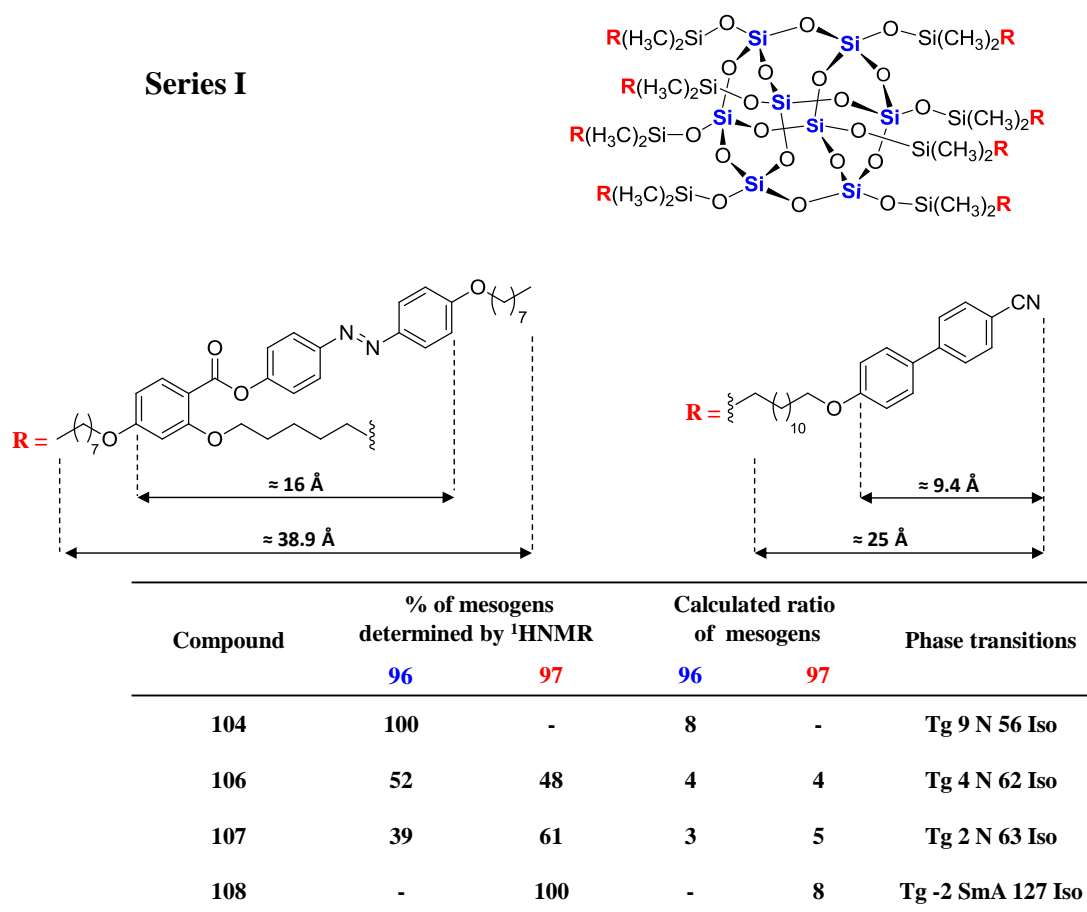


Figure 146: Scheme of series I.

Compound 104

The phase structure of the silsesquioxane derivatives was investigated using XRD measurements. As these materials are very viscous, preparation of samples for analysis was thus rather challenging. Usually samples are prepared by flow filling of capillaries in the liquid crystal phase however due to the high viscosity of the materials this was found to be difficult. After preparing a sample using this method XRD diffraction patterns were collected showing the typical features of liquid crystalline materials. An example of the diffraction pattern for compound **104** prepared by this method can be found in Figure 147.

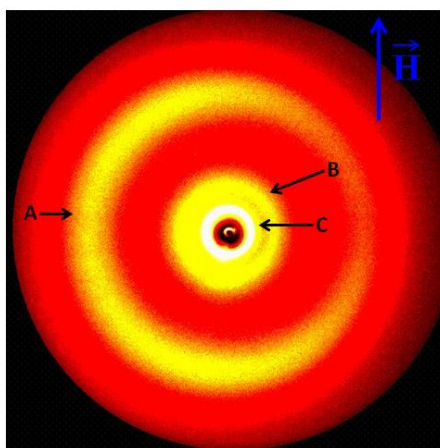


Figure 147: Diffraction pattern of an unaligned sample of compound **104**.

The 2D diffractogram shows three concentric rings suggesting an isotropic sample or an unaligned nematic material. Considering the DSC and microscopy results the latter case occurs for **104**. In the wide angle region a diffuse reflection at ($2\theta = 19.52$) 4.55 \AA , characteristic of the liquid crystalline chains very similar to the one found for compound **96** discussed previously ($2\theta = 19.58$; 4.54 \AA) can be detected. In the small angle region two reflections can be observed: B ($2\theta = 6.48$) at 13.64 \AA and reflection C at ($2\theta = 3.38$) 26.14 \AA . However despite χ -scans suggesting higher intensities at 127° and 245° for reflection A (see Figure 147 and Figure 148 b)), reflections B and C show a homogenous distribution except for a peak around 256° for peak B and 257° for peak C (Figure 148 c) and d) respectively).

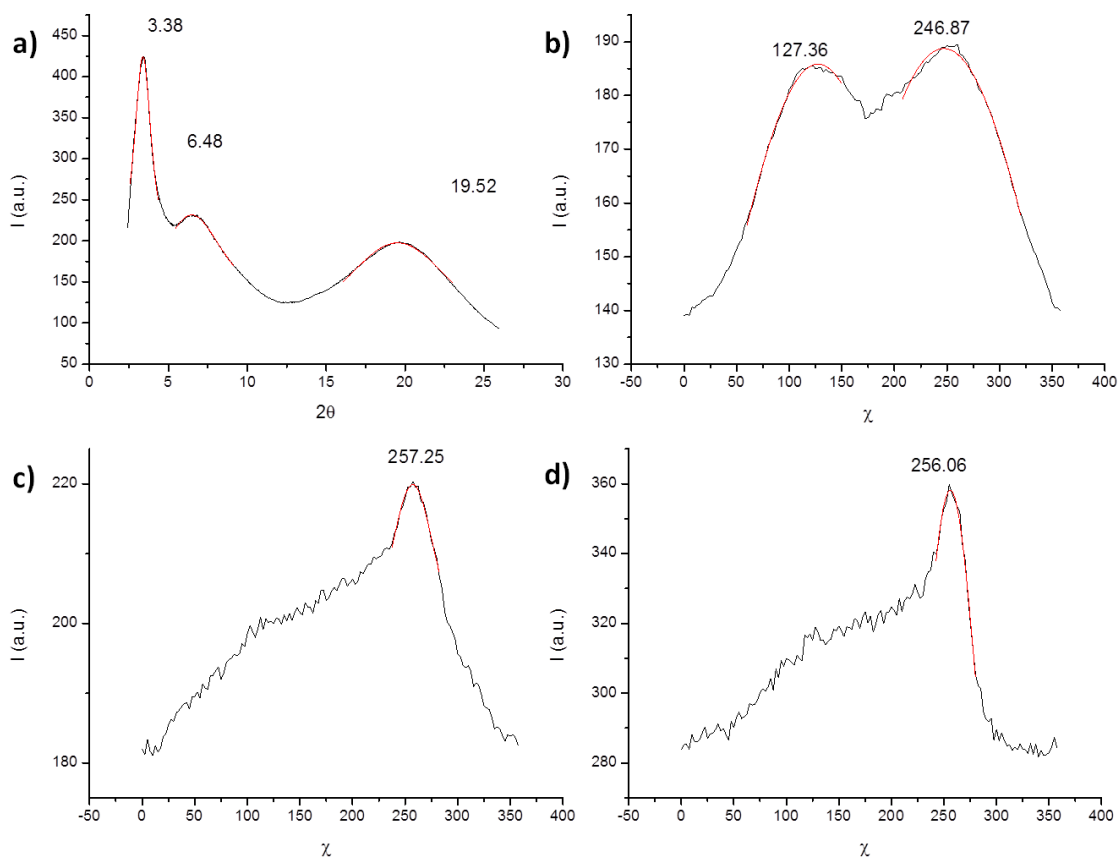


Figure 148: a) Radially integrated scans, b), c) and d) Azimuthally integrated scans for peak A, peak B and peak C respectively.

It is noted that the reflections are more intense on the left side of the diffractogram than on the right side, which could be due to a non homogeneous sample. In order to draw a clear picture of the phase structure of these materials, investigation on aligned samples seemed to be crucial.

In order to solve this problem, fibres were produced from the liquid crystalline phase. The samples were placed on a glass slide and heated until the mesophase temperature was reached. At this point, a needle was used to pull a fibre that was extended to a second glass slide as represented in Figure 149 a). Due to the low glass transition temperature, when the fibre was produced it started to curl and so by extending it between two glass slides this process was prevented. The fibres were cooled to the glassy state so that they would be stiff enough to be cut and also to keep the alignment induced in the mesophase. The fibres obtained were around 150 μm thick as shown in Figure 149 b).

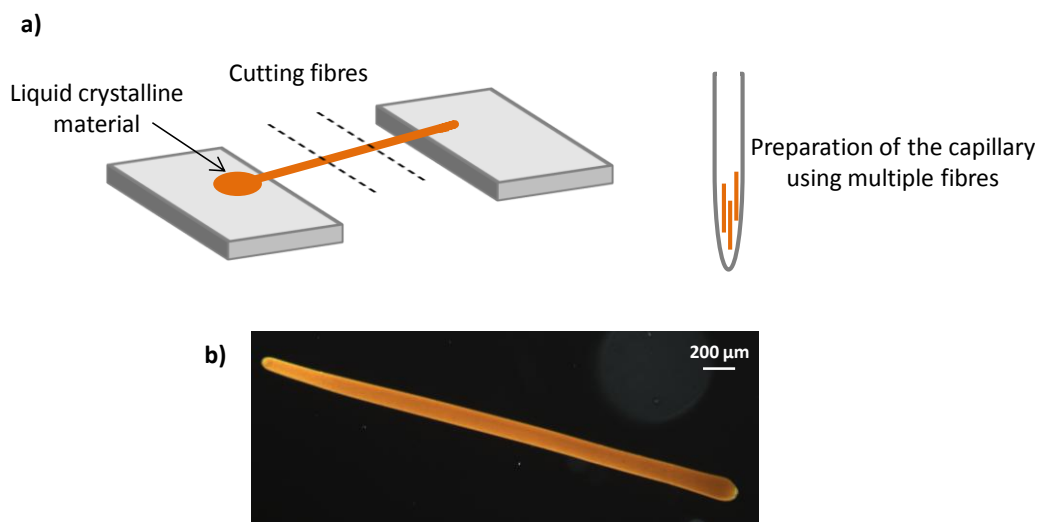


Figure 149: a) Representation of the process of preparation of fibre samples. b) Example of the fibres used in the XRD experiments.

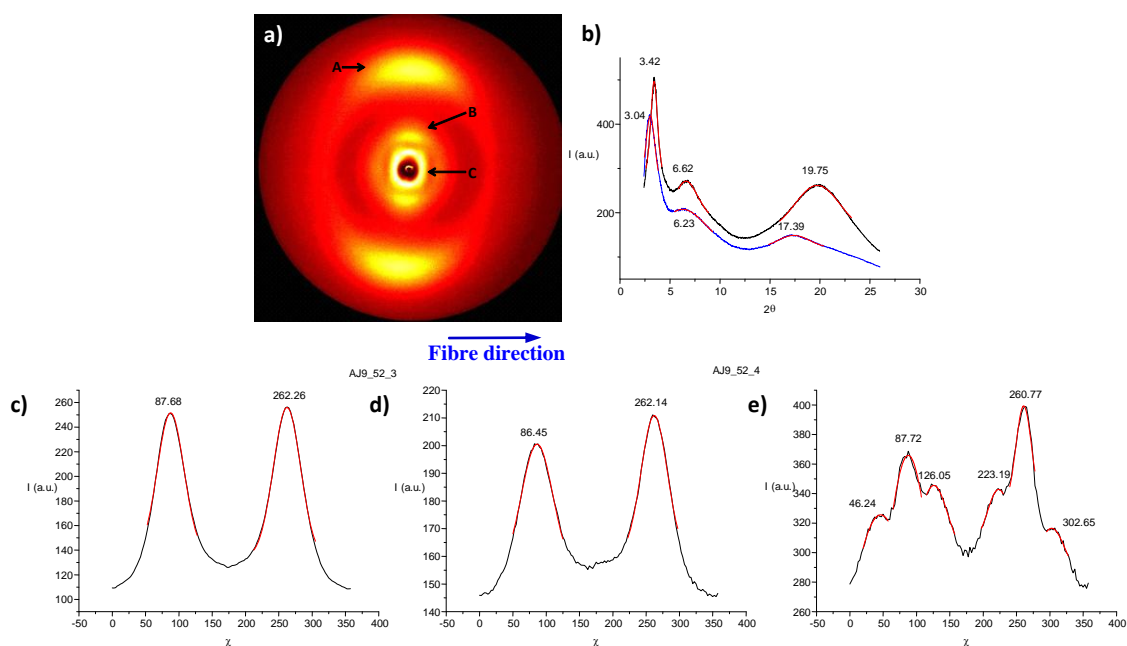


Figure 150: X-Ray diffraction data from compound **104**. a) 2D diffraction pattern. b) radially integrated scans, black curve data collected parallel to \vec{H} and blue line data integrated perpendicular to \vec{H} . c), d) and e) azimuthally integrated scans of peaks A, B and C, respectively.

Table 13: Calculated distances for compound **104**.

peak	Parallel to magnetic field			Perpendicular to magnetic field		
	A	B	C	A	B	C
2θ	19.75	6.62	3.42	17.39	6.23	3.04
d (Å)	4.50	13.35	25.84	5.10	14.19	29.07

The diffraction pattern of a multiple fibre sample of **104** at room temperature is shown in Figure 150 a). At this temperature the sample is liquid crystalline as confirmed by

DSC and OPM where a marbled texture (Figure 116) was observed, indicating the existence of a nematic mesophase as discussed previously. When comparing Figure 147 a) and Figure 150 a) the existence of three reflections is a common feature, however the main difference is that Figure 150 a) shows an aligned sample. Peaks A and B of Figure 150 a) are no longer diffuse rings but reflections concentrated on the meridian. This is clearer in Figure 150 c) and d) where the azimuthally integrated diffraction intensities for peaks A and B are shown. The observation that all the reflections were situated in the meridian region was rather surprising as it implies a layer arrangement, not common for the nematic phase. It is noted that an external magnetic field \vec{H} does not alter the alignment of fibres prepared by mechanical alignment. The results observed are also surprising, when compared to silsesquioxanes with not very dissimilar mesogenic groups though containing a more flexible spacer shown in Figure 151 below.⁴⁸ The silsesquioxane derivatives showed columnar and nematic phase behaviour. The latter is particularly interesting for this discussion and therefore the 2D diffractogram for the nematic phase of this related system is depicted below.

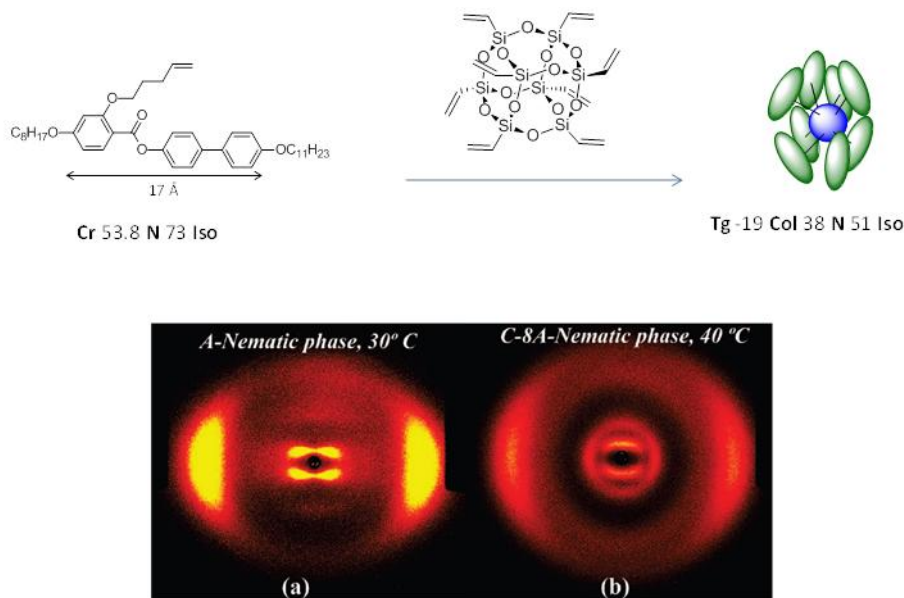


Figure 151: Top: System studied by Karahaliou *et al.*⁴⁸ Bottom: a) 2D diffraction pattern of mesogen b) 2D diffraction pattern of silsesquioxane derivative.

The diffraction patterns of mesogens are similar; however the diffraction pattern of the silsesquioxane derivatives is very different. The differences between the diffractograms obtained for the nematic phase of **104** and the system represented above, in which the diffraction peaks are situated both on the meridian and on the equator as expected for a nematic phase, as opposed to the diffraction pattern found for **104** where they are all situated on the meridian.

Figure 150 b) shows the radially integrated diffraction intensities as a function of the diffraction angle 2θ . The intensities integrated within the meridian (parallel to the external magnetic field) are represented by the black curve while the blue curve represents the integration within the equatorial sector (perpendicular to the magnetic field).

The integration along the magnetic field shows in the wide angle region a diffraction corresponding to the intermolecular distances of 4.5 Å between the mesogens in the liquid crystalline state (Table 12). The persistence of these peaks in the meridian suggests that the mesogenic groups are aligned perpendicularly to the magnetic field, (note: the magnetic field is part of the experimental set-up but has in this mechanically oriented fibre system, no impact on the orientation of the mesogens) that is, in the direction parallel to the fibres main axis. The second pseudo-Bragg peak of 13 Å is attributed to the distances between two silsesquioxane cores that are situated in the same direction as the mesogenic groups.

Also in the small angle region the reflection at approximately 26 Å, is related to the length of the mesogenic units see Figure 150 e) and Table 13. The full length of mesogen **96** is approximately 39 Å implying that the mesogenic groups interdigitate. The analyses of the azimuthally integrated reflection of peak C shows two peaks with higher intensities in the meridian plus four off meridian intensities. The calculated angle between these reflections is 40° and can be explained by the presence of SmC-like cybotactic clusters. The value of 26 Å, smaller than the full length of the mesogen, then corresponds to the layer spacing within these cybotactic clusters. When compared with the pure monomer, compound **96**, the calculated values for peaks A and C are very similar, indicating that the nematic features of **96**, such as the presence of cybotactic clusters, are retained in the silsesquioxane compounds. Even though the orientation of the diffraction reflections pointed towards a layered structure implying maybe a smectic phase, this hypothesis is contradicted by the extremely low intensity of peak C, when compared to a first order reflection of a smectic mesophase, as well as the marbled texture presented by the material throughout the entire temperature range, indicating the existence of a nematic phase.

The correlation length of the molecules was calculated using Scherrer's equation:

$$\xi = \frac{K\lambda}{B\cos\theta}$$

In which, K is a constant dependent on the crystallite shape and in this case a value of (0.89) was used, λ is the x-ray wavelength = 1.542 Å, B is FWHM (in radians) = $\frac{FWHM \times \pi}{180}$ and θ_B is the Bragg angle, also in radians. $\frac{\theta \times \pi}{180}$.

For **104**, $\xi = 79$ Å, corresponding to ≈ 2 molecules.

Tschierske *et al.*⁴⁹ reported the existence of lamellar nematic phases (LamN) in T-shaped bolaamphiphilic LC systems as discussed before. These compounds have three different structural features: rodlike units, combined with polar hydroxide groups that promote the existence of hydrogen bonding, and siloxanes or carbosilanes as lateral chains, as shown in Figure 152.

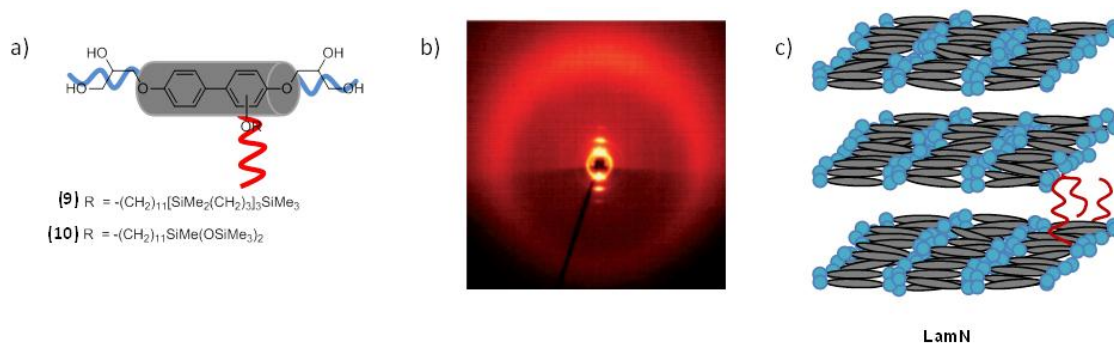


Figure 152: Left: Systems studied by Tschierske *et al.* b) Diffraction pattern of compound **10**⁴⁹ c) Model proposed for the LamN phase of compound **10**.⁴⁹

The 2D diffraction pattern for compound **10** is depicted above. It is noted that the pseudo Bragg reflections are situated exclusively in the meridian region, as observed for **104**. The X-ray data was explained by the occurrence of a lamellar nematic phase structure schematically represented in Figure 152 c) above. Two primary forces contribute to this arrangement, the hydrogen bonding between the polar hydroxyl groups promoting the packing of the aromatic units side by side, and microsegregation between the organic rod-like unit and the inorganic laterally attached spacer. Due to this phenomenon, the spacers are situated between the organic groups promoting a layer arrangement.⁴⁹

Compound **104** shows a few structural similarities with the T-shaped systems discussed above, such as two distinct regions formed by the inorganic inner core and the organic mesogens covalently linked to the silsesquioxane core from which they emerge radially. These chemical differences are clearly conducive to microsegregation. Considering the above discussion in relation with the X-ray data collected for **104** in which a laminated structure seems to be present, and the identification of a lamellar nematic phase in T-shaped systems promoted by microsegregation, together with the OPM observations of

a marbled texture, the nematic phase shown by this compound is assigned as a lamellar nematic phase.

In order to have a full description of the self-assembly molecular arrangement the dimensions of unit cells were calculated using the molecular volume of the materials and the XRD data, which provides the length of the repeating units.

The molecular volume V_m , can be determined by

$$V_m = \frac{M}{N_A \rho}$$

Where M is the molecular weight of the compound, N_A is the avogadro number (6.022×10^{23}) and the density, ρ , for an organic compound is $\approx 10^3 \text{ Kg m}^{-3}$.

The V_m estimated for this compound is $10021 \text{ x } \text{Å}^3$. In order to arrive at a self-assembly arrangement using as the length of the repeating unit the notional d-spacing of 25.84 Å obtained from the XRD scattering experiments. Considering the volume and the length of the molecular unit, it is possible to calculate the area, since $10021 \text{ Å}^3 / 25.84 \text{ Å} \approx 388 \text{ Å}^2$.

As discussed previously, since the full length of the azo mesogen (39 Å) is smaller than length of the molecular unit, interdigitation of the alkyl chains of adjacent molecules is expected to occur (length of eight methylene groups is estimated to be approximately 9 Å).

A packing with an antiparallel organisation of the aromatic groups, as shown below, would not fall within the size of this arrangement, as the two aromatic groups make up a length of 34 Å , so such an arrangement should be discounted, see Figure 153.

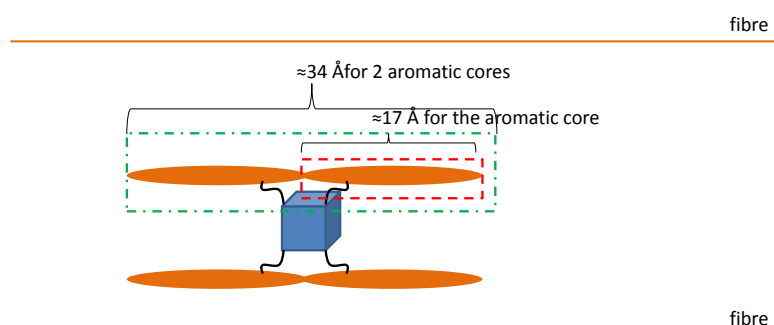


Figure 153: Representation of an antiparallel organization in 104.

More likely is an arrangement as shown in Figure 154, where the molecules are densely packed around the central silsesquioxane cube.

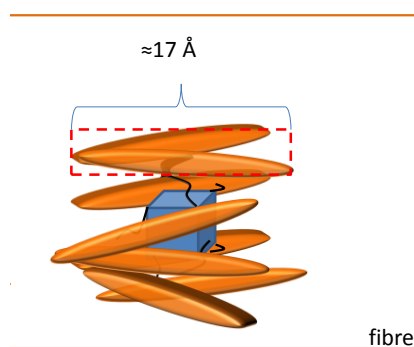


Figure 154: Proposed molecular arrangement of the azobenzene mesogens in turn of the silsesquioxane core.

A cylindrical model was initially considered such as the one represented in Figure 155.

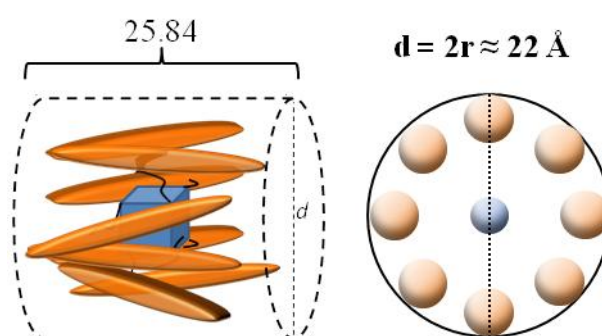


Figure 155: Representation of a cylindrical model.

Considering an area of 388 \AA^2 , it is possible to calculate the diameter of this cylindrical unit, $d \approx 22 \text{ \AA}$ ($d = 2r$; $r = (388 \text{ \AA}^2 / \pi)^{1/2}$; $d = 2 \times 11.1 \text{ \AA}$) Figure 155. In order to confirm if the molecules are accommodated by this molecular tube, the maximum extension of the molecules from the centre of the silsesquioxane molecule is calculated as $\approx 16.3 \text{ \AA}$ this value takes into account: (cube radius $\approx 2.2 \text{ \AA}$; length of Si-O-Si bond $\approx 3.1 \text{ \AA}$; spacer group $\approx 6 \text{ \AA}$, aromatic diameter $\approx 5 \text{ \AA}$). However the distance between two molecules should also be considered adding $4.50 \text{ \AA} / 2 \approx 2.3 \text{ \AA}$ to the previously calculated 16.3 \AA . The distance between two molecules is obtained from the XRD diffraction pattern, which corresponds to the average distance between liquid crystalline groups ($2\theta = 19.75$, $d = 4.50 \text{ \AA}$), leading to a final value of 37.2 \AA ($16.3 \text{ \AA} + 2.3 \text{ \AA} = 18.6 \text{ \AA}$ and $18.6 \times 2 = 37.2 \text{ \AA}$). This is larger than the calculated cylindrical footprint indicating that the cylindrical footprint falls easily within the molecular dimensions. However this maximum molecular length can be used to estimate the maximum and minimum sizes of the molecular footprint. In the simplest case of fully extended molecules, the maximum length is, as calculated before, 37.2 \AA , this would leave the third value at $388/37.2 \approx 10 \text{ \AA}$. This value is very small since the minimum extension that can be considered is the stacking of two aromatic groups ($1.5 \text{ \AA} \times 2 = 3 \text{ \AA}$) that

together with the distances between the molecules $4.5 + 2(4.5 \text{ \AA}/2)$ yields a minimum thickness of about 12.3 \AA , this molecular arrangement is represented in Figure 156.

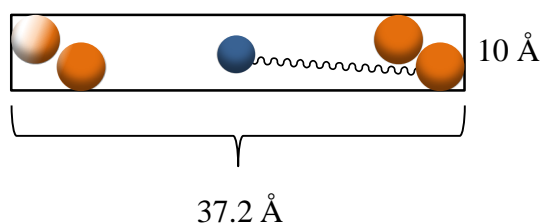


Figure 156: Molecular arrangement considering the minimum thickness possible for 104.

This in turn would require a third dimension of $388/12.3 = 31.54 \text{ \AA}$.

An arrangement of four mesogens on “top” and “below” a silsesquioxane core would require a width of $4 \times 5 \text{ \AA}$ (the diameter of planar aromatic group $\sim 20 \text{ \AA}$ plus $4 \times 4.65 \text{ \AA}$ resulting in a width of 38.65 \AA that do not fall within the calculated width of 31.54 \AA therefore, the structure represented in Figure 157 is not possible.

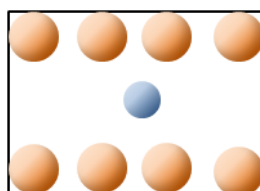


Figure 157: Molecular arrangement of 104 considering four mesogens on top and bottom of the silsesquioxane core.

However if 3 mesogens were on the top and bottom and one on each side, one arrives at a width of $3 \times 5 \text{ \AA} = 15 \text{ \AA} + 3 \times 4.65 \text{ \AA} = 28.95 \text{ \AA}$ which fits within the 31.54 \AA calculated, so considering this value 28.95 \AA the calculated value for the third dimension of $388/28.95 = 13.40 \text{ \AA}$ which is large enough to accommodate the value of 12.3 \AA needed therefore such an arrangement with three mesogens at the bottom and top each and two slightly offset could form a possible packing arrangement, fully in line with the observed XRD intensities structure a); b) is a more likely variation of a).

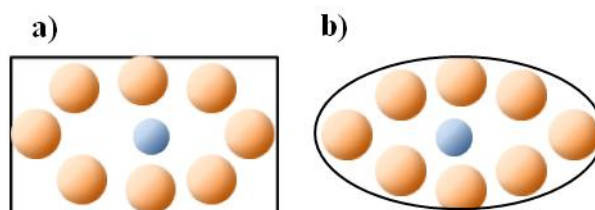


Figure 158: Molecular arrangement of 104 considering three mesogens on top and bottom of the silsesquioxane core.

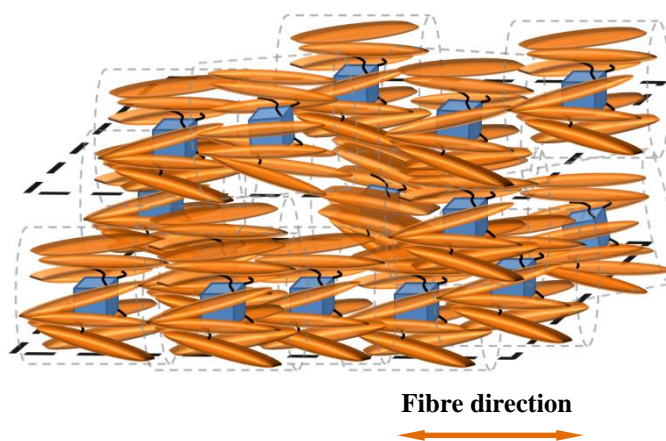


Figure 159: Model proposed for the lamellar nematic phase of compound 104.

In this model, the dark black lines, situated along the fibre length (perpendicular to the magnetic field) as suggested by the diffuse reflections in the wide angle region ($2\theta = 19.75, 4.5^\circ$) represent the alkyl chains. The distance between two silsesquioxane cores is 13 \AA in the direction parallel to the fibre length. The calamitic units are mainly positioned parallel to the fibre length yet cybotactic clusters of SmC-like layers with a tilt angle of 40° are present.

Because of the unusual features of this nematic phase, experiments were made in which a multiple fibre sample was submitted to a heating program from 25°C to 70°C , and for each increment of 5°C the sample was annealed for 30 min. The motivation behind this was to align the sample with an external magnetic field. However, this procedure failed, no realignment occurred, and so the sample was heated to 170°C , which is 110°C above the clearing point, subsequently the sample was then cooled to 25°C and data was collected every 5°C for 1800s.

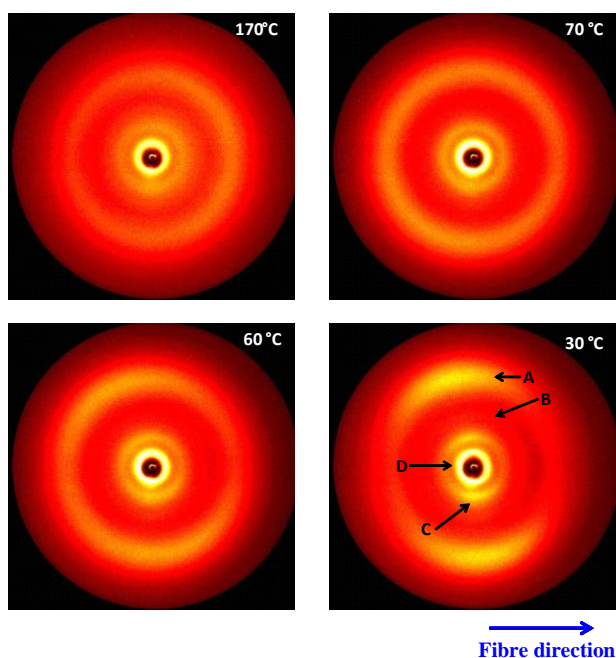


Figure 160: 2D diffraction patterns for 104 collected on cooling. The data was collected every 5 °C for 1800 s.

In Figure 160 selected diffractograms are shown, the top two are in the isotropic phase while the bottom ones are in the nematic mesophase. It is evident that at 60 °C, a preferential alignment within the meridian region can already be seen and at 30 °C the diffraction pattern is identical to the one discussed above in Figure 150. In Figure 162, radially and azimuthally integrations at 30 °C are shown. There are no significant changes within the radially integrated intensities except from an extra peak, with low intensity, at $10.69 \text{ } 2\theta$ value (8.27 \AA). Apart from this the diffractograms are very similar and the peaks are also situated in the meridian. The diffraction pattern shown in Figure 147 at 30 °C is represented in black and white (Figure 161) where this extra peak (peak B) can be observed.

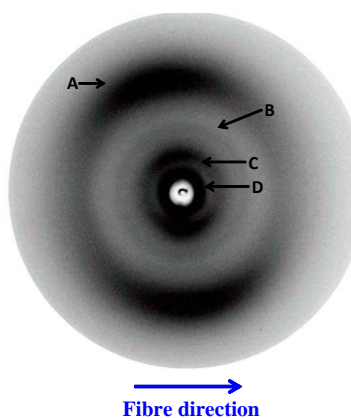


Figure 161: Diffraction pattern represented in Error! Reference source not found., T = 30 °C.

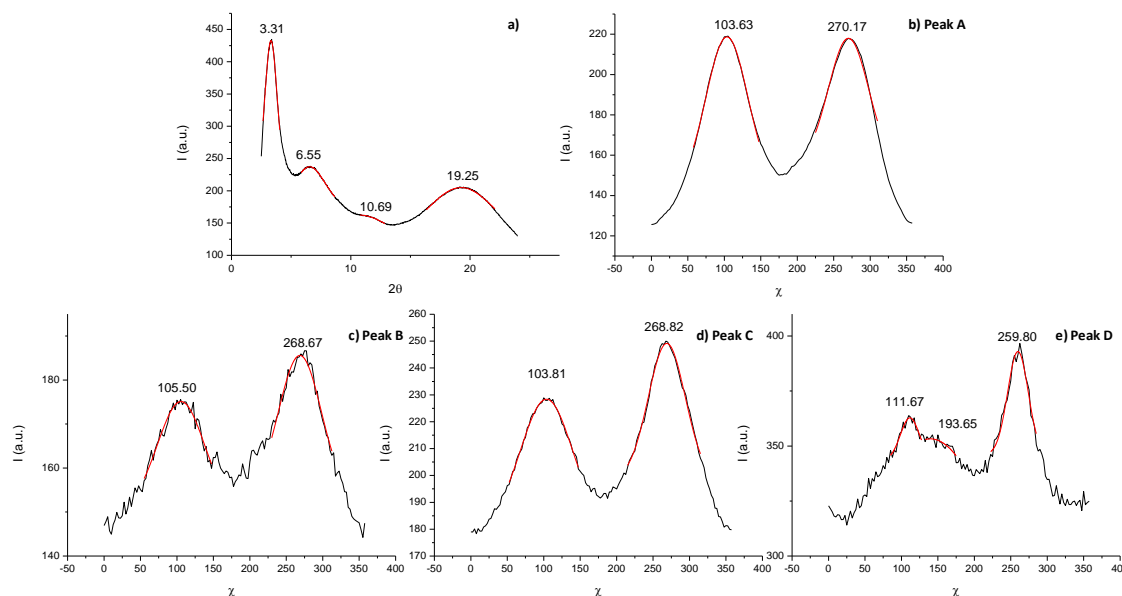


Figure 162: X-ray diffraction data from compound 104-exp.1. a) radially integrated scans, b), c), d) and e) azimuthally integrated scans of peaks A, B, C, and D, respectively.

For the χ -scans, there is a slight difference in the angle at which the maximum intensity is observed from approximately 87° (Figure 150 c) and d) to 103° (Figure 162 b) and c), yet the main differences occur in the distribution of the intensities of the small angle region (Figure 150 e) and Figure 162 e)).

Table 14: Calculated distances for the 2θ -plot shown in Figure 162.

	Peak A	Peak B	Peak C	Peak D
2θ	19.25	10.69	6.55	3.31
d (Å)	4.61	8.27	13.50	26.70

The appearance of a fourth peak aligned within the meridian region ($2\theta = 10.69, 8.27^\circ$) is unexpected as it was not present before in the mechanically aligned fibre sample (see Figure 150 b) and Figure 162 b). Another change occurred in the distribution of the intensities in the small angle region (Figure 150 e) and Figure 162 e). When comparing the two plots, the changes are apparent and it seems that the cybotactic features were almost lost. The temperature dependence of intensities with diffraction angle and the distribution of intensities for peak D are represented in Figure 163 a) and b).

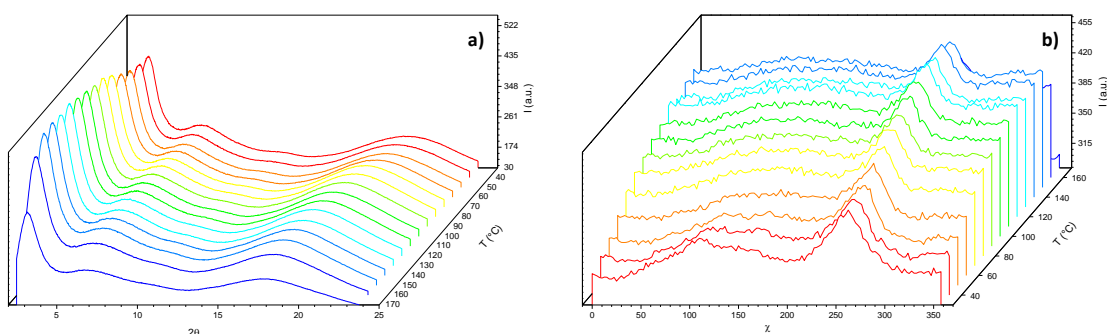


Figure 163: a) Temperature dependence of the diffraction angle for 104 at 30 °C. b) Temperature dependence of the distribution of intensities at 30 °C.

The θ scans did not show significant changes with temperature, except that the intensities have diminished at 170 °C (see Figure 163). The χ -scan plots show that the peak situated around 260 ° does not change significantly with temperature, and does not correspond to any particular reflection noticed on the 2D pattern. A similar peak can be observed for some of the compounds investigated and an explanation is proposed in later stages of this discussion. In contrast, the peak at smaller values of χ becomes narrower with a decrease in temperature and at temperatures below 50 °C it is possible to observe that it splits in two (Figure 163 b)). As discussed previously, these peaks correspond to the formation of cybotactic clusters with SmC-like layers with a tilt angle of 41°. It should be noted that when compared with Figure 150 e), the separation of these peaks is quite subtle. Considering that the sample was heated well above the clearing point and cooled to room temperature over a 15 hour period, it seems that the material possesses high degree of memory of the phase structure induced in the mesophase during the fibre fabrication process. However it seems likely that by melting the fibres and allowing the sample to cool slowly, the cybotactic clusters are lost (as shown by less evident splitting of peak C Figure 162 d). By heating the material up to 170 °C some reorientation by the external magnetic field might have occurred as suggested by the less evident presence of cybotactic clusters and the appearance of peak B. This peak could be related with the inorganic core and the siloxane spacer which has a length of ≈ 9 Å. This explains the existence of an extra peak and persistence of the intensities mainly in the meridian regions, associated with a slightly less ordered lamellar nematic phase.

In order to understand better the phase structure of this compound, the capillary was rotated by 90° and data was collected, but no differences in the diffraction pattern were apparent.

A further experiment consisted of collecting data along the length of the fibres as depicted in Figure 164 a).

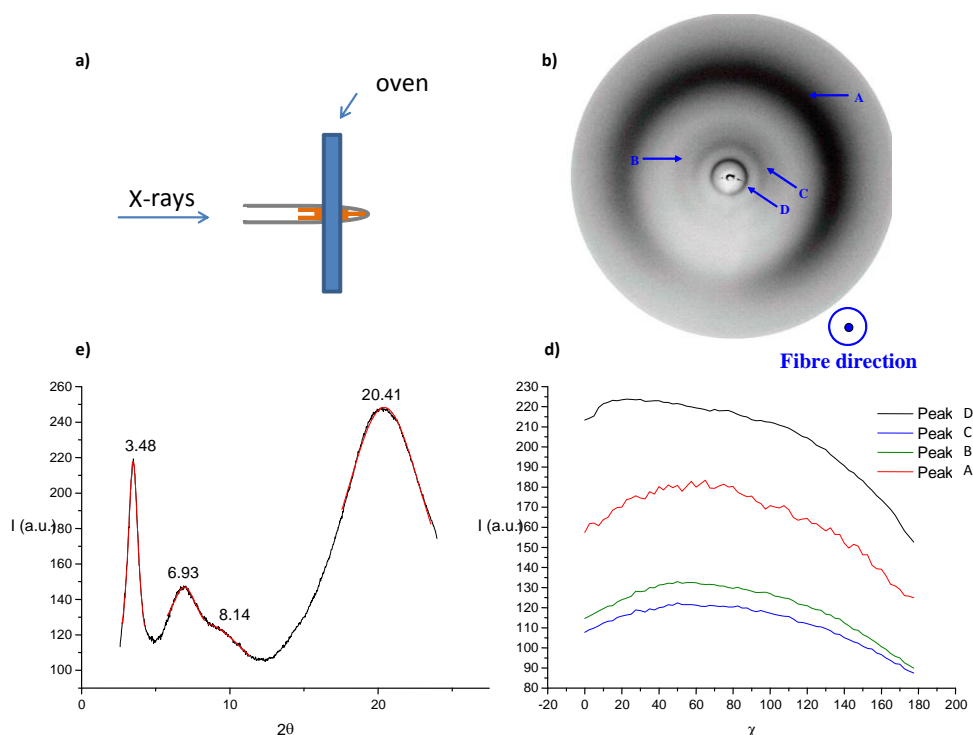


Figure 164: a) scheme of the experimental set up. b) 2D diffraction pattern of compound 104-exp2. c) Radially integrated scans. d) Azimuthally integration for peaks A to D.

The results obtained are summarised in the Figure 164. The existence of diffuse concentric rings suggests a liquid like sample and therefore a low ordered liquid crystalline phase similar to that found for a non-aligned sample as discussed above (see Figure 150). The existence of four intensities in the θ scans was surprising.

Table 15: Calculated distances for the 2 θ -scan presented in Figure 164

Peak	A	B	C	D
2 θ	20.41	8.14	6.93	3.48
d (Å)	4.35	10.86	12.76	25.39

Since no preferential alignment was found from the azimuthally integrated scans, it is not possible to deduce further information on the phase apart from the observation that along the fibre axis the material has the appearance of a nematic or isotropic system, in other words there is no indication of a helical superstructure.

Since there is a strong tendency for the mesogens to align in the direction of the fibre, the question whether the lamellar nematic phase discussed before was exclusively related with the imposed alignment when preparing the fibres had to be considered. In order to clarify this point, the material was aligned with the magnetic field. This process was time consuming and initial experiments were undertaken in a sample composed of small portions of the material cut with a scalpel and introduced into the capillary. This approach was based on the assumption that not mechanically aligning the system would facilitate an alignment induced by the magnetic field. The sample was annealed for 16 hours at 75 °C. After this period, data was collected every 5 °C for 30 minutes followed by another long annealing (\approx 16h) at 75 °C. Despite long annealing times above the clearing temperature, alignment of the sample by the magnetic field was not achieved. Another approach consisted of a fibre sample subjected to consecutive cooling cycles from above the isotropisation temperature to 40 °C. During cooling, the temperature was decreased by 1 °C/1800s and data collected for 1800s. Six cycles were carried out to obtain a successful alignment with the magnetic field as demonstrated in the sequence of diffractograms below (Figure 165) where it is visible that the isotropic state consisting of three concentric diffuse scattering rings ($T = 68$ °C and 63 °C) and the nematic phase (57 °C and 49 °C) where the pseudo Bragg reflections are situated within the equator, contrary to what was observed previously (Figure 165).

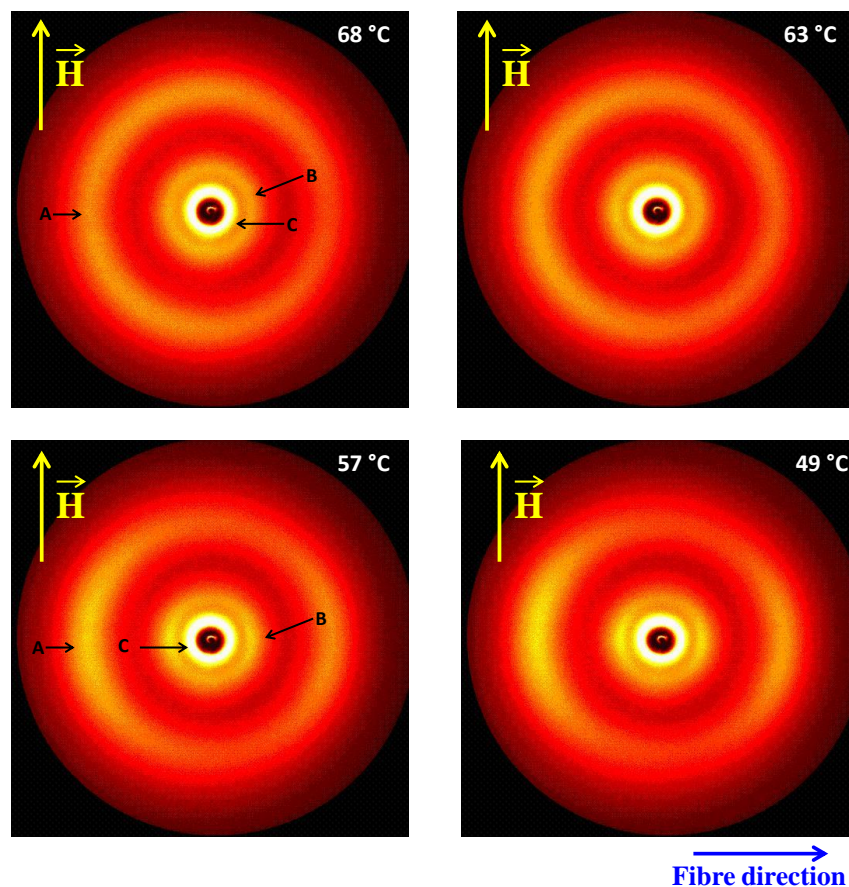


Figure 165: 2D diffraction patterns for 104 exp. 3 collected on cooling. The data was collected every 1 K for 1800 s.

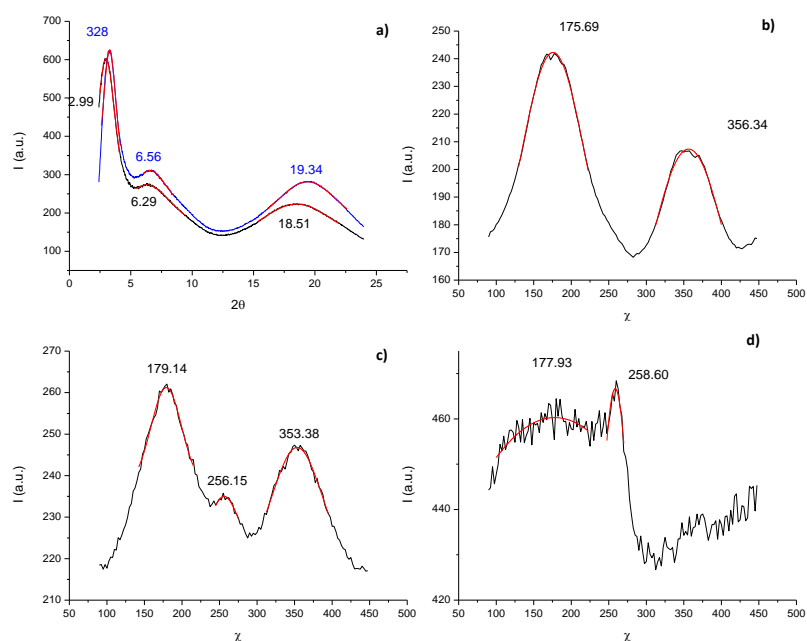


Figure 166: x-ray diffraction data from compound 104-exp.3. a) radially integrated scans, b), c) and d) azimuthally integrated scans of peaks A, B and C, respectively.

In the nematic phase, the radial intensities in the direction parallel and perpendicular to the magnetic field, as a function of the diffraction angle were plotted as shown in Figure

166 a). The diffraction intensity in the direction perpendicular to the magnetic field is now higher than in the parallel direction, contrary to what was observed before Figure 150 b). It is also of interest to note that there is a slight difference (about 0.88 and 0.96) in 2θ values for the parallel and perpendicular directions. This difference changes with the alignment of the sample. The higher 2θ values being obtained in the direction of the preferential alignment, in this case perpendicular to the magnetic field.

The distances corresponding to the three peaks are in Table 16 and seem to be in agreement with the values obtained before (see Table 13) and correspond to; the distance between the mesogenic groups, distance between two silsesquioxane cores, and the length of the mesogenic groups (peak A, peak B and peak C, respectively).

Table 16: Calculated distances for the plots represented in Figure 166

Peak	Parallel to magnetic field			Perpendicular to magnetic field		
	A	B	C	A	B	C
2θ	18.51	6.29	2.99	19.34	6.56	3.28
d (Å)	4.79	14.05	29.55	4.59	13.48	26.94

The distribution of the wide-angle scattering along χ for peak A in the nematic phase shows a preferential alignment of the mesogenic groups with the magnetic field, which is also the case for peak B. However a third peak of low intensity can be noticed in the χ -scan plot at 256° (see graph c of Figure 166). The presence of a peak with roughly the same angle (259°) is also observed in Figure 166 d). A similar peak was detected also in Figure 148. It could be that this peak is related with the experimental set up, since these diffraction peaks are close to the centre of the detector, it is possible that some leakage of the beam stop occurs, interfering with the diffraction of the material. Contrary to what was observed before, (Figure 150 e) and Figure 162 e)) there does not seem to exist a preferential alignment for peak C and the cybotactic features are not present, perhaps because the sample is not well aligned enough for them to be detected. As the existence of cybotactic clusters cannot be confirmed, the reason for the intensity associated length related with the mesogenic units (26.9 \AA) to be smaller than the length of the mesogen cannot be unequivocally explained, however considering the results discussed so far the most plausible explanation for this result is interdigitation of the mesogens in the nematic phase.

All the results presented previously support the initially proposed lamellar nematic phase depicted in Figure 159. It is also apparent that the lamellar nematic phase is not restricted to an alignment imposed on fibre samples. It seems that the appearance of a fourth peak in exp.3, could be related with a loss in order of the phase structure related with isotropization of the sample and strong alignment memory inherent to these materials. The persistence of a lamellar nematic phase even when samples are subject to high temperatures or consecutive heating and cooling cycles, leading to an alignment of the sample with the magnetic field shows the robustness of this phase structure. The lack of orientation within the main fibre axis is interesting.

Compound 106

Phase structure studies on compound 106 were carried out on a multiple fibre sample prepared according to the method described above. The 2D-diffraction pattern collected at 25 °C for this material is shown in Figure 167 and the radially integrated patterns are represented in Figure 168.

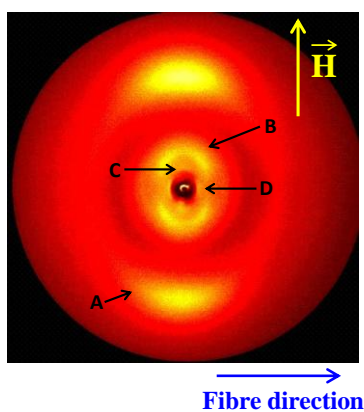


Figure 167: Diffractogram of compound 106.

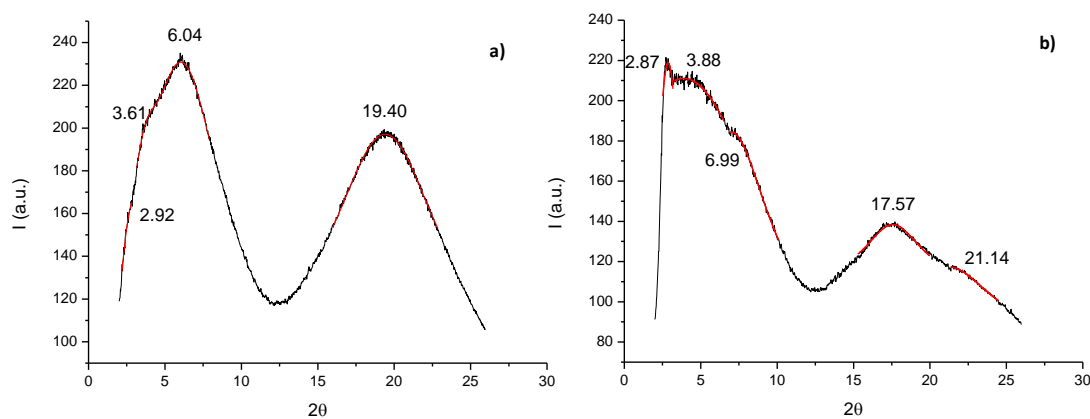


Figure 168: Radially integrated pattern of compound 106. a) Integration parallel to the magnetic field \vec{H} and b) Integration perpendicular to the magnetic field \vec{H} .

The radially integrated XRD pattern of compound 106 at 25 °C is shown in Figure 168 Figure 168:a) and b), corresponding to an integration parallel and perpendicular to the magnetic field. As observed and already discussed, there is a slight difference in the values of θ . Initial analyses of the θ scans in Figure 168 suggests the existence, in the small angle region, of three reflections, denoted on the table below (peaks B - D). To identify the three peaks in question, an amplification of the small angle region of the diffraction pattern is shown below, Figure 169.

Table 17: Calculated distances for the plots represented in Figure 168.

Peak	Parallel to magnetic field				Perpendicular to magnetic field				
	A	B	C	D	A	A ₁	B	C	D
2 θ	19.40	6.04	3.61	2.92	21.14	17.57	6.99	3.88	2.87
d (Å)	4.58	14.63	24.48	30.26	4.15	5.05	12.65	22.77	30.79

Initially the existence of peak C was not recognized in the 2D diffraction pattern but its presence in the radially integrated curves with intensity similar to the other reflections prompted a closer inspection of the diffractogram. The amplification of the small angle region area of the diffractogram is shown in Figure 169 a). Initially it was assumed that peak C was due to the reflection pointed out with the arrow, which would potentially be related to the beam stop. θ scans of the region represented in the Figure 169 a) were collected both above and below the equator, as it was expected to obtain different spectra for these two regions. In Figure 169 b), the two collected diffraction patterns are shown and the existence of peak C (2θ 4.6, $d = 19.38$ Å) is confirmed as the diffraction pattern from both regions is identical.

The 2θ value obtained for peak C by integrating the region represented below is different from the values described in Table 17. This is not surprising since the area integrated is much smaller therefore less noise is integrated and the integration of diffuse scattering belonging to the edges of the reflexions is minimized.

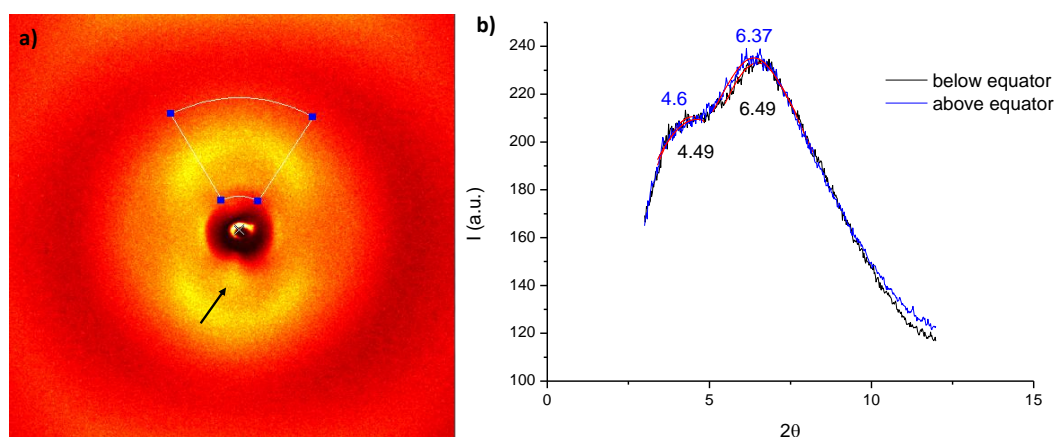


Figure 169: a) Amplification of the small angle region of the 2D diffraction pattern of compound 106. b) Radially integrated pattern for the region represented in a) Blue plot integration above the equator, black plot integration below the equator.

Azimuthally integrated scans of the region represented in Figure 170 a) were made and the results are plotted in Figure 170 b). Unfortunately the results obtained are not entirely conclusive.

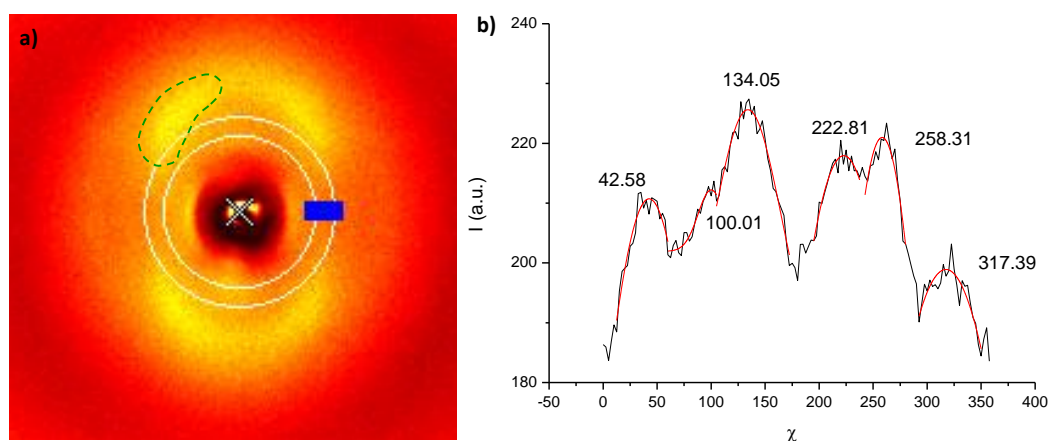


Figure 170: a) Diffractogram of compound 106 and representation of the are integrated of 2θ over χ . b) Azimuthally integrated XRD pattern.

In the χ -scan plot the peaks in Figure 170 b) approximately at 43° , 134° , 223° and 317° corresponding to the edges of peak B are highlighted by the green dashed line in Figure 170 a). Two other peaks at 100° and 258° are present, assuming they are related it would be expected that the second peak in the plot of Figure 170 b) would be around 280° . Examining the plot there seems to be a subtle shoulder around that area. However

the peak at 258° could be related with the peak identified with an arrow in Figure 169. In order to be certain if this peak could be due to a diffraction from the beam stopper, as discussed before, χ -scan of the region represented in Figure 170 a) at different temperatures were plotted in Figure 171 where it is shown that there is a change in the plot with temperature. The shape of the peak at approximately 258° does not change much and neither does its intensity as can be observed at 85°C , red line. This supports the interpretation made above regarding the experimental results for the distribution of the intensities.

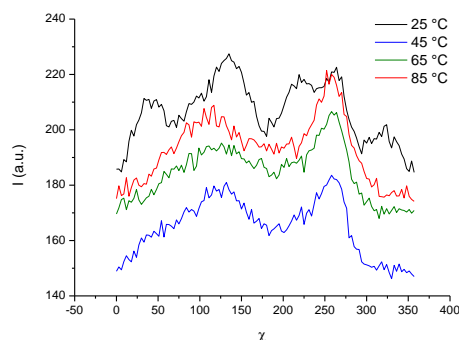


Figure 171: Temperature dependence of the distribution of intensities for the area represented in Figure 170 a).

The azimuthally integrated scans for peaks A, B and D are represented below.

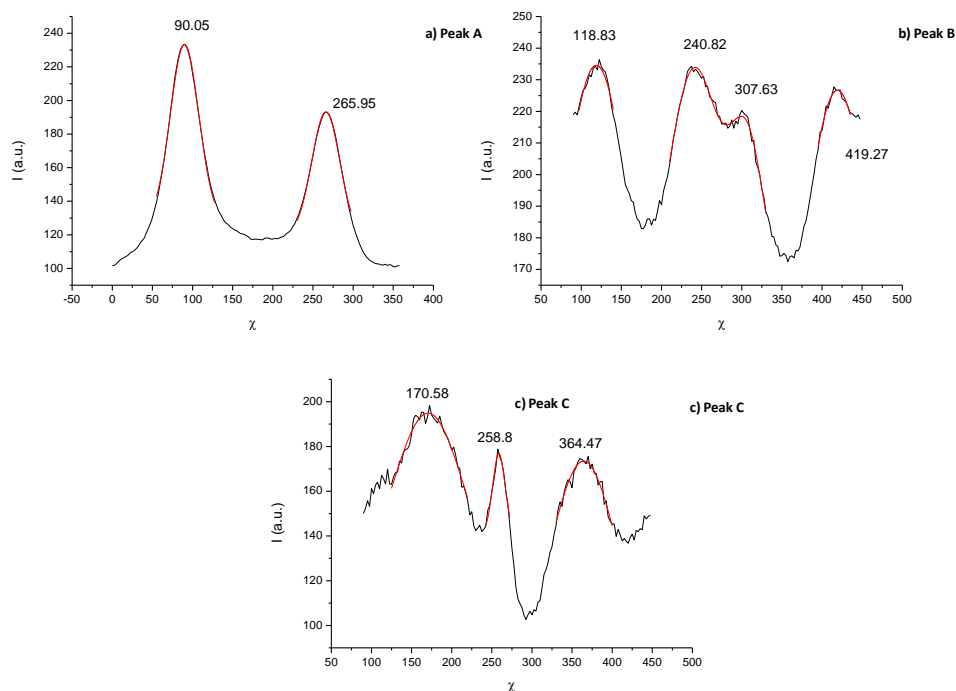


Figure 172: Azimuthally integrated XRD patterns of 106. a) b) and c) represent the χ plots for peaks A, B and C respectively.

Viewing the plots it is apparent that there is a tendency for the peaks to be situated around the meridian region. Peak B shows four peaks deviating from the meridian by 30° . Peak D shows two peaks situated along the equator and a sharp peak at 258.8° which resembles the one found for Peak C, sustaining the hypothesis introduced that this peak is situated in the meridian region and the peak expected at 280° is suppressed because of the intensity of the peak at 258° .

With this analysis in mind, an image of the phase structure can start to be defined. When compared to **104** there are a few differences that should be noted.

The first is the existence of an extra peak in **106** in the small angle region (30.79 \AA) situated on the equator. As observed for **104**, all the other peaks are situated in the meridian, however a change occurs for peak B that shows four off-meridian peaks at 14.63 \AA corresponding to the average distances of the siloxane cores, contrary to what was observed in **104** where 4 off-meridian reflections were detected for the diffraction of the peaks corresponding to the mesogenic groups, 25.39 \AA . Considering these observations it seems that we are in the presence of a nematic phase, where the siloxane cores organize into SmC-like cybotactic clusters with an angle of approximately 30° .

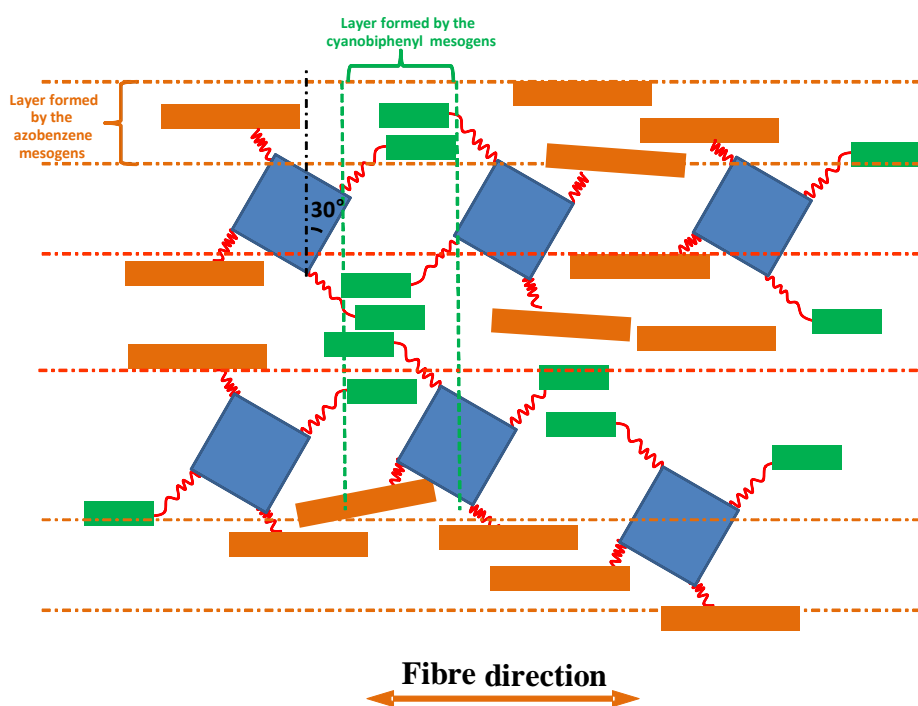


Figure 173: Schematic representation of the lamellar nematic phase.

In Figure 173 there is a representation of the possible phase structure for this material. Considering the preferential alignment in the meridian region for Peaks A and C it is possible to say that the mesogenic units containing azobenzene groups, are situated

parallel to the fibre main axis. In Figure 172 the azobenzene groups are represented by the orange rectangles that are arranged parallel to the layer. Since the distance obtained from the θ -scans plot, Figure 168 a), of $\approx 24.5 \text{ \AA}$ is smaller than the full length of the azobenzene molecules ($\approx 39 \text{ \AA}$), it is possible to say that interdigitation of these groups occurs, as represented in the model. Regarding peak B (Figure 167), associated with the distance between two siloxane cubes which was calculated as 14.6 \AA , it seems that this value is slightly higher than what was recorded for related systems where the values are found are between $13\text{-}14 \text{ \AA}$.^{47, 48} Yet the main feature of this peak is the existence of four off meridian spots which are usually related with the formation of cybotactic clusters. In this specific case the tilt angle is 30° as represented in Figure 173 by the tilted squares. Finally peak D (see Figure 167) situated in the equator having an associated distance of $\approx 30 \text{ \AA}$ was not present for compound **104** leading to the conclusion that this peak is related to the presence of cyanobiphenyl groups. It was previously reported that silsesquioxane systems substituted with cyanobiphenyls form SmA phases.¹³⁶ Therefore, considering that this sample contains about 50 % of cyanobiphenyl units, it was not surprising that in these systems there seems to be a microphase segregation arising from a competition between the organization of cyanobiphenyl and silsesquioxanes groups in a SmA phase-like organization and the organization of the azobenzene derivatives and silsesquioxanes in the lamellar nematic phase proposed for compound **104**. So in this model the cyanobiphenyls, represented in green are aligned parallel to the layer arrangement given that it was already shown that the magnetic field has no influence in the alignment of a fibre sample, being the overriding effect the mechanical alignment induced by the fibres.

As the diffraction intensity is situated in the equator and at this point in the discussion it is suggested that this is only possible due to the large spacer (C11 alkyl chain), that allows these groups to form a local smectic A modulation. It is also important to mention that while the azobenzene derivative unit is attached to the silsesquioxane core laterally, the cyanobiphenyl mesogen is connected end on. This being the case, there will be some free space since there is no longer an environment of mesogens closely “surrounding” the inorganic core, it is possible that the tilt experienced by the inorganic cores, promoted by microsegregation, facilitates the packing of the cyanobiphenyl units. This suggests that within a nematic layer the cyanobiphenyls that are aligned in the fibre direction and as a consequence of their long spacer are sticking out from the silsesquioxane core, will have an antiparallel organization in a SmA-like manner. The electron modulation of these very diffuse layers, since overall this is a nematic phase,

will be situated in the direction of the magnetic field, explaining the associated intensity in the equator region. It is possible that the existence of azobenzene derivatives in the *cis* form contributes to the nematic behaviour.

The height of a smectic layer would be $\approx 30 \text{ \AA}$, suggesting interdigitation of the aromatic groups.

The correlation lengths of the mesogenic units were determined using the Scherrer's equation as described before. The calculated value for this compound at $25 \text{ }^\circ\text{C}$ was $\xi \approx 194$, corresponding approximately to 3 molecular lengths.

A self – assembly molecular organization can be drawn considering the value of the notional d-spacing obtained from the XRD diffraction pattern as well as the calculated molecular volume of 8233 \AA^3 .

Considering the value of 30.79 \AA as the length of the repeating unit in the self - assembly structure, and $V_m \approx 8233 \text{ \AA}^3$. The same approach followed to **104** was undertaken and the calculated values for the structures represented in Figure 155 to Figure 157 did not accommodate the molecular dimensions. Considering that these molecules possess cyanobiphenyl units with an undecyl spacer and taking into account the X-ray data are aligned parallel to the fiber direction, the length of the molecules has to be larger. The approximate length calculated was $\approx 60 \text{ \AA}$ and this considers the cyanobiphenyl group ($\approx 10.8 \text{ \AA}$), the undecyl spacer ($\approx 13.9 \text{ \AA}$), the siloxane unit ($\approx 3.1 \text{ \AA}$) and the radius of the silsesquioxane core ($\approx 2.2 \text{ \AA}$).

This value is roughly the double of the d spacing found from the XRD data. If this value is used to calculate the area occupied by the molecules, we arrive at a value of 133.7 \AA^2 ($8233 \text{ \AA}^3 / 61.5 \text{ \AA} \approx 134 \text{ \AA}^2$) considering a cylindrical footprint, the height of this cylinder is $\approx 13 \text{ \AA}$. Taking into account that the minimum height that the molecules occupy is 12.3 \AA , discussed previously, this cylindrical model seems to accommodate the dimensions of the molecules. A schematic representation of this model is shown in the figure below (Figure 174).

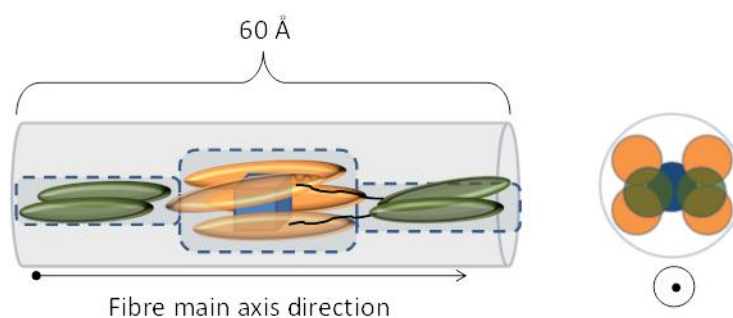


Figure 174: Representation of the molecular unit cell of 106.

This molecular model accounts for four azobenzenes surrounding the silsesquioxane core, creating a bulkier area in the center, and four cyanobiphenyl mesogens sticking out from this central bulky region.

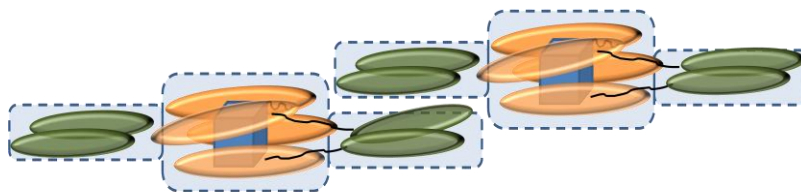


Figure 175: Representation of molecular packing of 106 considering the model proposed.

Considering the molecular shape proposed, the packing of the molecules is depicted in Figure 175. Due to the wider shape in the central region the molecules are prevented from sliding and form columnar or smectic layers. This model also explains the electron density diffraction corresponding to the size of the cyanobiphenyl mesogens ($\approx 31 \text{ \AA}$). An arrangement of the molecules as suggested in Figure 176 supports the XRD data and the proposal of a lamellar nematic phase.

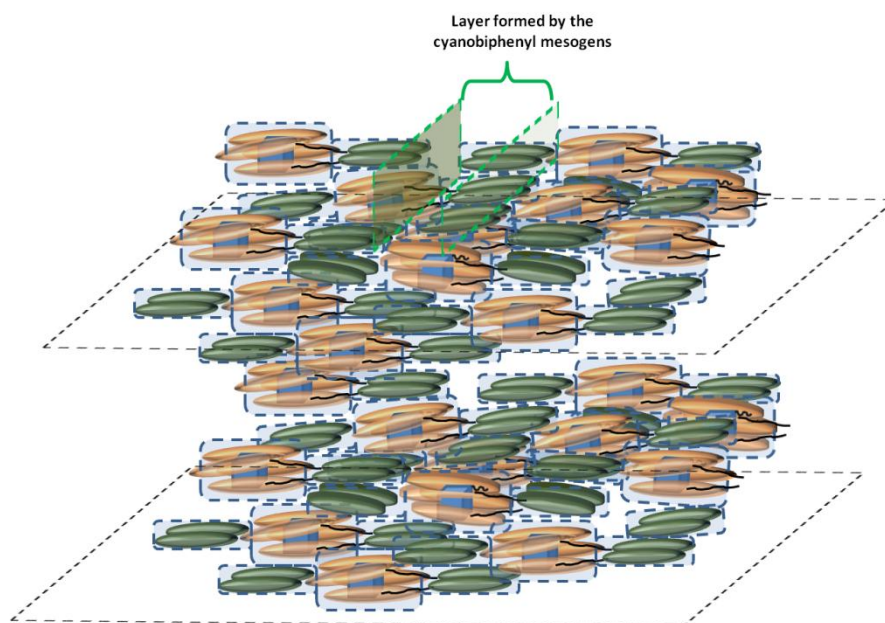


Figure 176: Lamellar nematic molecular arrangement for 106.

Compound 105

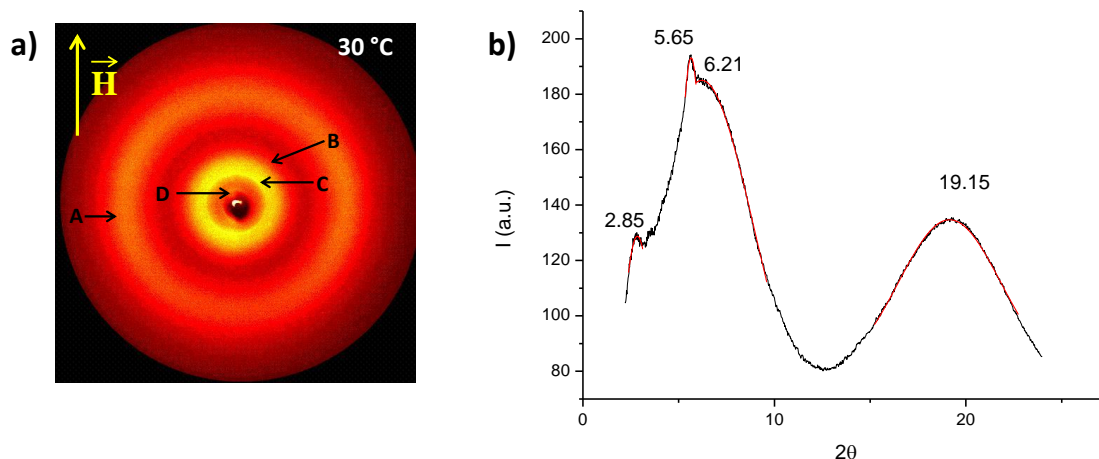


Figure 177: a) 2D diffraction pattern of compound **105**. b) Radially integrated pattern of **105**.

XRD of compound **105** was carried out in a capillary of a flow filled sample and for this reason the information we can draw from this experiment is limited.

In the 2D diffraction pattern, Figure 177 a), it is possible to see that the sample is not as well oriented as **104** or **106**.

The existence of 4 peaks is in agreement to what was observed for **106**. Considering the calculated d values shown in Table 18, it seems that peak C and D could be first and second order reflections of the smectic-like arrangement of the cyanobiphenyl molecules.

Table 18: Calculated distances for **105**.

Peak	A	B	C	D
2θ	19.15	6.21	5.65	2.85
d (Å)	4.64	14.23	15.64	31.00

Despite the similarities in the θ -scan it is noteworthy that peak C is much more intense than observed for compound **106** and the 2θ value of 5.65 ($d = 15.64$ Å) is much higher than the 2θ value ($2\theta = 3.61$, $d = 24.48$ Å) obtained for peak C for compound **106**. This might be related to the composition of this material. **105** has a much higher proportion of cyanobiphenyl (≈ 70 % in contrast with 48 % in **106**). The χ -scans of the diffraction reflections were plotted, however the results were not conclusive due the lack of alignment of the sample the signal to noise ration was low therefore the data collected was not conclusive. Notwithstanding this, the OPM observations of a marbled texture point to a nematic phase. Considering the results discussed so far it seems that as the content of cyanobiphenyl increases, their local arrangement in a SmA-like arrangement

becomes more pronounced despite not being strong enough to overrule the formation of a Lam N phase.

Compound 108

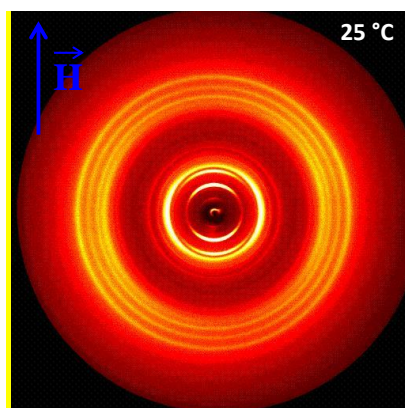


Figure 178: Diffractogram of 108 at 25 °C

The above figure shows the diffractogram of **108** at 25 °C and at this temperature the material is crystalline. At 85 °C, however, the diffraction pattern is quite different and in the wide angle region the set of sharp concentric rings gives way to diffuse reflections situated in the equator region, with a 2θ value of 17.19, corresponding to a distance of $\approx 5\text{\AA}$, characteristic of the liquid crystalline state.

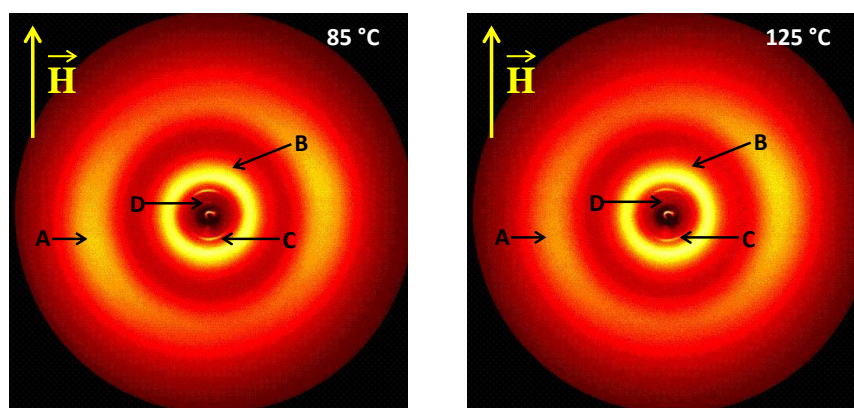


Figure 179: Diffractograms of compound 108 at 85 °C and 125 °C.

The diffractograms in Figure 179 were collected in the mesophase (25 °C) and near the clearing temperature (125 °C) they were radially integrated parallel and perpendicular to the magnetic field since the intensities of the pseudo Bragg reflections are situated in both directions, and the patterns are depicted in Figure 180 and Figure 181, respectively.

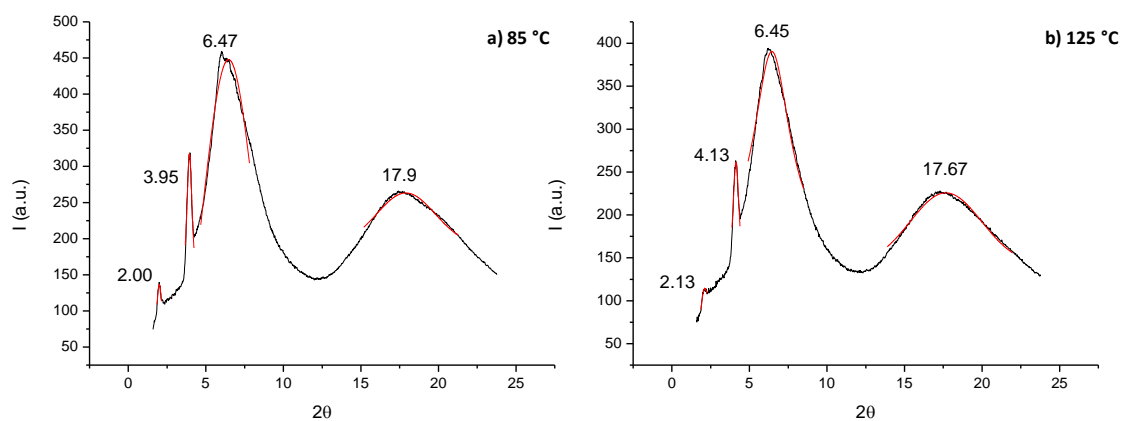


Figure 180 : Radially integrated plots parallel to the magnetic field \vec{H} at a) 85 °C and b) 125°C.

The peaks at 2θ values of 2 and 3.95 correspond to the first and second order diffraction of the smectic layer and agree with the ratio of 1:2, characteristic for this molecular arrangement. The value of 13.66 is the average distance between two cubes and 5 Å the intermolecular distance between two mesogens.

Table 19: d values calculated for the 2θ scans represented in Figure 180.

	85 °C				125 °C			
Peak	A	B	C	D	A	B	C	D
2θ	17.92	16.47	3.95	2.00	17.67	6.45	4.13	2.13
d (Å)	4.96	13.66	22.37	44.18	5.02	13.70	21.40	41.48

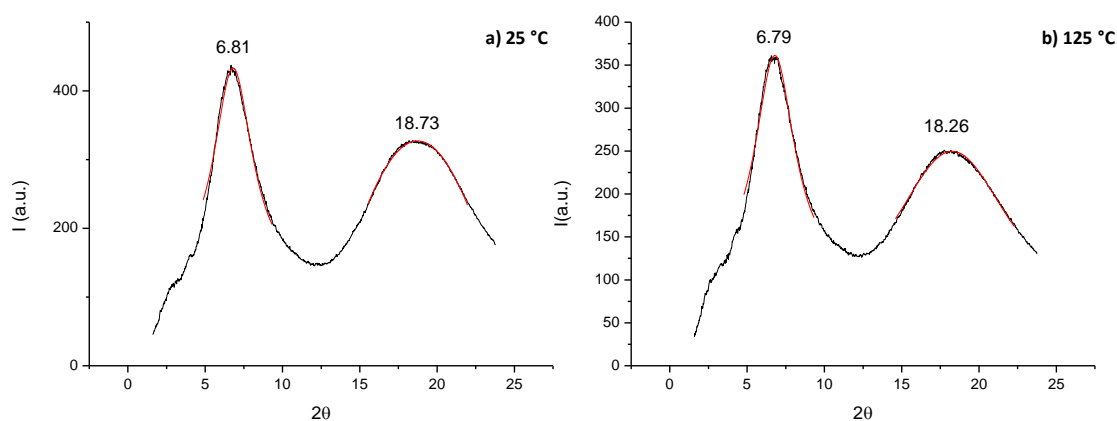


Figure 181: Radially integrated plots perpendicular to the magnetic field \vec{H} at a) 85 °C and b) 125°C.

Table 20: d values calculated for the 2 θ scans represented on Figure 181.

	85 °C		125 °C	
Peak	A	B	A	B
2 θ	18.73	6.81	18.26	6.79
d (Å)	4.74	13.66	4.86	13.02

The layer spacing of 44 Å was calculated from the first order diffraction peak and it is smaller than the length of a fully extended molecule (≈ 58 Å), suggesting interdigitation of the mesogens.

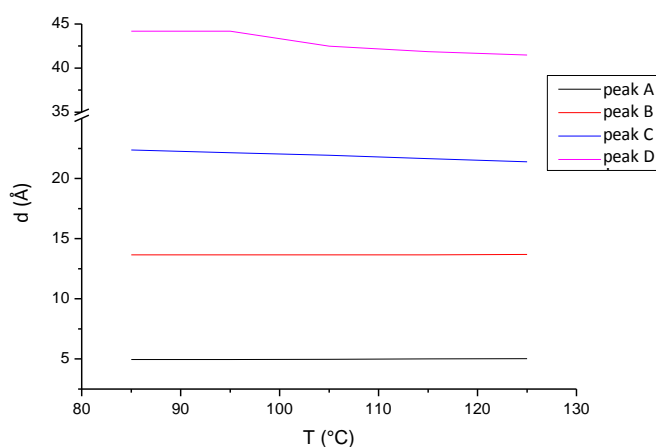


Figure 182: Variation of the layer spacing of compound 108 with temperature.

Variation of the layer spacing with temperature for compound **108** is plotted in Figure 182. There is a slight decrease of the layer spacing with an increase in temperature attributed to an increase in the disorder of the molecules within the layers. These results are in agreement with previously published data.¹³⁶

The χ -scans for peaks D and C are represented in Figure 183 below and confirm that the diffraction peaks are situated in the meridian region. Azimuthally integrated patterns for peak D (see a) and b) Figure 183) show some differences between the peaks above and below the equator. The peak around 260° is quite sharp at both temperatures, when compared to the peak situated at approximately 90°. It is possible that the some leakage by the beam stop occurs, considering that the 2 θ value for peak D is rather small. Also visible is a decrease in the intensity value as the sample is closer to the clearing temperature.

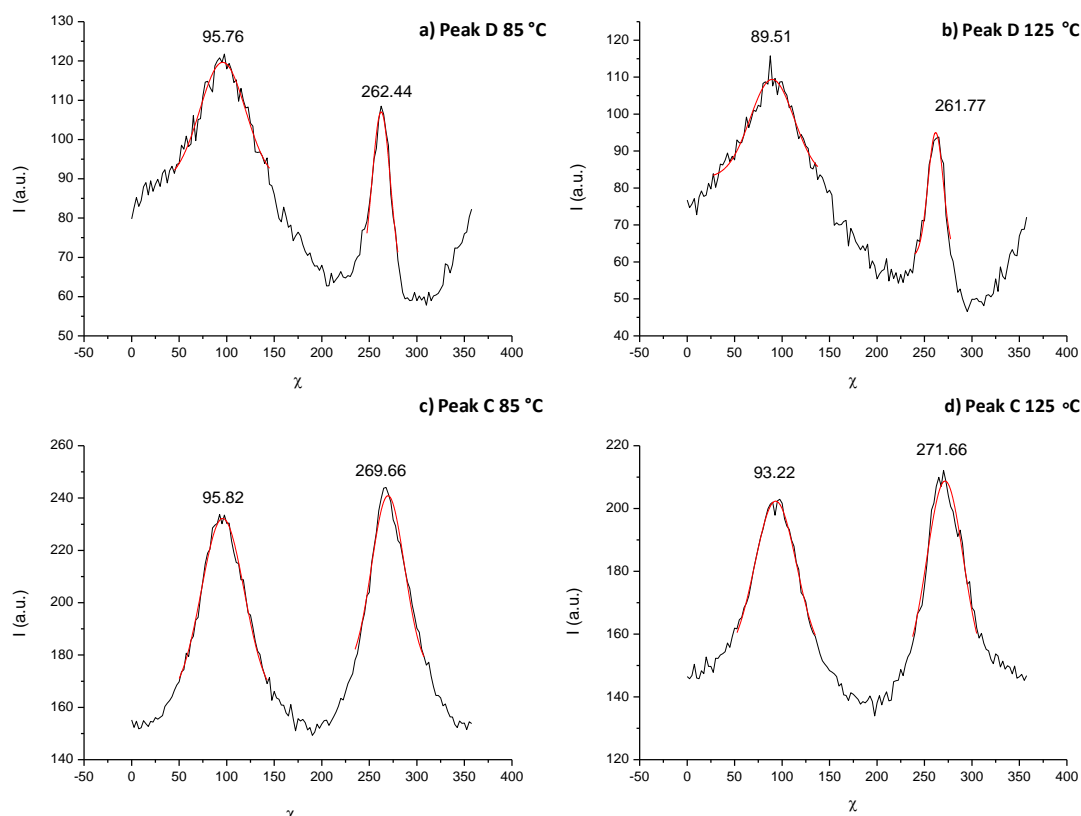


Figure 183: a) to d) azimuthally integrated plots for peaks D and C at 85 °C and 125 °C.

In contrast with plots a) and b) Figure 183, there is no strong difference between the integrated peaks, see c) and d) Figure 183, there is however a decrease in intensity as the temperature rises.

The diffraction corresponding to peak B (Figure 179) is very broad and intense and it was difficult to choose how to azimuthally integrate this peak. Since 2 θ - scans of this broad reflection in the directions parallel and perpendicular to the magnetic field did not show any extra peaks. The region used for the χ -scans is represented in Figure 184 and has a narrow 2 θ interval including sole peak B.

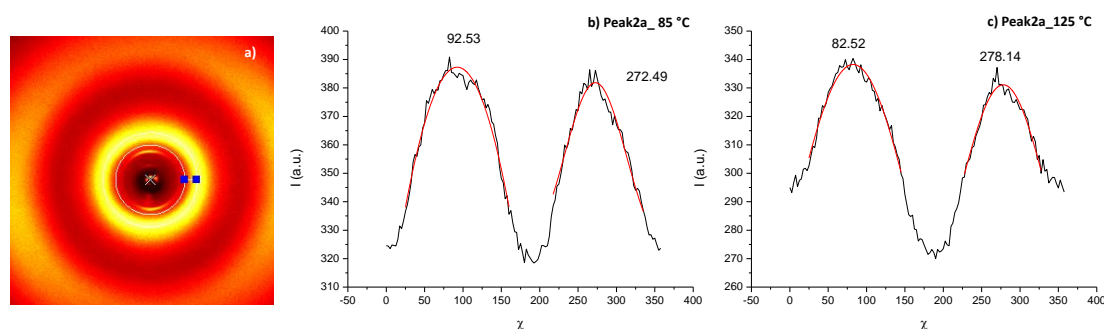


Figure 184: a) Diffraction pattern and representation of azimuthally integrated region. b) Azimuthally integrated plot for compound 108 at 85 °C. c) Azimuthally integrated plot for compound 108 at 125 °C.

The integration represented in Figure 184 a) to c)) shows the existence of two peaks situated in the meridian region.

The XRD data collected confirms that this compound has a SmA phase and the correlation length calculated using Scherrer's equation has a value of 292 Å, corresponding to approximately five molecular lengths.

The molecular volume calculated for this compound is 6300 Å³ following the same approach described above and using the d spacing value obtained from the diffraction patterns of 44.18 Å, the diameter a simple model of a cylinder would be ≈ 13.47 Å, this value is large enough to accommodate two aromatic cores when compared to ≈ 13 Å obtained for the minimum height required to accommodate two stacking aromatic cores (1.5 x 2 = 3 Å) and the distances between them (5 + 2 (5/2)). In this case the molecules align with the magnetic field and a representation of the molecular packing as the one represented below (Figure 185) is in agreement with the data collected from XRD experiments.

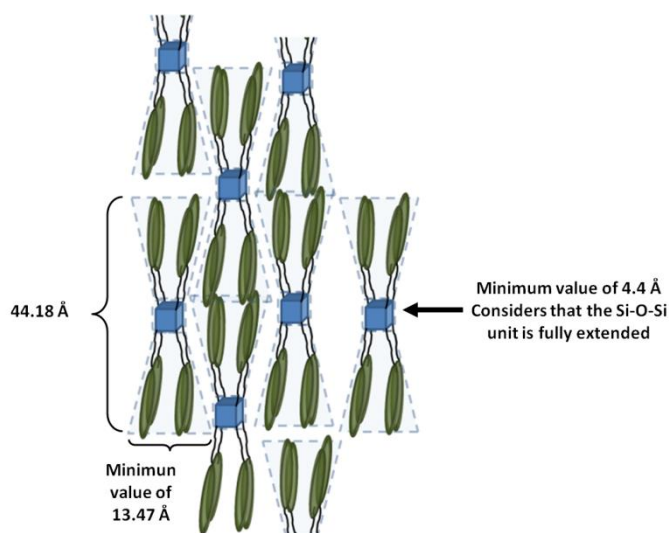


Figure 185: Model representing the self-assembly of 108.

Regarding the molecular packing suggested above, the molecules are represented as having a spindle shape, thinner in the centre and larger on the edges. This is easily explained since the minimum width occupied by two mesogens is 13 Å, while the size of the silsesquioxane core (represented by the blue squares) is only 4.4 Å. The siloxane spacer should be taken into account since it can be fully extended or not. The first one considers a slimmer rectangle representing the Si-O-Si bond parallel to the magnetic field, this would give the minimum distance in the central area of 4.4 Å (considering only the silsesquioxane core). In the extreme situation where the Si-O-Si unit is oriented

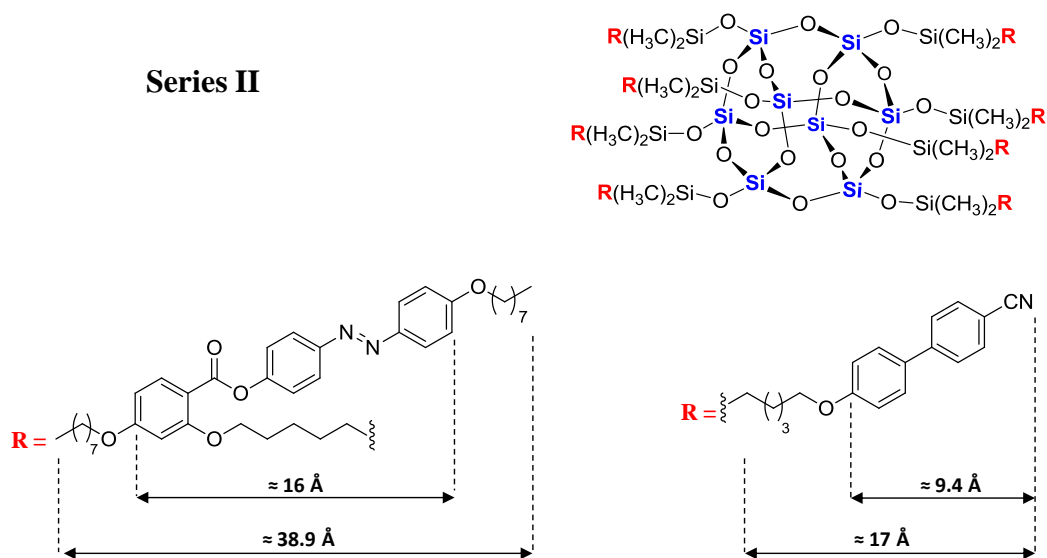
perpendicularly to the external magnetic field, the central area would be larger and the maximum width could be 10.6 Å (4.4 Å + 2(3.1 Å)). Interdigitation between the cyanobiphenyl groups is likely to occur, considering that the calculated length of the fully extended molecules is 59.64 Å (this value accounts for two mesogens (24.52 Å) + silsesquioxane core (4.4 Å) + Si-O-Si groups (6.2 Å)), which is larger than the d spacing obtained by XRD diffraction.

For this series of compounds it is possible to see that the Lam N phase is persistent even when a mesogen such as cyanobiphenyl with an undecyl spacer, which has a strong tendency to form smectic phases, is present in large amounts. Changing the proportions of azobenzene and cyanobiphenyl introduces some changes in the phase structure yet the packing in a Lam N phase is overriding.

With increasing amount of cyanobiphenyl it seems that arrangement of the cyanobiphenyl in a smectic-like manner becomes stronger until the formation of a SmA phase in compound **108** where no azobenzene is present. The existence of the *cis* isomer of the azobenzene mesogen contributes possibly to the formation of the N phase.

XRD discussion of Series II

Series II



Compound	% of mesogens determined by ¹ HNMR		Calculated ratio of mesogens		Phase transitions
	96	98	96	98	
104	100	-	8	-	Tg 9 N 56 Iso
109	64	36	5	3	Tg 8 N 52 Iso
110	25	75	2	6	Tg 17 N 58 Iso
111	-	100	-	8	I 130 Sm 85 Iso

Figure 186: Scheme of series II.

Compound 109

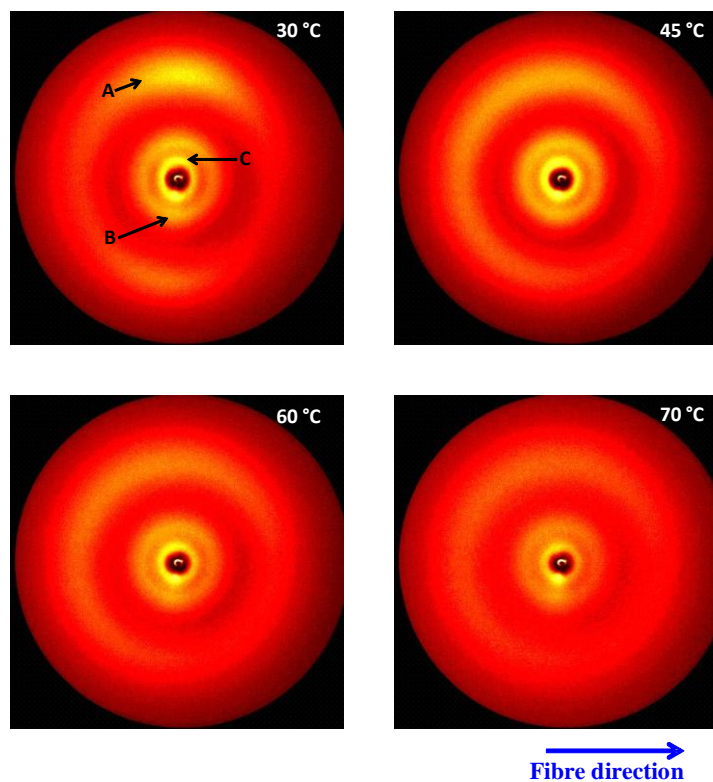


Figure 187: Diffractograms of compound 109 at different temperatures.

The figure shows four 2D diffractograms of compound **109**, collected in the mesophase (30 °C and 45 °C) and for the isotropic state (60 °C and 70 °C). The θ scans for these temperatures are presented below and there is a decrease of the 2θ values for the three peaks with increasing temperature.

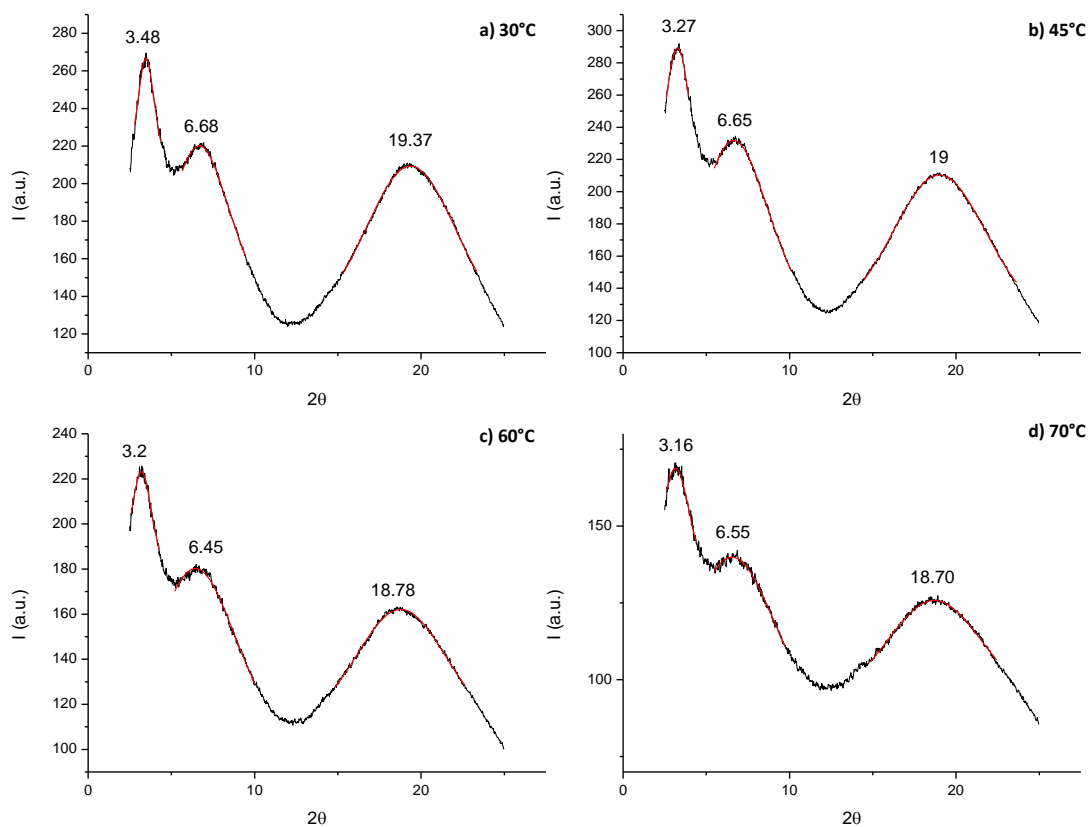


Figure 188: Radially integrated plots for 109: a) 30 °C; b) 45 °C; c) 60 °C; d) 70 °C.

The 2θ values are shown in Table 21. At 30 °C, peak A is related to the distance between the liquid crystalline groups, peak B is associated with the distance between two silsesquioxanes and peak C can be connected to the length of the mesogenic units. The assignment of peak C can be made considering the calculated lengths of both mesogens. The aromatic core of **96** is about 34 Å which is larger than 25.39 Å calculated for peak C. The cyanobiphenyl aromatic core is ≈ 17 Å that is smaller than the d-spacing value obtained. Having this in mind, and the values obtained before for the d-spacings, it is more likely that the value associated with peak C is related with the azobenzene unit. As the experimentally found length (≈ 25 Å) is smaller than the calculated value (≈ 34 Å) this suggests that interdigitation of the azobenzene molecules occurs.

Table 21: d values calculated for the 2θ scans represented on Figure 188.

	30 °C			45 °C			60 °C			70 °C		
Peak	A	B	C	A	B	C	A	B	C	A	B	C
2θ	19.37	6.68	3.48	19.00	6.65	3.27	18.78	6.45	3.20	18.70	6.55	3.16
d (Å)	4.58	13.23	25.39	4.67	13.29	27.02	4.73	13.70	27.61	4.75	13.50	27.96

In χ -scan shown for peak A, the intensities are situated in the meridian region, in agreement to what was observed for the aligned samples of previously discussed compounds.

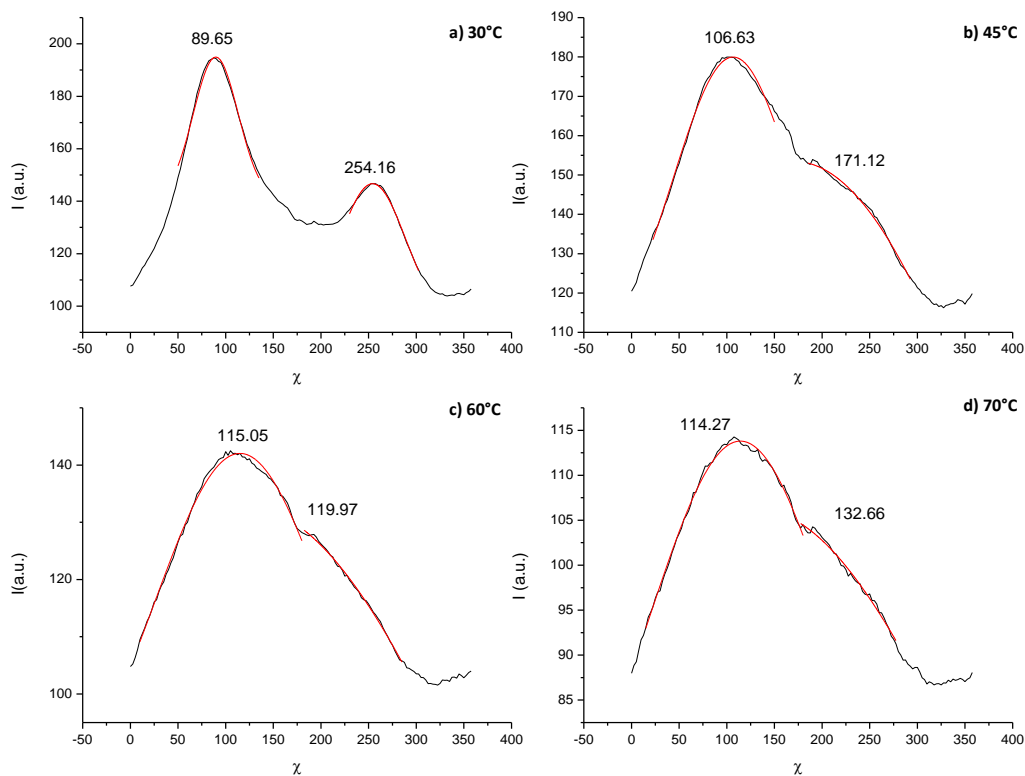


Figure 189: Azimuthally integrated plots of peak A for compound **109** at several temperatures.

The two peaks in Figure 189 a) show a large difference in intensities that is also visible in the 2D diffraction patterns (Figure 187). This could be related to a non homogeneous distribution of the fibres within the capillary. The changes between plot a) and b) Figure 189 are dramatic as the separation between the two peaks with approximately χ values of 90° and 254° is lost. This change in the plots could point to isotropisation of the sample yet this temperature (45°C) is 7°C below the clearing point obtained from the DSC curve, a surprising observation as other samples such as **110** retain some alignment even when heated at temperatures well above the clearing point.

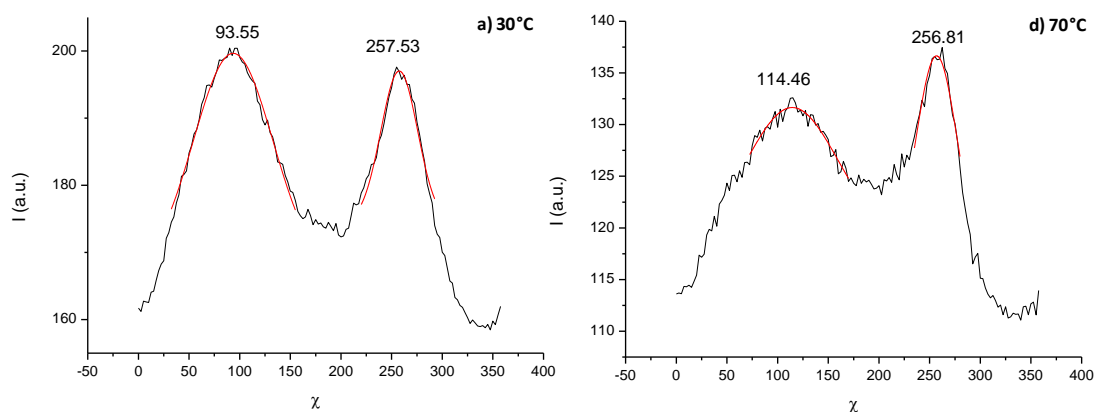


Figure 190: Azimuthally integrated plots of peak B for compound 109. a) 30 °C and b) 70 °C.

In the small angle region, the intensities related to peak B are also centered in the meridian region where the difference in intensities between the two peaks in the plot at 30 °C is almost none existing. An increase in temperature broadens the peaks, as they become less intense Figure 190 b). At 70 °C, there is a clear difference in the shape of both peaks with χ values of 114° and 257°. This last peak is reminiscent of the peaks found in previous compounds, and it is possible that some effect of the beam stop is present.

The χ -scans for peak C are also plotted and it is evident that the mesogens are also aligned perpendicularly to the magnetic field as the intensities are mainly situated in the meridian region.

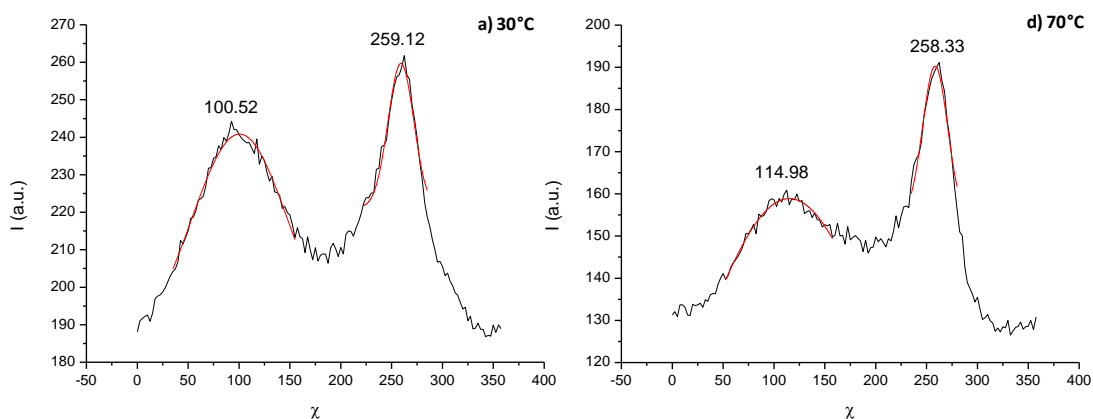


Figure 191: Azimuthally integrated plots of peak C for compound 109. a) 30 °C and b) 70 °C.

The difference in intensities between the two peaks is also apparent here and it supports the hypothesis that there is some interference of the beam stop in the peak at approximately 260°, as well.

In terms of structural arrangement of the molecules, the results point to a lamellar nematic phase as proposed for compound **104**. However considering that this material has also two different mesogens (azobenzene and cyanobiphenyl with a pentyl spacer)

and the results discussed previously for **106** and **105**, the absence of a fourth peak or any suggestion of formation of local smectic layers was surprising. This could be related with the amount of cyanobiphenyl present in this material, contrary to previous samples where the amount of this co-mesogen was at least 50 %, while in this sample this amount is only 36%. It is possible that the effect of local smectic layer formation is not strong enough for it to be evident. Nevertheless this could also be a consequence of a reduction of length of the alkyl chain spacer, see Figure 186, which is now of the same size as that of azobenzene unit.

In this series, the length of the cyanobiphenyl spacer decreases from an undecyl (discussed previously) to a pentyl group. The correlation length of the molecules was calculated and a value of 68 Å corresponding to 1.5 molecules was obtained.

Considering the diffraction patterns the mesogens are aligned also in the fibre direction. The calculated V_m for this material is 8339 Å³ and the layer spacing obtained from the XRD data is ≈ 25.39 Å, which was attributed to the length of the interdigitated azobenzenes.

An initial approach using this value as the length of a cylinder led to a molecular area of $8339 \text{Å}^3 / 25.39 = 328.44 \text{Å}^2$. The cylinder associated with this area has a diameter of 20.45 Å, which despite being large enough to accommodate the stacking of two aromatic groups and the distance between these molecules ($1.5 \times 2 + 2 \times 4.58 = 12.16$ Å) does not accommodate the length of the molecules of 44.6 Å (two cyanobiphenyls ($\approx 17 \times 2 = 34$ Å) + two Si-O-Si spacers ($3.1 \times 2 = 6.2$ Å) + silsesquioxane core 4.4 Å).

This compound has now a higher proportion of azobenzene materials suggesting that the situation could resemble the molecular arrangement discussed for **104** of a bulkier central area due to the distribution of the azobenzenes around the silsesquioxane core but as discussed above, this model does not accommodate the length of the molecules. In order to do so, it was considered that the length of the molecular tube was the double of the layer spacing. Therefore, $8339 \text{Å}^3 / (25.39 \times 2) = 164.22 \text{Å}^2$. Considering a cylindrical arrangement, the height of this cylinder would be 14.46 Å, which is enough to accommodate the minimum height of two stacked aromatic groups. When compared to **106** or **105** the diameter of the central area is higher (13.2 Å and 12.6 Å respectively) which is not surprising as the number of azobenzenes accommodated in this area varies from 4 in **106** to 3 in **105** and 5 in the molecule here discussed.

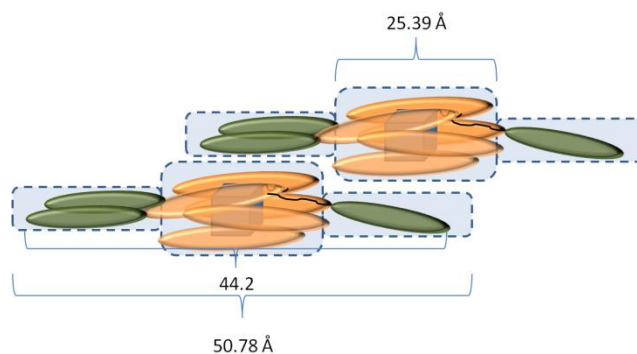


Figure 192: Representation of possible packing of molecules in the Lam N phase in 109.

The packing shown in Figure 192 fits with the layer spacing observed in the XRD data. As the molecules have a more bulky centre because of the higher content of azobenzenes and the cyanobiphenyl content is smaller as is the length of these molecules, no interdigitation of the cyanobiphenyls aromatic units occurs. In this case the interdigitation of the molecules is larger, approximating the central bulkier cores together, fitting with the observation of the layer spacing. This model also takes into account the absence of electronic modulation of the cyanobiphenyls in the XRD diffractograms, contrary to what was observed for **106**, or **105** where it was present.

Compound 110

The XRD measurements for this compound were also carried out in a multiple fibre sample. Initially images were collected every 5 °C on heating from 25 °C to 80 °C (Program I). A second experiment was performed where data was collected on cooling (every 5 °C) from 160 °C to 25 °C. In the figure below selected diffractograms in the mesophase (25 °C and 45 °C), immediately above the clearing point 60 °C and in the isotropic state 80 °C are depicted, the blue frame sequence represents Program II. For both sets of pictures it is possible to see that in the isotropic state the diffraction patterns consisted of three diffuse concentric rings being responsible for three sets of diffuse pseudo Bragg reflections in the mesophase.

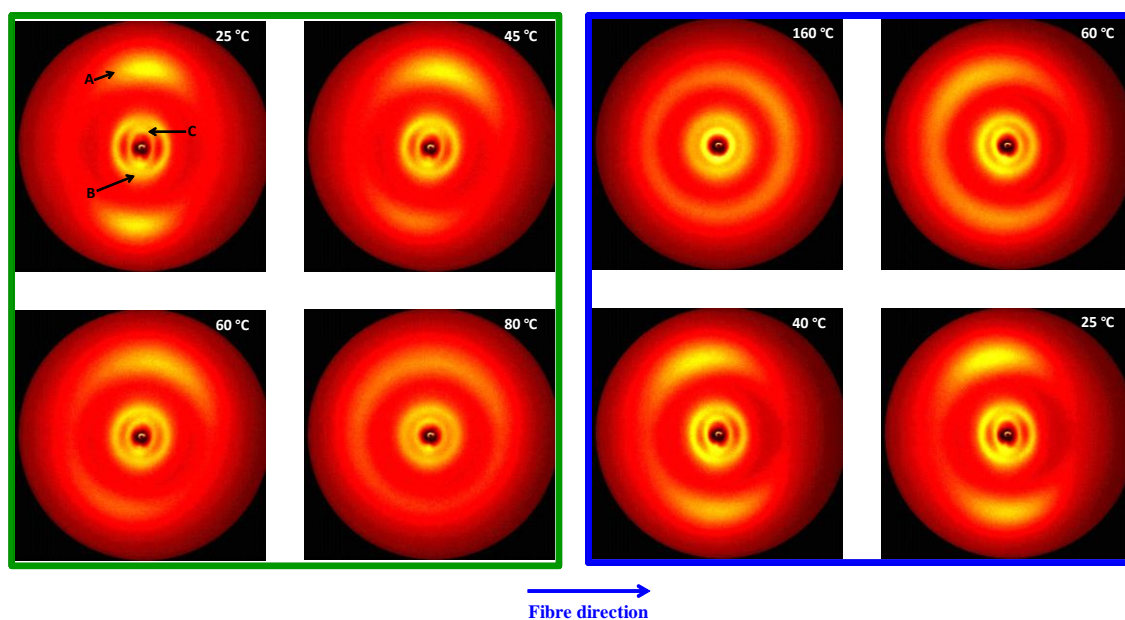


Figure 193: Diffraction patterns for 110, where the green sequence corresponds to Program I and the Blue to Program II.

The apparent deviation from the meridian region of the intensities of peaks A to C is surprising since this feature persists on cooling (Program II) but now the tilt is to the left of the meridian region. (Figure 193 T = 25 °C for example).

In order to try to determine the phase structure the focus will be on data collected from Program I.

The radially integrated scans for the temperatures represented in the 2D diffraction patterns of Figure 193, Program I, are plotted in Figure 194. Three peaks are present in the set of temperatures depicted and their 2θ values change slightly with increasing temperature. At 25 °C, peak A at 19.40 \AA ($2\theta = 4.56$) corresponds to the intermolecular distances of the oriented mesogens. The second diffuse peak in the small angle region corresponds to the distance between two silsesquioxane cores 13.5 \AA ($2\theta = 6.53$) and finally 18.9 being the length associated with the mesogens ($2\theta = 4.67$). The θ scans were plotted for the entire temperature range as well as the variation of the distance with the temperature for peaks A to C as represented in and Figure 195 a) and b), respectively.

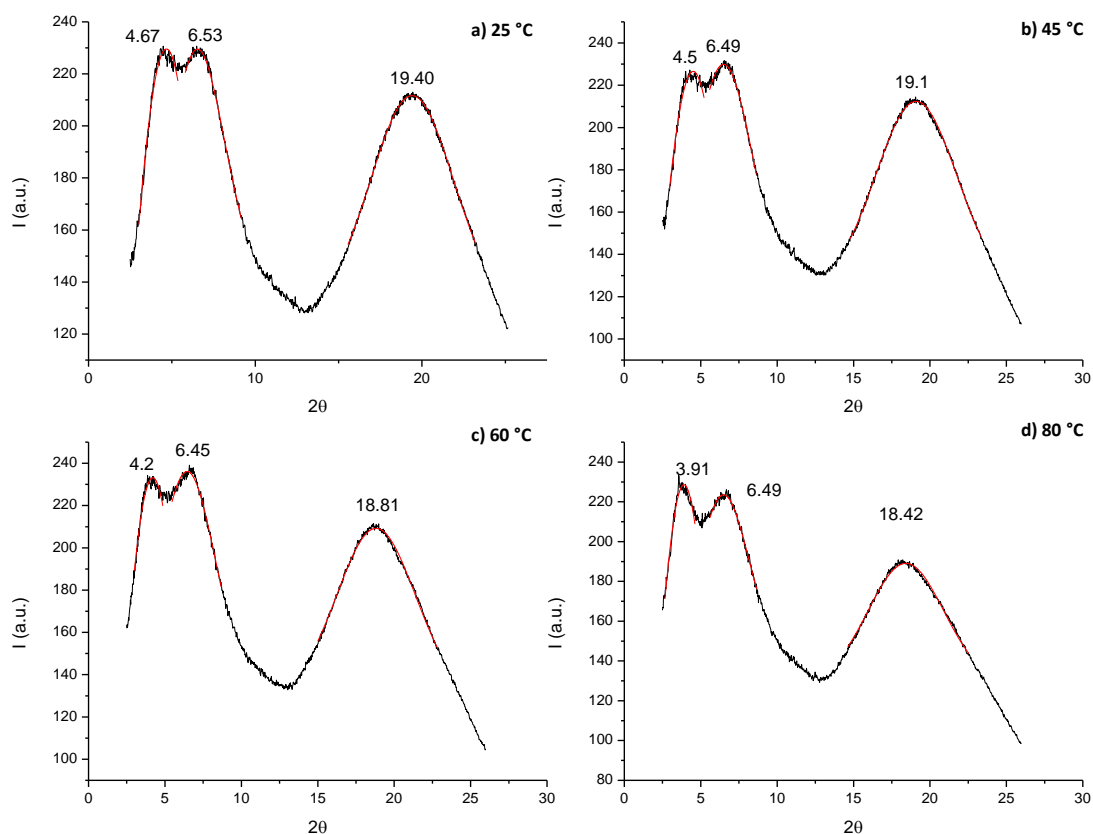


Figure 194: Radially integrated patterns of 110 for a) 25 °C, b) 45 °C, c) 60 °C and d) 80 °C.

Table 22: d values calculated for the 2θ scans represented on Figure 194.

	30 °C			45 °C			60 °C			70 °C		
Peak	A	B	C	A	B	C	A	B	C	A	B	C
2θ	19.47	6.53	4.67	19.1	6.49	4.50	18.81	6.45	4.20	18.42	6.49	3.91
d (Å)	4.56	13.54	18.92	4.65	13.62	19.64	4.72	13.70	21.04	4.82	13.62	22.60

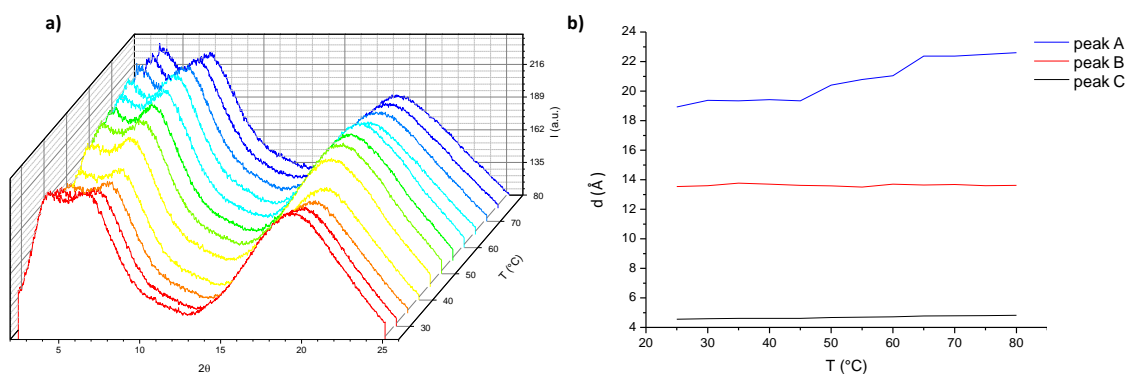


Figure 195: Radially integrated scans with temperature b) variation of distance with temperature.

Looking at Figure 195 a) it is possible to see that there is a shift in the 2θ values for peaks A and C, as well as a slight decrease in intensity with the temperature see Figure 194.

We can observe a slight increase within the intermolecular distances of the mesogens (black line) the silsesquioxanes however do not change much. On the other hand there is a clear increase in the “layer spacing” Figure 195 b).

The χ -scans are represented in the plots of Figure 196, Figure 197 and Figure 198, for peaks A, B and C respectively.

The χ -scans for the pseudo Bragg reflection on the wide angle region Peak A show that the intensities are situated in the meridian region at approximately 85° and 265° at 25°C confirming the tilt observed in the 2D pattern for the wide angle region. Since this tilt is mainly observed for the diffraction peaks situated above the equator, see Figure 193 Program I and II at 25°C , this tilt is not considered to be related with the phase structure. As the temperature increases a shift to smaller angles occurs and the intensity of the peak around 250° (Figure 196 a) to d)) diminishes. This might be because of the nature of the sample used. It is possible that with rising temperature the fibres melt and move position if this is the case X-rays will hit sample as well as air, explaining the difference in intensities observed, for example for the isotropic diffractogram (Figure 196, 60°C).

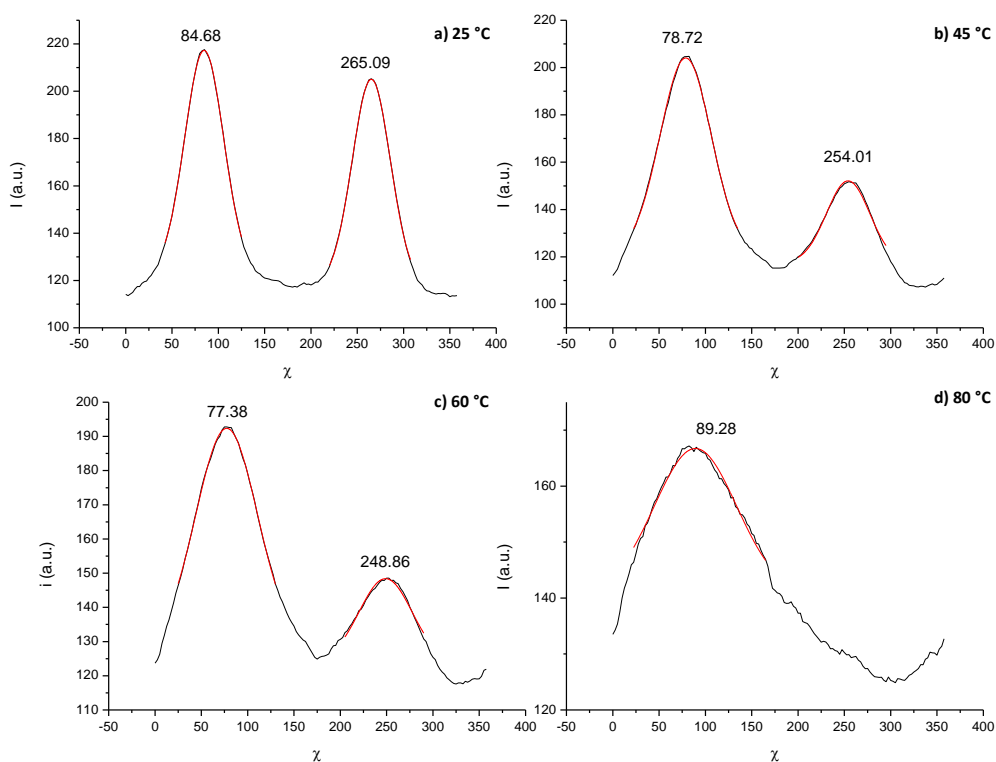


Figure 196: Azimuthally integrated plots of peak A for compound 110 for several temperatures, the plots show that the splitting of the peak for temperatures above 25°C these intensities have merged.

The χ -scan for Peak B at 25 °C show features resembling the one previously found for cybotactic clusters. The first peak of this plot Figure 197 a) shows a splitting that corresponds to $\approx 41^\circ$ from the meridian. Nevertheless in the second peak of the same plot this feature is not as prominent therefore the peak was integrated with single Gaussian curve and a maximum intensity recorded at 263°. These features seem to be lost with temperature and peak two (in plots a) to d) Figure 197 around 262°) gets sharper, which might be a consequence of some leakage from the beam stop, the central region of Figure 193 both at 25 °C and at 80 °C, corresponding to the mesophase and isotropic state, were expanded and are shown in Figure 198. It is noticeable a stronger reflection at angles close to 270° (that fit with the angles observed in the plots) occurs. This is highlighted by an arrow and it also seems that with temperature this feature becomes sharper, covering perhaps the splitting of second peak in the χ -scans at 25 °C, Figure 197.

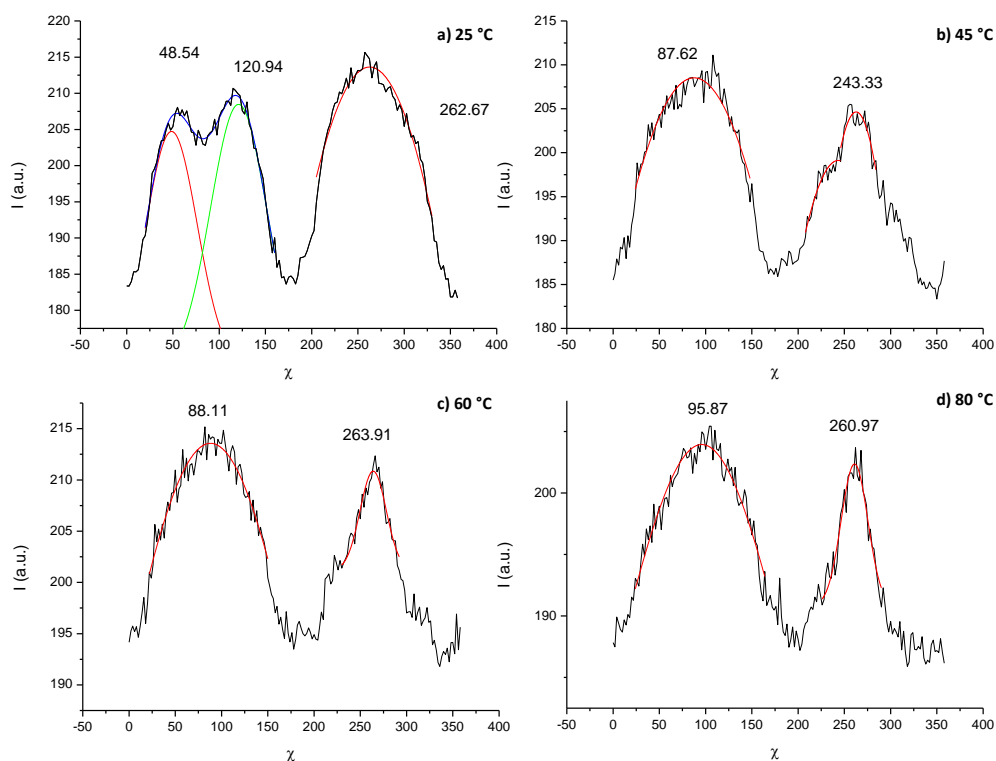


Figure 197: Azimuthally integrated plots of peak B for compound 110 at several temperatures, top figure shows at 25 °C a splitting of the peak. Above this temperature the intensities have merged.

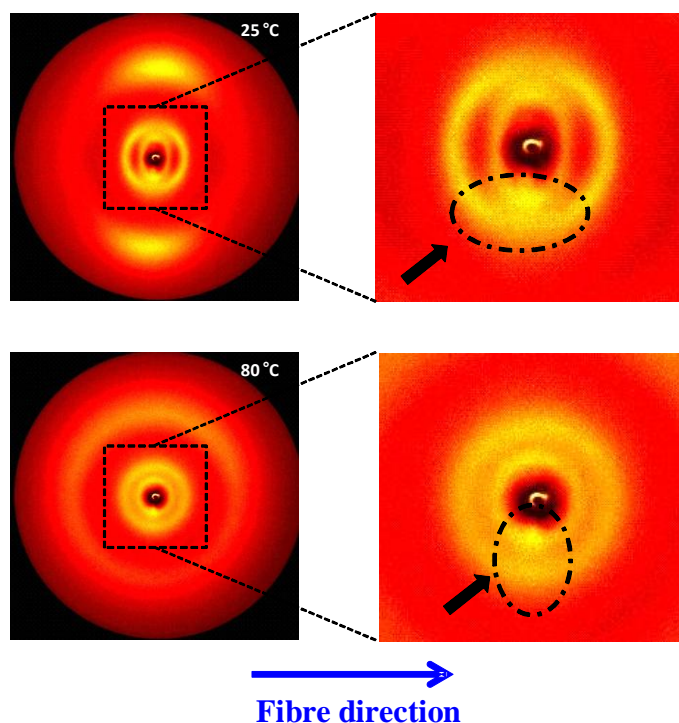


Figure 198: Amplification of the small angle region of the diffractograms of compound 110 at 25 °C top image and 80 °C bottom image.

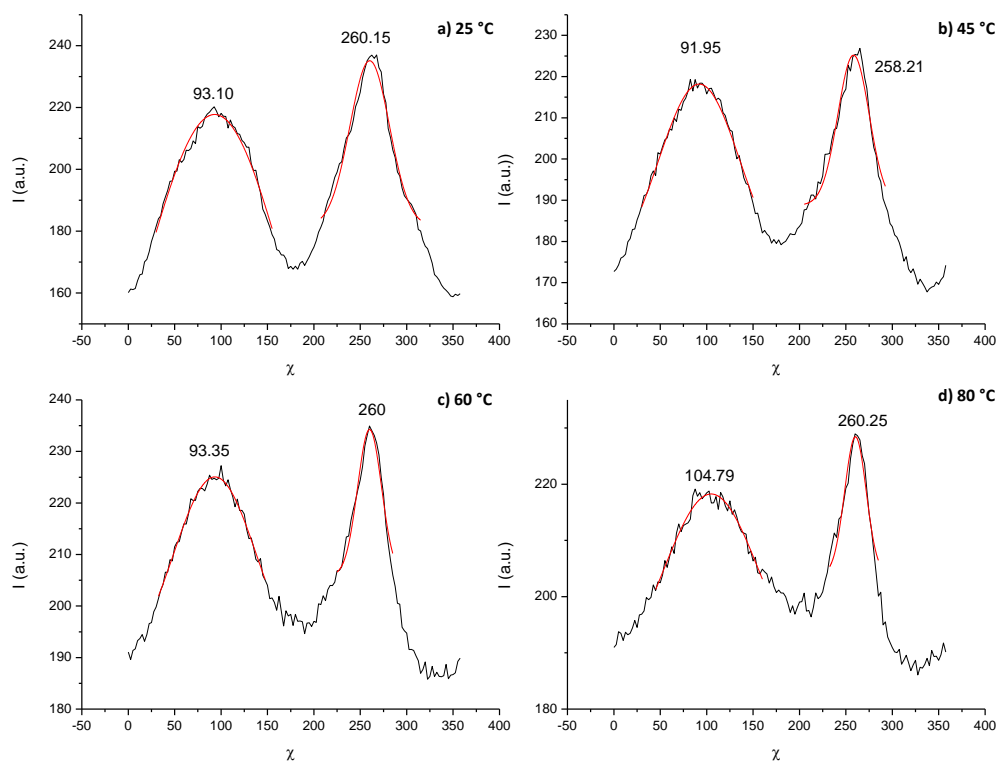


Figure 199: Azimuthally integrated plots of peak C for compound 110 at several temperatures.

Peak C is situated in the meridian region suggesting a layered structure. In the plots of Figure 199 it is evident that the peaks position does not change much with temperature

and that the peak at $\approx 260^\circ$ is considerably sharper and more intense when compared with the one situated around 90° .

When comparing compounds **109** and **110**, they differ mainly in the ratio of azobenzene derivative to cyanobiphenyl units (64% : 36%, **109** and 25% : 75% **110**- (azobenzene to Cyanobiphenyl)), the difference in the 2θ value related with peak C changes from $\approx 25^\circ$ at 30°C in **109** to $\approx 19^\circ$ at 25°C for **110**. This might suggest that in this latter compound, peak C is actually related to the length of the cyanobiphenyl ($\approx 17^\circ$) and that the peak associated with the azobenzene mesogen is not apparent, due to the fact that this is present in much lower concentrations in the system. The calculated value of $\approx 19^\circ$ indicates the lack of interdigitation between the cyanobiphenyl units, which could explain the absence of the formation of local diffuse smectic layers by these units within the lamellar nematic phase.

It seems that the higher content of cyanobiphenyl derivative in **110**, promotes the formation of cybotactic clusters by the silsesquioxane cores. However, despite the elevated content of cyanobiphenyl there was also no suggestion of the formation of local smectic layers in this compound. So it seems that the ratio between azobenzene and cyanobiphenyl promotes the formation of cybotactic clusters comprising the inorganic-organic silsesquioxane cores, while the length of the cyanobiphenyl mesogen, including the spacer, determines the formation of smectic layers-like within the lamellar nematic phase.

The correlation length of the molecules was calculated and the obtained value was $\approx 33^\circ$, corresponding to ≈ 1 molecular length.

The molecular volume calculated for this compound is 3882° . The estimation of the diameter is based on a simple model of a cylinder. Since the d spacing obtained from the diffraction studies of $\approx 19^\circ$ is too small to accommodate a full extended molecule, whose calculated length was $44 \approx^\circ$. It is proposed that the length used in the determination of the molecular unit parameter, should be twice the layer spacing obtained by XRD, this is $\approx 37.84^\circ$. Considering this value, the diameter of the cylinder can be calculated, $3882^\circ / 37.84 = 102.6^\circ$ and then $(102.6/\pi)^{1/2}$ and the value obtained is $\approx 11.42^\circ$. Although this value is smaller than the minimum value needed of 12.12° is not too distant that such arrangement could not form a possible molecular packing.

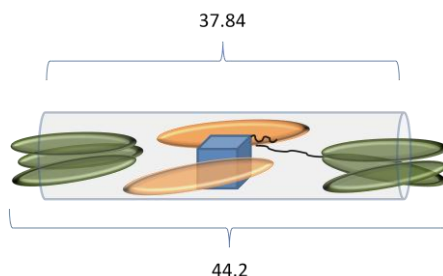


Figure 200: Representation of the molecular unit cell of 110.

The difference between the full length of the molecules 44.2 Å and the molecular footprint used (37.84 Å), can be accommodated by interdigitation of the cyano groups (≈ 2.5 Å) since $44.2 \text{ Å} - 37.84 \text{ Å} = 6.36 \text{ Å}$ which in turn this value leaves 3.18 Å at each side of the unit cell represented above. Together with some disorder of the alkyl spacers including perhaps some gauche conformation the cylinder model proposed above, seems to be in agreement with the X-Ray data obtained.

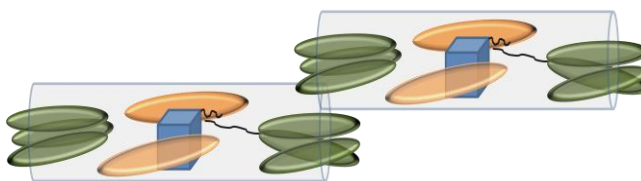


Figure 201: Representation of molecular packing of 110 considering the model proposed.

The molecular packing is represented in Figure 201, and it takes into account some interdigitation of the cyanobiphenyl units as discussed before. Regarding the phase structure, it is proposed that **110** has a lamellar nematic phase, has discussed previously, with weak interdigitation of the cyanobiphenyl groups and cybotactic clusters formed by the silsesquioxane cores with a tilt of 41° .

Compound 111

111 was assigned as a monotropic liquid crystal, and for that reason the X-ray diffraction experiments were made on cooling. In the figure below we can see the 2D diffraction patterns for the isotropic (180 °C) and the liquid crystalline phase (120 °C or 115 °C) and finally the diffractogram of the crystalline state (110 °C).

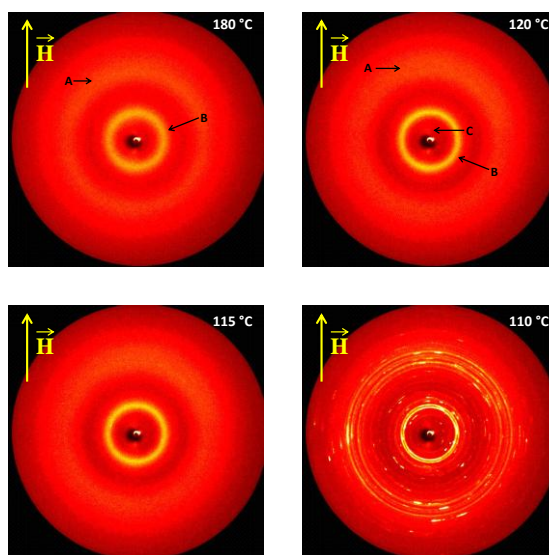


Figure 202: Diffractograms of compound 111 at different temperatures.

Compared to previous experiments the alignment in this sample is not as good, which is due to the fact that it was much more difficult to produce fibres from this material. This is a consequence of the temperature behaviour of the sample, as it is crystalline and even when fibres were pulled from the liquid crystalline state they tended to break quite easily (due to the absence of a glassy state), making them difficult to use.

From the isotropic to the LC phase, Figure 202, it is possible to identify that peak B becomes quite sharp, and despite being very weak, a sharp peak in the small angle region appears. At 110 °C the figure is typical of a crystal structure with many sharp rings.

In terms of θ scans the results are depicted below.

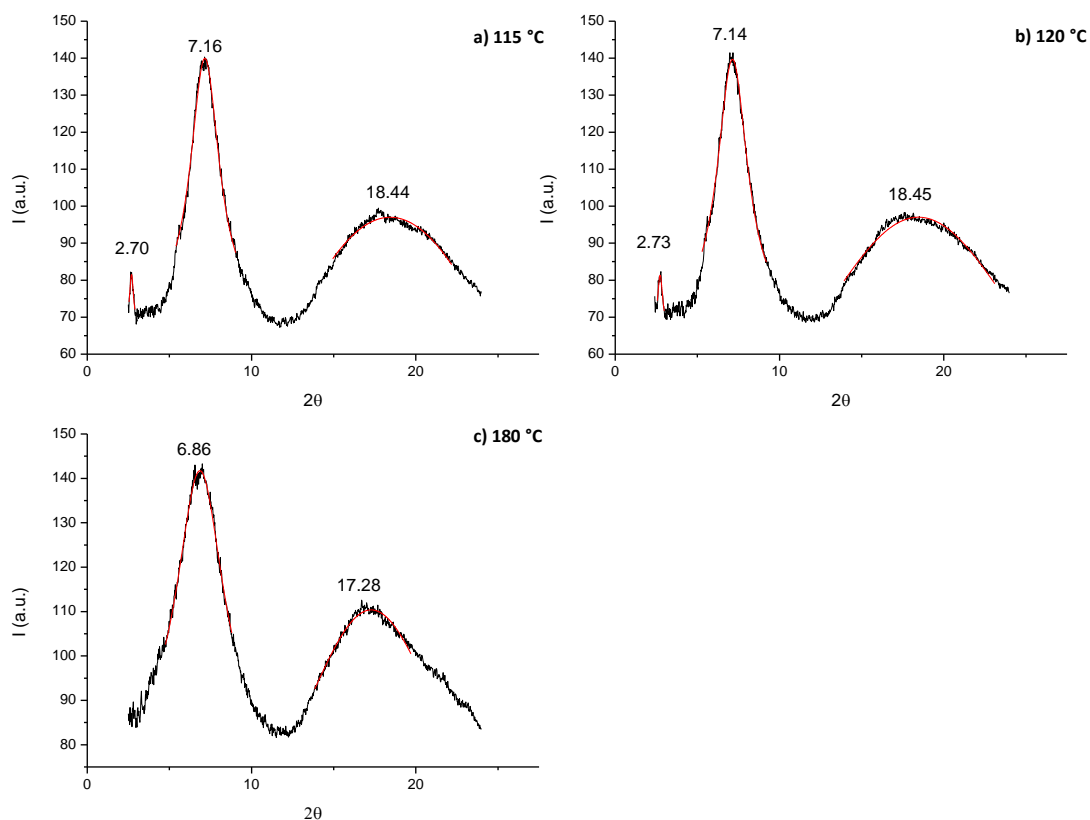


Figure 203: Radially integrated patterns of 111 for a) 115 °C, b) 120 °C and c) 180 °C.

The integration parallel to the magnetic field is presented above (Figure 203). In the LC phase a sharp peak that could correspond to the first order diffraction of the smectic phase is observed at a $2\theta = 2.70$ and d of 32.73 \AA , considering that the full length of a molecule is slightly bigger (35 \AA) that the calculated value it seems that the existence of weak interdigitation between the mesogenic groups is present. However the small value of intensity is very surprising. This peak is absent in the isotropic state. Peak B (see Table 23) is related to the distance between silsesquioxanes and compared to values obtained previously, this is slightly smaller. Finally peak A is associated with the molten chains in a liquid crystalline sample.

Table 23: Calculated distances for the 2θ values obtained at 115 °C.

Peak	A	B	C
2θ	18.44	7.16	2.7
$d \text{ (\AA)}$	4.81	12.35	32.73

χ -scan of peak A are shown in Figure 204.

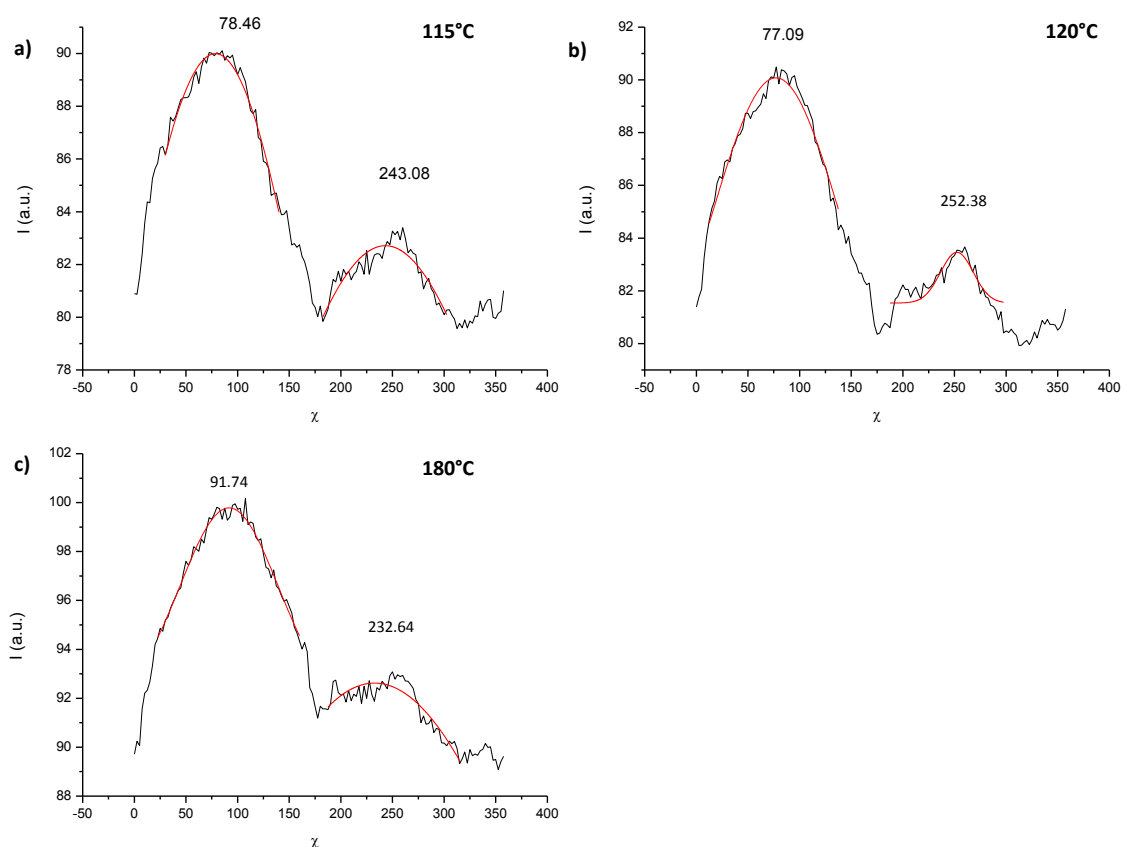


Figure 204: Azimuthally integrated plots of peak A for compound 111 at several temperatures.

It seems that there is a tilt in the reflection of the wide angle region from the isotropic to the LC phase of approximately 10° .

The χ -scans for peaks B and C are represented in Figure 205 and Figure 206 respectively. The lack of symmetry between 0 to 180 χ and 180 to 360 χ is evident and was already discussed however in this case, due to a high signal to noise ratio as well as a small number of counts, it makes it impossible to draw clear conclusions on the phase structure of this compound.

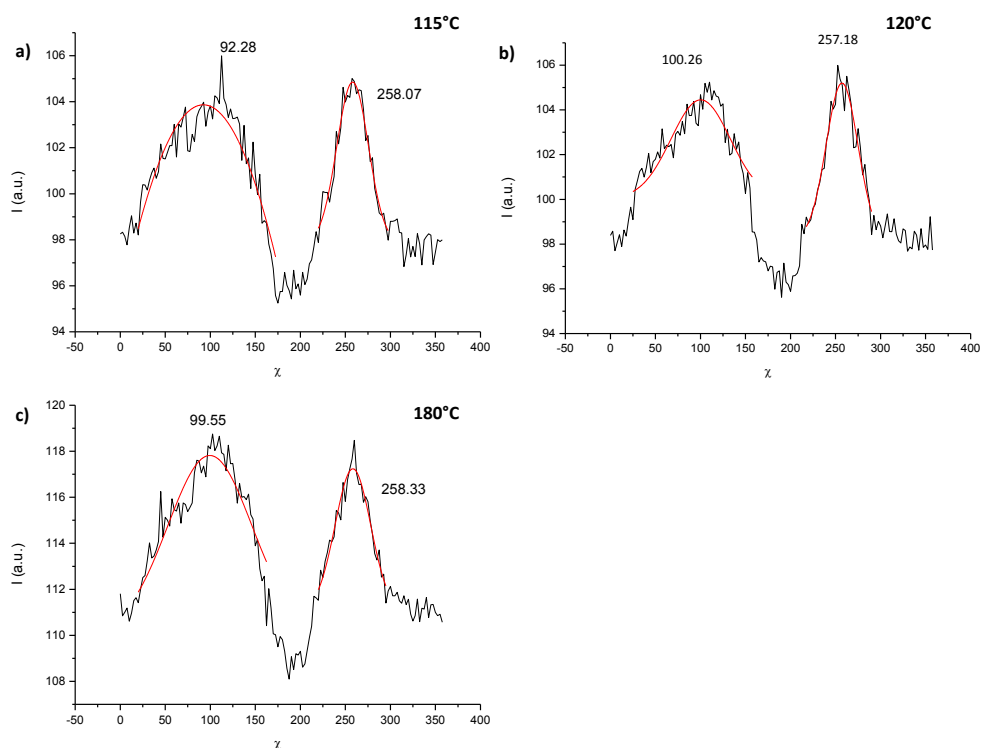


Figure 205: Azimuthally integrated plots of peak B for compound 111 at several temperatures.

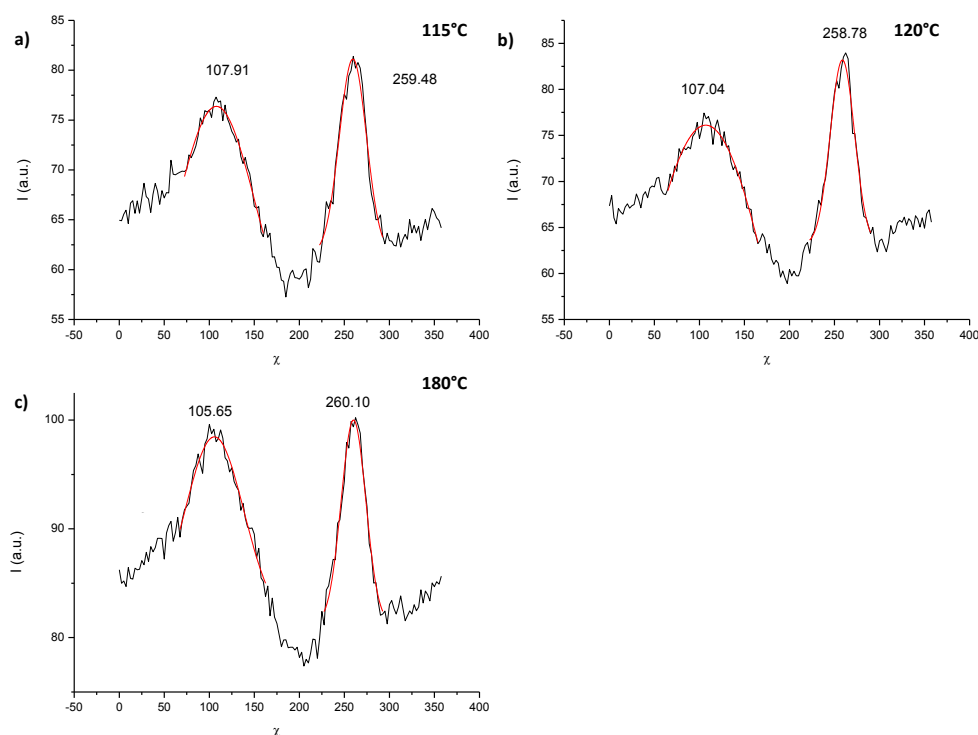


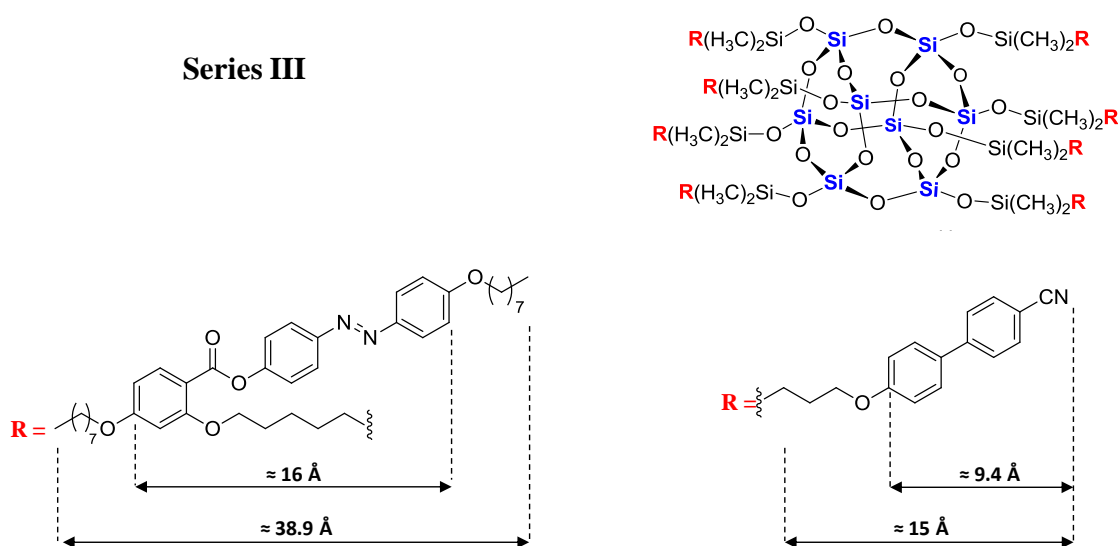
Figure 206: Azimuthally integrated plots of peak C for compound 111 at several temperatures.

The correlation length was calculated and the value obtained was 328 Å corresponding to roughly 11 molecular lengths.

The XRD data could not fully confirm the phase structure, as the sample could not be aligned, however all data obtained are in line with the formation of a SmA phase.

Series II is characterised by a shorter alkyl spacer of the cyanobiphenyl. Some changes of the structure of the lamellar N phase were observed such as the absence of smectic features, observed in Series I. The high content of cyanobiphenyl leads to the formation of cybotactic clusters of the silsesquioxane groups. In the absence of azobenzene mesogen, the formation of smectic phases is present.

XRD discussion of Series III



Compound	% of mesogens determined by ¹ HNMR		Calculated ratio of mesogens		Phase transitions
	96	99	96	99	
104	100	-	8	-	Tg 9 N 56 Iso
112	43	56	3	5	Tg 20 N 37 Iso
113	45	55	4	4	Tg 10 X 310* Iso
114	-	100	-	8	Tg 31SmA 121 Iso

* Highest temperature at which the compound was heated in the DSC and no endothermic peaks were observed

Figure 207: Scheme of series III.

Compound 112

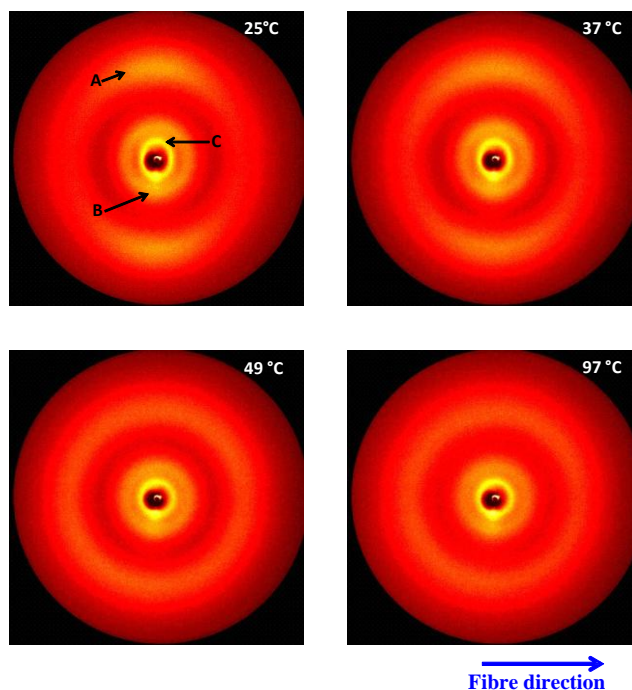


Figure 208: Diffractograms of compound 112 at different temperatures.

The XRD diffraction patterns for compound **112** acquired in a heating program from 25 °C to 115 °C were collected every 3 °C, and the exposure time was 1800s. In Figure 208 diffraction patterns collected in the mesophase at 25 °C, at 37 °C (corresponding to the onset temperature on the DSC data and therefore at the transition temperature to the liquid crystalline phase) are portrayed. The diffractograms show an aligned sample. 2D diffraction pattern for 49 °C and 97 °C are both above the clearing point and in the isotropic state, as suggested by the circular diffuse reflections.

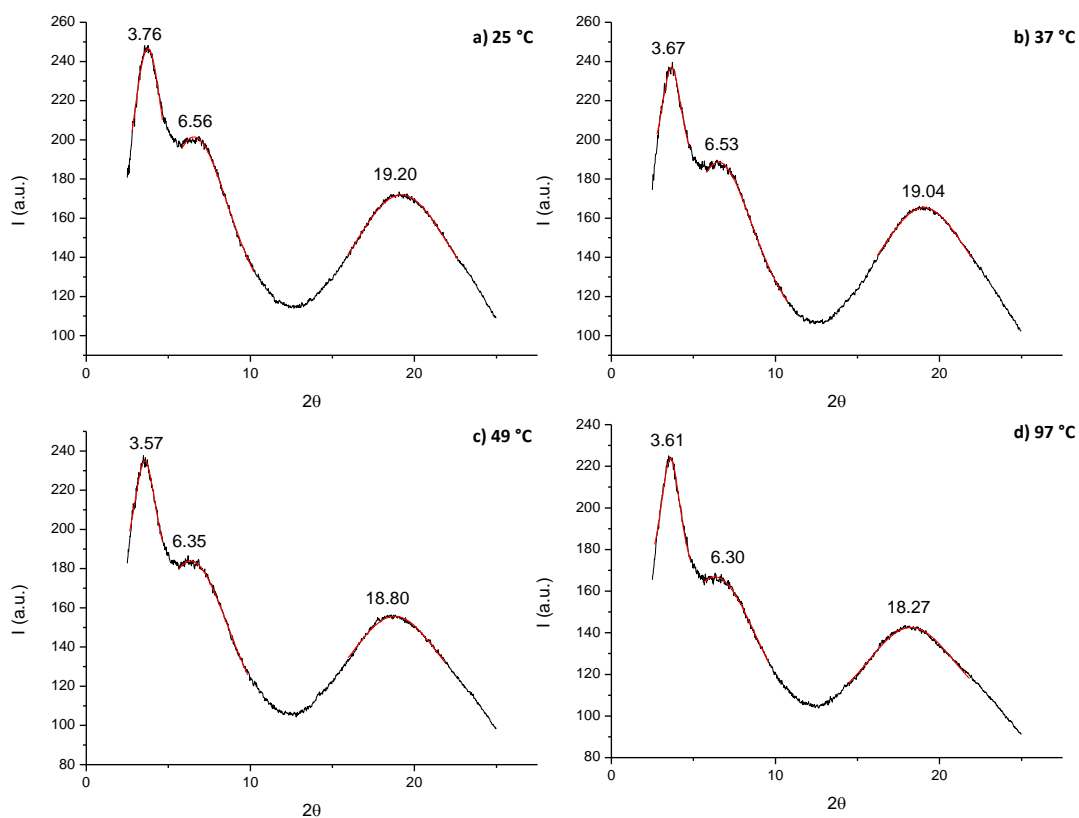


Figure 209: Radially integrated patterns of 112 for a) 25 °C, b) 37 °C, c) 49 °C and d) 97 °C.

In order to determine the mesophase structure an analysis of the data at 25 °C will be made. The XRD data for these systems shows the existence of three diffraction peaks, which are discussed next. In the wide angle region, the broad peak (peak A) $2\theta = 19.20$ and $d = 4.62 \text{ \AA}$, corresponds to the lateral distances between the liquid crystalline groups. In the small angle region there are two peaks attributed to the distances between two silsesquioxane cores, 13.48 \AA ($2\theta = 6.56$) and the length of the aromatic cores, 23.50 \AA ($2\theta = 3.76$). In Figure 210, the variation of the radially integrated plots with temperature is represented. The 2θ values do not change dramatically with temperature, however the intensity of the peaks decreases, reflecting a decrease in order.

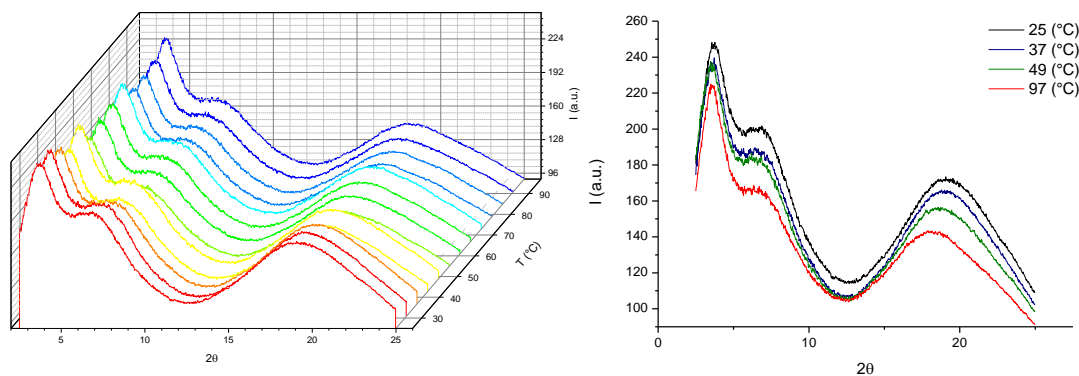


Figure 210: Dependence of θ scans with temperature.

The azimuthally integrated plots for peaks A, B and C are represented in Figure 211, Figure 212 and Figure 214.

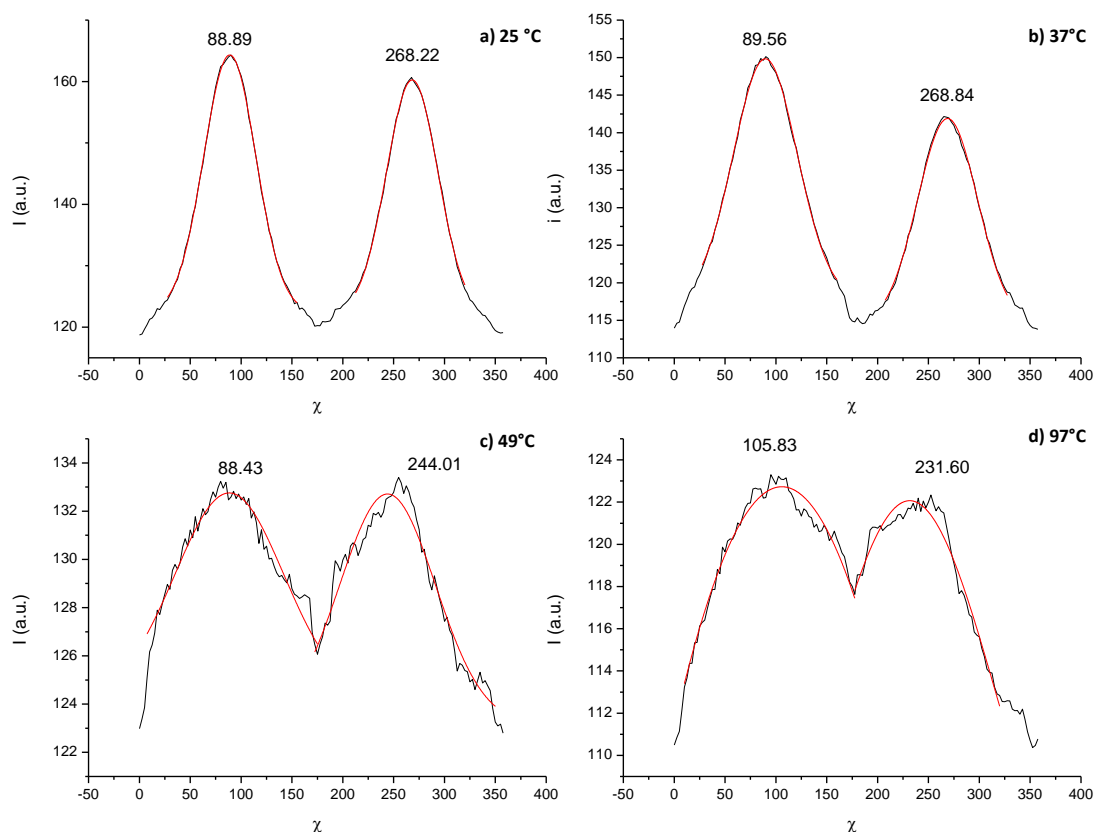


Figure 211: Azimuthally integrated plots of peak A for compound 112 at several temperatures.

Azimuthally integrated patterns of peak A are represented above. At 25 °C two peaks are situated in the meridian region, meaning that the molecules are aligned perpendicular to the magnetic field, in the direction of the fibre as observed for **104**, for example. With an increase in temperature these peaks tend to broaden and merge but contrary to what is expected for an isotropic sample, there seems that at 97 °C, well above the clearing point, the liquid crystalline groups, associated with peak A, still have preferred alignment along the meridian. Taking into account that compound **104**

showed a strong alignment memory, it is possible that this material has the same behaviour, explaining the apparent alignment along the meridian at 97 °C, Figure 211.

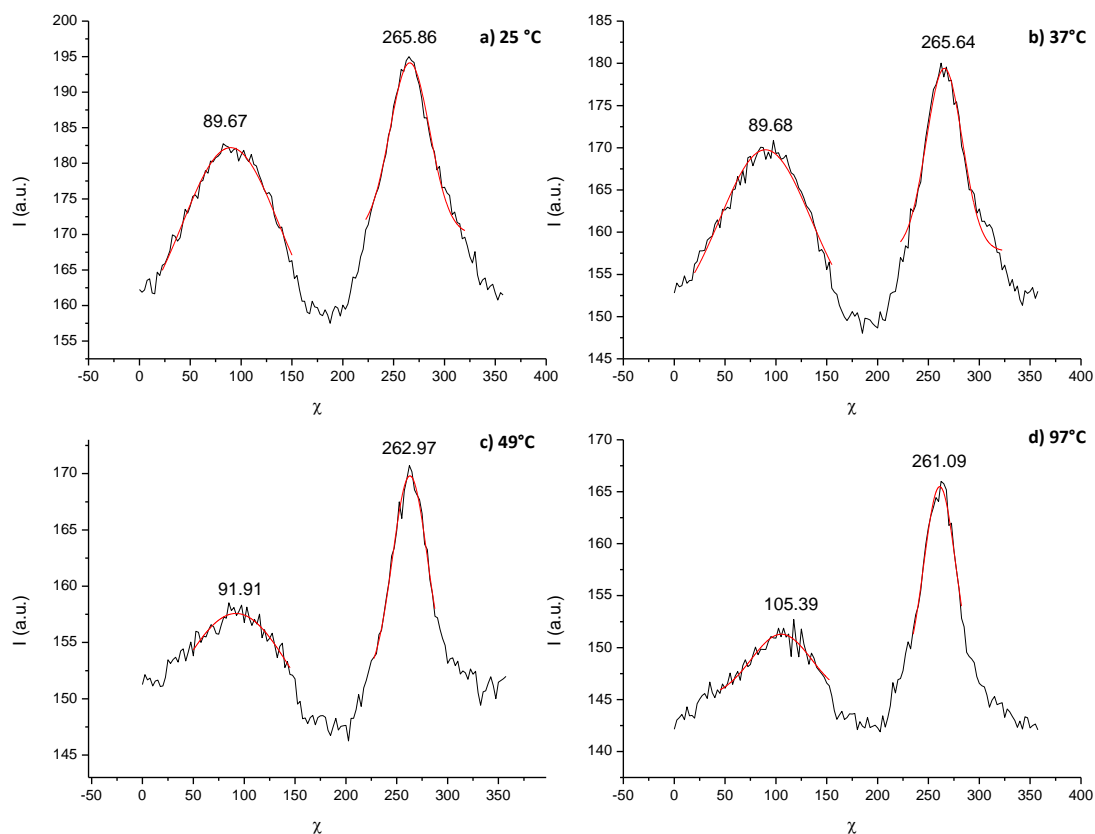


Figure 212: Azimuthally integrated plots of peak B for compound 112 at several temperatures.

Regarding peak B (Figure 212) it is also situated in meridian region and a significant difference both in the shape and intensity of the peaks at $\approx 90^\circ$ and $\approx 260^\circ$, is observed. The peak at approximately 90° is broader and less intense than the peak situated at approximately 270° . An expansion of the small angle region of the diffractogram at 25 °C is represented in Figure 213 and shows a more intense region at about that angle, which could explain the differences in the peaks. This feature could correspond to some leakage of the beam stop.

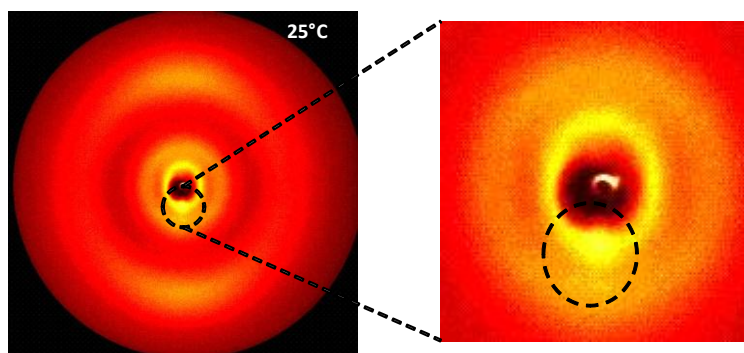


Figure 213: Amplification of the small angle region of the diffractogram of compound 112 at 25 °C.

The scattering distribution for peak C along χ is represented in Figure 214.

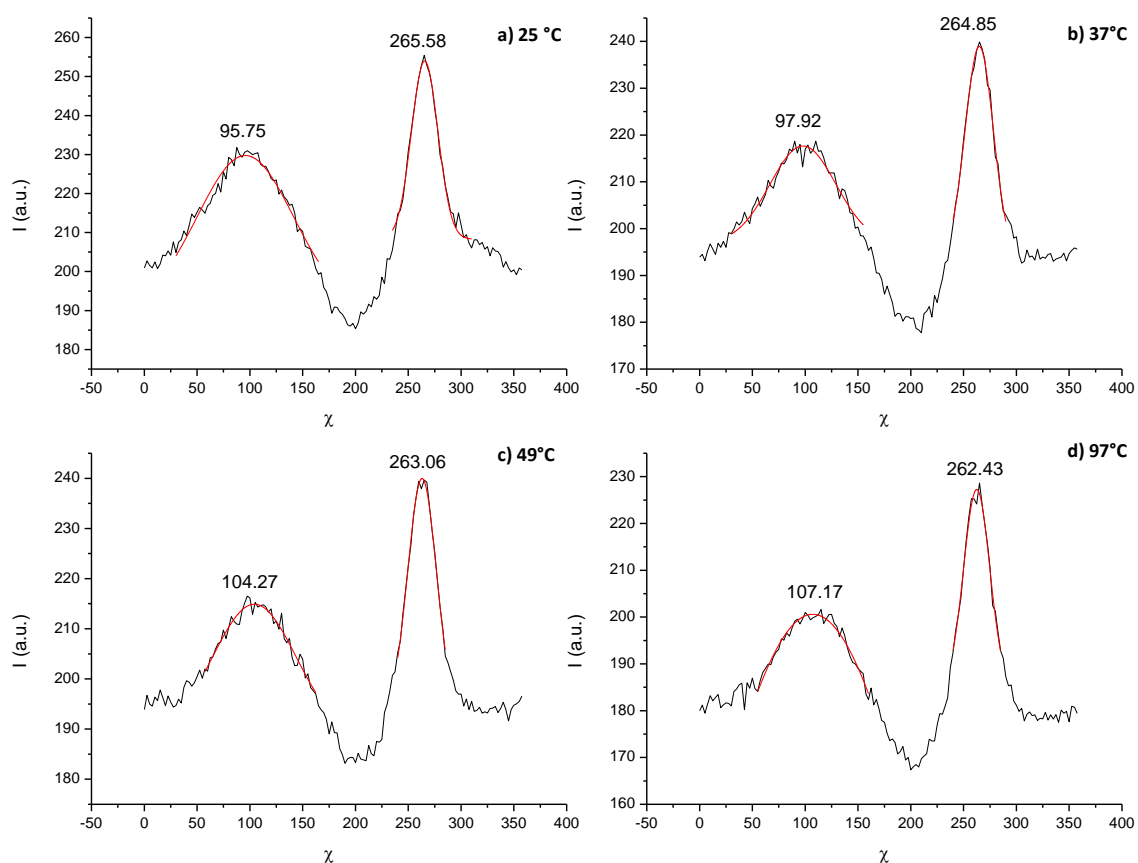


Figure 214: Azimuthally integrated plots of peak C for compound 112 at several temperatures.

The intensities of peak C are also distributed along the meridian region and no intensities at other angles are apparent. These results resemble the results obtained for compound **104** where a lamellar nematic phase with cybotactic clusters formed by the mesogenic units was proposed. In this compound, features of the lamellar nematic phase are present, yet the formation of cybotactic clusters does not occur. When compared with **106** which contains 48% of cyanobiphenyl units with an undecyl spacer, the formation of cybotactic clusters of SmC-like layers of the silsesquioxane cores, would be expected. Since this compound has a content of 56% of cyanobiphenyl units, the lack of the formation of cybotactic clusters by the silsesquioxane cores can be attributed to the short propyl spacer. From the examples discussed up to now, it should be emphasized the variety of phase structures presented by this series of compounds, where cybotactic clusters were observed either for the mesogenic groups **104** or for the silsesquioxane cores.

The molecular correlation length is $\approx 61.3 \text{ \AA}$ calculated using the Scherrer's equation and it corresponds to the length of one and a half molecules.

The molecular volume calculated for this molecule is 5636 \AA^3 and the layer spacing obtained by XRD experiments is 23.5 \AA corresponding to the length of the azobenzene. As the size of the length of the molecule is $\approx 37.2 \text{ \AA}$ (2 cyanobiphenyl units $2 \times 13.3 + \text{Si-O-Si spacer } 6.2 + \text{silsesquioxane core } 4.4 \text{ \AA}$) is larger than the layer spacing, a cylinder with twice the length of the layer spacing (47 \AA) will be considered. The associated diameter calculated is $\approx 12.4 \text{ \AA}$ ($5636 / 47 \approx 120 \text{ \AA}^2$ and $r = (120 / \pi)^{1/2} \approx 6.18 \text{ \AA}$, $d \approx 12.4 \text{ \AA}$) which is large enough to accommodate the minimum value calculated for two stacked aromatic rings 12.24 \AA .

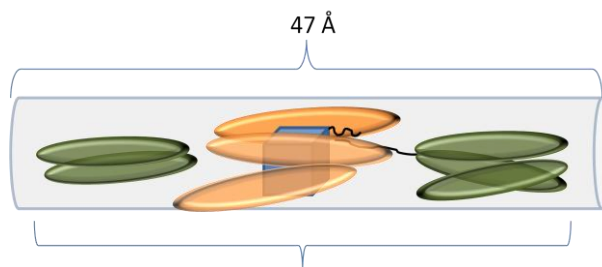


Figure 215: Proposed molecular packing for compound 112.

As suggested before, for compound **112**, when the molecules have a higher content of cyanobiphenyl, the volume of the molecule becomes more homogeneous and the central part is no longer so bulky therefore they fit better in a cylinder unit. The lamellar nematic arrangement of the molecules would be as represented in Figure 216.

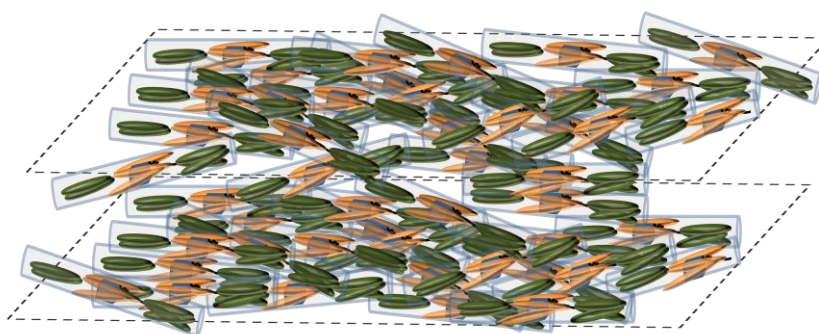


Figure 216: Proposed molecular arrangement on the lamellar nematic of compound 112.

Compound 113

The liquid crystalline behaviour **113** was discussed before; the X-ray studies were also performed in order to investigate the phase structure of this compound. The preliminary results obtained show a high ordered phase structure, very distinct from the lamellar nematic phase presented by the compounds discussed so far. This is surprising yet it

should be taken into account the GPC results discussed in Part I of the discussion. Investigations to clarify the phase structure of this compound are still ongoing.

Compound 114

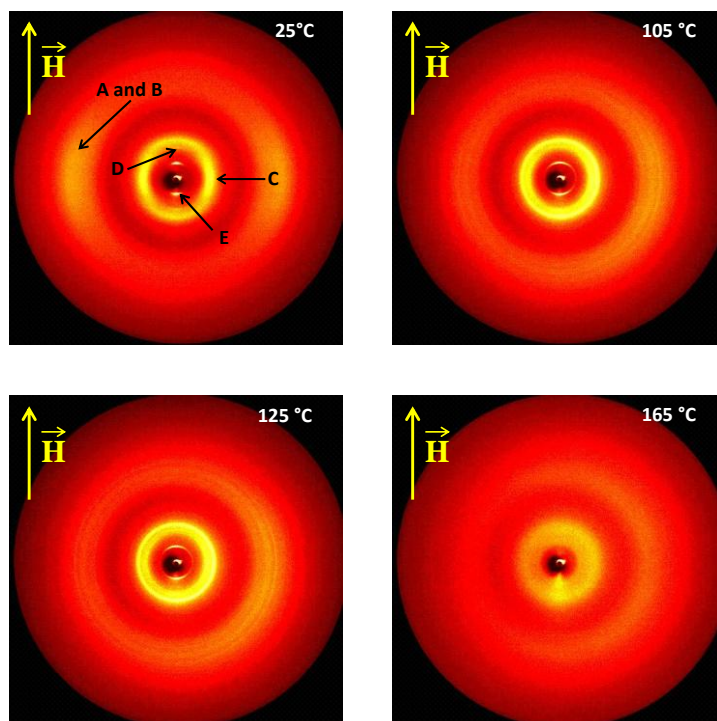


Figure 217: Diffractograms of compound **114** at different temperatures.

In the above figure the diffractograms for compound **114** can be seen. The diffractograms were collected at room temperature, just above the isotropization temperature and approximately 20 °C above clearing point correspond to temperatures of 25 °C, 105 °C and 125°C, 165 °C, respectively.

Comparing the diffraction patterns, there is a variation with increasing temperature. The wide angle region seems to change from a diffuse scattering, typical for the liquid crystalline state (Figure 217, 25 °C) to a set of diffuse quasi rings with stripes, see Figure 217 at 105°C). In order to emphasize this amplification of the wide angle region for temperature 25 °C and 105 °C are presented below (Figure 218).

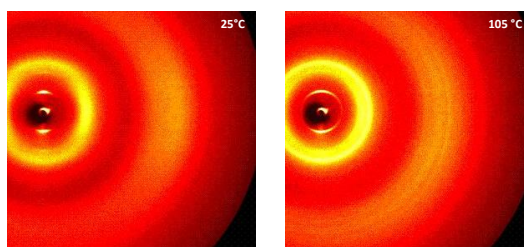


Figure 218: Amplification of the wide angle region of 114 at 25 °C and 105 °C.

Changes in the small angle region are also noticeable, the second order reflection associated with a smectic phase has disappeared and a sharp ring is now visible, the reflections situated in the equator are now also rings. In terms of the θ scans these changes are clearly visible in Figure 219.

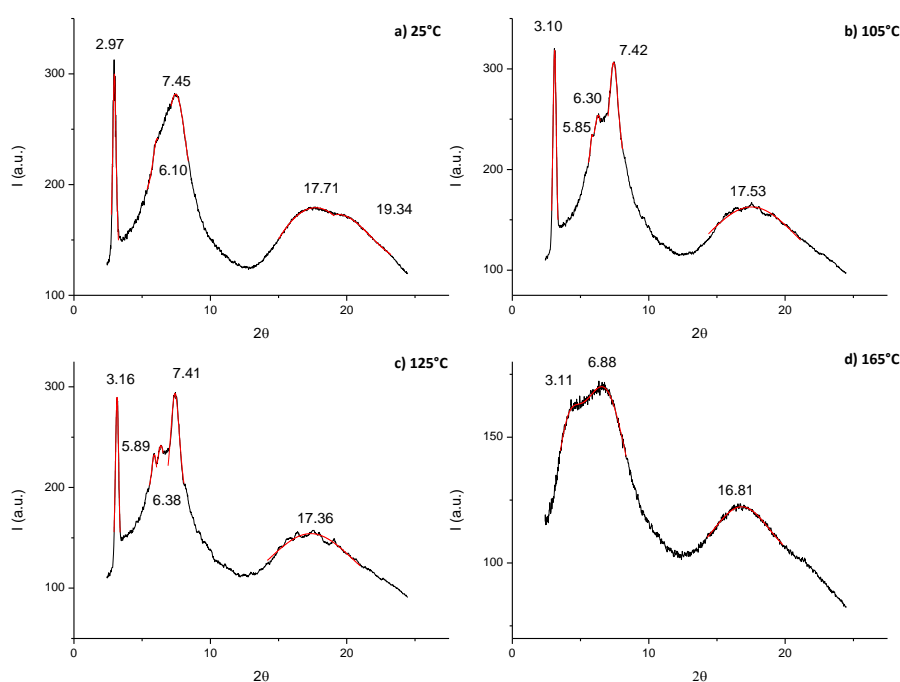


Figure 219: Radially integrated patterns of 114 for a) 25 °C, b) 105 °C, c) 125 °C and d) 165 °C.

The peak at 2θ value of 7.45 becomes sharp and more intense, (plots a), b) and c) of Figure 219) two other peaks seem to develop in the wide angle region; it seems that this peak has a detailed structure that disappears at 165 °C (Figure 219). From 125 °C to 165 °C, some peaks in the small angle region disappear. These data seem much more in line to what is expected for an isotropic sample, the sharp peaks corresponding to the layer spacing of the smectic phase become broader and less intense.

At 25 °C the X-ray spacings found are listed on the table below.

Table 24: Calculated distances for the 2 θ values obtained at 25 °C.

Peak	A	B	C	D	E
20	19.34	17.71	7.45	6.10	2.79
2.79	4.59	5.01	11.87	14.49	31.67

Peaks E and D are related with the first and second order pseudo-Bragg reflections associated with the smectic layer thickness and indicate a high degree of smectic order in the sample. However for a smectic phase a higher value of intensity was expected. In fact the intensity values are in the same order of the ones obtained previously for the nematic phases.

Since peaks A and B are mainly in the equator, θ scans in the direction perpendicular to the magnetic field were also plotted and the results are shown below (Figure 220).

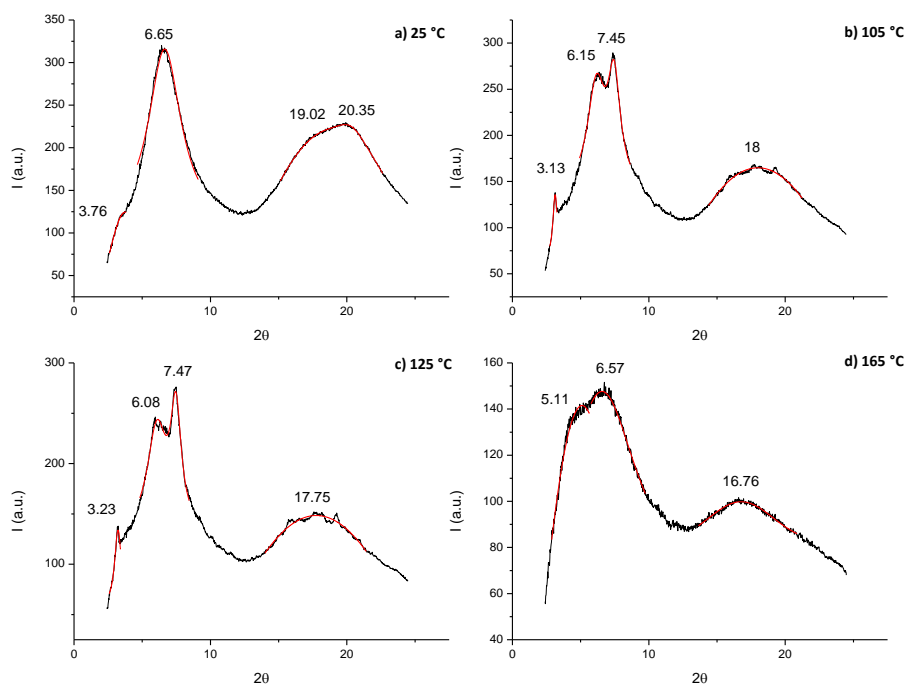


Figure 220: Radially integrated patterns of 114 for a) 25 °C, b) 105 °C, c) 125 °C and d) 165 °C, integration of the equator region.

The peak corresponding to the first order has almost disappeared at 25 °C but it seems to be more visible at 105 °C (in the mesophase) and at 125 °C (just above isotropisation temperature), while the second order reflection is not visible at any temperatures, which is expected. Peaks related to the distances between two siloxane cubes and lateral distances between aliphatic chains are present throughout the entire temperature range. As observed in plot a) Figure 219 at 25 °C there are two peaks in the wide angle region, distances of 4.67 Å and of 4.36 Å, while at 105 °C and 125 °C the peak in the wide

angle region seems to have a detailed structure that disappears giving rise to a single peak at 165 °C.

χ -scans from peaks A to E were plotted and are presented in the figures below. Peak E is situated in the meridian region as shown in the plots in Figure 221. With increasing temperature there is a decrease in intensity however in plot d) there is a big difference between the peaks with values of approximately 90° and 267°.

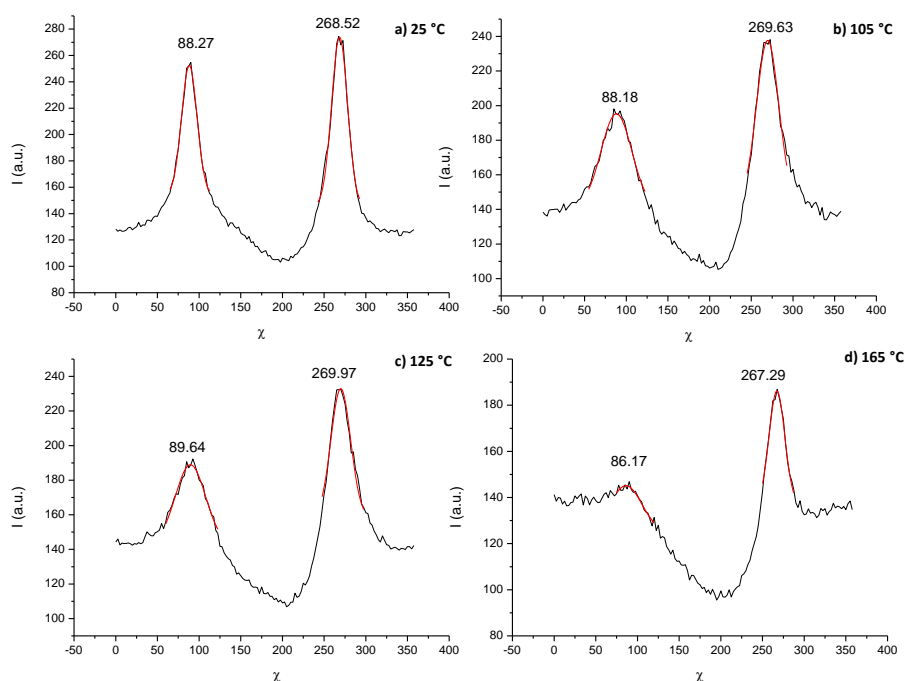


Figure 221: Azimuthally integrated plots of peak A for compound 114 at several temperatures.

Peaks D and C are very close (see Figure 217 at 25 °C and Figure 219 a)) despite having different orientations (peak D is situated in the meridian and peak C is mainly situated in the equator) yet because of their proximity, they were integrated together due to software reasons and the resulting χ -scans are represented below, in Figure 223. In Figure 222 is a magnification of the small angle region and peaks C and D are highlighted.

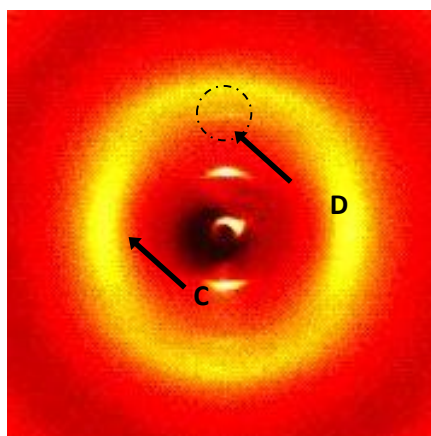


Figure 222: Amplification of the small angle region of the 2D diffraction pattern of 114 at 25 °C.

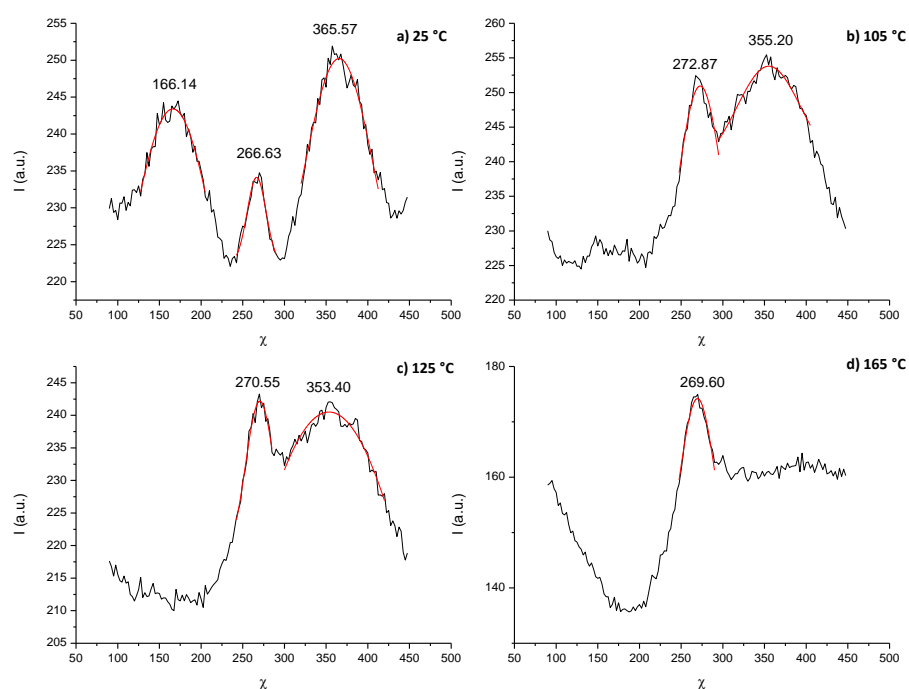


Figure 223: Azimuthally integrated plots of peak C and D for compound 114 at several temperatures.

The distribution of the intensities in the equator region is confirmed at 25 °C, with increasing temperature a loss in alignment seems to occur, as the sample becomes isotropic.

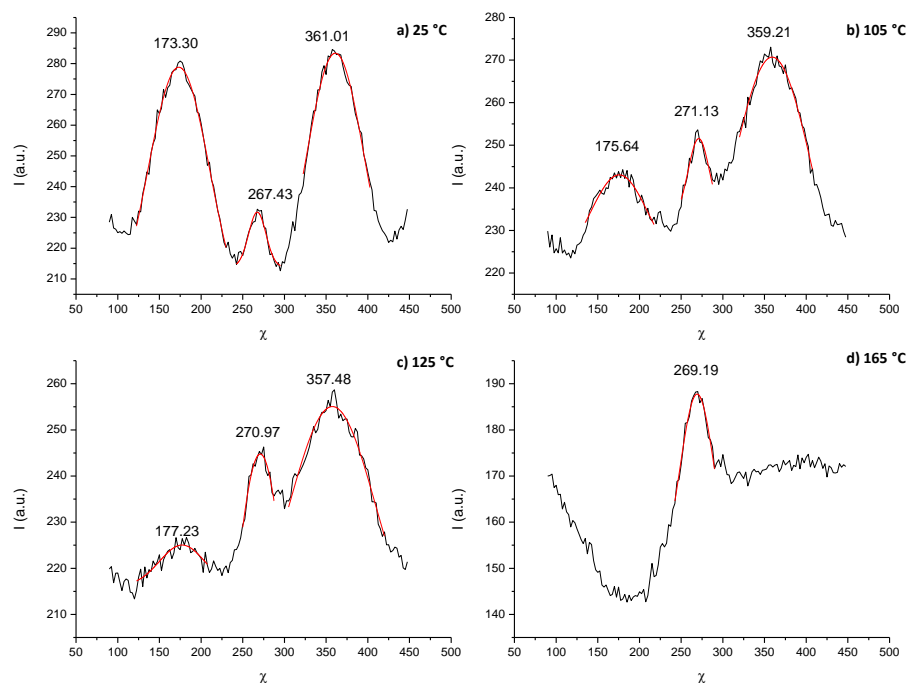


Figure 224: Azimuthally integrated plots of peak D for compound 114 at several temperatures.

An attempt to isolate peak D and perform the azimuthally integrated plots was made but not successfully see Figure 224, where a preferential alignment in the equator area is present.

Lastly the χ scans of the wide angle region show that they are preferentially situated in the equator as expected for a SmA phase.

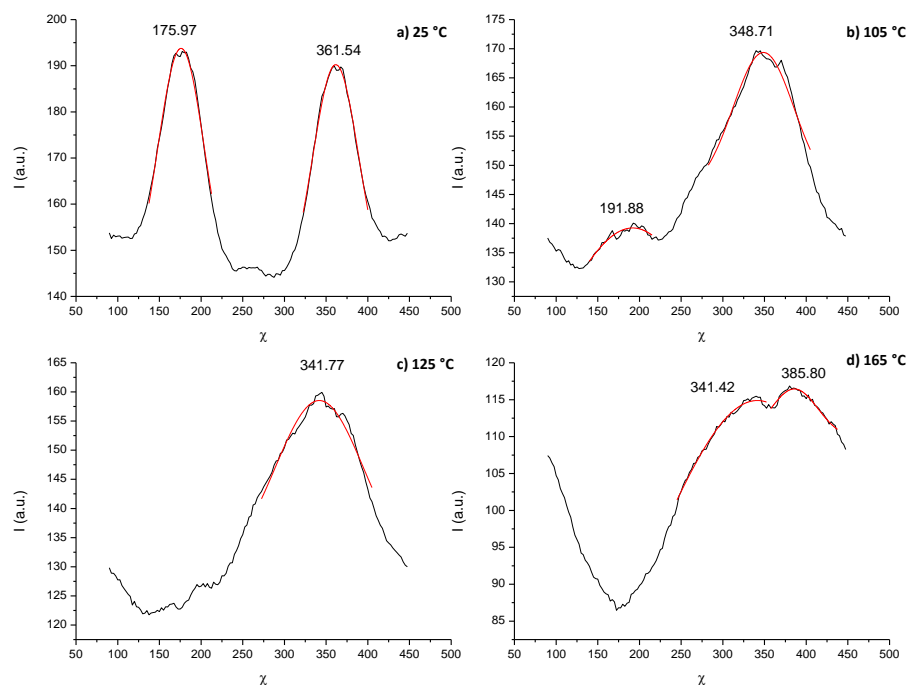


Figure 225: Azimuthally integrated plots of peak A and B for compound 114 at several temperatures.

Noticeable is some sharpening of the intensity in the wide angle region as shown in Figure 218. These accounted intensities are large and not close to the noise level, so this ought to be taken into consideration.

However a possibility could be that the mesogenic groups acquire more rotational flexibility with increasing temperature, leading to some antiparallel formation as depicted in Figure 226, resulting in small differences in the lateral mesogenic distances. The model previously discussed for **108** is suitable for this material. The details of which were already discussed, and the model is represented with the dimensions related with this molecule.

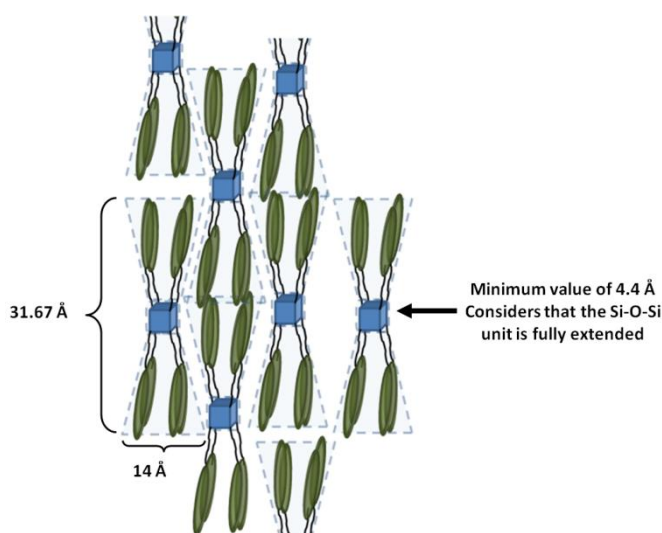


Figure 226: Molecular packing proposed for **114**.

The correlation of the molecular length was determined as described before and the calculated value was 343 Å that corresponds to 8 molecular lengths.

In this series, three compounds were investigated, **112** which has a lamN phase resembling the one shown by **104**. Compound **113** shows a different behaviour from any of the compounds synthesized, with a very high clearing temperature observed. The XRD studies of this compound are still ongoing and clarification of its phase structure is expected to be achieved in the near future. Compound **114** shows a SmA phase, typical for cyanobiphenyl substituted silsesquioxanes.

XRD discussion of Series IV

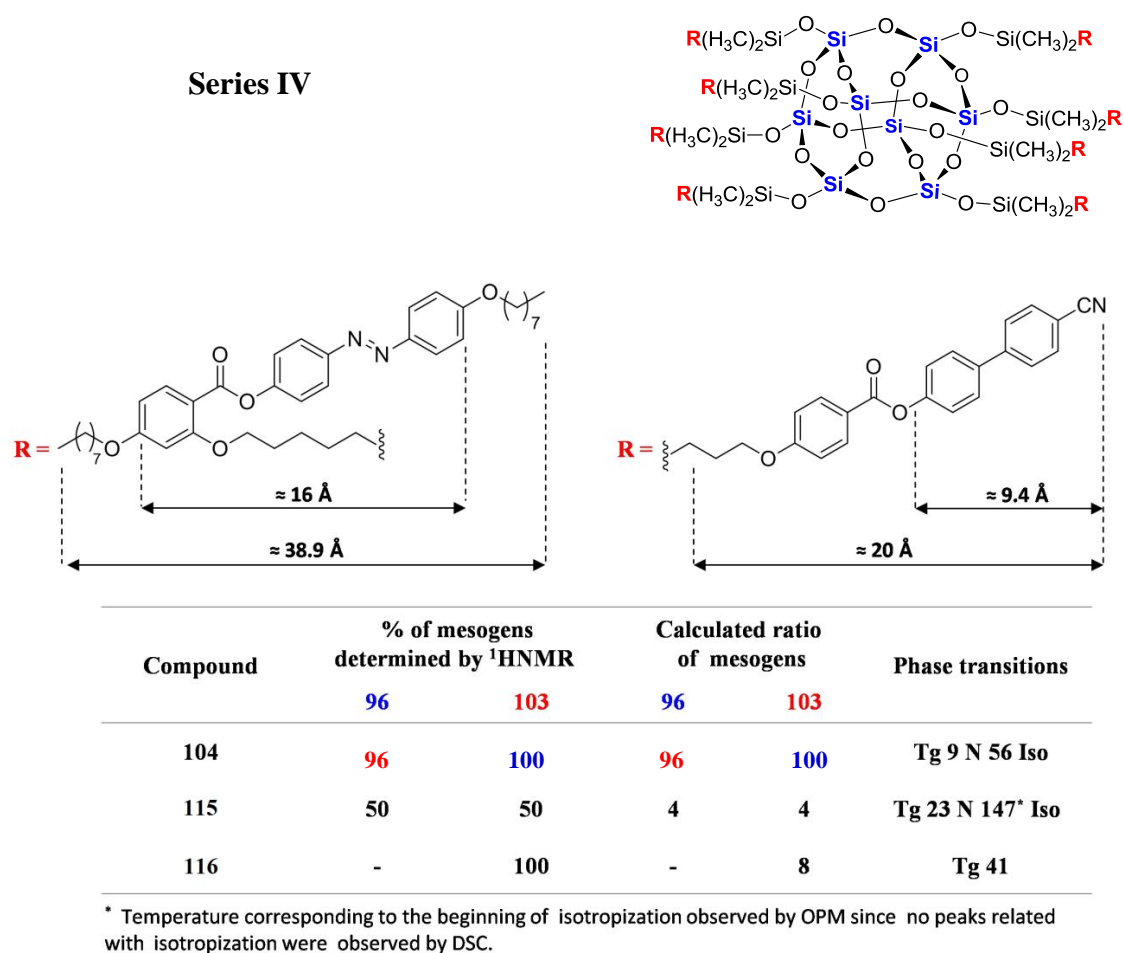


Figure 227: Scheme of series IV.

Compound 115

The phase structure of **115** was studied by X-ray diffraction and the results obtained from two experiments will be presented. The first experiment used a fibre sample and a heating program was carried out. The temperature was raised by 5 °C and data collected every 5 °C for a period of 1800s. The starting temperature of this program was 45 °C and the final temperature recorded was 170 °C; this is Program I. After completion of Program I, Program II was initiated this involved a cooling program starting at 170 °C. The temperature was decreased 20 °C and data collected for 1800s, every 20 °C until the final temperature 30 °C was achieved.

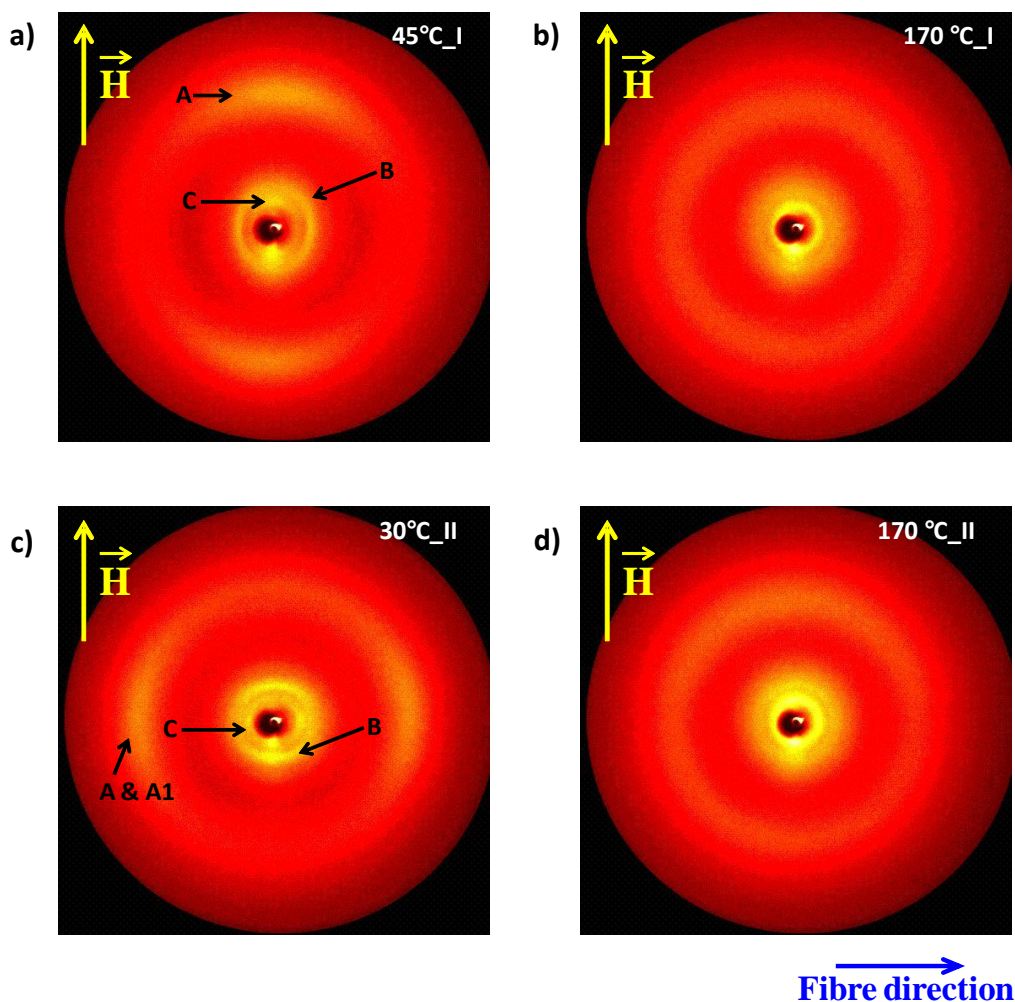


Figure 228: Diffractograms of compound 115. Top: Program I and bottom: Program II.

In Figure 228 above 2D diffraction patterns collected from both programs are shown. On the top of Figure 228, data collected from the mesophase (45 °C) and from the isotropic state (170 °C) during Program I are depicted. On the bottom of Figure 228, the data shown was collected during Program II, and reveals the mesophase at 30 °C and the isotropic state at 170°C. From the 2D diffraction patterns it is clear a difference in the patterns is seen and the results collected by both programs will be discuss next.

Program I

The θ -scans for compound **115** in the mesophase and in the isotropic state, collected during Program I, are shown in Figure 228 a) and b) respectively and they were integrated along the magnetic field.

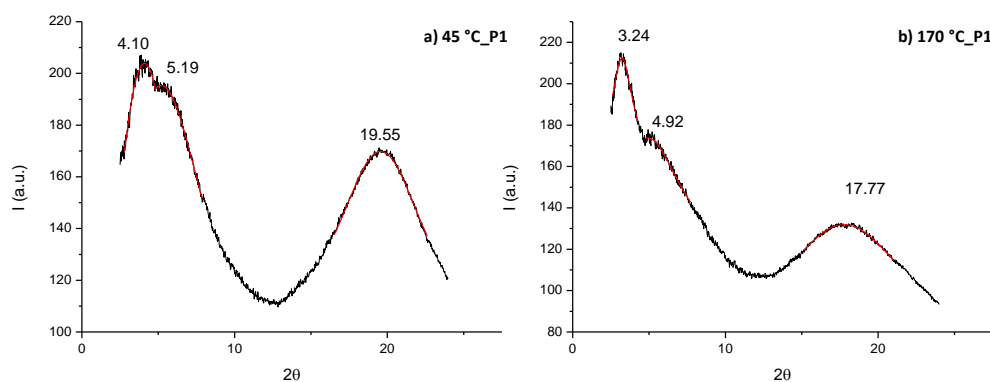


Figure 229: θ -scans for compound 115, obtained from data collected from program I.

The presence of three reflections is expected and the calculated distances are shown in Table 25.

Table 25: Calculated distances determined by X-ray diffraction for compound 115.

peak	Program I					
	45 °C			170 °C		
	A	B	C	A	B	C
2θ	19.55	5.19	4.10	17.77	4.92	3.24
d (Å)	4.54	17.03	21.55	4.99	17.96	27.27

Despite the existence of three peaks both in the 2D diffraction patterns and in the 2θ -scans, the calculated distance for peak B of ≈ 17 Å, $2\theta = 5.19$, was surprising as this value is much larger than the value expected for the distance between two neighbouring silsesquioxane cores. In the compounds discussed so far, the values obtained for the distance between two silsesquioxane cores was around 13 – 14 Å, associated with a 2θ value of approximately 6.3 – 6.8. As a result, it seems that peak B is not related with the distance between two silsesquioxane cores.

Compound 115 comprises two mesogens in a 1:1 ratio, attached to the silsesquioxane. The system is represented in Figure 227 where the length of both mesogens is also represented.

It is possible that both peaks B ($2\theta = 5.19$, $d \approx 17$ Å) and C ($2\theta = 4.10$, $d \approx 22$ Å) are related with diffraction from both mesogens represented in Figure 227. The assignment of any of these peaks is not straight forward; however, in previous systems the diffraction peak related with the azobenzene mesogen was associated with distances between 24 and 30 Å. It seems that peak B ($2\theta = 5.19$, $d \approx 17$ Å) is related to the length of the cyanobiphenyl substituent and peak C is attributed to the length of the

azobenzene substituent. The observation that calculated distance is smaller than the full length of the mesogen, implies the existence of interdigitation between the alkyl chains. Peak A is characteristic of liquid crystalline systems and is related to the distance between two neighbouring mesogenic units, $2\theta = 19.55$, $d \approx 4.5 \text{ \AA}$. In the isotropic state, the 2θ values are slightly smaller which is not surprising since the degree of order decreases in the isotropic state.

The absence of a peak related to the silsesquioxane cores is very surprising. The distribution of the intensities of the diffracted peaks are represented in Figure 230 for the mesophase and for the isotropic state.

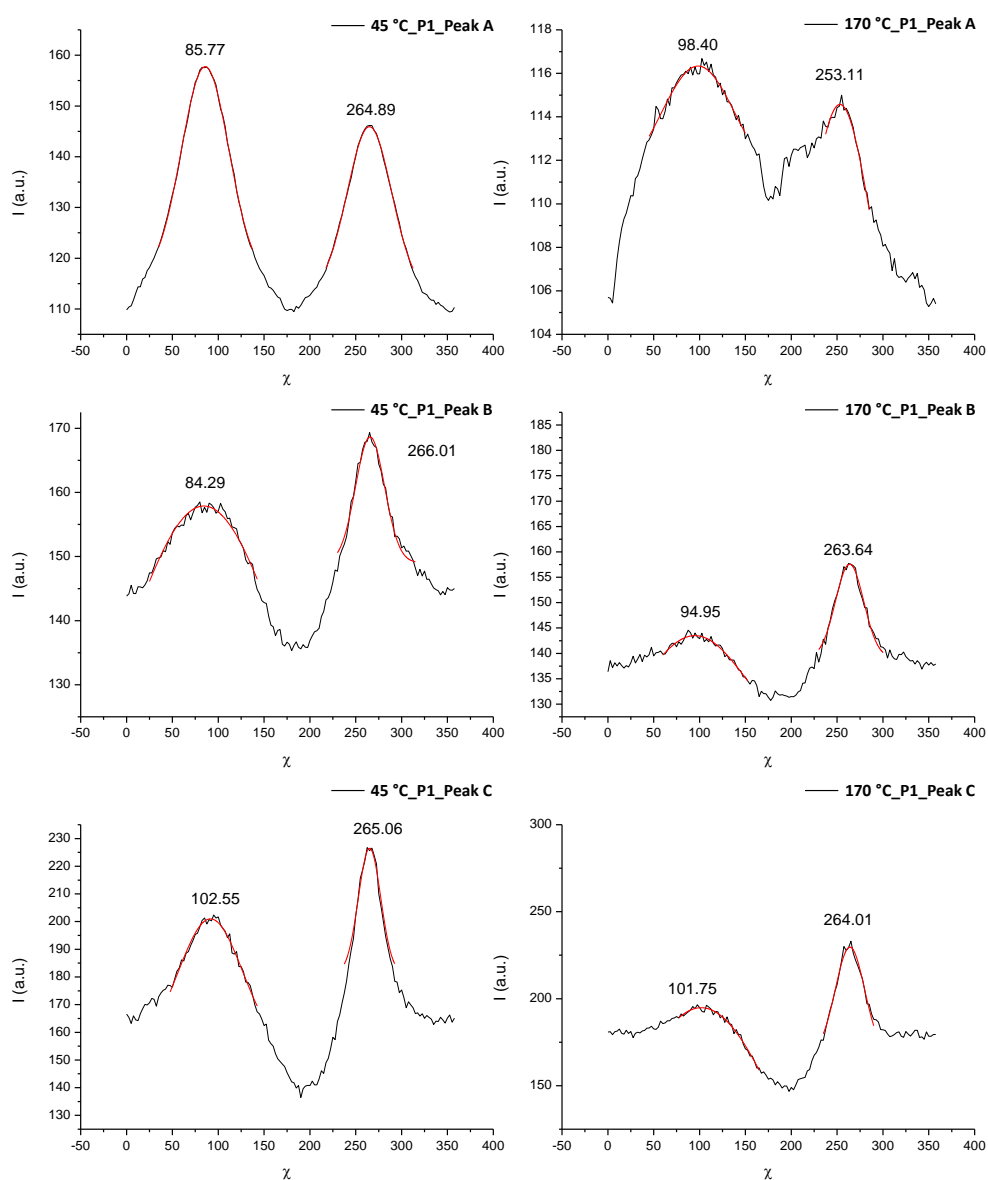


Figure 230: Azimuthally integrated plots for peaks A to C in the mesophase (45 °C) and in the isotropic state (170 °C) for program I.

The χ -scans show that all the peaks are situated in the meridian region. It also seems that in the isotropic state some alignment of the molecules related with the mesophase is retained; see plots in Figure 230 at 170 °C.

Taking into account previous discussions, and the observation of a marbled texture by POM, Figure 131), it seems that this sample has a lamellar nematic phase. In which both mesogens are organized perpendicularly to the magnetic field as described for **104**, for example. The layer structure is suggested by the distribution of the intensities in the meridian region.

Program II:

The 2D diffractograms for program II are shown in the bottom of Figure 228. An initial comparison between the diffraction patterns obtained for both programs shows clear differences. Contrary to the previously discussed results of Program I, the preferred orientation for the diffracted peaks is not predominantly distributed in the meridian region but is now spread between the meridian and equator regions.

The Azimuthally integrated plots in Figure 231 correspond to: a) Integration using a χ interval from 0 to 360°, b) integration perpendicular to the magnetic field, c) integration parallel to the magnetic field.

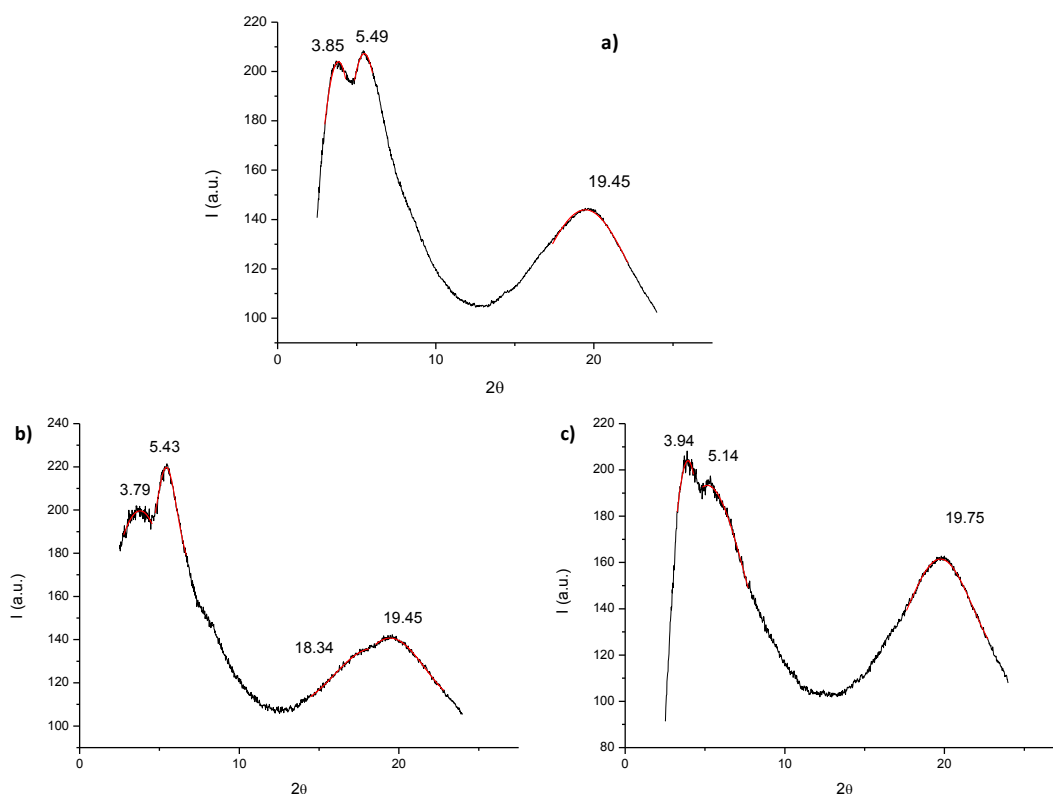


Figure 231: θ -scans for compound 115, obtained from data collected during Program II.

The calculated values for the peaks of plot c) Figure 231 are depicted in Table 26 below.

Table 26: Calculated values for the peaks in the parallel integration data collected at 30 °C.

Program II				
30 °C				
peak	A	A₁	B	C
2θ	19.45	18.34	5.43	3.79
d (Å)	4.56	4.84	16.28	23.32

In the wide angle region there are now two peaks corresponding at ≈ 4.6 Å and ≈ 4.8 Å which are attributed to the distances between the mesogenic units, and are associated with liquid crystalline behaviour. The existence of two peaks could be related with the fact that there are two mesogens present in this compound in a 1:1 ratio and microsegregation might occur at a molecular level. Surprisingly a peak corresponding to the distance between two silsesquioxane cores is still absent.

The radially integrated plots for the peaks at 30 °C are shown below. Peaks A and A1 are situated in the equator region contrary to what was observed in plot a). Peak B is still in the meridian region and Peak C is now distributed along the equator, in contrast to what was observed during Program I, see Figure 232.

As peaks B and C were attributed to mesogens containing cyanobiphenyl and azobenzene groups, respectively, it seems that they are placed perpendicularly to each other resembling what was observed for compound **106**.

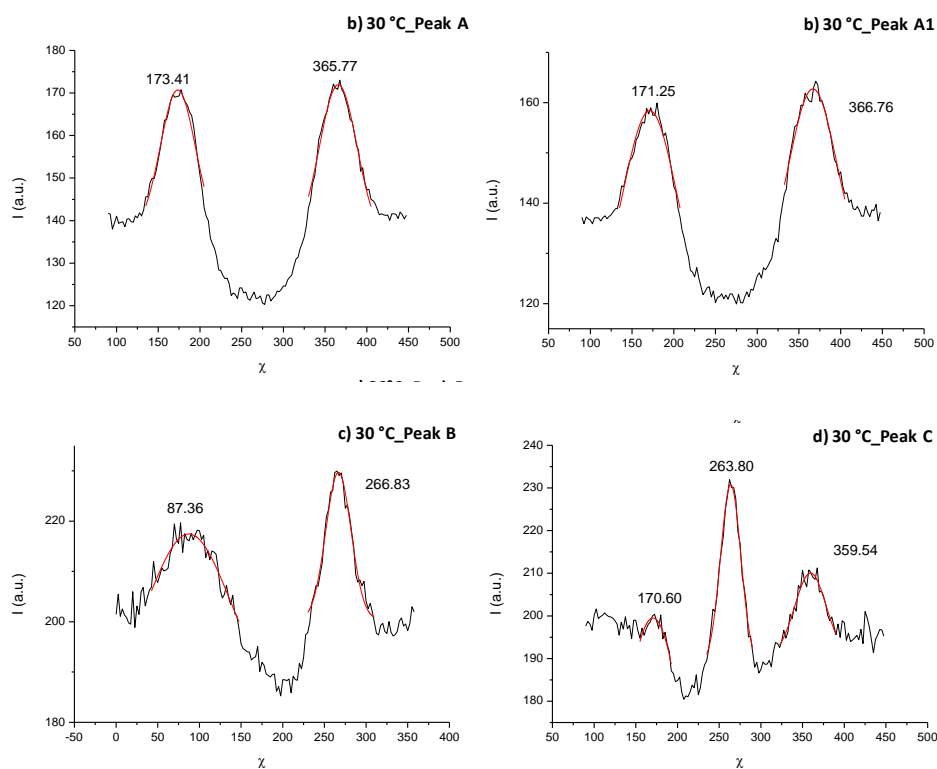


Figure 232: Radially integrated scans for compound 115 at 30 °C. Data collected during Program II

Comparing the results obtain by program I and program II it seems that the initial lamellar nematic phase was lost when fast cooling occurred. This could be because the molecules did not have time to rearrange in the preferred lamellar phase. This lost of order was already observed for **104**. However in this case the degree of disorder seems to be much higher as for a typical nematic phase. This could be related with the “design” of the cyanobiphenyl mesogen, where the ester group may allow some freedom.

Using Scherrer’s equation, the correlation length was calculated, the obtained value was $\approx 41.11 \text{ \AA}$ which corresponds approximately to one molecular length.

The calculated molecular volume is 10332 \AA^3 and the layer spacing is 21.55 \AA , smaller than the full length of the extended molecule of 50.6 \AA (2 cyanobiphenyls, $2 \times 20 \text{ \AA}$ + silsesquioxane core 4.4 \AA + Si-O-Si groups 2×3.1). Considering a unit cell of 43.10 \AA , the calculated diameter for a cylinder model would be $\approx 17.5 \text{ \AA}$, as represented in Figure 233.

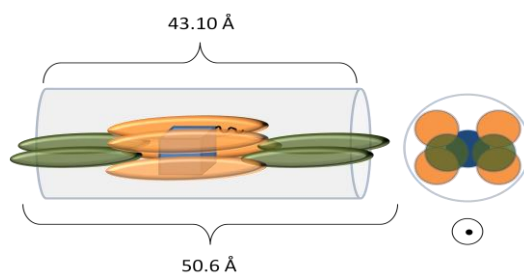


Figure 233: Representation of the molecular unit cell of 115.

Considering the model presented above accommodates the dimension of the molecule. The azobenzene mesogens interdigitate and in the XRD diffraction patterns there is no electron density corresponding to the cyanobiphenyls, therefore a packing of the molecules as shown below is proposed.



Figure 234: Representation of the molecular packing considering the above model.

Compound 116

The 2D patterns obtained from X-ray diffraction studies are shown in Figure 235 at 25 °C and at 190 °C. The samples are not well aligned as the diffraction intensities are rings at both temperatures. The differences between the two diffractograms are related to peak A, where the ring at 25 °C gives rise to a diffuse scattering. Some changes in peaks B and C are also observed, but these are minor.

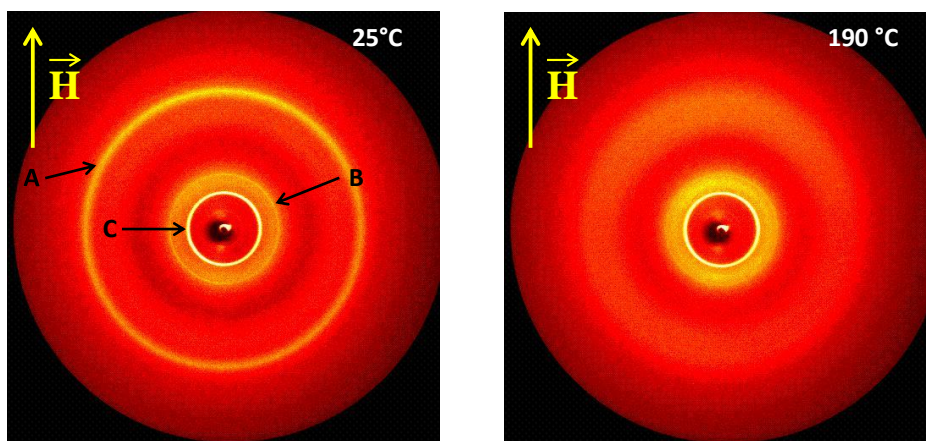


Figure 235: Diffractograms of compound 116 at the mesophase (25 °C) and in the isotropic state (190 °C).

The radially integrated scans are shown in Figure 236 and the associated distances are shown in Table 27.

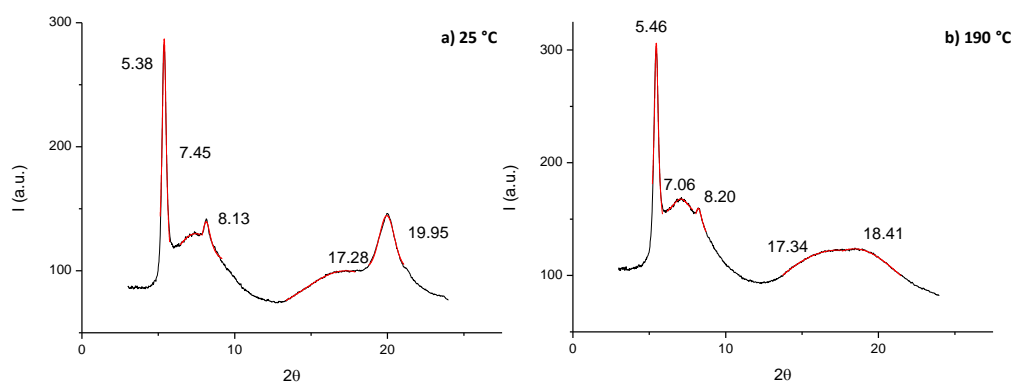


Figure 236: Radially integrated patterns of 116 for a) 25 °C and b) 190 °C.

The radially integrated patterns plotted in Figure 236 are fairly similar, the largest difference occurs in the wide angle region where the peak with 2θ value of 19.95 becomes smoother and less intense at 190 °C. At this temperature, the wide angle region suggests that this material is liquid crystalline.

Table 27: Calculated distances for plot b in Figure 236.

30 °C					
peak	A	A ₁	D	B	C
2θ	18.41	17.34	8.20	7.06	5.46
d (Å)	4.82	5.11	10.78	12.52	16.19

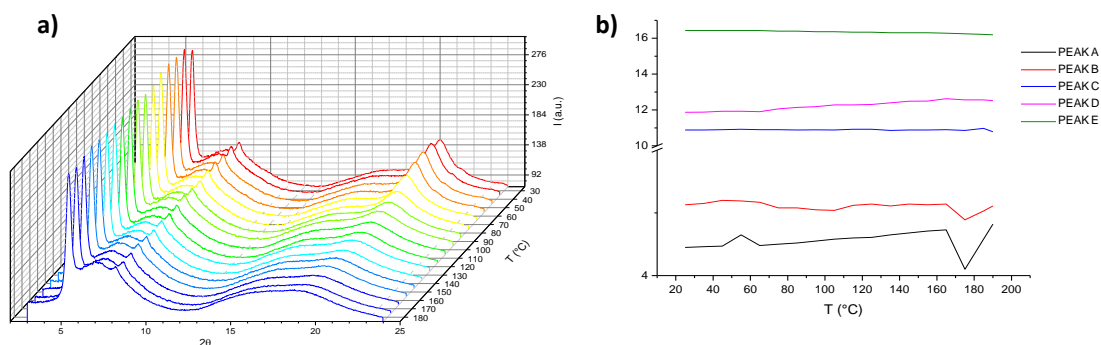


Figure 237: Dependence of θ -scans with temperature. a) For the entire temperature range collected and b) Variation of d (Å) with temperature.

Figure 236 and Figure 237 show that with decreasing temperature the wide angle peak becomes sharper, as the material is more ordered at lower temperatures.

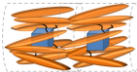
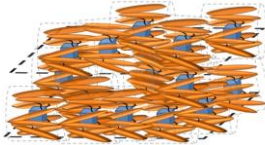
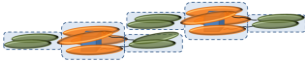
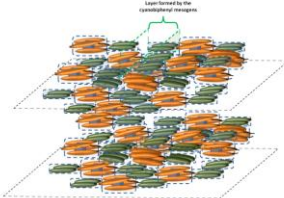
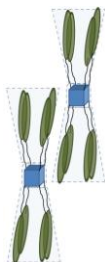
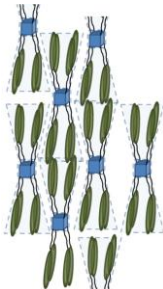
As it was not possible to align XRD sample in the magnetic field or as fibres, due to a very high viscosity which possibly had affected OPM studies as well, phase identification was not possible.

The persistence of sharp and persistent reflections in the small angle region suggests the formation of a high ordered LC phase, though there are not sufficient peaks present to differentiate between a smectic (eg SmA or SmB) and columnar phases.

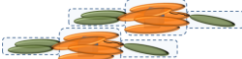
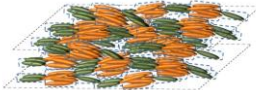
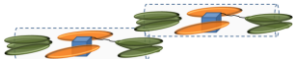
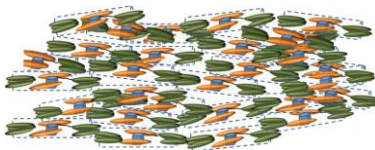
In series IV the addition of a benzyl ester did not affect the presence of a lamN phase which was confirmed. The fast cooling of compound **115** showed the formation of a less ordered normal nematic phase. The phase structure of compound **116** could not be identified clearly, however the data points towards the formation of a smectic phase.

A summary of the molecular assemblies and phase structures of the compounds investigated is presented in the next pages.

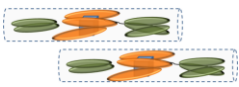
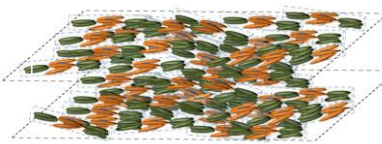

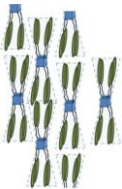
Series I

Compound	Molecular assembly	Phase structure	Comments
104			<ul style="list-style-type: none"> • Interdigitation of mesogens occurs. • Formation of cybotactic clusters of SmC-like layers of the mesogens.
106			<ul style="list-style-type: none"> • Formation of SmC-like cybotactic clusters of the silsesquioxane core. • Occurrence of a local SmA-like layer arrangement of the cyanobiphenyls.
105	XRD studies were inconclusive as the material could not be aligned. θ -scans show 1 st and 2 nd order diffraction peaks suggesting a SmA-like layer arrangement of the cyanobiphenyl as discussed for 106. Due to the a marbled texture observed by OPM, a phase structure as observed for 106 is most likely.		
108			<ul style="list-style-type: none"> • Interdigitation of the cyanobiphenyl groups occurs. • The molecules have a spindle-like shape.

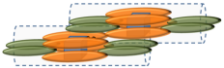
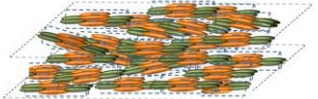
Series II

Compound	Molecular assembly	Phase structure	Comments
109			<ul style="list-style-type: none"> • Interdigitation of cyanobiphenyl groups does not occur. • Arrangement of cyanobiphenyls in a SmA-like local layer does not occur.
110			<ul style="list-style-type: none"> • Formation of cybotactic clusters of silsesquioxanes. • No suggestion of the occurrence of SmA-like layer arrangement of the cyanobiphenyl as discussed in Series I.
111	XRD studies were inconclusive because the material could not be aligned . However all the data collected for this material points towards the formation of a SmA phase similar to that proposed for 108.		

Series III

Compound	Molecular assembly	Phase structure	Comments
112			<ul style="list-style-type: none"> • Interdigitation of cyanobiphenyl groups does not occur. • Arrangement of cyanobiphenyls in a SmA-like local layer does not occur.
113	Preliminary XRD results point to a high ordered phase structure. Investigations to clarify the molecular assembly in this compound are still ongoing.		
114			<ul style="list-style-type: none"> • Interdigitation of the cyanobiphenyl groups occurs. • The molecules have a spindle-like shape.

Series IV

Compound	Molecular assembly	Phase structure	Comments
115			<ul style="list-style-type: none"> • Interdigitation of cyanobiphenyl groups does not occur. • Arrangement of cyanobiphenyls in a SmA-like local layer does not occur. • Formation of cybotactic clusters is not observed. • Fast cooling induces disappearance of lamellar structure.
116	XRD studies were inconclusive as the material could not be aligned. However all the data collected for this material points towards formation of a higher ordered phase structure such as smectic or columnar phase.		

DISCUSSION-PART III

7.7 - Discussion of photoorientation and SRG inscription

The work discussed here was carried out in collaboration Jarloslaw Tomczyk from the group of Professor Joachim Stumpe of the Fraunhofer Institute for Applied Polymer Research, in Potsdam, Germany, under the Dendreamers project (Marie Curie actions, seventh framework programme).

A quantitative data analysis, which is out of the scope of this thesis, can be found in the PhD thesis of Jarloslaw Tomczyk from Potsdam University, but in this discussion a presentation of the data in a more qualitative way will be made as well as a detailed description of the process.

The work presented here anticipated the synthesis of new photochromic liquid crystalline materials and their full characterization that was made previously, finally the application of the synthesised materials which will be described next.

The first step to study photoalignment is the preparation of thin films. In order to do this, it is important that the materials have good film forming properties; that is formation of homogenous films which is essential for photoalignment studies.

The films were prepared in two steps; first preparation of solutions of known concentration, typically $3.9 \times 10^{-6} \text{ mol dm}^{-3}$. The solvent chosen depends on the solubility of the materials, and the ability to form films so that the solvent could be easily evaporated after film preparation. In the present case the solvent used was 1,1,2-trichloroethane. The yellow solutions (due to the azobenzene molecules) were clear, therefore homogeneous, and the concentration chosen was adequate for the preparation of the films. If the initial solutions are too concentrated difficulties in obtaining a homogeneous spread of the solution arises, impinging on the quality of the films obtained. The second stage in the process of forming thin films using a glass substrate is the preparation of the substrate. The substrate was carefully cleaned (with ethanol) in order to remove grease and dust that would in later stages of the work disturb the interaction of linearly polarized light with the materials.

Finally, the films were prepared by a spin coating technique involving deposition of the dilute solution into the glass substrate that is then accelerated to the desired rotation rate 2000 rpm. Due to centrifugal force, the liquid will flow radially up to the edges of the substrate and the excess will be thrown out of the edges. The thickness of the film will keep decreasing until disjoining pressure (that results from attractive interactions

between the two surfaces: liquid solution and solid substrate) effects cause the film to reach an equilibrium thickness or until, as a consequence of evaporation, an extremely viscous state is attained and it is solid-like.

In order to get the best possible quality for the thin films two deposition techniques were used; one in which the sample is applied while the spin coater is off, meaning that there is no initial acceleration, and the second on which the sample is applied after the spin coater being switched on. In this case there will be an initial acceleration and the samples were loaded when the spin coater was spinning at 2000 rpm and at constant speed.

In Figure 238 a) and b) are depicted the steps described above for the preparation of the thin films, in a) a clear and homogeneous solution used to prepare the thin films and in b) the spin coater used with a glass substrate ready to be loaded.

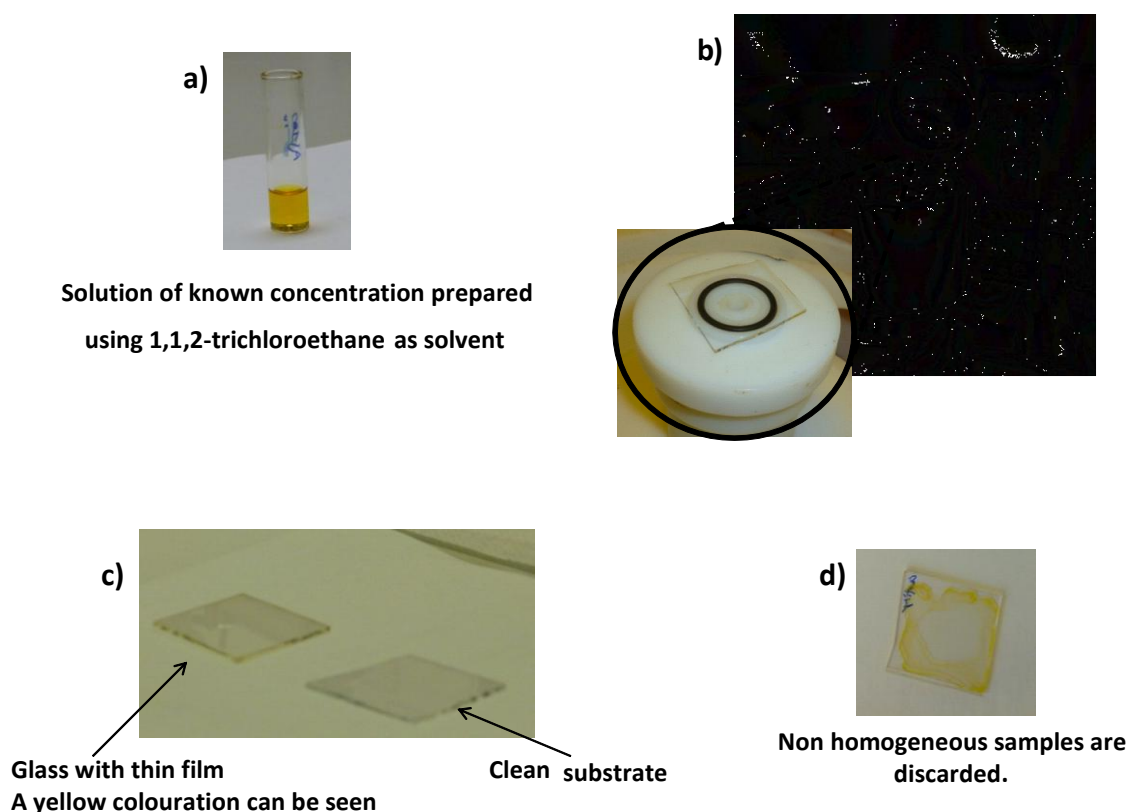


Figure 238: a) and b) Steps for the preparation of the thin films. c) Shows two substrates, one is loaded and a yellow colouration can be observed. The other is clean and transparent d) Example of a non homogeneous sample.

For the preparation of these films the method chosen was the static method, where the sample was loaded while the spin coater was off as it produced the more uniform samples. The loaded samples could be identified by a yellow coloration, as depicted in Figure 238 c), and after the production of films their quality was assessed. All the non homogeneous samples, such as the one shown in Figure 238 d), were discarded and the

resultant samples were kept for analysis. Ten good samples were produced from which the best eight were analysed.

After loading the sample holders the UV/Vis spectra was traced, the apparatus incorporated a Glan-Thompson prism with a computer-driven stepper that is rotated by 5° in the end of acquisition of each spectrum which was used for the angular-dependent measurements of absorbance. This means that 36 UV/Vis spectra are recorded (from 0 to 180°) for each sample, corresponding to the different orientations of the sample. The spectra presented in the Figure 239 correspond to an isotropic organization of the molecules so the absorption behaviour of the sample is the same in all directions in the plane of the film.

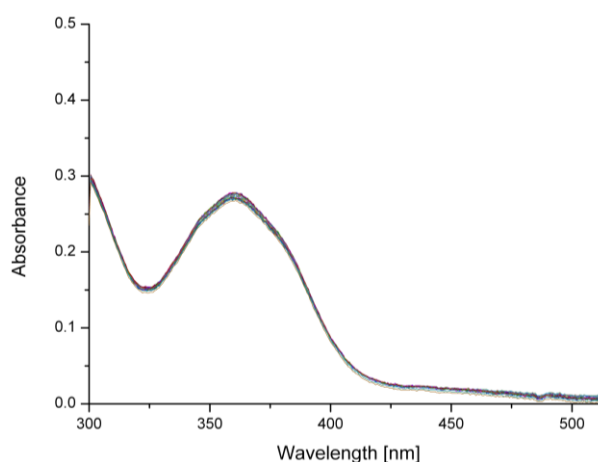


Figure 239: UV/Vis spectra of the non irradiated sample.

The absorption maxima is at 356 nm corresponding to the π - π^* transition of the azobenzene. The samples were afterwards irradiated for 30 min at room temperature with linearly polarized light of an Ar^+ laser (Innova4, Coherent) using the green line at 488 nm (100 mW/cm^2). The UV/Vis spectra were recorded for the irradiated samples and are depicted in Figure 240.

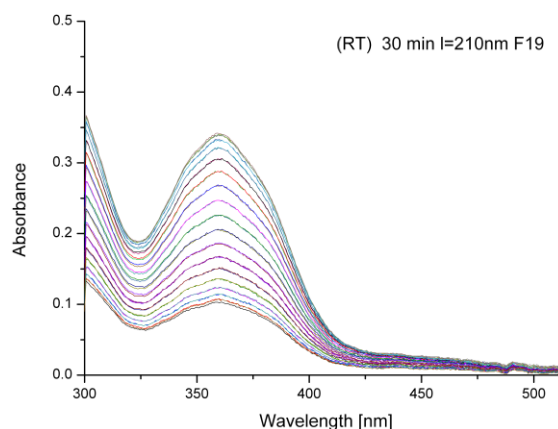


Figure 240: UV/Vis spectra of irradiated samples.

Observation of the UV/Vis spectra for the irradiated samples shows that there is a decrease in the absorption of the sample at (356 nm) from the parallel to the perpendicular direction of the incident light (this is for the spectra corresponding from 0° to 90° (lowest absorption value and highest absorption value respectively)).

The different absorption values for the different directions are a consequence of preferential direction of absorption, in this case the direction perpendicular to the direction of the electric field vector (\vec{E}) of the incident linearly polarized light. This is a significant difference compared to the samples prior to irradiation. It demonstrates that there was a photoorientation of the azobenzene groups induced during the irradiation procedure. The photoorientation phenomenon discussed in Chapter II was then observed for this material and the dichroism, D , was calculated using equation 10.

$$D = \frac{A_{\text{perp}} - A_{\text{par}}}{A_{\text{perp}} + A_{\text{par}}} \quad (10)$$

Where A_{perp} is the absorption value perpendicular to the polarization direction of the irradiation light and A_{par} is the absorption value parallel to the polarization direction of the irradiation light. For the sample under discussion the dichroic value calculated was 0.7.

The angular-dependent absorbance spectra for the absorbance maxima $\lambda = 356$ nm are shown in Figure 241, and it demonstrates clearly that optical anisotropy was induced in the material in question and it shows the maximum absorbance perpendicular to the electric field vector of the incident light. This photoorientation process occurs due to a cooperative orientation of the mesogens by *trans-cis* isomerisation of the azobenzene, which is much higher than for amorphous materials.

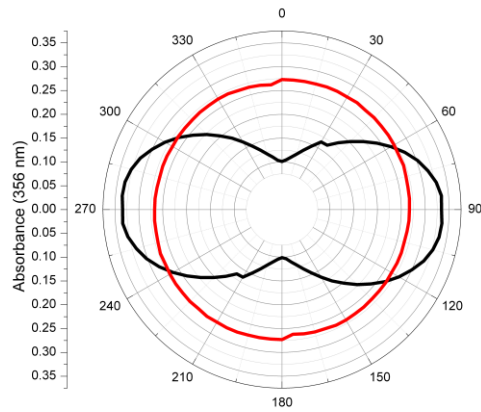


Figure 241: Polar plots of the absorbance at 365 nm in the initial film (black line) and after linear polarized irradiation (488nm).

After photoorientation inducement, the thickness of the samples was investigated. This process is carried out after acquisition of the above data since it is a destructive process. A contact profilometer (Dektak 150, Veeco Instruments Inc.) was used to measure the surface profile and quantify its roughness and thus its thickness. This equipment measures in the nanometer range and consequently they are extremely sensitive to any dust particles and vibrations, so for these reasons it was located in a clean room.

When performing these measures a thin scratch is made in the surface of the samples the profilometer will measure the height of this depression as represented in Figure 242. In order to obtain a good result, several measurements of the same sample were acquired and an average result is obtained.

For the samples analyzed three measurements per sample were collected for all of the eight samples the average thickness calculated were between 200 to 300 nm.

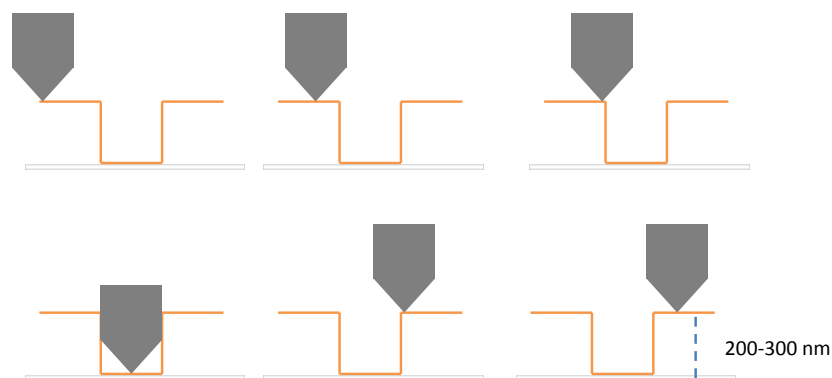


Figure 242: Representation of the measurements of the thickness of the samples using a profilometer.

Figure 242 shows how the profilometer works. The needle travels along the sample and detects any change on the surface texture such as the scratch induced and in this way a measurement of the thickness of the films is obtained.

SRGS inscription

In addition to studies of light induced anisotropy with a single homogeneous beam (measuring dichroism) this phenomenon can be studied by diffraction grating recording which is characterised by the diffraction efficiency. In these cases the material is exposed to a pattern irradiation, induced for example by the holography technique shown in the Figure 243.

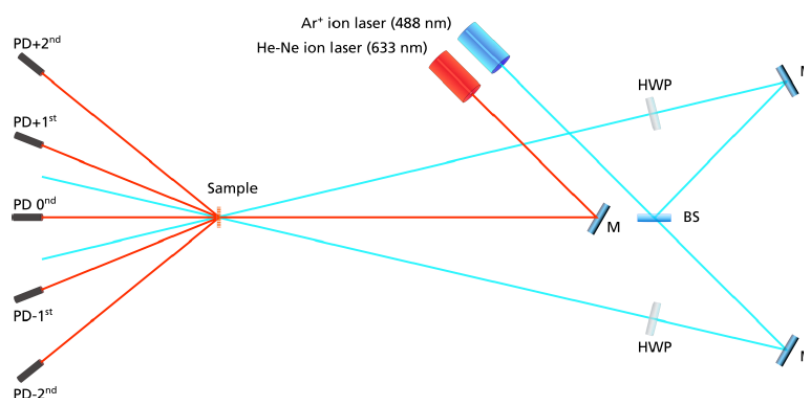


Figure 243: Experimental set up used to record SRGS.²⁸⁶

An Argon-ion laser at the wavelength of 488 nm was used. The laser beam was expanded and spatially selected in order to use only its homogeneous central part. The beam was split into two parts of equal intensities, and the sample was irradiated with a polarization interference pattern formed by the linearly orthogonally polarized beams. The irradiation of the sample with this technique results in the induction of periodic anisotropy. This is achieved by periodic changes of birefringence and dichroism being evident by the appearance of light diffraction. In quantitative studies, the process of grating formation is followed by monitoring the intensity of the first-order diffraction suffered by a low power s-polarized probe beam at 633 nm over time. The diffraction efficiency (ratio between the first diffracted intensity and the input beam intensity) indirectly provides information about the optical anisotropy. A qualitative description of the experimental results is possible and will follow.

In Figure 244 a thin film of compound **115** in a glass substrate is shown during diffraction grating recording experiment. The photograph was taken while the sample was being irradiated (45 min exposure). In Figure 244 the red dots to the left and to the right of the central point correspond to the first, second and third order interference diffraction fringes. The central red point, or zero order diffraction, corresponds to the direct s-polarized beam ($\lambda = 633$ nm), this is the beam that does not suffer diffraction. So this beam is used to verify if diffraction gratings are being recorded, when this

occurs, the laser suffers diffraction originating the red dots observed in the figure. If no diffraction gratings are recorded, the incident red laser is not diffracted and only the direct beam will be observed.

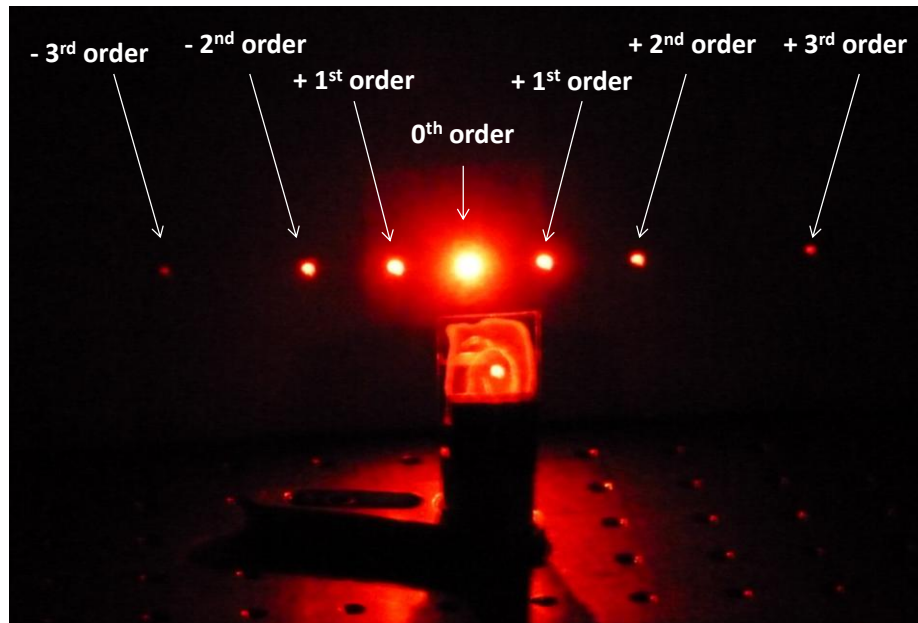


Figure 244: Recording of SRGS, where 1st, 2nd and 3rd order diffractions can be observed.

When observing Figure 244 it is possible to see that the sample is not completely homogeneous. Thus a homogeneous region of the sample was chosen to perform this experiment.

The holographic technique described here consists of a laser beam that was split into two linearly polarized beams of equal intensities with polarization planes of $\pm 45^\circ$ to the plane of incidence.

Interference of these two coherent beams can occur constructively or destructively, hence giving rise to a resultant wave with higher or lower amplitude respectively. The polarization interference pattern formed will be inscribed into the sample and induce a change in its surface, which was discussed in Chapter IV. So when the recorded sample was observed in a polarizing optical microscope between crossed polarisers the interference pattern was observed, see Figure 245.

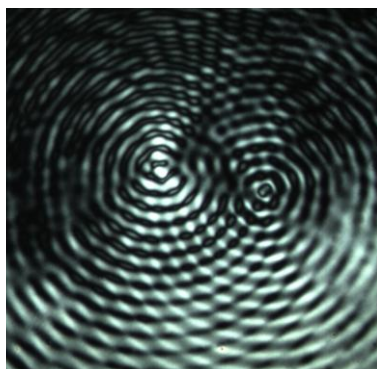


Figure 245: Sample observed by OPM after SRG inscription.

In azobenzene containing materials, surface relief grating occurs in addition to the photoinduced anisotropy contributing to the diffraction.

An AFM image was collected using a NanoScope IIIa controller from Digital AFM

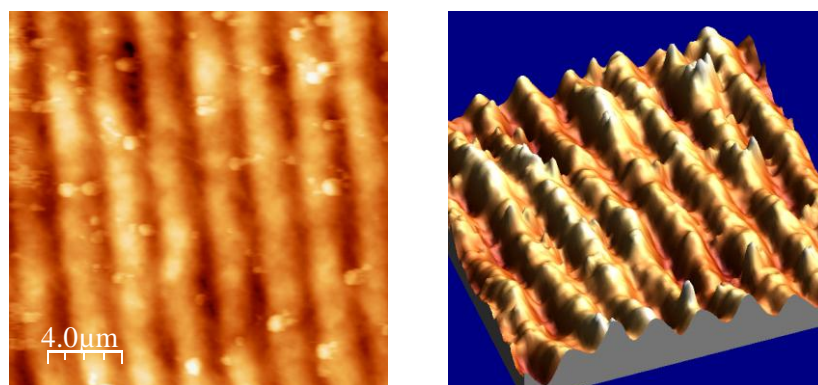


Figure 246: Profile of the surface of the sample of 116 after SRGS inscription.

instrument was used to determine the roughness of the surface. In Figure 246 it is possible to see that some gratings were recorded however it is also possible to observe that these are not smooth profiled gratings. For the recording of SRGs, it is necessary to have thicker films, between 600 and 800 nm, than the ones necessary for inducing photoorientation, so that mass migration can indeed occur. Despite the sample being prepared using the same procedure, the amount of material had to be increased. The resulting film was not as homogeneous as the previous samples and not clear. This is a drawback for the recording of SRGs since scattering of the light by the material will occur, affecting the interference fringe between the recording and reference beams.

As discussed before, the materials were synthesised using a combination of different mesogens that were attached to the silsesquioxane core. This strategy was used to produce materials with specific thermal properties (such as a glass transition at room temperature and a nematic mesophase) which are fundamental to retain both the induced photoorientation and SRGs (glass transition at room temperature) and to facilitate the

promotion of an amplification phenomenon that occurs when the material is heated in the mesophase. The material investigated seems to be suitable for photoorientation investigations yet the same cannot be said for the inscription of SRGs. It seems that the co-mesogen approach is not adequate for this last purpose, since polydisperse materials are obtained which can increase the amount of scattering observed. After these analyses we can conclude that the material under investigation has very good film properties suitable for promoting optical anisotropy as show by the circular dichroism value of 0.7.

CHAPTER 8: CONCLUSION AND OUTLOOK

8.1 Conclusions

Several series of liquid crystalline photoactive supermolecular systems were investigated which were based on a central silsesquioxane core. As the photoactive liquid crystal group a laterally connected azobenzene based mesogenic system promoting nematic phase behaviour was developed. The properties of the target materials were modulated by using a series cyanobiphenyl based mesogens as co-mesogens in co-polymerisation type of reactions. For these cyanobiphenyl based mesogens the length of the hydrocarbon spacer and the extension of the aromatic core was varied systematically.

The optimisation target for these systems was to achieve a glass transition above room temperature and exclusively nematic phase behaviour. These goals were achieved.

The purpose of the investigation of nematic photoactive materials was to obtain systems which can be built up in a modular manner and which are accessible by relatively short synthetic routes. The goal was to obtain materials which can be used for photoactive thin film technology, and where the know-how and technology has the potential for a short pull-through to industrial uses.

The project involved the design, synthesis and characterisation of molecular materials based on low molar mass mesogens attached to a cuboid silsesquioxane architecture. The materials designed were optimized in iterative steps having in focus clear parameters, such as transition temperatures, glass transitions and phase behaviour.

The photoactive properties of the prepared materials were studied by UV/vis studies in solution and by $^1\text{H-NMR}$ studies and the dichroic behaviour of the materials was investigated in thin films. Starting from non-oriented films a high photodichroism with a value of 0.7 could be inscribed.

The liquid crystal properties of the materials were characterised by optical polarizing microscopy, differential scanning calorimetry and temperature dependent X-ray diffraction studies of magnetically and mechanically oriented fibres.

A very surprising result of these investigations was that the nematic structure of the investigated systems was found to be much more complex than anticipated. Most of the investigated systems form a lamellar nematic phase, which has rarely been observed before and has so far not been detected for this class of photoactive materials. This observation required extensive studies, of samples aligned in external magnetic fields

and of mechanically uniaxial aligned samples as fibres at various temperatures involving as well the study of realignment processes.

The phase structure these systems form is characterised by a subtle interplay of the volume requirements and the chemical structure of the different mesogens attached to the central core. The phase behaviour observed ranged from almost “typical” nematic structures with SmC like cybotactic clustering, lamellar nematic phase behaviour, with or without clustering to SmA like structures. In structural terms, the wide variety of subtle structural variations of the nematic phase has not been observed before and represents a clear and significant advancement in the knowledge of photoactive self-organized soft matter.

Overall, this project involved, the design of materials and optimisation of their structures focused on clear parameters, synthesis of the materials, their full chemical characterisation, the investigation and characterisation of their photoactive properties in solution and as dichroic thin films and the extensive investigation of the liquid crystal phase behaviour of these materials and their modes of assembly using a wide range of techniques.

8.2 Outlook

Speaking in terms of technological requirements, the achievement of materials with a higher optical dichroism would be an attractive research target. Here the investigation of amplification processes and mass transport processes of photoactive matter is still not fully understood and is an attractive and relevant research target.

In practical synthetic terms the study of materials which could be crosslinked after photoalignment would be an attractive technological target. Here the introduction of photo-crosslinkable groups, sensitive to specific irradiation wavelengths would be interesting.

In terms of wider scientific issues the investigation of the transition from the “normal” nematic phase to the lamellar nematic phase in dependence of molecular composition to the formation of higher ordered LC phases such as the SmA phase and columnar phases observed for structural related materials, would be of high interest, especially in conjunction the ability of switching between phase structures by irradiation.

CHAPTER 9: REFERENCES

- 1 P. Palffy-Muhoray, *Physics Today*, 2007, **60**, 54.
- 2 R. P. Lemieux, *Accounts of Chemical Research*, 2001, **34**, 845.
- 3 J. C. P. Gabriel and P. Davidson, *Advanced Materials*, 2000, **12**, 9.
- 4 M. Baron, *Pure and Applied Chemistry*, 2001, **73**, 845.
- 5 G. W. Smith, Z. G. Gardlund, and R. J. Curtis, *Molecular Crystals and Liquid Crystals*, 1973, **19**, 327.
- 6 G. W. Gray, *Molecular Crystals and Liquid Crystals*, 1973, **21**, 161.
- 7 D. Demus and G. Wartenberg, *Pramana*, 1975, **1**, 363.
- 8 R. Eidenschink, D. Erdmann, J. Krause, and L. Pohl, *Angewandte Chemie*, 1977, **89**, 103.
- 9 S. Chandrasekha, B. K. Sadashiva, and K. A. Suresh, *Pramana*, 1977, **9**, 471.
- 10 N. Boden, R. Borner, D. R. Brown, R. J. Bushby, and J. Clements, *Liquid Crystals*, 1992, **11**, 325.
- 11 H. Zimmermann, R. Poupko, Z. Luz, and J. Billard, *Z. Naturforsch., teil A*, 1985, **40**, 149.
- 12 D. Vorländer, *Ber. Dtsch. Chem. Ges.*, 1929, **62**, 2831.
- 13 D. Vorländer and A. Apel, *Ber. Dtsch. Chem. Ges.*, 1932, **65**, 1101.
- 14 A. Eremin and A. Jakli, *Soft Matter*, 2012, **9**, 615.
- 15 M. A. Bates, *Physical Review E*, 2006, **74**.
- 16 G. R. Luckhurst, *Thin Solid Films*, 2001, **393**, 40.
- 17 P. J. Camp, M. P. Allen, and A. J. Masters, *Journal of Chemical Physics*, 1999, **111**, 9871.
- 18 P. I. C. Teixeira, A. J. Masters, and B. M. Mulder, *Molecular Crystals and Liquid Crystals Science and Technology Section a-Molecular Crystals and Liquid Crystals*, 1998, **323**, 167.
- 19 M. A. Bates and G. R. Luckhurst, *Physical Review E*, 2005, **72**.
- 20 A. M. Donald and A. H. Windle, 'Liquid crystalline polymers', Cambridge University Press, 1992.
- 21 J. W. Goodby, I. M. Saez, S. J. Cowling, V. Gortz, M. Draper, A. W. Hall, S. Sia, G. Cosquer, S.-E. Lee, and E. P. Raynes, *Angewandte Chemie-International Edition*, 2008, **47**, 2754.

- 22 G. W. Gray and Society of Chemical Industry (Great Britain), 'Thermotropic liquid crystals', Published on behalf of the Society of Chemical Industry by John Wiley & Sons, 1987.
- 23 C. Tschierske and D. J. Photinos, *Journal of Materials Chemistry*, 2010, **20**, 4263.
- 24 G. R. Luckhurst, *Angewandte Chemie-International Edition*, 2005, **44**, 2834.
- 25 C. Keith, A. Lehmann, U. Baumeister, M. Prehm, and C. Tschierske, *Soft Matter*, 2010, **6**, 1704.
- 26 L. J. Yu and A. Saupe, *Physical Review Letters*, 1980, **45**, 1000.
- 27 A. M. F. Neto, Y. Galerne, A. M. Levelut, and L. Liebert, *Journal De Physique Lettres*, 1985, **46**, L499.
- 28 A. M. F. Neto, A. M. Levelut, L. Liebert, and Y. Galerne, *Molecular Crystals and Liquid Crystals*, 1985, **129**, 191.
- 29 A. M. F. Neto, L. Liebert, and Y. Galerne, *Journal of Physical Chemistry*, 1985, **89**, 3737.
- 30 H. H. Wensink and G. J. Vroege, *Physical Review E*, 2005, **72**.
- 31 H. H. Wensink, G. J. Vroege, and H. N. W. Lekkerkerker, *Physical Review E*, 2002, **66**.
- 32 A. Stroobants and H. N. W. Lekkerkerker, *Journal of Physical Chemistry*, 1984, **88**, 3669.
- 33 R. Storz, A. Komp, A. Hoffmann, and H. Finkelmann, *Macromolecular Rapid Communications*, 2009, **30**, 615.
- 34 K. Severing, E. Stibal-Fischer, A. Hasenhindl, H. Finkelmann, and K. Saalwachter, *Journal of Physical Chemistry B*, 2006, **110**, 15680.
- 35 K. Severing and K. Saalwachter, *Physical Review Letters*, 2004, **92**.
- 36 H. F. Leube and H. Finkelmann, *Makromolekulare Chemie-Macromolecular Chemistry and Physics*, 1991, **192**, 1317.
- 37 F. Hessel and H. Finkelmann, *Polymer Bulletin*, 1986, **15**, 349.
- 38 C. Cruz, J. L. Figueirinhas, D. Filip, G. Feio, A. C. Ribeiro, Y. Frere, T. Meyer, and G. H. Mehl, *Physical Review E*, 2008, **78**, 051702.
- 39 M. Cardoso, J. L. Figueirinhas, C. Cruz, A. Van-Quynh, A. C. Ribeiro, G. Feio, D. Apreutesei, and G. H. Mehl, *Molecular Crystals and Liquid Crystals*, 2008, **495**, 700.
- 40 A. De Vries, *Mol. Cryst. Liq. Cryst.*, 1970, **10**, 219.

- 41 S. Stojadinovic, A. Adorjan, S. Sprunt, H. Sawade, and A. Jakli, *Physical Review E*, 2002, **66**.
- 42 A. Soldera, M. A. Beaudoin, G. O'Brien, and J. Lessard, *Liquid Crystals*, 2005, **32**, 1223.
- 43 J. M. Montornes, J. A. Reina, and J. C. Ronda, *Journal of Polymer Science Part a-Polymer Chemistry*, 2004, **42**, 3002.
- 44 O. Francescangeli, M. Laus, and G. Galli, *Physical Review E*, 1997, **55**, 481.
- 45 M. F. Achard, S. Lecommandoux, and F. Hardouin, *Liquid Crystals*, 1995, **19**, 581.
- 46 V. Percec, P. W. Chu, G. Ungar, and J. P. Zhou, *Journal of the American Chemical Society*, 1995, **117**, 11441.
- 47 P. K. Karahaliou, P. H. J. Kouwer, T. Meyer, G. H. Mehl, and D. J. Photinos, *Soft Matter*, 2007, **3**, 857.
- 48 P. K. Karahaliou, P. H. J. Kouwer, T. Meyer, G. H. Mehl, and D. J. Photinos, *Journal of Physical Chemistry B*, 2008, **112**, 6550.
- 49 R. Kieffer, M. Prehm, K. Pelz, U. Baumeister, F. Liu, H. Hahn, H. Lang, G. Ungar, and C. Tschierske, *Soft Matter*, 2009, **5**, 1214.
- 50 N. Chattham, C. Zhu, X. Cheng, J. Limtrakul, C. Tschierske, J. E. MacLennan, and N. A. Clark, *Soft Matter*, 2011, **7**, 9978.
- 51 M. Prehm, X. H. Cheng, S. Diele, M. K. Das, and C. Tschierske, *Journal of the American Chemical Society*, 2002, **124**, 12072.
- 52 X. H. Cheng, M. Prehm, M. K. Das, J. Kain, U. Baumeister, S. Diele, D. Leine, A. Blume, and C. Tschierske, *Journal of the American Chemical Society*, 2003, **125**, 10977.
- 53 M. Prehm, S. Diele, M. K. Das, and C. Tschierske, *Journal of the American Chemical Society*, 2003, **125**, 614.
- 54 X. H. Cheng, M. K. Das, S. Diele, and C. Tschierske, *Angewandte Chemie-International Edition*, 2002, **41**, 4031.
- 55 P. Riala, A. Andreopoulou, J. Kallitsis, A. Gitsas, and G. Floudas, *Polymer*, 2006, **47**, 7241.
- 56 T. Kim, L. Arnt, E. Atkins, and G. N. Tew, *Chemistry-a European Journal*, 2006, **12**, 2423.
- 57 B. Carbonnier, T. Pakula, and D. A. M. Egbe, *Journal of Materials Chemistry*, 2005, **15**, 880.

- 58 K. Fu, N. Sekine, M. Sone, M. Tokita, and J. Watanabe, *Polymer Journal*, 2002,
34, 291.
- 59 J. W. Goodby, G. W. Gray, D. Demus, J. Goodby, G. W. Gray, H. W. Spiess,
and V. Vill, in 'Guide to the Nomenclature and Classification of Liquid
Crystals', 1998.
- 60 P. J. Collings, in 'Liquid crystals : nature's delicate phase of matter.' 1990.
61 in 'Nikon microscopy:
<http://www.microscopyu.com/articles/polarized/polarizedintro.html>'.
- 62 I. Dierking, in 'Polarizing Microscopy', 2004.
- 63 R. E. Stoiber and S. A. Morse, 'Crystal Identification with the Polarizing
Microscope', Chapman & Hall, 1994.
- 64 H. F. Gleeson, in 'Liquid Crystal Devices & Their Physics', ed. L. c. w.
workshop, hull, 2010.
- 65 C. S. P. Tripathi, P. Losada-Perez, C. Glorieux, A. Kohlmeier, M.-G. Tamba, G.
H. Mehl, and J. Leys, *Physical Review E*, **84**.
- 66 V. P. Panov, R. Balachandran, M. Nagaraj, J. K. Vij, M. G. Tamba, A.
Kohlmeier, and G. H. Mehl, *Applied Physics Letters*, **99**.
- 67 M. Cestari, S. Diez-Berart, D. A. Dunmur, A. Ferrarini, M. R. de la Fuente, D. J.
B. Jackson, D. O. Lopez, G. R. Luckhurst, M. A. Perez-Jubindo, R. M.
Richardson, J. Salud, B. A. Timimi, and H. Zimmermann, *Physical Review E*,
84.
- 68 A. P and P. J, in 'Atkins' Physical Chemistry', 2010.
- 69 S.Kumar, in 'Liquid crystals Experimental Study of Physical Properties and
Phase Transitions', 2001.
- 70 J. M. Seddon, D. Demus, J. Goodby, G. W. Gray, H. W. Spiess, and V. Vill, in
'Physical Properties of Liquid Crystals', 1998.
- 71 J. M. Seddon, D. Demus, J. Goodby, G. W. Gray, H. W. Spiess, and V. Vill, in
'Structural Studies of Liquid Crystals by X-Ray Diffraction', 1998.
- 72 E. van den Pol, A. V. Petukhov, D. M. E. Thies-Weesie, D. V. Byelov, and G. J.
Vroege, *Physical Review Letters*, 2009, **103**.
- 73 X. H. Cheng, M. K. Das, S. Diele, and C. Tschierske, *Angewandte Chemie
International Edition*, 2002, **41**, 4031.
- 74 S. Kumar, in 'Liquid crystals Experimental Study of Physical Properties and
Phase Transitions', 2001.

- 75 B. Donnio, S. Buathong, I. Bury, and D. Guillon, *Chemical Society Reviews*,
2007, **36**, 1495.
- 76 E. Buhleier, W. Wehner, and F. Vogtle, *Synthesis-Stuttgart*, 1978, 155.
- 77 D. A. Tomalia, H. Baker, J. Dewald, M. Hall, G. Kallos, S. Martin, J. Roeck, J.
Ryder, and P. Smith, *Polymer Journal*, 1985, **17**, 117.
- 78 G. R. Newkome, Z. Q. Yao, G. R. Baker, and V. K. Gupta, *Journal of Organic
Chemistry*, 1985, **50**, 2003.
- 79 A. Cammidge, *Polymer International*, 2003, **52**, 186.
- 80 J. I. Paez, M. Martinelli, V. n. Brunetti, and M. C. Strumia, *Polymers*, 2012, **4**,
355.
- 81 A. Carlmark, C. J. Hawker, A. Hult, and M. Malkoch, *Chemical Society
Reviews*, 2009, **38**, 352.
- 82 J. M. J. a. T. Fréchet, D. A., in 'Introduction to the Dendritic State, in
Dendrimers and Other Dendritic Polymers ', ed. L. John Wiley & Sons,
Chichester, UK, 2002.
- 83 M. V. Walter and M. Malkoch, *Chemical Society Reviews*, 2012, **41**, 4593.
- 84 V. Percec and M. Kawasumi, *Macromolecules*, 1992, **25**, 3843.
- 85 M. Marcos, R. Martin-Rapun, A. Omenat, and J. L. Serrano, *Chemical Society
Reviews*, 2007, **36**, 1889.
- 86 D. Guillon and R. Deschenaux, *Current Opinion in Solid State & Materials
Science*, 2002, **6**, 515.
- 87 B. Donnio and D. Guillon, in 'Liquid crystalline dendrimers and polypedes, in
Supramolecular Polymers Polymeric Betains Oligomers', 2006.
- 88 J. Barbera, B. Donnio, L. Gehringer, D. Guillon, M. Marcos, A. Omenat, and J.
L. Serrano, *Journal of Materials Chemistry*, 2005, **15**, 4093.
- 89 S. A. Ponomarenko, E. A. Rebrov, N. I. Boiko, N. G. Vasilenko, A. M.
Muzafarov, Y. S. Freidzon, and V. P. Shibaev, *Vysokomolekulyarnye
Soedineniya Seriya a & Seriya B*, 1994, **36**, 1086.
- 90 S. A. Ponomarenko and V. P. shibaev, *Polymer Science, Ser. C*, 2001, **43**, 1.
- 91 G. H. Mehl and J. W. Goodby, *Chemische Berichte*, 1996, **129**, 521.
- 92 K. Merkel, A. Kocot, J. K. Vij, G. H. Mehl, and T. Meyer, *Journal of Chemical
Physics*, 2004, **121**, 5012.
- 93 C. P. J. Schubert, M. G. Tamba, and G. H. Mehl, *Chemical Communications*,
2012, **48**, 6851.

- 94 C. Keith, G. Dantlgraber, R. A. Reddy, U. Baumeister, M. Prehm, H. Hahn, H.
Lang, and C. Tschierske, *Journal of Materials Chemistry*, 2007, **17**, 3796.
- 95 H. Ocak, B. Bilgin-Eran, M. Prehm, and C. Tschierske, *Soft Matter*, 2012, **8**,
7773.
- 96 D. B. Cordes, P. D. Lickiss, and F. Rataboul, *Chemical Reviews*, 2010, **110**,
2081.
- 97 D. Gnanasekaran, K. Madhavan, and B. S. R. Reddy, *Journal of Scientific &
Industrial Research*, 2009, **68**, 437.
- 98 R. M. Laine, *Journal of Materials Chemistry*, 2005, **15**, 3725.
- 99 B. Donnio, S. Buathong, I. Bury, and D. Guillon, *Chemical Society Reviews*,
2007, **36**, 1495.
- 100 L. Cui, J. P. Collet, G. Xu, and L. Zhu, *Chemistry of Materials*, 2006, **18**, 3503.
- 101 F. J. Feher, D. Soulivong, A. G. Eklund, and K. D. Wyndham, *Chemical
Communications*, 1997, 1185.
- 102 F. J. Feher, T. A. Budzichowski, R. L. Blanski, K. J. Weller, and J. W. Ziller,
Organometallics, 1991, **10**, 2526.
- 103 F. J. Feher, D. A. Newman, and J. F. Walzer, *Journal of the American Chemical
Society*, 1989, **111**, 1741.
- 104 J. R. Severn, R. Duchateau, R. A. van Santen, D. D. Ellis, and A. L. Spek,
Organometallics, 2002, **21**, 4.
- 105 R. Duchateau, H. C. L. Abbenhuis, R. A. van Santen, A. Meetsma, S. K. H.
Thiele, and M. F. H. van Tol, *Organometallics*, 1998, **17**, 5663.
- 106 F. J. Feher and R. L. Blanski, *Journal of the American Chemical Society*, 1992,
114, 5886.
- 107 N. Maxim, P. Magusin, P. J. Kooyman, J. van Wolput, R. A. van Santen, and H.
C. L. Abbenhuis, *Chemistry of Materials*, 2001, **13**, 2958.
- 108 C. Bonhomme, P. Toledano, J. Maquet, J. Livage, and L. BonhommeCoury,
Journal of the Chemical Society-Dalton Transactions, 1997, 1617.
- 109 A. R. Bassindale, D. J. Parker, M. Pourny, P. G. Taylor, P. N. Horton, and M. B.
Hursthouse, *Organometallics*, 2004, **23**, 4400.
- 110 A. R. Bassindale, M. Pourny, P. G. Taylor, M. B. Hursthouse, and M. E. Light,
Angewandte Chemie-International Edition, 2003, **42**, 3488.
- 111 R. Y. Kannan, H. J. Salacinski, P. E. Butler, and A. M. Seifalian, *Accounts of
Chemical Research*, 2005, **38**, 879.
- 112 M. S. Soh, A. Sellinger, and A. U. J. Yap, *Current Nanoscience*, 2006, **2**, 373.

- 113 D.Hoebbel, I. Pitsch, and D. Heidemann, *Eurogel* 1992, **91**, 467.
- 114 I. HASEGAWA, *Journal of Sol-Gel Science and Technology*, 1993, **1**, 57.
- 115 I. Hasegawa and S. Motojima, *Journal of Organometallic Chemistry*, 1992, **441**,
373.
- 116 J. J. Schwab and J. D. Lichtenhan, *Applied Organometallic Chemistry*, 1998, **12**,
707.
- 117 M. E. Wright, D. A. Schorzman, F. J. Feher, and R. Z. Jin, *Chemistry of
Materials*, 2003, **15**, 264.
- 118 S.-C. Chan, S.-W. Kuo, H.-S. She, H.-M. Lin, H.-F. Lee, and F.-C. Chang,
Journal of Polymer Science Part a-Polymer Chemistry, 2007, **45**, 125.
- 119 Y. Ni and S. Zheng, *Journal of Polymer Science Part a-Polymer Chemistry*,
2007, **45**, 1247.
- 120 L. Zheng, R. J. Farris, and E. B. Coughlin, *Journal of Polymer Science Part a-
Polymer Chemistry*, 2001, **39**, 2920.
- 121 T. S. Haddad and J. D. Lichtenhan, *Macromolecules*, 1996, **29**, 7302.
- 122 M. Ikeda and H. Saito, *Reactive & Functional Polymers*, 2007, **67**, 1148.
- 123 M. Z. Asuncion, I. Hasegawa, J. W. Kampf, and R. M. Laine, *Journal of
Materials Chemistry*, 2005, **15**, 2114.
- 124 G. H. Mehl and I. M. Saez, *Applied Organometallic Chemistry*, 1999, **13**, 261.
- 125 J. Y. Park, M. G. Kim, and J.-B. Kim, *Macromolecular Rapid Communications*,
2008, **29**, 1532.
- 126 I. Hasegawa, W. Imamura, and T. Takayama, *Inorganic Chemistry
Communications*, 2004, **7**, 513.
- 127 M. S. Soh, A. U. J. Yap, and A. Sellinger, *European Polymer Journal*, 2007, **43**,
315.
- 128 R. Gunawidjaja, F. Huang, M. Gumenna, N. Klimenko, G. A. Nunnery, V.
Shevchenko, R. Tannenbaum, and V. V. Tsukruk, *Langmuir*, 2009, **25**, 1196.
- 129 S. Sulaiman, A. Bhaskar, J. Zhang, R. Guda, T. Goodson, III, and R. M. Laine,
Chemistry of Materials, 2008, **20**, 5563.
- 130 M. F. Roll, M. Z. Asuncion, J. Kampf, and R. M. Laine, *Acs Nano*, 2008, **2**, 320.
- 131 M. Z. Asuncion, M. F. Roll, and R. M. Laine, *Macromolecules*, 2008, **41**, 8047.
- 132 G. Cheng, N. R. Vautravers, R. E. Morris, and D. J. Cole-Hamilton, *Organic &
Biomolecular Chemistry*, 2008, **6**, 4662.
- 133 K. Takahashi, S. Sulaiman, J. M. Katzenstein, S. Snoblen, and R. M. Laine,
Australian Journal of Chemistry, 2006, **59**, 564.

- 134 C. M. Brick, R. Tamaki, S. G. Kim, M. Z. Asuncion, M. Roll, T. Nemoto, Y.
Ouchi, Y. Chujo, and R. A. Laine, *Macromolecules*, 2005, **38**, 4655.
- 135 Y. Hagiwara, A. Shimojima, and K. Kuroda, *Chemistry of Materials*, 2008, **20**,
1147.
- 136 G. H. Mehl and J. W. Goodby, *Angewandte Chemie-International Edition in
English*, 1996, **35**, 2641.
- 137 I. M. Saez and J. W. Goodby, *Liquid Crystals*, 1999, **26**, 1101.
- 138 A. Sellinger, R. M. Laine, V. Chu, and C. Viney, *Journal of Polymer Science
Part a-Polymer Chemistry*, 1994, **32**, 3069.
- 139 C. X. Zhang, T. J. Bunning, and R. M. Laine, *Chemistry of Materials*, 2001, **13**,
3653.
- 140 F. H. Kreuzer, R. Maurer, and P. Spes, *Makromolekulare Chemie-
Macromolecular Symposia*, 1991, **50**, 215.
- 141 R. Elsasser, G. H. Mehl, J. W. Goodby, and D. J. Photinos, *Chemical
Communications*, 2000, 851.
- 142 I. M. Saez, J. W. Goodby, and R. M. Richardson, *Chemistry-a European
Journal*, 2001, **7**, 2758.
- 143 K. M. Kim and Y. Chujo, *Journal of Polymer Science Part a-Polymer
Chemistry*, 2001, **39**, 4035.
- 144 K.-M. Kim and Y. Chujo, *Polymer Bulletin*, 2001, **46**, 15.
- 145 K. H. Kim and Y. Chujo, *Polymer Bulletin*, 2001, **46**, 15.
- 146 Q. Pan, X. Chen, X. Fan, Z. Shen, and Q. Zhou, *Journal of Materials Chemistry*,
2008, **18**, 3481.
- 147 E. Bialecka-Florjanczyk and J. T. Soltysiak, *Journal of Organometallic
Chemistry*, 2010, **695**, 1911.
- 148 X. Wang, C. M. Cho, W. Y. Say, A. Y. X. Tan, C. He, H. S. O. Chan, and J. Xu,
Journal of Materials Chemistry, 2011, **21**, 5248.
- 149 H. Durr and H. Bouas-Laurent, 'Photochromism molecules and systems',
Elsevier, 2003.
- 150 K. G. Yager and C. J. Barrett, in 'Azobenzene Polymers for Photonic
Applications', 2008.
- 151 G. S. Hartley, *Nature*, 1937, 281.
- 152 C. Barrett, A. Natansohn, and P. Rochon, *Macromolecules*, 1994, **27**, 4781.
- 153 T. Seki, *Bulletin of the Chemical Society of Japan*, 2007, **80**, 2084.

- 154 K. G. Yager and C. J. Barrett, *Journal of Photochemistry and Photobiology a-
Chemistry*, 2006, **182**, 250.
- 155 A. Natansohn and P. Rochon, *Chemical Reviews*, 2002, **102**, 4139.
- 156 J. Stumpe, O. Kulikovska, L. M. Goldenberg, and Y. Zakrevskyy, in 'Photo-
Induced Phenomena in Supramolecular Azobenzene Materials', 2008.
- 157 T. Seki, *Polymer Journal*, 2004, **36**, 435.
- 158 J. Trzaska and Z. Galewski, *Opto-Electronics Review*, 2009, **17**, 129.
- 159 M. Parra, P. Hidalgo, E. Carrasco, J. Barbera, and L. Silvino, *Liquid Crystals*,
2006, **33**, 875.
- 160 J. Garcia-Amoros, A. Szymczyk, and D. Velasco, *Physical Chemistry Chemical
Physics*, 2009, **11**, 4244.
- 161 K. Ichimura, *Chemical Reviews*, 2000, **100**, 1847.
- 162 T. Ikeda, *Journal of Materials Chemistry*, 2003, **13**, 2037.
- 163 T. Ikeda, M. Nakano, Y. L. Yu, O. Tsutsumi, and A. Kanazawa, *Advanced
Materials*, 2003, **15**, 201.
- 164 Y. L. Yu and T. Ikeda, *Macromolecular Chemistry and Physics*, 2005, **206**,
1705.
- 165 U. Wiesner, N. Reynolds, C. Boeffel, and H. W. Spiess, *Makromolekulare
Chemie-Rapid Communications*, 1991, **12**, 457.
- 166 J. Stumpe, L. Lasker, T. Fischer, M. Rutloh, S. Kostromin, and R. Ruhmann,
Thin Solid Films, 1996, **284**, 252.
- 167 T. Ikeda, S. Horiuchi, D. B. Karanjit, S. Kurihara, and S. Tazuke,
Macromolecules, 1990, **23**, 36.
- 168 T. Ikeda, S. Horiuchi, D. B. Karanjit, S. Kurihara, and S. Tazuke,
Macromolecules, 1990, **23**, 36.
- 169 T. Ikeda, T. Miyamoto, S. Kurihara, and S. Tazuke, *Molecular Crystals and
Liquid Crystals Incorporating Nonlinear Optics*, 1990, **188**, 223.
- 170 T. Ikeda, T. Miyamoto, T. Sasaki, S. Kurihara, and S. Tazuke, *Molecular
Crystals and Liquid Crystals Incorporating Nonlinear Optics*, 1990, **188**, 235.
- 171 T. Ikeda, T. Sasaki, and H. B. Kim, *Journal of Physical Chemistry*, 1991, **95**,
509.
- 172 T. Sasaki, T. Ikeda, and K. Ichimura, *Macromolecules*, 1992, **25**, 3807.
- 173 T. Ikeda and O. Tsutsumi, *Science*, 1995, **268**, 1873.
- 174 O. Tsutsumi, Y. Demachi, A. Kanazawa, T. Shiono, T. Ikeda, and Y. Nagase,
Journal of Physical Chemistry B, 1998, **102**, 2869.

- 175 M. Hasegawa, T. Yamamoto, A. Kanazawa, T. Shiono, and T. Ikeda, *Advanced Materials*, 1999, **11**, 675.
- 176 M. Hasegawa, T. Yamamoto, A. Kanazawa, T. Shiono, and T. Ikeda, *Chemistry of Materials*, 1999, **11**, 2764.
- 177 T. Yamamoto, A. Ohashi, S. Yoneyama, M. Hasegawa, O. Tsutsumi, A. Kanazawa, T. Shiono, and T. Ikeda, *Journal of Physical Chemistry B*, 2001, **105**, 2308.
- 178 A. S. Matharu, S. Jeeva, and P. S. Ramanujam, *Chemical Society Reviews*, 2007, **36**, 1868.
- 179 K. Ichimura, Y. Suzuki, T. Seki, A. Hosoki, and K. Aoki, *Langmuir*, 1988, **4**, 1214.
- 180 H. S. Blair, H. I. Pague, and J. E. Riordan, *Polymer*, 1980, **21**, 1195.
- 181 H. S. Blair and C. B. McArdle, *Polymer*, 1984, **25**, 1347.
- 182 K. Kago, M. F \ddot{A} rst, H. Matsuoka, H. Yamaoka, and T. Seki, *Langmuir*, 1999, **15**, 2237.
- 183 H. Finkelmann, E. Nishikawa, G. G. Pereira, and M. Warner, *Physical Review Letters*, 2001, **87**, 015501.
- 184 P. M. Hogan, A. R. Tajbakhsh, and E. M. Terentjev, *Physical Review E*, 2002, **65**, 041720.
- 185 M. H. Li, P. Keller, B. Li, X. G. Wang, and M. Brunet, *Advanced Materials*, 2003, **15**, 569.
- 186 Y. L. Yu, M. Nakano, A. Shishido, T. Shiono, and T. Ikeda, *Chemistry of Materials*, 2004, **16**, 1637.
- 187 Y. L. Yu, M. Nakano, and T. Ikeda, *Pure and Applied Chemistry*, 2004, **76**, 1467.
- 188 Y. L. Yu, M. Nakano, and T. Ikeda, *Nature*, 2003, **425**, 145.
- 189 M. Camacho-Lopez, H. Finkelmann, P. Palffy-Muhoray, and M. Shelley, *Nature Materials*, 2004, **3**, 307.
- 190 N. Tabiryan, S. Serak, X. M. Dai, and T. Bunning, *Optics Express*, 2005, **13**, 7442.
- 191 C. Li, C.-W. Lo, D. Zhu, C. Li, Y. Liu, and H. Jiang, *Macromolecular Rapid Communications*, 2009, **30**, 1928.
- 192 C. S. Li, C. W. Lo, D. F. Zhu, C. H. Li, Y. Liu, and H. R. Jiang, *Macromolecular Rapid Communications*, 2009, **30**, 1928.

- 193 T. Todorov, N. Tomova, and L. Nikolova, *Optics Communications*, 1983, **47**,
123.
- 194 A. Natansohn, P. Rochon, M. Pezolet, P. Audet, D. Brown, and S. To,
Macromolecules, 1994, **27**, 2580.
- 195 R. Hagen and T. Bieringer, *Advanced Materials*, 2001, **13**, 1805.
- 196 A. Y. Bobrovsky, A. A. Pakhomov, X. M. Zhu, N. I. Boiko, V. P. Shibaev, and
J. Stumpe, *Journal of Physical Chemistry B*, 2002, **106**, 540.
- 197 R. Deloncle and A.-M. Caminade, *Journal of Photochemistry and Photobiology
C-Photochemistry Reviews*, 2010, **11**, 25.
- 198 J. P. Majoral and A. M. Caminade, *Chemical Reviews*, 1999, **99**, 845.
- 199 A. Momotake and T. Arai, *Polymer*, 2004, **45**, 5369.
- 200 A. Momotake and T. Arai, *Journal of Photochemistry and Photobiology C-
Photochemistry Reviews*, 2004, **5**, 1.
- 201 H. B. Mekelburger, K. Rissanen, and F. Vogtle, *Chemische Berichte-Recueil*,
1993, **126**, 1161.
- 202 A. Archut, F. Vogtle, L. De Cola, G. C. Azzellini, V. Balzani, P. S. Ramanujam,
and R. H. Berg, *Chemistry-a European Journal*, 1998, **4**, 699.
- 203 N. Boiko, X. M. Zhu, A. Bobrovsky, and V. Shibaev, *Chemistry of Materials*,
2001, **13**, 1447.
- 204 X. T. Wang, Y. K. Yang, Z. F. Yang, X. P. Zhou, Y. G. Liao, C. C. Lv, F. C.
Chang, and X. L. Xie, *Journal of Thermal Analysis and Calorimetry*, 2010, **102**,
739.
- 205 X. Su, S. Guang, H. Xu, X. Liu, S. Li, X. Wang, Y. Deng, and P. Wang,
Macromolecules, 2009, **42**, 8969.
- 206 E. Bialecka-Florjanczyk and J. T. Soltysiak, *Molecular Crystals and Liquid
Crystals*, 2011, **548**, 28.
- 207 F. Weigert, *Dt. Physik. Ges.*, , 1919, **21**, 479.
- 208 N. K. Viswanathan, D. Y. Kim, S. P. Bian, J. Williams, W. Liu, L. Li, L.
Samuelson, J. Kumar, and S. K. Tripathy, *Journal of Materials Chemistry*, 1999,
9, 1941.
- 209 A. Natansohn and P. Rochon, in 'Azobenzene-containing polymers: Digital and
holographic storage', 1997.
- 210 Y. Q. Shi, W. H. Steier, L. P. Yu, M. Chen, and L. R. Dalton, *Applied Physics
Letters*, 1991, **59**, 2935.
- 211 A. Natansohn and P. Rochon, *Advanced Materials*, 1999, **11**, 1387.

- 212 Y. Shi, W. H. Steier, L. Yu, M. Chen, and L. R. Dalton, *Applied Physics Letters*,
1991, **58**, 1131.
- 213 O. Watanabe, M. Tsuchimori, and A. Okada, *Journal of Materials Chemistry*,
1996, **6**, 1487.
- 214 A. Shishido, O. Tsutsumi, A. Kanazawa, T. Shiono, T. Ikeda, and N. Tamai,
Journal of the American Chemical Society, 1997, **119**, 7791.
- 215 J. A. Delaire and K. Nakatani, *Chemical Reviews*, 2000, **100**, 1817.
- 216 T. Todorov, L. Nikolova, and N. Tomova, *Applied Optics*, 1984, **23**, 4309.
- 217 A. Natansohn, P. Rochon, X. S. Meng, C. Barrett, T. Buffeteau, S. Bonenfant,
and M. Pezolet, *Macromolecules*, 1998, **31**, 1155.
- 218 O. K. Song, C. H. Wang, and M. A. Pauley, *Macromolecules*, 1997, **30**, 6913.
- 219 T. Buffeteau, A. Natansohn, P. Rochon, and M. Pezolet, *Macromolecules*, 1996,
29, 8783.
- 220 M. S. Ho, A. Natansohn, and P. Rochon, *Macromolecules*, 1995, **28**, 6124.
- 221 P. Rochon, J. Gosselin, A. Natansohn, and S. Xie, *Applied Physics Letters*,
1992, **60**, 4.
- 222 R. H. Tredgold, R. A. Allen, P. Hodge, and E. Khoshdel, *Journal of Physics D-
Applied Physics*, 1987, **20**, 1385.
- 223 K. Anderle, R. Birenheide, M. Eich, and J. H. Wendorff, *Makromolekulare
Chemie-Rapid Communications*, 1989, **10**, 477.
- 224 K. Anderle, R. Birenheide, M. J. A. Werner, and J. H. Wendorff, *Liquid
Crystals*, 1991, **9**, 691.
- 225 S. Ivanov, I. Yakovlev, S. Kostromin, V. Shibaev, L. Lasker, J. Stumpe, and D.
Kreysig, *Makromolekulare Chemie-Rapid Communications*, 1991, **12**, 709.
- 226 H. Yu and T. Ikeda, *Advanced Materials*, 2011, **23**, 2149.
- 227 L. Lasker, J. Stumpe, T. Fischer, M. Rutloh, S. Kostromin, and R. Ruhmann,
*Molecular Crystals and Liquid Crystals Science and Technology Section a-
Molecular Crystals and Liquid Crystals*, 1995, **261**, 371.
- 228 Y. L. Wu, Y. Demachi, O. Tsutsumi, A. Kanazawa, T. Shiono, and T. Ikeda,
Macromolecules, 1998, **31**, 349.
- 229 Y. L. Wu, Y. Demachi, O. Tsutsumi, A. Kanazawa, T. Shiono, and T. Ikeda,
Macromolecules, 1998, **31**, 1104.
- 230 Y. L. Wu, Y. Demachi, O. Tsutsumi, A. Kanazawa, T. Shiono, and T. Ikeda,
Macromolecules, 1998, **31**, 4457.

- 231 Y. L. Wu, A. Kanazawa, T. Shiono, T. Ikeda, and Q. J. Zhang, *Polymer*, 1999,
40, 4787.
- 232 Y. L. Wu, Q. J. Zhang, A. Kanazawa, T. Shiono, T. Ikeda, and Y. Nagase,
Macromolecules, 1999, **32**, 3951.
- 233 R. Loucifsaibi, K. Nakatani, J. A. Delaire, M. Dumont, and Z. Sekkat, *Chemistry
of Materials*, 1993, **5**, 229.
- 234 M. Dumont and Z. Sekkat, in 'Dynamic Study of Photoinduced Anisotropy and
Orientational Relaxation of Azo Dyes in Polymeric Films - Poling at Room-
Temperature', 1993.
- 235 H. Yu and T. Ikeda, *Advanced Materials*, **23**, 2149.
- 236 X. Meng, A. Natansohn, C. Barrett, and P. Rochon, *Macromolecules*, 1996, **29**,
946.
- 237 M. Eich and J. H. Wendorff, *Makromolekulare Chemie-Rapid Communications*,
1987, **8**, 467.
- 238 M. Eich, J. H. Wendorff, B. Reck, and H. Ringsdorf, *Makromolekulare Chemie-
Rapid Communications*, 1987, **8**, 59.
- 239 K. Okano, O. Tsutsumi, A. Shishido, and T. Ikeda, *Journal of the American
Chemical Society*, 2006, **128**, 15368.
- 240 K. Okano, A. Shishido, and T. Ikeda, *Advanced Materials*, 2006, **18**, 523.
- 241 K. Okano, A. Shishido, and T. Ikeda, *Macromolecules*, 2006, **39**, 145.
- 242 K. Okano, A. Shishido, O. Tsutsumi, T. Shiono, and T. Ikeda, *Journal of
Materials Chemistry*, 2005, **15**, 3395.
- 243 T. Fischer, L. Lasker, M. Rutloh, S. Czaplá, and J. Stumpe, *Molecular Crystals
and Liquid Crystals Science and Technology Section a-Molecular Crystals and
Liquid Crystals*, 1997, **299**, 293.
- 244 J. Stumpe, T. Fischer, M. Rutloh, R. Rosenhauer, and J. G. Meier, in
'Photoinduced alignment of LC polymers by the combination of photoorientation
and thermotropic self-organization', 1999.
- 245 J. Stumpe, L. Muller, D. Kreysig, G. Hauck, H. D. Koswig, R. Ruhmann, and J.
Rubner, *Makromolekulare Chemie-Rapid Communications*, 1991, **12**, 81.
- 246 L. Lasker, T. Fischer, J. Stumpe, S. Kostromin, S. Ivanov, V. Shibaev, and R.
Ruhmann, *Molecular Crystals and Liquid Crystals Science and Technology
Section a-Molecular Crystals and Liquid Crystals*, 1994, **246**, 347.

- 247 L. Lasker, T. Fischer, J. Stumpe, S. Kostromin, S. Ivanov, V. Shibaev, and R.
Ruhmann, *Molecular Crystals and Liquid Crystals Science and Technology*
Section a-Molecular Crystals and Liquid Crystals, 1994, **252**, 293.
- 248 T. Fischer, L. Lasker, S. Czapla, J. Rubner, and J. Stumpe, *Molecular Crystals*
and Liquid Crystals Science and Technology Section a-Molecular Crystals and
Liquid Crystals, 1997, **297**, 489.
- 249 S. J. Zilker, T. Bieringer, D. Haarer, R. S. Stein, J. W. van Egmond, and S. G.
Kostromine, *Advanced Materials*, 1998, **10**, 855.
- 250 R. Siewertsen, H. Neumann, B. Buchheim-Stehn, R. Herges, C. Naether, F.
Renth, and F. Temps, *Journal of the American Chemical Society*, 2009, **131**,
15594.
- 251 D. Gabor, *Nature*, 1948, **4098**, 777.
- 252 F.-K. Bruder, R. Hagen, T. Roelle, M.-S. Weiser, and T. Faecke, *Angewandte*
Chemie-International Edition, 2011, **50**, 4552.
- 253 H. Y. a. T. Kobayashi, 'Azobenzene-Containing Materials for Hologram,
Holograms - Recording Materials and Applications, Izabela Naydenova (Ed.)
InTech, Available from: [http://www.intechopen.com/books/holograms-
recording-materials-and-applications/azobenzene-containing-materials-for-
hologram](http://www.intechopen.com/books/holograms-recording-materials-and-applications/azobenzene-containing-materials-for-hologram)', 2011.
- 254 Y. L. Yu and T. Ikeda, *Journal of Photochemistry and Photobiology C-
Photochemistry Reviews*, 2004, **5**, 247.
- 255 X. L. Jiang, J. Kumar, D. Y. Kim, V. Shivshankar, and S. K. Tripathy, *Applied*
Physics Letters, 1996, **68**, 2618.
- 256 K. G. Yager and C. J. Barrett, in 'Azobenzene Polymers for Photonic
Applications', 2006.
- 257 L. M. Goldenberg, Y. Gritsai, O. Kulikovska, and J. Stumpe, *Optics Letters*,
2008, **33**, 1309.
- 258 S. Choi, K. R. Kim, K. Oh, C. M. Chun, M. J. Kim, S. J. Yoo, and D. Y. Kim,
Applied Physics Letters, 2003, **83**, 1080.
- 259 J. W. Kang, M. J. Kim, J. P. Kim, S. J. Yoo, J. S. Lee, D. Y. Kim, and J. J. Kim,
Applied Physics Letters, 2003, **82**, 3823.
- 260 C. Ye, K. Y. Wong, Y. He, and X. Wang, *Optics Express*, 2007, **15**, 936.
- 261 P. Rochon, E. Batalla, and A. Natansohn, *Applied Physics Letters*, 1995, **66**,
136.

- 262 D. Y. Kim, S. K. Tripathy, L. Li, and J. Kumar, *Applied Physics Letters*, 1995,
66, 1166.
- 263 Y. Shirota, K. Moriwaki, S. Yoshikawa, T. Ujike, and H. Nakano, *Journal of*
Materials Chemistry, 1998, **8**, 2579.
- 264 H. Nakano, T. Takahashi, T. Kadota, and Y. Shirota, *Advanced Materials*, 2002,
14, 1157.
- 265 J. G. Victor and J. M. Torkelson, *Macromolecules*, 1987, **20**, 2241.
- 266 C. Sanchez, R. Alcala, S. Hvilsted, and P. S. Ramanujam, *Applied Physics*
Letters, 2000, **77**, 1440.
- 267 C. Jager, T. Bieringer, and S. J. Zilker, *Applied Optics*, 2001, **40**, 1776.
- 268 K. G. Yager and C. J. Barrett, *Current Opinion in Solid State & Materials*
Science, 2001, **5**, 487.
- 269 Y. Zakrevskyy, J. Stumpe, and C. F. J. Faul, *Advanced Materials*, 2006, **18**,
2133.
- 270 M. Helgert, L. Wenke, S. Hvilsted, and P. S. Ramanujam, *Applied Physics B-*
Lasers and Optics, 2001, **72**, 429.
- 271 D. Bublitz, M. Helgert, B. Fleck, L. Wenke, S. Hvilsted, and P. S. Ramanujam,
Applied Physics B-Lasers and Optics, 2000, **70**, 863.
- 272 N. C. R. Holme, L. Nikolova, S. Hvilsted, P. H. Rasmussen, R. H. Berg, and P.
S. Ramanujam, *Applied Physics Letters*, 1999, **74**, 519.
- 273 X. L. Jiang, L. Li, J. Kumar, D. Y. Kim, and S. K. Tripathy, *Applied Physics*
Letters, 1998, **72**, 2502.
- 274 H. S. Nalwa, 'Polymeric Nanostructures and Their Applications', American
Scientific Publishers, 2006.
- 275 S. Z. Yang, L. Li, A. L. Cholli, J. Kumar, and S. K. Tripathy, *Journal of*
Macromolecular Science-Pure and Applied Chemistry, 2001, **38**, 1345.
- 276 Z. Mahimwalla, K. G. Yager, J.-i. Mamiya, A. Shishido, A. Priimagi, and C. J.
Barrett, *Polymer Bulletin*, **69**, 967.
- 277 K. G. Yager and C. J. Barrett, "Light-Induced Nanostructure Formation using
Azobenzene Polymers" in *the Encyclopedia of NanoScience and*
NanoTechnology, H. S. Nalwa and S. Miyata, eds., CRC Press, Boca Raton,
Florida (2006). Chapter 5, 243–272.' 2006.
- 278 D. Zhao, Z. Xu, G. Wang, H. Cao, W. Li, W. He, W. Huang, Z. Yang, and H.
Yang, *Physical Chemistry Chemical Physics*, **12**, 1436.

- 279 O. Kulikovska, L. Kulikovsky, L. M. Goldenberg, and J. Stumpe, in 'Generation
of microstructures in novel supramolecular ionic materials based on azobenzene
- art. no. 69990I', 2008.
- 280 C. J. Barrett, A. L. Natansohn, and P. L. Rochon, *Journal of Physical Chemistry*,
1996, **100**, 8836.
- 281 A. Stracke, J. H. Wendorff, D. Goldmann, and D. Janietz, *Liquid Crystals*, 2000,
27, 1049.
- 282 N. Zettsu, T. Fukuda, H. Matsuda, and T. Seki, *Applied Physics Letters*, 2003,
83, 4960.
- 283 Y. Morikawa, S. Nagano, K. Watanabe, K. Kamata, T. Iyoda, and T. Seki,
Advanced Materials, 2006, **18**, 883.
- 284 A. Knoll, A. Horvat, K. S. Lyakhova, G. Krausch, G. J. A. Sevink, A. V.
Zvelindovsky, and R. Magerle, *Physical Review Letters*, 2002, **89**.
- 285 H. F. Yu, K. Okano, A. Shishido, T. Ikeda, K. Kamata, M. Komura, and T.
Iyoda, *Advanced Materials*, 2005, **17**, 2184.
- 286 J. Tomczyk, A. Sobolewska, Z. T. Nagy, D. Guillon, B. Donnio, and J. Stumpe,
Journal of Materials Chemistry C, **1**, 924.
- 287 D. Nicholls and Warburto.Ba, *Journal of the Chemical Society a -Inorganic
Physical Theoretical*, 1970, 346.
- 288 A. Sanchez and R. H. Derossi, *Journal of Organic Chemistry*, 1993, **58**, 2094.
- 289 P. Liu, L. Huang, and M. M. Faul, *Tetrahedron Letters*, 2007, **48**, 7380.